UCLA
UCLA Electronic Theses and Dissertations

Title
Multiscale Computational Fluid Dynamics Modeling: Parallelization and Application to Design and Control of Plasma-Enhanced Chemical Vapor Deposition of Thin Film Solar Cells

Permalink
https://escholarship.org/uc/item/7c26z2d3

Author
Crose, Marquis Grant

Publication Date
2018

Peer reviewed|Thesis/dissertation

eScholarship.org Powered by the California Digital Library
University of California

UNIVERSITY OF CALIFORNIA

Los Angeles

Multiscale Computational Fluid Dynamics Modeling: Parallelization and Application to Design and Control of Plasma-Enhanced Chemical Vapor Deposition of Thin Film Solar Cells

A dissertation submitted in partial satisfaction of the
requirements for the degree Doctor of Philosophy
in Chemical Engineering

by

Marquis Grant Crose

2018

ABSTRACT OF THE DISSERTATION

Multiscale Computational Fluid Dynamics Modeling: Parallelization and Application to Design and Control of Plasma-Enhanced Chemical Vapor Deposition of Thin Film Solar Cells

by

Marquis Grant Crose

Doctor of Philosophy in Chemical Engineering

University of California, Los Angeles, 2018

Professor Panagiotis D. Christofides, Chair

Today, plasma-enhanced chemical vapor deposition (PECVD) remains the dominant processing method for the manufacture of silicon thin films due to inexpensive production and low operating temperatures. Nonetheless, thickness non-uniformity continues to prevent the deposition of high quality thin film layers across large wafer substrates; thickness deviations up to 20% are typical for 200 mm and above wafers. Regardless of industry, be it solar cell production or microelectronic devices, the demand for densely packed die with high quality creates a need for improved modeling and operational strategies. Over the past two decades, a number of research groups have built microscopic models for thin film growth, as well as macroscopic reactor models to approximate the gas phase reaction and transport phenomena present within PECVD systems. Unfortunately, many of the proposed modeling and simulation techniques have been overly simplified in order to reduce computational demands, or fail to capture both the macro- and microscopic domains simultaneously. In order to address persistent issues related to thickness non-uniformity in silicon processing, advanced multiscale models are needed.

Motivated by these considerations, novel reactor modeling and operational control strategies are developed in this dissertation. Specifically, a macroscopic reactor scale model is presented

which captures the creation of a radio frequency (RF) plasma, transport throughout the reactor domain, and thirty-four dominant plasma-phase reactions. In Chapters 2 and 3, the gas-phase dynamics are approximated using a first principles-based model, whereas the latter half of this dissertation relies on a computational fluid dynamics approach. At the microscopic scale, the complex particle interactions that define the growth of *a*-Si:H thin film layers are tracked using a hybrid kinetic Monte Carlo algorithm. These scales are linked via a dynamic boundary condition which is updated at the completion of each time step. A computationally efficient parallel programming scheme allows for significantly shortened computational times and solutions to previously infeasible system sizes. Transient batch deposition cycles using the aforementioned multiscale model provide new insight into the operation of PECVD systems; spatial non-uniformity in the concentration of SiH_3 and H above the substrate surface is recognized as the primary mechanism responsible for non-uniform thin film product thicknesses. Two key modes are identified to address the aforementioned non-uniformity: (1) run-to-run control of the wafer substrate temperature through the adaptation of an exponentially-weighted moving average algorithm, and (2) the design of new CVD geometries which minimize spatial variations in the concentration of deposition species. These efforts have resulted in optimized PECVD showerhead designs and spatial temperature profiles which limit the thin film thickness non-uniformity to within 1% of the product specification.

The dissertation of Marquis Grant Crose is approved.

Dante A. Simonetti

Philippe Sautet

Mathieu Bauchy

Panagiotis D. Christofides, Committee Chair

University of California, Los Angeles

2018

Contents

List of Figures viii

List of Tables xiii

1 Introduction 1
- 1.1 Motivation . . . 1
- 1.2 Objectives and Organization of the Dissertation . . . 4

2 Multiscale Modeling for PECVD of Thin Film Solar Cells 7
- 2.1 Introduction . . . 7
- 2.2 PECVD process description and modeling . . . 9
  - 2.2.1 Gas phase model . . . 9
  - 2.2.2 Surface microstructure model . . . 10
- 2.3 Open-loop results . . . 18
  - 2.3.1 Growth rates and roughness . . . 18
  - 2.3.2 Film surface morphology at light wavelength scale . . . 21
  - 2.3.3 Film thickness non-uniformity . . . 22
- 2.4 Regulation of film thickness . . . 26
  - 2.4.1 Growth rate relations . . . 26
  - 2.4.2 Regulating substrate temperature . . . 28
  - 2.4.3 Roughness dependence on substrate temperature variation . . . 29
  - 2.4.4 Robustness to model uncertainty . . . 31
- 2.5 Conclusions . . . 34

3 Multiscale Modeling for PECVD with Run-to-Run Control 35
- 3.1 Introduction . . . 35
- 3.2 Process description and modeling . . . 37
  - 3.2.1 Gas-phase model . . . 38
  - 3.2.2 Surface microstructure model . . . 41
- 3.3 Parallel computation . . . 49
- 3.4 Open-loop results . . . 51
  - 3.4.1 Plasma composition, film roughness and hydrogen content . . . 52
  - 3.4.2 Batch-to-batch variability . . . 55
- 3.5 R2R control of film thickness . . . 58
  - 3.5.1 EWMA formulation . . . 59

3.5.2 Closed-loop operation 60
3.6 Spatial non-uniformity in PECVD systems 62
3.6.1 EWMA extension to concentric reactor zones 64
3.7 Conclusions 68

4 Two-Dimensional CFD Modeling for PECVD Systems 69
4.1 Introduction 69
4.2 Process description and modeling 71
4.2.1 CFD geometry and meshing 72
4.2.2 Gas-phase model 75
4.2.3 Surface microstructure model 79
4.3 Simulation workflow 89
4.4 Parallel computation 90
4.5 Steady-state behavior 92
4.5.1 Plasma composition, porosity and hydrogen content 92
4.6 Multiscale CFD analysis 98
4.7 Conclusions 102

5 Three-Dimensional CFD Modeling for PECVD Systems 103
5.1 Introduction 103
5.2 Three-dimensional modeling 106
5.2.1 CFD geometry and meshing 106
5.2.2 Gas-phase model 108
5.2.3 Microscopic domain 112
5.2.4 Multiscale workflow 123
5.2.5 Parallel computation 125
5.3 Results 128
5.3.1 Non-uniform deposition 130
5.3.2 Adjusted reactor geometry 131
5.4 Conclusions 134

6 3D CFD Modeling for PECVD Systems with Run-to-Run Control 136
6.1 Introduction 136
6.2 Three-dimensional modeling 137
6.2.1 Gas-phase model 139
6.2.2 Electron density profile 141
6.3 Microscopic domain 143
6.3.1 Thin-film growth chemistry 144
6.3.2 Lattice characterization and relative rates 147
6.3.3 Kinetic Monte Carlo algorithm 150
6.4 Multiscale workflow 152
6.5 Parallel computation 154
6.6 Open-loop results 157
6.6.1 Non-uniform deposition 158
6.6.2 Adjusted reactor geometry 158

6.7 Run-to-run control 161
6.7.1 Batch-to-batch operation 164
6.8 Conclusions 168

7 Conclusions **169**

Bibliography **172**

List of Figures

1.1 Multiscale PECVD considerations: (a) Non-uniform, steady-state SiH_3 concentration within the macroscopic, reactor domain. (b) Kinetic Monte Carlo simulations which capture the complex interactions at the microscopic scale. (Note: figures have been drawn from Ch. 6) . . . 2

2.1 Macroscopic (left) and microscopic (right) PECVD simulation regimes. . . . 10
2.2 Chemical model illustration showing particle-surface interactions. . . . 12
2.3 Solid-on-solid lattice representation showing four microscopic processes. (a) Processes from left to right: physisorption, migration, chemisorption, and hydrogen abstraction. (b) Typical particle life cycle. . . . 13
2.4 Normalized frequency of reaction events within the present kMC scheme at T = 500 K, P = 1 Torr, and a SiH_3 mole fraction of 8.62×10^{-5}. . . . 17
2.5 Evolution of surface roughness during the growth of an L = 100 flat film up to a thickness of $\bar{\tau}$ = 50 nm. Surfaces at 1 and 5 nm have been omitted for clarity. . . . 19
2.6 Comparison of experimental and simulated rms roughness at various film thicknesses. 20
2.7 Preservation of grating shape after the growth of a 300 nm thick *a*-Si:H thin film. (a) The grated wafer (bottom curve in left plot) at H and P = 300 nm, with an $\bar{\tau}$ = 300 nm final film deposited above (top curve in left plot). (b) Thin film surface overlayed on the initial grating showing retention of desired sinusoidal shape. Note: Circles have been added to the grating profile for clarity. . . . 22
2.8 (left) Discrete PECVD reactor showing four independent, concentric substrate temperature control zones. (right) Microscopic simulation domain for a single grating period. . . . 23
2.9 Open-loop growth of sinusoidally grated thin films at 500 K and 1 Torr. From left to right: x_{SiH_3} = 8.62, 8.35, 7.86, and 7.25×10^{-5}, respectfully. Note: Lattices are shown side by side for clarity, physical zones are composed of $\sim8\times10^4$ periods. . . 24
2.10 Evolution of the thickness (nm) of the four radial wafer zones over time. Note: Zone mole fractions are shown $\times10^5$. . . . 24
2.11 Evolution of the RMS roughness of the four radial wafer zones over time. Note: Zone mole fractions are shown $\times10^5$. . . . 25
2.12 Relationship between growth rate, substrate temperature, and gas-phase mole fraction of SiH_3. Mole fractions, x_{SiH_3}, are shown $\times10^5$. . . . 27
2.13 Linear relationships between growth rate and temperature for each reactor zone. Mole fractions, x_{SiH_3}, are shown $\times10^5$. A single data point exists for x_{SiH_3} = 7.25 as zone 4 remains a fixed reference. . . . 28

2.14 Surface microstructure and thickness of sinusoidally grated thin films with spatially dependent temperatures. From left to right: x_{SiH_3} = 8.62, 8.35, 7.86, and 7.25×10^{-5}, respectfully. Note: Lattices are shown side by side for clarity, physical zones are composed of ∼8×10^4 periods. 30
2.15 Relationship between surface roughness, substrate temperature, and gas-phase mole fraction of SiH_3. Mole fractions, x_{SiH_3}, are shown ×10^5. 31

3.1 Macroscopic (left) and microscopic (right) PECVD simulation regimes. 38
3.2 Chemical model illustration showing particle-surface interactions. 42
3.3 Triangular lattice representation showing four microscopic processes. Processes from left to right: migration, physisorption, chemisorption, and hydrogen abstraction. 43
3.4 Surface relaxation for physisorbed radicals. (a) Incident particle location. (b) Surface Si particle in lattice. (c) Predefined triangular lattice site with one nearest neighbor. (d) Stable position for incident particle (two nearest neighbors). 45
3.5 Normalized frequency of reaction events within the present kMC scheme at T = 475 K, P = 1 Torr, and a SiH_4^{in} mole fraction of 0.9. 48
3.6 Time evolution of dominant gas-phase species at T = 475 K and P = 1 Torr. 52
3.7 Comparison of experimental and simulated rms roughness at various film thicknesses. 53
3.8 Hydrogen content dependence on deposition temperature. 54
3.9 Representation of voids within a typical simulated lattice. (Note: Only a fraction of the full size lattice is shown in order to highlight porosity.) 56
3.10 Relationship between film SOR and hydrogen content. 56
3.11 Batch-to-batch drift in the film thickness. 57
3.12 Relationships between growth rate and temperature for the nominal operation parameters. 59
3.13 Run-to-run operation of PECVD reactor. 60
3.14 Drift cancellation via a R2R controller. 61
3.15 Comparison of different learning factor values. 62
3.16 Radial non-uniformity in [SiH_3] at T = 475 K and P = 1 Torr. 63
3.17 Open-loop drift and spatial non-uniformity in the four radial wafer zones. 64
3.18 Discrete PECVD reactor schematic showing four independent, concentric substrate temperature control zones. 65
3.19 Relationships between growth rate and temperature for each reactor zone. 65
3.20 R2R control of four independent wafer zones. 67

4.1 Macroscopic (left) and microscopic (right) PECVD simulation regimes. 72
4.2 2D axisymmetric PECVD geometry. 73
4.3 Structured mesh containing 120,000 cells. 74
4.4 Individual unit cell for structured mesh. 75
4.5 Boundary cell adjacent to wafer surface. 78
4.6 Electron density within 2D axisymmetric PE-ALD geometry (cm^{-3}). 79
4.7 Chemical model illustration showing particle-surface interactions. 81
4.8 Triangular lattice representation showing four microscopic processes. Processes from left to right: migration, physisorption, chemisorption, and hydrogen abstraction. 82

4.9 Surface relaxation for physisorbed radicals. (a) Incident particle location. (b) Surface Si particle in lattice. (c) Predefined triangular lattice site with one nearest neighbor. (d) Stable position for incident particle (two nearest neighbors). 84
4.10 Normalized frequency of reaction events within the present kMC scheme at T = 475 K, P = 1 Torr, and a SiH_4^{in} mole fraction of 0.9. 87
4.11 Multiscale simulation workflow detailing the coordination between the macroscopic and microscopic events. 89
4.12 Communication between host and nodes within the MPI architecture. 91
4.13 Steady-state profile of x_{SiH_4} at T = 475 K and P = 1 Torr. 93
4.14 Steady-state profile of x_{H_2} at T = 475 K and P = 1 Torr. 93
4.15 Steady-state profile of x_{SiH_3} at T = 475 K and P = 1 Torr. 94
4.16 Steady-state profile of x_H at T = 475 K and P = 1 Torr. 94
4.17 Representation of voids within a typical simulated lattice. (Note: Only a fraction of the full size lattice is shown in order to highlight porosity.) 96
4.18 Hydrogen content dependence on deposition temperature. 96
4.19 Relationship between film SOR and hydrogen content. 98
4.20 Radial gradient in the concentration of SiH_3 above the wafer surface. 99
4.21 Radial gradient in the concentration of H above the wafer surface. 99
4.22 Four discrete locations across the wafer surface in which a representative thin film layer will be grown in order to investigate non-uniformities in the amorphous product. 100
4.23 Open-loop drift and spatial non-uniformity in the four radial wafer zones. 101
4.24 Open-loop drift and spatial non-uniformity in the four radial wafer zones. 102

5.1 (a) 2D axisymmetric geometry after discretization using a structured mesh containing 120,000 cells. (b) Collection of 1.5 million polygons which define the unstructured, 3D mesh. 105
5.2 Individual unit cell within the unstructured mesh. 109
5.3 Electron density within 3D axisymmetric PECVD geometry (cm^{-3}). 112
5.4 (a) Finite element adjacent to the substrate surface with dynamic boundary condition calculated via microscopic simulation domain. (b) Kinetic Monte Carlo setup within overall multiscale simulation. Wafer substrate discretized in both the x and y directions forming a 'grid' structure. 113
5.5 Chemical model illustration showing particle-surface interactions. 115
5.6 Triangular lattice representation showing four microscopic processes. Processes from left to right: migration, physisorption, chemisorption, and hydrogen abstraction. 117
5.7 Spatial distribution of kinetic Monte Carlo simulations. One representative microscopic simulation (i.e., a 1200 particle wide lattice) is executed within each overlapping grid location. The hashed corners represent regions which do not overlap the substrate surface. 118
5.8 Normalized frequency of reaction events within the present kMC scheme at T = 475 K, P = 1 Torr, and a SiH_4^{in} mole fraction of 0.9. 122
5.9 Multiscale simulation workflow detailing the coordination between the macroscopic and microscopic events. 124
5.10 Communication between host and nodes within the MPI architecture. 126

5.11 (a) Distribution of 2D structured mesh across computational cores on a typical personal workstation with a quad-core CPU. (b) Unstructured mesh containing 1.5 million cells distributed across 128 computational cores (note: the colored regions denote different assignments). 127
5.12 Expected speed-up due to parallelization across N nodes. 129
5.13 (a) Velocity magnitude within 3D PECVD reactor showing dead-zone near substrate center. (b) Non-uniform, steady-state SiH_3 concentration. 132
5.14 (a) Cross section of SiH_3 concentration taken just above the surface of the wafer substrate (b) SiH_3 concentration above the wafer surface for the adjusted reactor geometry. 133
5.15 (a) SiH_3 mole fraction as a function of radial position, r, and azimuthal position, θ. (b) Radial a-Si:H product thickness for both the original and adjusted reactor geometries. 135

6.1 Collection of 1.5 million tetrahedral cells which define the unstructured, 3D mesh. . 138
6.2 Electron density cross section within 3D axisymmetric PECVD geometry (cm^{-3}). . 143
6.3 (a) Finite element adjacent to the substrate surface with dynamic boundary condition calculated via microscopic simulation domain. (b) Kinetic Monte Carlo setup within overall multiscale simulation. Wafer substrate discretized in both the x and y directions forming a 'grid' structure. 144
6.4 Chemical model illustration showing particle-surface interactions. 145
6.5 Triangular lattice representation showing four microscopic processes. Processes from left to right: migration, physisorption, chemisorption, and hydrogen abstraction. 147
6.6 Spatial distribution of kinetic Monte Carlo simulations. One representative microscopic simulation (i.e., a 1200 particle wide lattice) is executed within each overlapping grid location. The hashed corners represent regions which do not overlap the substrate surface. 149
6.7 Visualization of randomized event choices. 151
6.8 Multiscale simulation block diagram detailing the coordination between the macroscopic and microscopic events. 153
6.9 Communication between host and nodes within the MPI architecture. Node coloring corresponds to the mesh partitioning shown in Fig. 6.10. 154
6.10 Unstructured mesh containing 1.5 million cells distributed across 128 computational cores (note: the colored regions denote different core assignments as reflected by Fig. 6.9). 155
6.11 Expected speed-up due to parallelization across N nodes. 156
6.12 (a) Velocity magnitude within 3D PECVD reactor showing dead-zone near substrate center. (b) Non-uniform, steady-state SiH_3 concentration [16]. 159
6.13 (a) Cross section of SiH_3 concentration taken just above the surface of the wafer substrate (b) SiH_3 concentration above the wafer surface for the adjusted reactor geometry [16]. 160
6.14 SiH_3 mole fraction as a function of radial position, r, and azimuthal position, θ. . . 161
6.15 Four concentric wafer zones as defined by the EWMA algorithm. 162

6.16 (a) Control action resulting from EWMA algorithm. Temperatures shown correspond to PECVD reactor with polar showerhead geometry. (b) Batch-to-batch thin film thickness within polar PECVD geometry. 165
6.17 (a) Batch 1 film thickness. (b) Batch 10 film thickness. 166
6.18 Batch-to-batch thin film thickness within nominal (i.e., rectangular) PECVD showerhead geometry. 167

List of Tables

2.1 Sticking coefficients and reaction rates composing the chemical model. 15
2.2 Quantitative non-uniformity of four radial wafer zones. 25
2.3 Calculated operating parameters by zone. 29
2.4 Quantitative non-uniformity of four radial wafer zones. 29
2.5 Final film thickness for sinusoidally grated thin films in the presence of independent variations in x_{SiH_3} and T. 32
2.6 Final thin film thickness for sinusoidally grated wafers in the presence of concurrent variations in x_{SiH_3} and T. 33

3.1 Reactions included in the gas-phase model. Note: Rate constants have units of cm^3/sec and have been adopted from the collection prepared by Kushner et al. [41]. 39
3.2 Sticking coefficients and reaction rates composing the chemical model. 46
3.3 Required time to complete a sample batch-to-batch simulation and the speedup time achieved. 51

4.1 Reactions included in the gas-phase model. Note: Rate constants have units of cm^3/sec and have been adopted from the collection prepared by Kushner et al. [41]. 77

5.1 Macroscopic reaction set. Note: Rate constants have units of cm^3/sec and have been adopted from the collection prepared by Kushner et al. [41]. 111

6.1 Gas-phase reaction model. Note: Rate constants have units of cm^3/sec and have been adopted from the collection prepared by Kushner et al. [41]. 142

ACKNOWLEDGEMENTS

First and foremost, I need to express heartfelt gratitude to my advisor, Panagiotis D. Christofides, not only for guidance throughout my graduate studies and research, but for taking me on as a young student and having faith in my abilities. There is a difficult balance in being a professor between driving your students too hard and allowing them so much freedom as to undermine any academic progress; Dr. Christofides, as far as I'm concerned, has perfected this balance. I was challenged many times over the past four years but I always felt confident and comfortable in myself and the work we were doing as a group. For that, and for the life lessons which I've been able to draw from you, thank you Dr. Christofides.

I would be remiss to go on without recognizing the significant contribution that my family has made to my success. Whether they realize it or not, the support from my parents and long-time partner Christine has facilitated each and every achievement that I've made. In addition, I want to acknowledge the valuable conversations and time spent with my friends and collaborators: Anh Tran, Ian McRae and Keita Nagashima. Though it would be difficult to list all the people who have contributed to my success, I must thank Matthew Ellis, Joseph Kwon, Helen Durand, Liangfeng Lao, Larry Gao, Zhe Wu, Zhihao Zhang, Weiqi Zhang, and in particular, Michael Nayhouse and Dr. Orkoulas for help with my research, career and life.

I would also like to thank Professor Dante Simonetti, Professor Philippe Sautet and Professor Mathieu Bauchy for serving on my doctoral committee.

Finally, financial support from the National Science Foundation (NSF), the Department of Energy (DOE), and a Dissertation Year Fellowship from UCLA's graduate division are gratefully acknowledged.

With regard to the research that forms the foundation for this work:

Chapter 2 contains a version of: M. Crose, JSI. Kwon, A. Tran, and P. D. Christofides. Multiscale modeling and operation of PECVD of thin film solar cells. *Chem. Eng. Sci.*, 136:50–61, 2015.

Chapter 3 is a version of: M. Crose, JSI. Kwon, A. Tran, and P. D. Christofides. Multiscale

modeling and run-to-run control of PECVD of thin film solar cells. *Renewable Energy*, 100:129–140, 2017.

Chapter 4 is a version of: M. Crose, A. Tran, and P. D. Christofides. Multiscale Computational Fluid Dynamics: Methodology and Application to PECVD of Thin Film Solar Cells. *Coatings*, 7:22–54, 2017.

Chapter 5 is a version of: M. Crose, W. Zhang, A. Tran, and P. D. Christofides. Multiscale three-dimensional CFD modeling for PECVD of amorphous silicon thin films. *Comp. & Chem. Eng.*, 113:184–195, 2018.

Chapter 6 contains a version of the manuscript: M. Crose, W. Zhang, A. Tran, and P. D. Christofides. Run-to-Run Control of PECVD Systems: Application to a Multiscale Three-Dimensional CFD Model of Thin Film Silicon Solar Cell Deposition. *AIChE J.*, *submitted*, 2018.

VITA

2009–2014	Bachelor of Science, Chemical and Biomolecular Engineering Department of Chemical and Biomolecular Engineering University of California, Los Angeles
2014–2018	Graduate Student Department of Chemical and Biomolecular Engineering University of California, Los Angeles
2014–2017	Teaching Assistant/Associate Department of Chemical and Biomolecular Engineering University of California, Los Angeles
2017–2018	Dissertation of the Year Department of Chemical and Biomolecular Engineering University of California, Los Angeles
2018	Outstanding Student Award Department of Chemical and Biomolecular Engineering University of California, Los Angeles
2018	Distinguished Speaker Award 4th Year Symposium University of California, Los Angeles

JOURNAL PUBLICATIONS

1. M. Crose, W. Zhang, A. Tran, and P. D. Christofides. Multiscale three-dimensional CFD modeling for PECVD of amorphous silicon thin films. *Comp. & Chem. Eng.*, 113:184–195, 2018.

2. M. Crose, W. Zhang, A. Tran, and P. D. Christofides. Run-to-Run Control of PECVD Systems: Application to a Multiscale Three-Dimensional CFD Model of Thin Film Silicon Solar Cell Deposition. *AIChE J.*, *submitted*, 2018.

3. A. Tran, M. Pont, M. Crose and P. D. Christofides. Real-Time Furnace Balancing of Stem Methane Reforming Furnaces. *Chem. Eng. Res. & Des.*, 134:238–256, 2018.

4. A. Tran, M. Pont, A. Aguirre, H. Durand, M. Crose and P. D. Christofides. Bayesian Model Averaging for Estimating the Spatial Temperature Distribution in a Steam Methane Reforming Furnace. *Chem. Eng. Res. & Des.*, 131:465–487, 2018.

5. M. Crose, A. Tran, and P. D. Christofides. Multiscale Computational Fluid Dynamics: Methodology and Application to PECVD of Thin Film Solar Cells. *Coatings*, 7:22–54, 2017.

6. A. Tran, A. Aguirre, H. Durand, M. Crose and P. D. Christofides. CFD Modeling of an Industrial-scale Steam Methane Reforming Furnace. *Chem. Eng. Sci.*, 171:576–598, 2017.

7. M. Crose, JSI. Kwon, A. Tran, and P. D. Christofides. Multiscale modeling and run-to-run control of PECVD of thin film solar cells. *Renewable Energy*, 100:129–140, 2017.

8. A. Tran, A. Aguirre, M. Crose, H. Durand and P. D. Christofides. Temperature Balancing in Steam Methane Reforming Furnace via an Integrated CFD/Data-Based Optimization Approach. *Comp.* & *Chem. Eng.*, 104:185–200, 2017.

9. M. Crose, JSI. Kwon, A. Tran, and P. D. Christofides. Multiscale modeling and operation of PECVD of thin film solar cells. *Chem. Eng. Sci.*, 136:50–61, 2015.

10. M. Nayhouse, A. Tran, JSI. Kwon, M. Crose, G. Orkoulas and P. D. Christofides. Modeling and control of ibuprofen crystal growth and size distribution. *Chem. Eng. Sci.*, 134:414–422, 2015.

11. V. Heng, M. Nayhouse, M. Crose, A. Tran and G. Orkoulas. Direct determination of triple-point coexistence through cell model simulation. *J. Chem. Phys.*, 137:141101, 2012.

Chapter 1

Introduction

1.1 Motivation

Plasma enhanced chemical vapor deposition (PECVD) is widely used in the microelectronics and solar cell industries to deposit thin films from a mixture of gas-phase species onto a solid substrate [35]. Specifically, in the solar cell industry, PECVD is broadly used in the production of thin film silicon solar cells to deposit amorphous silicon semiconductor layers due to low manufacturing costs via silane recycling [40], the possibility for extremely low operating temperatures ($\leq$250 °C) [73], and the desirable dielectric properties of amorphous silicon thin films [60]. However, even high quality amorphous silicon solar cells suffer from efficiencies (of solar power conversion) that are lower than their crystalline counterparts which has motivated significant efforts to improve other thin film light trapping attributes to increase solar power conversion [27]. In this direction, periodic surface textures have been recently proposed in an effort to increase light scattering on the thin film surface or interface and to obtain photocurrents from a-Si:H thin film solar cells competitive with other existing solar cell technologies [20, 28, 75, 63]. Optical simulations of thin films with periodic surface textures (grown on appropriately grated wafers) have demonstrated up to 35% more photocurrent when compared to traditional, flat interfaces [9], particularly when the surface roughness and height-height correlation length are comparable to visible light wavelength

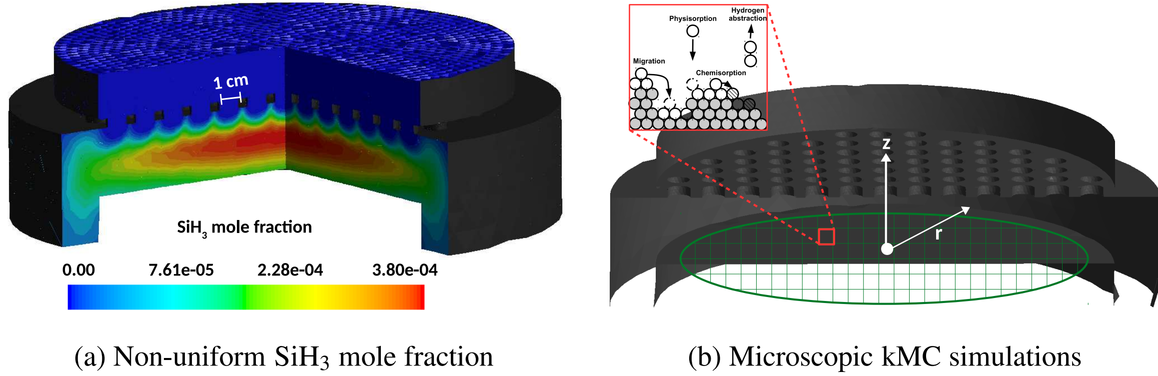

(a) Non-uniform SiH_3 mole fraction

(b) Microscopic kMC simulations

Figure 1.1: Multiscale PECVD considerations: (a) Non-uniform, steady-state SiH_3 concentration within the macroscopic, reactor domain. (b) Kinetic Monte Carlo simulations which capture the complex interactions at the microscopic scale. (Note: figures have been drawn from Ch. 6)

length scales. Although photolithographic fabrication techniques allow for the creation of grated wafer substrates [70], in practice, it is not easy to achieve consistent morphology of the surface of an absorbing layer due to the need to deposit thin films over a large area. Significant non-uniformity in final film thickness and variations in surface morphology may occur due to the consumption of reactants as process gases travel radially across the wafer (see Fig. 1.1a), leading to radially-varying deposition rates (e.g., [11, 67, 64]).

In the context of thin film surface morphology control, several model-based control schemes have been applied to deposition process models with the goal of improving solar cell performance through the achievement of periodic film surface textures (e.g., [29, 30]). These models typically rely on kinetic Monte Carlo (kMC) algorithms to simulate deposition processes, focusing on evolution of thin film surface microstructure in nano- to micrometer length scales. The concept of using grated wafers to impart periodic surface textures to thin films has existed for some time [25], and over the past three decades extensive efforts have been made in optimizing grating shape for the purposes of light trapping [9, 20, 28, 75, 63]. Four parameters define the final shape of textured thin films: periodic shape (e.g., rectangular wave, pyramidal, sinusoidal, etc.), height H, period P, and film thickness τ. Given that film growth is driven by the formation of dangling bonds, surface migration has little effect on the shape of thin films beyond local roughness, and as a result, grated

wafers can consistently impart optimized textures to thin films. However, practical applications of the existing modeling and control approaches to deposit thin films with tailored surface textures need to address the fact that the film deposition takes place over a large area (e.g., Fig. 1.1b), leading to the possibility of non-uniformity in film thickness at the reactor scale. Specifically, non-uniformity in reactant and product gas phase species concentrations is negligible on the scale of a single grating period (on the order of hundreds of nanometers), nullifying the need for spatially controlled film thickness at the nanoscale. However, at the reactor length scale (for example, a 20 cm wafer is used in this work) consumption of reactants across the wafer surface has been shown to yield growth rate differences greater than 19% [11, 67, 64], prompting the need for reactor scale control.

In addition to film thickness uniformity control, the physics of the gas-phase species and film surface interactions should be carefully modeled in the microscopic film growth model when the film growth takes place in a PECVD process. Specifically, due to the vast number of species introduced by the presence of plasma, microscopic modeling of film growth by PECVD is a challenging task. Often the level of modeling detail must be compromised in lieu of simulation efficiency: for example, Novicov et al. [53] developed a kMC algorithm capable of simulating films several hundred monolayers thick, however, important surface phenomena such as diffusion (migration) were ignored. Conversely, Pandey et al. [54] conducted more detailed kMC simulations that included diffusion of surface radicals, and although their results appeared in good agreement with experimental data, their work was limited to a relatively small number of monolayers. A close look in the literature indicates a broad agreement of accounting for microscopic events such as the physisorption, migration, and chemisorption of surface radicals in the modeling of the nanostructure of growing thin films in PECVD.

While the above motivations apply largely to the deposition of *a*-Si:H for thin film solar cells, the need for improved modeling techniques can be seen throughout the microelectronics industry. Recently, computational fluid dynamics (CFD) models have shown promise in capturing the behavior of CVD reactors [12, 37, 18]. Issues facing the large scale adoption of CFD-based modeling

for PECVD are akin to those discussed above: first, researchers typically focus on a single domain and fail to capture the overall reactor dynamics. Second, the approximate geometries used allow for rapid calculations but cannot provide complete information needed for designing improved chamber geometries and operational strategies. Given rapid advances in computational power, an opportunity exists to link the macroscopic reactor domain (i.e., Fig. 1.1a) with microscopic surface simulations (see Fig. 1.1b) in order to capture accurate growth of *a*-Si:H thin films. Models of this type would allow for novel operation of PECVD systems without the restriction of limited in-situ monitoring. Additionally, multiscale CFD models may act as a design tool and thus significantly reduce the costs typically spent on machining and retooling of production hardware.

1.2 Objectives and Organization of the Dissertation

This dissertation considers industrially relevant issues related to the deposition of amorphous silicon thin films via plasma-enhanced chemical vapor deposition. Specifically, the objectives of this dissertation are summarized as follows:

1. To develop multiscale models for PECVD systems which capture both the gas-phase transport and reaction phenomena and microscopic thin film growth

2. To adapt run-to-run control strategies to the operation of PECVD using exponentially-weighted moving average (EWMA) algorithms

3. To address the common issue of non-uniform deposition of amorphous silicon thin film layers

4. To develop computational fluid dynamic (CFD) models which capture the complex gas-phase phenomena within PECVD systems

5. To design improved PECVD reactor geometries which reduce spatial non-uniformities in the thickness of *a*-Si:H products

6. To develop parallel programming techniques which allow for efficient computation of transient batch simulations

The dissertation is organized as follows. In Chapter 2, a multiscale model for PECVD of amorphous silicon is developed which connects a first principles model of the plasma phase to a kinetic Monte Carlo approximation for microscopic thin film growth. The model is applied to the deposition of 300 nm thick *a*-Si:H layers revealing significant thickness non-uniformity. An open-loop operational strategy is presented which reduces the overall thickness non-uniformity through manipulation of the substrate temperature in four independent zones.

In Chapter 3, a batch-to-batch control strategy is implemented as a closed-loop control layer for the multiscale model developed in Chapter 2. An exponentially-weighted moving average (EWMA) algorithm is defined which updates the substrate temperature in four concentric reactor zones between batch deposition cycles. The resulting run-to-run control system is shown to reduce the thin film thickness non-uniformity to less than 1% for both the nominal PECVD system, as well as for reactors experiencing drift due to fouling.

In Chapter 4, a computational fluid dynamics (CFD) model is developed based on a two-dimensional axisymmetric approximation of the PECVD system used in Chapters 2 and 3. Connection of the CFD model with radially spaced microscopic thin film simulations is shown to accurately capture the behavior of chambered parallel plate reactors. The increased resolution in species concentration data throughout the reactor space (when compared to earlier first principles models) reveals significant variations in x_{SiH_3} and x_H, which explain non-uniformities in thin film product thickness and porosity often experienced in industrially used systems.

In Chapter 5, the two-dimensional model presented in Chapter 4 is used as a basis for building a three-dimensional (3D) PECVD reactor geometry. Although significant computational costs are associated with the use of 3D, transient simulations, the third spatial dimension provides needed insight into the role of showerhead geometries on thin film thickness uniformity. Specifically, the nominal rectangular showerhead layout is adjusted to a polar arrangement which reduces thickness non-uniformity from 8% to less than 4% for identical operational parameters.

In Chapter 6, a run-to-run controller based on an exponentially-weighted moving average (EWMA) algorithm is introduced to the operation of the 3D multiscale CFD model. Additionally, a computationally efficient parallel programming structure is presented which reduces the substantial computational requirements of this work to within practical limits. The 4% offset provided by the polar geometry in Chapter 5 represents a significant improvement from the nominal system, but demand in the microelectronics industry for silicon products of high quality requires tighter uniformity still. Application of the run-to-run controller to 10 serial batch deposition cycles suggests that manipulation of the substrate temperature is sufficient to drive the a-Si:H thin film to within 1% of the thickness set-point.

Chapter 7 summarizes the main results of the dissertation.

Chapter 2

Multiscale Modeling and Operation of PECVD of Thin Film Solar Cells

2.1 Introduction

As discussed in Chapter 1, the primary issue in the manufacture of *a*-Si:H thin film solar cells is non-uniform grating shape and film thickness which adversely affect light capture efficiency. To that end, this chapter proposes a multiscale modeling and operation framework for plasma-enhanced chemical vapor deposition (PECVD) of thin film amorphous silicon solar cells. The interdependence of the gas phase and film growth phenomena means that neither can be ignored; as an example, the film growth rate and roughness are strongly tied to the rate of physisorption of surface radicals, which in turn is governed by the inlet concentration of silane and hydrogen gases. Conversely, hydrogen abstraction from the surface into the gas phase influences the overall concentration of reactive radicals. Given the computational challenge of using a single microscopic model to describe the entire PECVD process behavior, the disparity in scales necessitates the need for a multiscale model capable of capturing both the macro and microscopic phenomena involved in thin film growth processes. Therefore, a multiscale model is developed capturing both the gas-phase reaction and transport phenomena that lead to the deposition of the thin film

across the wafer as well as multiple microscopic models that describe the evolution of the thin film surface microstructure at equispaced, discrete spatial locations across the wafer. While the gas phase model is standard, the microscopic model, describing the a-Si:H thin film surface evolution, is computationally efficient and accounts for four microscopic processes: physisorption, surface migration, hydrogen abstraction, and chemisorption. Specifically, a nanoscale hybrid kMC scheme originally developed by Tsalikis et al. [69] is applied to the growth of silicon films with periodic surface textures in an effort to maintain fidelity to established chemical models while allowing for practical computational requirements. The model considers the two dominant species involved in the growth of amorphous silicon films, H and SiH_3 [56, 24], and four corresponding surface processes: physisorption from the gas phase, hydrogen abstraction by SiH_3, chemisorption onto dangling bonds, and migration across neighboring, hydrogenated lattice sites. As opposed to traditional kMC formulations, surface migration is handled in a decoupled manner from the other processes allowing for efficient simulations in excess of 1000 monolayers. The results of the multiscale process model indicate that in order to produce an 20 cm thin film of uniform thickness with surface microstructure that optimizes light trapping: a) a sinusoidally-grated wafer surface should be used in which the grating period and depth should correspond to values that lead to film surface roughness and height-height correlation length that are on the order of visible light wavelength range, and b) the substrate temperature should be adjusted to compensate for a radially non-uniform deposition rate of the film on the wafer owing to gas-phase transport phenomena. This insight motivates an operation strategy that manipulates substrate temperature to produce of thin film silicon solar cells with uniform thickness and film surface microstructure that optimizes light trapping.

The structure of this chapter is as follows: first, the multiscale modeling and optimization framework for PECVD will be introduced including a brief description of the macroscale gas phase model and the microscale surface interactions. Next, a detailed description of the lattice implementation and corresponding hybrid kMC scheme are provided. Simulations using a flat lattice demonstrate that the proposed hybrid kMC algorithm reproduces experimentally obtained surface

morphologies and growth rates at the nanoscale, and that roughness is limited to a few nanometers. Grating is then applied to the wafer with a period and depth corresponding to values that lead to film surface roughness and height-height correlation length that are on the order of visible light wavelength range. Open-loop simulations also reveal a radially non-uniform deposition rate of the film on the wafer owing to gas-phase transport phenomena. Finally, a scheme using four concentric substrate temperature control zones is proposed to successfully regulate film thickness radially across the wafer surface while producing a desired thin film surface microstructure that is demonstrated to be robust with respect to model uncertainty.

2.2 PECVD process description and modeling

We consider a PECVD chamber shown in Fig. 2.1 utilizing two parallel electrodes with a single wafer placed on top of the lower electrode. A showerhead arrangement is employed in this PECVD process to uniformly distribute the influent gas stream consisting of silane and hydrogen throughout the chamber and an RF (radio frequency) power source generates plasma (i.e., chemically reactive mixture of ions, electrons, and radicals) from silane. Thin film growth occurs as radicals are transported to the wafer surface via diffusion and convection where they react to form amorphous silicon (*a*-Si:H). The objective of this process is to deposit a 300nm thick *a*-Si:H thin film on a wafer with a diameter of 20 cm.

Fig. 2.1 illustrates the multiscale character of this process and the need to capture both the microscopic surface interactions and growth, as well as the macroscopic gas-phase dynamic material balance. Details of both the macroscopic gas phase model and the microscopic surface model are given in the following sections.

2.2.1 Gas phase model

Continuum mass, energy and momentum balances allow for the modeling of the gas phase under the assumption of axisymmetric flow. The governing equations have been developed at length for

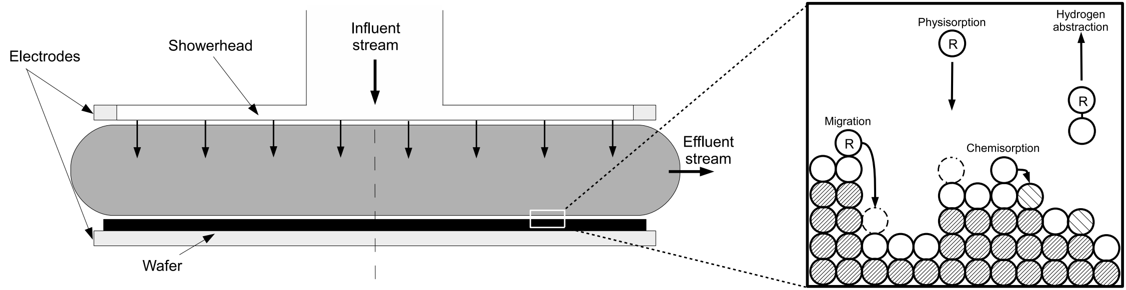

Figure 2.1: Macroscopic (left) and microscopic (right) PECVD simulation regimes.

CVD-type applications (e.g., [71, 45, 11]); however, here we apply the formulation by Armaou and Christofides [11] as radial dependence of species concentration is desired.

Specifically, the mathematical model of the PECVD reactor consists of a particle velocity profile and four nonlinear dynamic diffusion-convection-reaction equations in two (radial and axial) dimensions (a set of four coupled parabolic PDEs). Specifically, by treating the gas phase as a three-dimensional stagnation flow, the evolution of the velocity profile within the PECVD reactor is computed from the Navier-Stokes and continuity equations. The spatio-temporal evolution of the concentration of the species, SiH_4, SiH_2, SiH_3 and H, throughout the reactor are obtained by applying dynamic material balances to the gas-phase and accounting for diffusive and convective mass transfer, and bulk and surface reactions. Finite-difference methods are then applied in order to discretize the spatial derivative of the species concentration in the r and z directions (z is defined as the direction normal to the wafer surface; see Fig. 2.1). Finally, time integration of the resulting ordinary differential equations is performed using the alternate direction implicit (ADI) method. More details on the model structure can be found in Armaou and Christofides [11], and calculated steady-state concentration profiles are discussed further in the open-loop results section.

2.2.2 Surface microstructure model

Although kMC methodologies are commonly applied to the modeling of the growth of thin films, minor discrepancies in the physical phenomena included in the model can yield significantly different results. As such, the surface microstructure model is presented here in great detail, starting

with the chemical model which acts as the foundation for the developing algorithm.

Two species thin film growth

To model the thin film surface growth, the following reaction scheme, which has been proposed and verified experimentally by Perrin et al. [56] and Robertson [61], and is shown schematically in Fig. 2.2, is adopted. Specifically, at standard operating conditions ($T < 300$ °C) two species, SiH_3 and H, dominate the interactions on the growing film; therefore, all other species are ignored in the microscopic model. SiH_3 and H radicals reaching the film surface become physisorbed at hydrogenated silicon sites according to the following reactions:

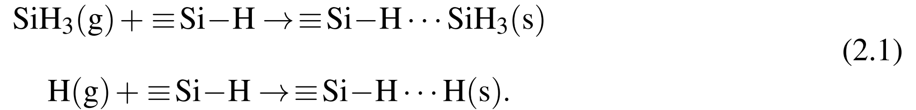

$$\begin{aligned} \mathrm{SiH_3(g)} + \equiv\mathrm{Si{-}H} &\rightarrow \equiv\mathrm{Si{-}H}\cdots\mathrm{SiH_3(s)} \\ \mathrm{H(g)} + \equiv\mathrm{Si{-}H} &\rightarrow \equiv\mathrm{Si{-}H}\cdots\mathrm{H(s)}. \end{aligned} \tag{2.1}$$

Physisorbed radicals rapidly diffuse across the surface according to the following reactions:

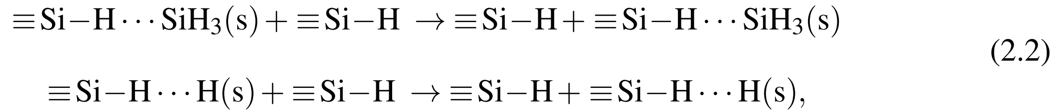

$$\begin{aligned} \equiv\mathrm{Si{-}H}\cdots\mathrm{SiH_3(s)} + \equiv\mathrm{Si{-}H} &\rightarrow \equiv\mathrm{Si{-}H} + \equiv\mathrm{Si{-}H}\cdots\mathrm{SiH_3(s)} \\ \equiv\mathrm{Si{-}H}\cdots\mathrm{H(s)} + \equiv\mathrm{Si{-}H} &\rightarrow \equiv\mathrm{Si{-}H} + \equiv\mathrm{Si{-}H}\cdots\mathrm{H(s)}, \end{aligned} \tag{2.2}$$

eventually contributing to one of two processes: hydrogen abstraction by a physisorbed SiH_3 radical forming SiH_4 and leaving behind a dangling bond according to the reaction:

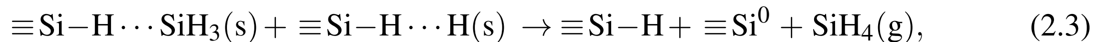

$$\equiv\mathrm{Si{-}H}\cdots\mathrm{SiH_3(s)} + \equiv\mathrm{Si{-}H}\cdots\mathrm{H(s)} \rightarrow \equiv\mathrm{Si{-}H} + \equiv\mathrm{Si^0} + \mathrm{SiH_4(g)}, \tag{2.3}$$

or chemisorption at an existing dangling bond site according to the following reactions:

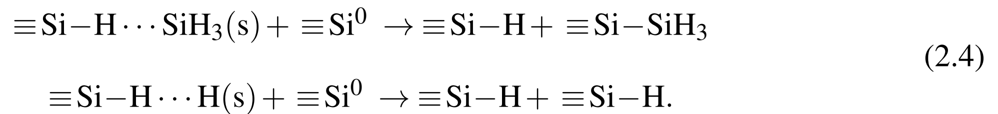

$$\begin{aligned} \equiv\mathrm{Si{-}H}\cdots\mathrm{SiH_3(s)} + \equiv\mathrm{Si^0} &\rightarrow \equiv\mathrm{Si{-}H} + \equiv\mathrm{Si{-}SiH_3} \\ \equiv\mathrm{Si{-}H}\cdots\mathrm{H(s)} + \equiv\mathrm{Si^0} &\rightarrow \equiv\mathrm{Si{-}H} + \equiv\mathrm{Si{-}H}. \end{aligned} \tag{2.4}$$

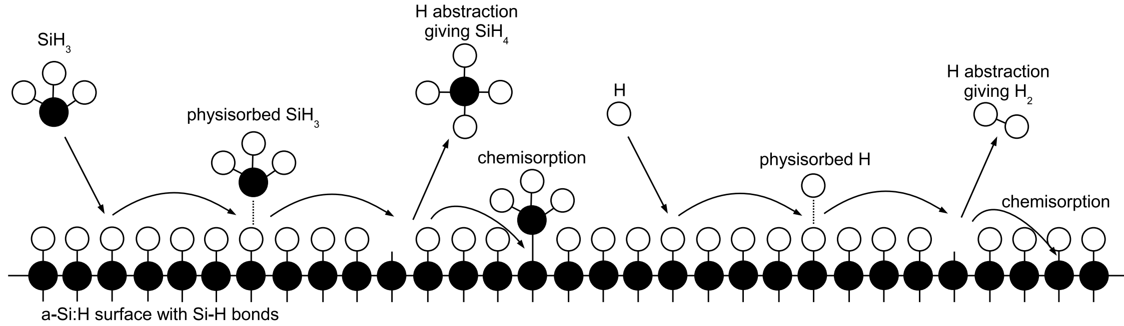

Figure 2.2: Chemical model illustration showing particle-surface interactions.

Chemisorption of SiH_3 grows the height of a film site by one, whereas chemisorption of H returns the surface site to a hydrogenated state.

Lattice Characterization

A one-dimensional solid-on-solid (SOS) lattice is used to model the thin film particle (each deposited species, SiH_3 or H, is modeled by a single particle) surface interactions via a hybrid kinetic Monte Carlo method which accounts for the four microscopic processes: physisorption, migration, hydrogen abstraction, and chemisorption.

The number of sites in the lateral direction is defined as the lattice size and denoted by L. Since a SOS lattice is used and the center of each particle is located on the lattice site, the heights of all sites are rounded to the nearest lattice site. The size of each lattice site is set to the diameter of a silicon atom $\sim$0.25 nm, therefore the physical size of the lattice can be calculated by $0.25\times L$. Particles are deposited with vertical incidence resulting in film growth normal to the lateral direction. The surface is roughened using 2400 randomly distributed deposition events to ensure that the initial configuration does not have a noticeable impact on the results. Periodic boundary conditions are applied at the edges of the lattice in the lateral direction.

As shown in Fig. 2.3a, the top particle at any lattice position can exist in one of three states: a hydrogenated silicon atom available for physisorption, a radical currently physisorbed, or a dangling bond site available for chemisorption by migrating radicals. Physisorption and migration are

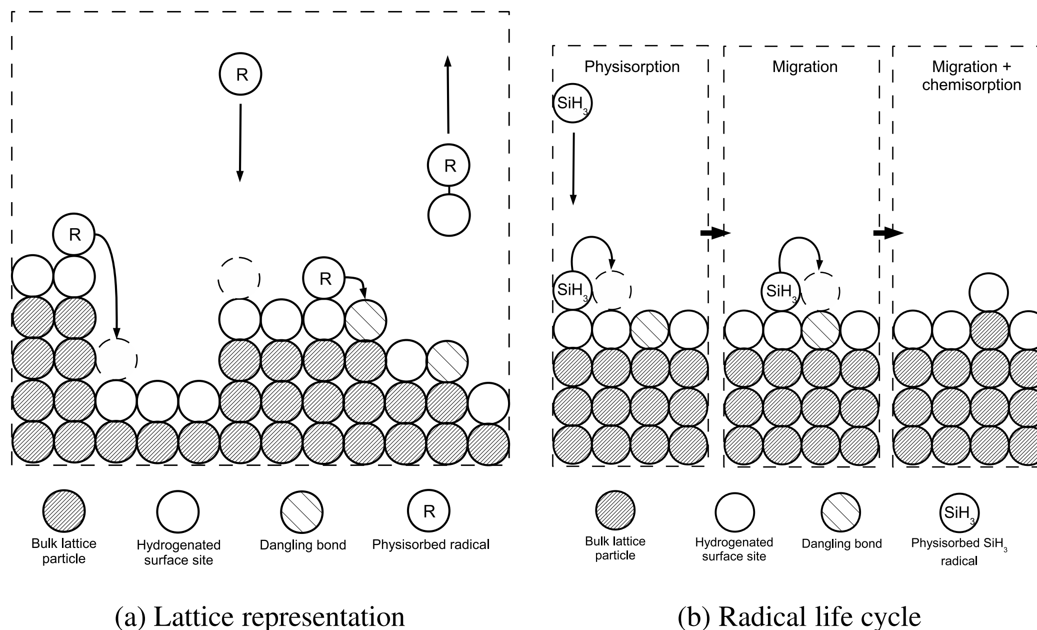

(a) Lattice representation

(b) Radical life cycle

Figure 2.3: Solid-on-solid lattice representation showing four microscopic processes. (a) Processes from left to right: physisorption, migration, chemisorption, and hydrogen abstraction. (b) Typical particle life cycle.

hindered by currently occupied sites as each lattice position can take only a single state (i.e., sites containing physisorbed radicals are unavailable as deposition or migration destinations). Once chemisorbed, particles are fixed at that position, and in the case of silicon radicals the height of the lattice site grows by one. All other lattice particles are considered as bulk and their positions are permanently fixed. Hydrogen abstraction, shown in Fig. 2.3a, cannot occur spontaneously, instead it requires the loss of a physisorbed radical. Although H and SiH_3 radicals both contribute to abstraction, in the present model only abstractions via SiH_3 radicals are considered due to the low operating temperatures ($<350\ ^\circ C$) [56].

The procedure for particle incorporation into the growing lattice can be seen in Fig. 2.3b. A gas phase particle becomes physisorbed by vertical deposition on a hydrogenated surface site. The physisorbed radical rapidly migrates across the hydrogenated surface layer until encountering a dangling bond site. Chemisorption occurs instantaneously, and in the case of an SiH_3 radical shown here, growth of the lattice occurs and the surface site is returned to a hydrogenated state.

Events are chosen randomly based on the relative rates of the microscopic phenomena described below.

Relative rates formulation

The surface kinetics presented below follow closely that of Tsalikis et al. [69]. Athermal or barrier-less reactions involving gas phase species (e.g., physisorption) are evaluated using the fundamental kinetic theory of gases yielding the following rate equation:

$$r_a = J s_c N_a \sigma, \tag{2.5}$$

where J is the flux of gas-phase radicals, s_c is the local sticking coefficient, N_a is the Avogadro number, and σ is the average area per surface site. J can be calculated via the following equations:

$$J = \eta \bar{u}, \tag{2.6}$$

$$\eta = \frac{p_i}{RT}, \tag{2.7}$$

$$\bar{u} = \sqrt{\frac{8k_B T}{\pi m_i}}, \tag{2.8}$$

where η is the number density of radical i (here the reactive gas phase is assumed to be ideal), $\bar{u}$ is the mean radical velocity, p_i is the partial pressure of i, R the gas constant, T is the temperature, k_B is the Boltzmann constant, and m is the molecular mass. Combining Eqs. (2.5)-(2.8) we obtain the overall reaction rate for an athermal radical i:

$$r_{a,i} = \frac{p_i}{RT}\sqrt{\frac{8k_B T}{\pi m_i}} s_c N_a \sigma. \tag{2.9}$$

Thermally activated kinetic events (e.g., migration and hydrogen abstraction) can be estimated

using a standard Arrehnius-type formulation:

$$r_{t,i} = v_i e^{-E_i/k_B T}, \tag{2.10}$$

where v_i is the attempt frequency prefactor (s^{-1}) and E_i is the activation energy of radical i. Values for these parameters are drawn from Perrin et al. [56] to correspond to the growth of *a*-Si:H films. Reaction mechanisms and resulting reaction rates for each kMC event are given in Table 2.1. Sticking coefficients are reported for athermal reactions as overall reaction rates depend on pressure and gas phase composition which typically vary. Thermally activated reaction rates are shown for T = 500 K to correspond to the operating temperature range used throughout this work.

Table 2.1: Sticking coefficients and reaction rates composing the chemical model.

Thermally activated		Athermal reactions	
Reaction type	Reaction rate ($s^{-1}site^{-1}$)	Reaction type	Sticking coefficient
hydrogen abstraction	3.35×10^5	SiH_3 physisorption	0.5
hydrogen migration	1.58×10^{11}	hydrogen physisorption	0.8
SiH_3 migration	1.16×10^{11}		

Kinetic Monte Carlo implementation

A standard n-fold kinetic Monte Carlo algorithm is applied to all events excluding migration which is handled using a one-dimensional lattice random walk process. The choice to exclude surface migration is made in the interest of computational efficiency and will be discussed in detail in the next subsection. The total reaction rate is defined as

$$r_{\text{total}} = r_a^H + r_a^{SiH_3} + r_t^{abs}, \tag{2.11}$$

where r_a^H is the rate of physisorption of hydrogen, r_t^{abs} is the rate of hydrogen abstraction, and $r_a^{SiH_3}$ is the rate of physisorption of SiH_3. A uniform random number, $\zeta_1 \in [0,1]$ is generated. If $\zeta_1 \leq r_a^H/r_{\text{total}}$, then a hydrogen physisorption event is executed. If $r_a^H/R_{\text{total}} < \zeta_1 \leq (r_a^H + r_t^{abs})/r_{\text{total}}$, then an abstraction event is executed. Finally, if $\zeta_1 > (r_a^H + r_t^{abs})/r_{\text{total}}$, then a silicon radical is physisorbed.

Physisorption proceeds by selecting a random lattice site from the available hydrogenated and dangling bond sites; if a dangling bond site is chosen, the radical is directly chemisorbed within the same kMC event. Otherwise, the radical is deposited onto the hydrogenated surface and execution continues. For the case of hydrogen abstraction, a random SiH_3 radical is chosen and removed. A dangling bond is created at the chosen site and kMC execution continues. Then, a second random number is drawn from a uniform distribution and the time increment for this kMC step is calculated by:

$$\delta t = \frac{-\ln(\zeta_2)}{r_{\text{total}}}. \tag{2.12}$$

Decoupling surface migration

Due to the high frequency of surface migration events relative to physisorption or abstraction, a brute force kMC algorithm would expend >99% of computation time on migration alone; see Fig. 2.4. At standard operating conditions, here T = 500 K, P = 1 Torr, and a gas phase SiH_3 mole fraction of 8.62×10^{-5}, it is clear that only a small fraction of computational time is spent on events contributing to reactions leading to film growth. Consequently, the simulation of surface particle migration is decoupled from our standard kMC implementation using a one-dimensional lattice random walk process.

As a result, we introduce a propagator to monitor the motion of physisorbed radicals. At the completion of each kMC cycle (a single physisorption or abstraction event), N_H hydrogen migration and N_{SiH_3} silane migration events are executed in succession, where N_H and N_{SiH_3} are defined as

$$N_H = \frac{r_t^H}{r_a^H + r_t^{abs} + r_a^{SiH_3}}, \quad N_{SiH_3} = \frac{r_t^{SiH_3}}{r_a^H + r_t^{abs} + r_a^{SiH_3}}, \tag{2.13}$$

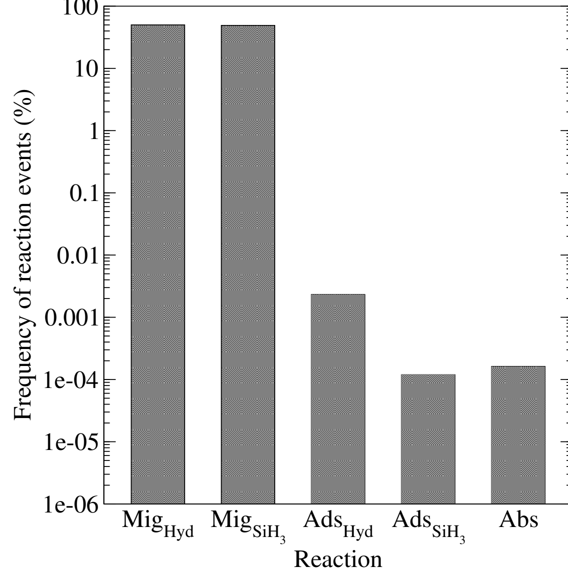

Figure 2.4: Normalized frequency of reaction events within the present kMC scheme at T = 500 K, P = 1 Torr, and a SiH_3 mole fraction of 8.62×10^{-5}.

where r_t^H and $r_t^{SiH_3}$ are the thermally activated migration rates of hydrogen and silane radicals, respectively. N_H and N_{SiH_3} are split evenly among the n_H and n_{SiH_3} physisorbed radicals. A one-dimensional, weighted random walk process is then initiated whereby the bulk motion of a chosen radical is modeled by the propagator. Propagation steps are weighted such that an exponentially higher probability exists for a particle to relax down the lattice as opposed to jumping up lattice positions. After walking N/n steps, the final location of the propagator is stored as the radical's new position. This cycle is executed $n_H + n_{SiH_3}$ times, allowing each radical to migrate before the next kMC event is chosen. Similar to Eq. (2.12), the time increment for a single migration step is calculated via the following equations:

$$\delta t_H = \frac{-\ln(\zeta_i)}{r_t^H}, \quad \delta t_{SiH_3} = \frac{-\ln(\zeta_i)}{r_t^{SiH_3}} . \tag{2.14}$$

Therefore, the total time required for all migration steps, Δt, is determined to be:

$$\Delta t = \frac{-\ln(\zeta_i)}{r_t^H} \cdot N_H + \frac{-\ln(\zeta_i)}{r_t^{SiH_3}} \cdot N_{SiH_3} . \tag{2.15}$$

Film growth continues to develop in this fashion until the specified film thickness is reached.

We have validated our methodology for decoupling diffusive processes from the remaining kinetic events by confirming that the underlying lattice random walk process results: (a) in growth rates on par with experimental values, and (b) surface morphologies appropriate for given operating parameters.

2.3 Open-loop results

2.3.1 Growth rates and roughness

The fidelity of the hybrid kMC formulation to experimentally obtained film characteristics is determined using a flat, 100 particle length (L = 100) lattice. The temperature, pressure, silane and hydrogen mole fractions are chosen as to represent industrially-used PECVD parameters and to correspond to conditions for which reliable experimental data exist for the film growth rate and surface morphology.

Two pressure regimes are tested against the hybrid kMC model: low-pressure ($<$1 Torr), and high-pressure ($\geq$1 Torr). Growth rates in the range of 1.3 to 5.5 Å/sec have been reported by Lee et al. [46] using substrate temperatures between 373 and 773 K in the low-pressure region. Although Lee et al. [46] utilized an argon diluted feed stream, the inert gas is ignored here, and by replicating their reported pressure and silane concentration (400 mTorr and 20% SiH_4 gas), a simulated 100 nm thick lattice is grown at 5.4 Å/sec at an operating temperature of 500 K. High deposition rates, $\sim$12 Å/sec, were achieved by Rech [59] and Perrin [56] using significantly higher operating pressures of 1-7 Torr. Our model exhibits a similar increase in growth rate within this region, with an average growth rate of 13.4 Å/sec across 10 runs. These results are in good agreement with experimentally established growth rates in both the high and low pressure regimes. The morphology of the growing film must next be considered.

Here the root mean square (RMS) roughness is used in order to make a quantitative comparison of simulated flat films to reference films grown experimentally. RMS roughness is calculated via

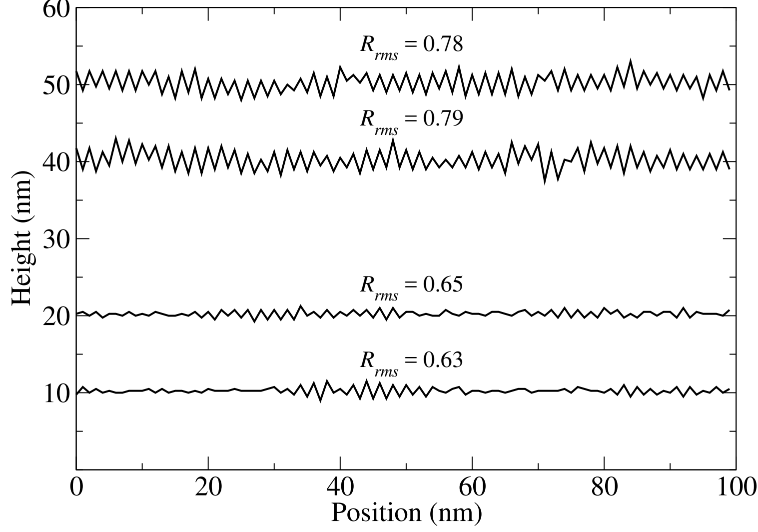

Figure 2.5: Evolution of surface roughness during the growth of an L = 100 flat film up to a thickness of $\bar{\tau}$ = 50 nm. Surfaces at 1 and 5 nm have been omitted for clarity.

Eq. (2.16):

$$R_{rms} = \sqrt{\frac{1}{L}\sum_{i=1}^{L}\left(h_i - \bar{h}\right)^2}, \tag{2.16}$$

where h_i is the height of the lattice at position i and $\bar{h}$ is the mean height of the lattice. It is important to note here that for flat (i.e., ungrated) thin films the height and thickness of the lattice are equivalent terms ($h_i = \tau_i$). However, this is not true for thin films that utilize grated wafer substrates; in this case the height is defined as the total of the thin film thickness and the grating height at a given lattice site (i.e., $h_i = \tau_i + H_i$).

Using scanning tunneling microscopy, Tanenbaum et al. [68] accurately measured the surface morphology during the evolution of a 50 nm thick amorphous silicon film deposited at 523 K and 540 mTorr. Mirroring these process parameters, a 100 particle lattice is grown and the rms roughness sampled at 1, 5, 10, 20, 40, and 50 nm thickness. Fig. 2.5 shows the evolution of surface roughness at each thickness. As represented by Fig. 2.6, the results match closely those reported by Tanenbaum et al. [68], owing further confidence to the hybrid kMC methodology utilized here.

The above results indicate that microscopic growth can only produce surface texture on the

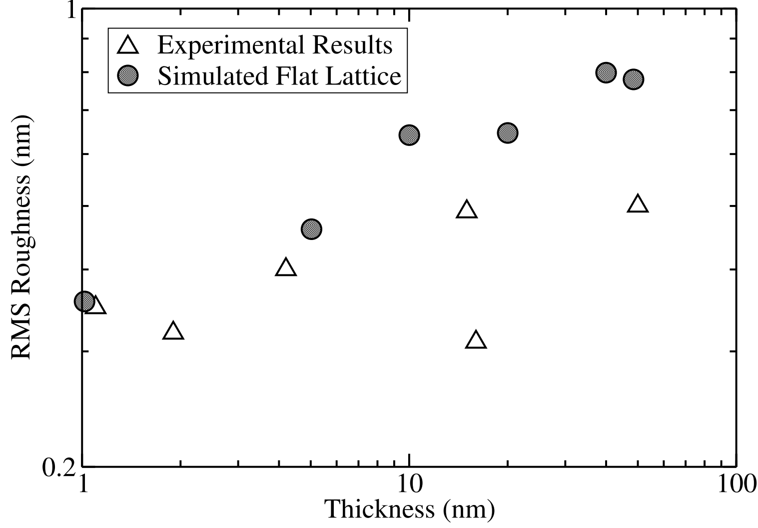

Figure 2.6: Comparison of experimental and simulated rms roughness at various film thicknesses.

order of a few nanometers. However, the diffusive transmittance of light has been characterized by Isabella et al. [32] to be dependent on roughness at significantly larger length scales. First, scattering can be enhanced using coarse grating where the geometrical dimensions of the rough surface are larger than the wavelength of light. Additionally, a second scattering mechanism becomes dominant when the vertical dimensions of the surface roughness become comparable to the wavelength of light. As a result, in an effort to increase light scattering and to obtain photocurrents from *a*-Si:H solar cells competitive with other existing solar cell technologies, surface roughness and height-height correlation length on the order of several hundred nanometers is desired [20, 28, 75, 63, 9, 33, 32, 47]. Here we introduce grating to the wafer surface in order to impart a periodic texture that has been optimized for light trapping. A sinusoidal grated wafer is used to initialize the deposition lattice and the initial heights of all particles are calculated as follows:

$$h_0(x) = \frac{H}{2}[\cos(2\pi x/P) + 1], \quad x \in [0, L) \tag{2.17}$$

where H is the peak-to-peak amplitude or height of the lattice and P is the period. In this work, L, H, and P are all set to 1200 in order to yield an initial grating with a period and height of 300 nm as specified for optimal absorbance [9].

2.3.2 Film surface morphology at light wavelength scale

Given that the migration of physisorbed radicals constitutes the vast majority of surface reactions, the shape of the wafer surface may be obscured after the deposition of the absorbing thin film layer. A full period (L = 1200) grated wafer is used here to determine the retention of initial grating shape parameters (i.e., height and period) after the growth of a 300 nm thick thin film. Fig. 2.7a shows the final film surface dimensions. The sinusoidal shape imparted by the grated wafer is retained after thin film growth: as can be seen from the overlay of the film surface onto the initial grating, Fig. 2.7b, apart from local roughness on the order of nanometers, the wafer grating dimensions are preserved. The reason for this consistency can be attributed to the dangling bond growth mechanism: unlike traditional solid-on-solid kMC schemes, here particles migrating down the lattice cannot directly contribute to film growth without chemisorbing at an existing dangling bond site. This reinforces the importance of hydrogen abstraction to the growth rate of *a*-Si:H thin films, and eliminates the need for microscopic control of surface morphology.

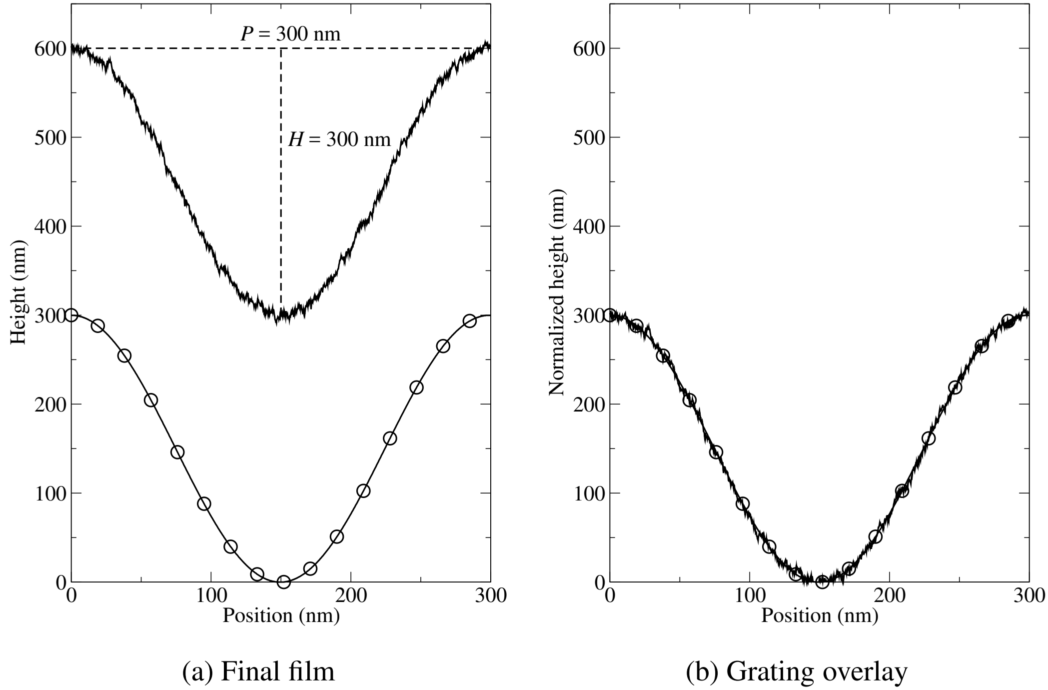

Figure 2.7: Preservation of grating shape after the growth of a 300 nm thick *a*-Si:H thin film. (a) The grated wafer (bottom curve in left plot) at H and P = 300 nm, with an $\bar{\tau}$ = 300 nm final film deposited above (top curve in left plot). (b) Thin film surface overlayed on the initial grating showing retention of desired sinusoidal shape. Note: Circles have been added to the grating profile for clarity.

2.3.3 Film thickness non-uniformity

Four parameters define the final shape of textured thin films: surface pattern, height H, period P, and film thickness τ. It has been shown that H and P are preserved from the initial grating, in this section, the proposed hybrid kMC model is applied at distinct locations across the wafer in order to investigate non-uniformity in film thickness due to the consumption of reactants across the wafer surface. As previously discussed, a steady-state concentration gradient for SiH_3 above the wafer surface has been calculated by Armaou and Christofides [11] using finite-difference and ADI methods. A radial non-uniformity >17% in the concentration of SiH_3 is observed from the center to the edge of the wafer. Here four zones are defined radially across the wafer surface and

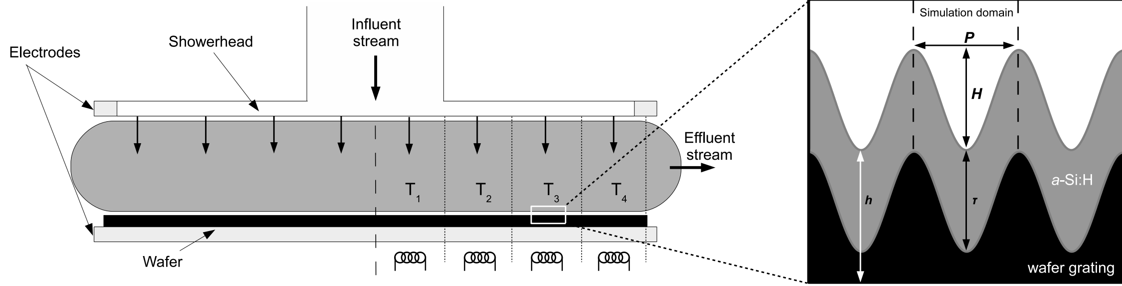

Figure 2.8: (left) Discrete PECVD reactor showing four independent, concentric substrate temperature control zones. (right) Microscopic simulation domain for a single grating period.

within each zone a single lattice period (L = 1200) is simulated (see Fig. 2.8). An SiH_3 mole fraction of $x_{SiH_3} = 8.62\times10^{-5}$ in the first zone and mole fractions of 8.35, 7.86, and 7.25×10^{-5} in zones 2-4, respectfully, are used to match the concentration profile adopted from Armaou and Christofides [11]. Identical sinusoidal grating is applied to each lattice with a height and period of 300 nm. The temperature of each zone is maintained at 500 K in a high-pressure region of 1 Torr. Experimental results suggest that an absorbing layer thickness of 300 nm be used for optimal light trapping in *a*-Si:H thin films [74]. Simulations using $x_{SiH_3} = 7.25\times10^{-5}$ (the mole fraction of zone 4) show an average deposition time of 246.996 seconds is required to reach the this thickness set-point ($\bar{\tau}$ = 300 nm). Therefore, each reactor zone is allowed to run for 246.996 seconds of physical growth (i.e., t = 246.996 is deposition time not computational time). Open-loop simulation results are shown in Figs. 2.9-2.11.

As evidenced by Figs. 2.9 and 2.10, a 17% difference in SiH_3 concentration yields a 15% difference in film thickness from the center (r = 0 cm) to the edge of the wafer (r = 10 cm). The hydrogen abstraction event frequency (f_a) and RMS roughness of each zone remained relatively unchanged (Table 2.2, Fig. 2.11) (a <2 nm increase in RMS roughness is negligible relative to the scale of visible light wavelengths). However, a marked decrease in event frequency from 3.36 to 2.85% for physisorption of SiH_3 (f_{SiH_3}) and increase from 63.31 to 63.81% for H (f_H) are present, as shown in Table 2.2. This result is expected due to the loss of SiH_3 radicals in the plasma phase as the process gas molecules travel across the wafer. An increased concentration of physisorbed

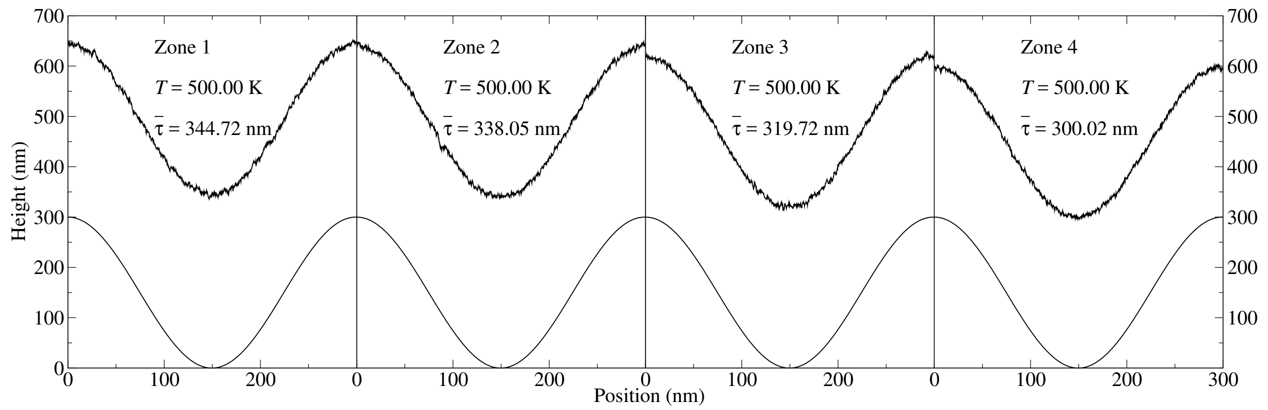

Figure 2.9: Open-loop growth of sinusoidally grated thin films at 500 K and 1 Torr. From left to right: x_{SiH_3} = 8.62, 8.35, 7.86, and 7.25×10^{-5}, respectfully. Note: Lattices are shown side by side for clarity, physical zones are composed of $\sim8\times10^4$ periods.

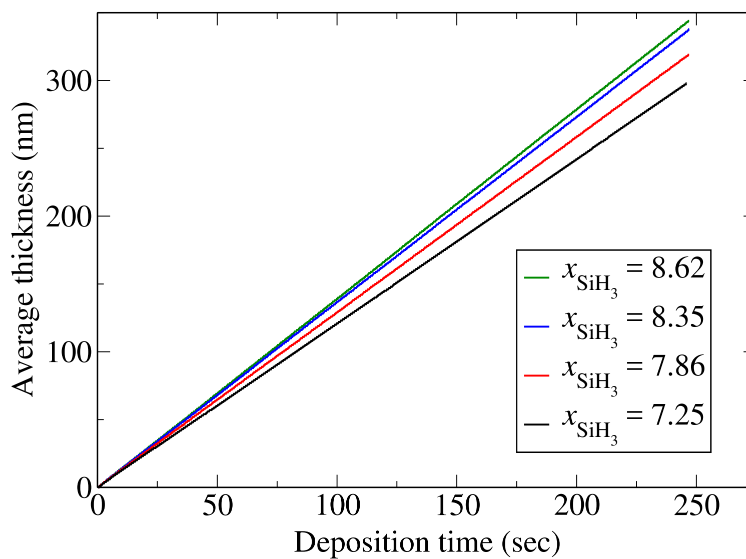

Figure 2.10: Evolution of the thickness (nm) of the four radial wafer zones over time. Note: Zone mole fractions are shown $\times10^5$.

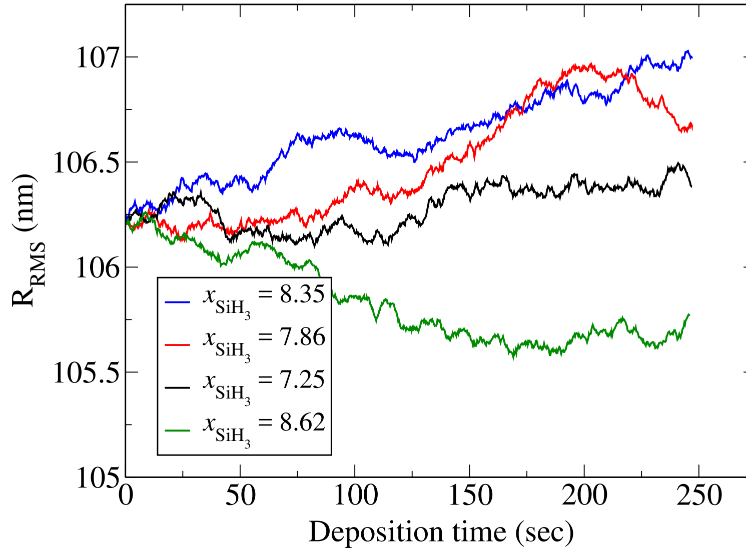

Figure 2.11: Evolution of the RMS roughness of the four radial wafer zones over time. Note: Zone mole fractions are shown $\times 10^5$.

Table 2.2: Quantitative non-uniformity of four radial wafer zones.

Zone	f_{SiH_3}	f_H	f_a	R$_{RMS}$	$\bar{\tau}$ (nm)
1	3.36	63.31	33.33	106.38	344.72
2	3.26	63.41	33.33	106.68	338.05
3	3.07	63.59	33.33	107.00	319.72
4	2.85	63.81	33.33	105.77	300.02

Note: Frequencies are expressed as a percentage of total events excluding migration.

SiH_3 relative to H near the center of the wafer allows for more rapid thin film growth as existing dangling bonds are more readily filled by migrating SiH_3 radicals. This effect can be overcome by either modulating the concentration of silane gas above the wafer using a closed-loop showerhead arrangement, or as proposed here, by utilizing radially spaced heating elements that allow for independently controlled substrate temperature zones.

2.4 Regulation of film thickness

A resulting non-uniformity in final film thickness of $\sim$15% suggests the implementation of an operation strategy on the PECVD process to improve uniformity at the wafer scale. An increased concentration of physisorbed SiH_3 relative to H near the center of the wafer allows for more rapid film growth as existing dangling bonds are more readily filled by migrating SiH_3 radicals. This effect can be overcome by either regulating the inlet concentration of silane gas above the wafer using a closed-loop showerhead arrangement [11], or, as proposed in this manuscript, by modulating the substrate temperature. Here four zones are defined radially across the wafer surface (Fig. 2.8) that allow for spatial manipulation of the substrate temperature. Due to the exponential dependence of hydrogen abstraction on surface temperature, the temperature set-point for each zone can be calculated a priori in order to overcome the SiH_3 concentration gap by increasing the fractional coverage of dangling bonds. Substrate temperature calculations are made using growth rate relations developed in the next section.

2.4.1 Growth rate relations

The relationship between substrate temperature (K), gas-phase mole fraction of SiH_3 (mol $\times 10^5$), and the thin film growth rate (Å/sec) is shown in Fig. 2.12. Each data point represents the average growth rate across ten runs of a sinusoidal lattice at p = 1 Torr (Note: Error bars have been omitted due to relatively small deviations and for clarity). Above 500 K growth is substantially slowed due to the inverse root dependence of SiH_3 physisorption on gas-phase temperature (see Eq. 2.9). To

avoid this plateau in growth, reactor operation is restricted to the region $\leq$500 K.

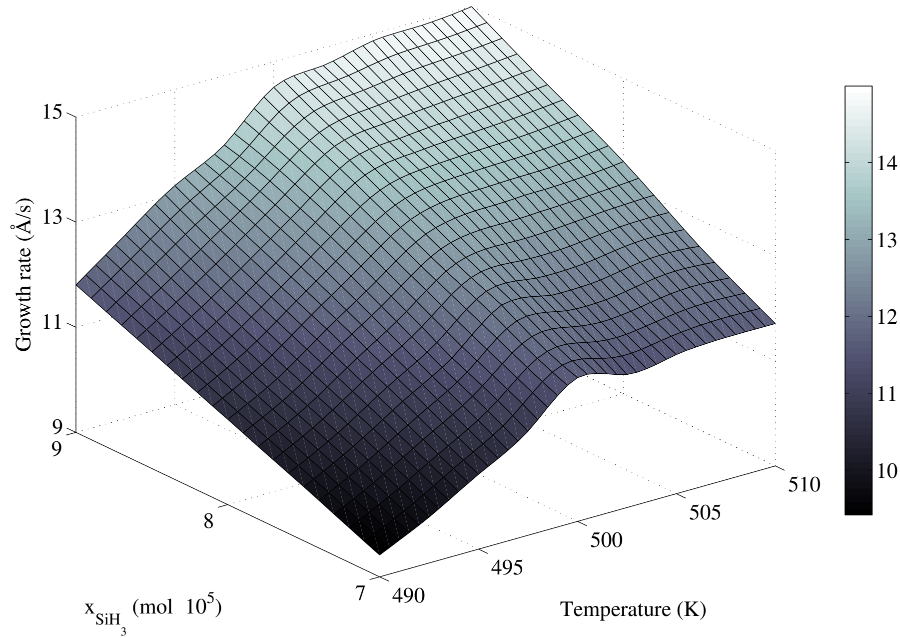

Figure 2.12: Relationship between growth rate, substrate temperature, and gas-phase mole fraction of SiH_3. Mole fractions, x_{SiH_3}, are shown $\times 10^5$.

As previously discussed, a steady-state concentration gradient for SiH_3 exists above the wafer surface with expected gas-phase concentrations of x_{SiH_3} = 8.62, 8.35, 7.86, and 7.25$\times 10^{-5}$ for substrate zones 1-4, respectively. By fixing the gas-phase composition at these values with a pressure of p = 1 Torr, film growth is observed to be roughly linear with respect to substrate temperature (Fig. 2.13 shows this relationship for the gas-phase mole fractions of SiH_3 in zones 1-3). As a result, the following linear growth rate equations can be fit using standard least squares methods:

$$
\begin{aligned}
G(T) &= 0.238\,T - 105.274 \; (\text{Å} \cdot K^{-1} s^{-1}),\; x_{SiH_3} = 8.62 \\
G(T) &= 0.254\,T - 113.673 \; (\text{Å} \cdot K^{-1} s^{-1}),\; x_{SiH_3} = 8.35 \qquad (2.18) \\
G(T) &= 0.227\,T - 100.875 \; (\text{Å} \cdot K^{-1} s^{-1}),\; x_{SiH_3} = 7.86
\end{aligned}
$$

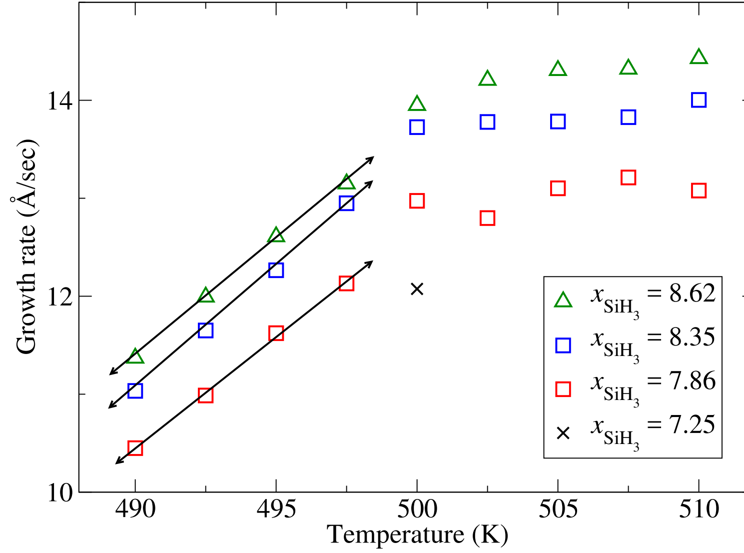

Figure 2.13: Linear relationships between growth rate and temperature for each reactor zone. Mole fractions, x_{SiH_3}, are shown $\times 10^5$. A single data point exists for x_{SiH_3} = 7.25 as zone 4 remains a fixed reference.

2.4.2 Regulating substrate temperature

The pressure within each zone is maintained at p = 1 Torr. Zone 4, the zone with the slowest relative growth, is used as a reference and hence the parameters remain fixed (x_{SiH_3} = 7.25 and T = 500 K). The mole fractions of zones 1-3 are set as described previously to 8.62, 8.35, and 7.86×10^{-5}, respectively. The necessary temperature set-point for each zone is calculated via Eq. (2.18) such that all growth rates match that of zone 4 (Note: zone 4 is chosen as a reference point in order to avoid operating the reactor above 500 K). The simulation parameters are summarized in Table 2.3.

Fig. 2.14 shows the film surface profile for each zone after t = 246.996 seconds of growth (the time required for zone 4 to reach $\bar{\tau}$ = 300 nm). Event frequency and thin film thickness data have been summarized in Table 2.4. A difference of ∼0.68% exists in the thickness of the a-Si:H thin film across the wafer. As discussed previously, the frequency of physisorption of SiH_3 shows a

Table 2.3: Calculated operating parameters by zone.

Zone	x_{SiH_3} ($\times 10^{-5}$)	p (Torr)	T (K)
1	8.62	1	493.06
2	8.35	1	495.07
3	7.86	1	497.58
4	7.25	1	500.00

Table 2.4: Quantitative non-uniformity of four radial wafer zones.

Zone	f_{SiH_3}	f_H	f_a	R_{RMS}	$\bar{\tau}$ (nm)
1	3.35	63.32	33.33	106.82	298.00
2	3.25	63.41	33.33	106.50	304.23
3	3.07	63.60	33.33	106.14	299.71
4	2.85	63.82	33.33	105.77	300.02

significant decrease toward the edge of the wafer due to the consumption of process gas. Although a greater number of SiH_3 radicals are present on the surface of the growing film, a decreased density of dangling bonds (due to a lower frequency of hydrogen abstraction f_a) in the inner zones allows for significant reduction in thin film thickness non-uniformity relative to deposition at a spatially-uniform substrate temperature.

2.4.3 Roughness dependence on substrate temperature variation

Regulation of the surface temperature may affect the roughness (R_{RMS}) leading to further non-uniformity between reactor zones. Here we simulate the growth of 300 nm thick thin film with sinusoidal grating at p = 1 Torr. The temperature is varied from 490-500 K and the mole fraction of SiH_3 in the gas-phase is varied from 7-9$\times 10^{-5}$. The relationship between substrate temperature (K), gas-phase mole fraction of SiH_3 (mol $\times 10^5$), and the surface roughness (R_{RMS}, nm) is shown in Fig. 2.15. Each data point represents the average roughness across ten runs of a sinusoidal

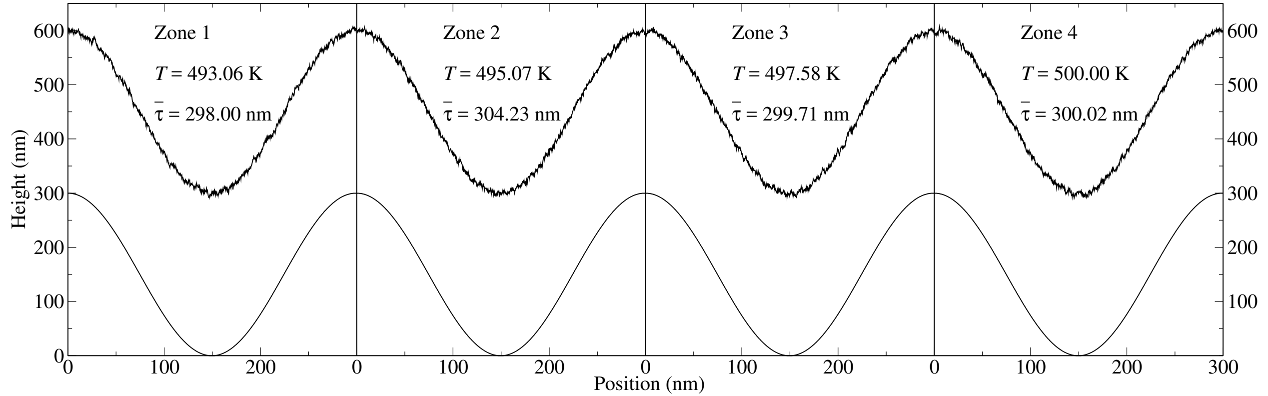

Figure 2.14: Surface microstructure and thickness of sinusoidally grated thin films with spatially dependent temperatures. From left to right: x_{SiH_3} = 8.62, 8.35, 7.86, and 7.25×10^{-5}, respectfully. Note: Lattices are shown side by side for clarity, physical zones are composed of $\sim8\times10^4$ periods.

lattice at p = 1 Torr (Note: Error bars have been omitted due to relatively small deviations and for clarity).

A slight trend of increasing roughness is shown to occur at low substrate temperatures and low gas-phase mole fractions of SiH_3 (Fig. 2.15). At low substrate temperatures the frequency of hydrogen physisorption is far greater than that of SiH_3 physisorption and hydrogen abstraction, as evidenced by Eqs. 2.9 and 2.10. As a result, the mobility of SiH_3 radicals is hindered which increases the roughness of the growing film surface. Additionally, at high SiH_3 gas-phase concentrations, SiH_3 radicals more readily physisorb at hydrogenated surface sites, effectively lowering the fractional coverage of hydrogen radicals and the observed surface roughness. A slight decrease in surface roughness is observed from zone 1 (which operates at T = 493 K and $x_{SiH_3} = 8.62\times10^{-5}$) to zone 4 (which operates at T = 500 K and $x_{SiH_3} = 7.25\times10^{-5}$) which may be attributed to the combined effect of the simultaneous increase in substrate temperature and decrease in SiH_3 mole fraction; evidence of this observed behavior is shown in Table 2.4. However, as discussed in previous sections, fluctuations in the surface roughness on the order of a few nanometers will not affect light trapping which occurs at the scale of visible light wavelengths.

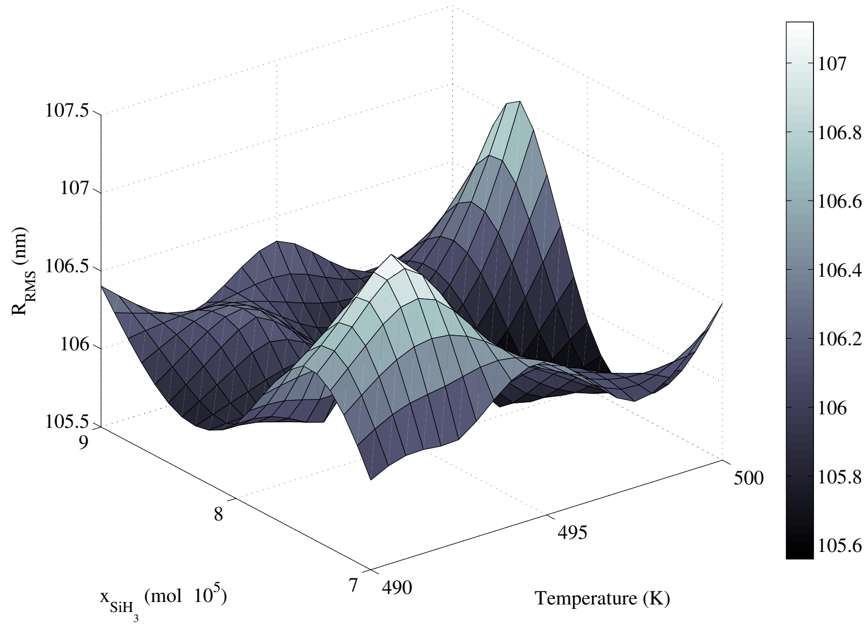

Figure 2.15: Relationship between surface roughness, substrate temperature, and gas-phase mole fraction of SiH_3. Mole fractions, x_{SiH_3}, are shown $\times 10^5$.

2.4.4 Robustness to model uncertainty

Uncertainties in radio frequency and heating element power may cause stochastic variation in process parameters that lead to increased non-uniformity in final film thickness. The robustness of our multiscale model to these fluctuations is explored using independent variation of the concentration of SiH_3 radicals, x_{SiH_3}, and the surface temperature, T, as well as concurrent variations in these parameters.

First, the necessary temperatures for zones 1-4 remain fixed at the values calculated previously to reduce radial thickness non-uniformity. In a similar manner to the previous section, the pressure within each zone is maintained at $p = 1$ Torr and zone 1, the innermost zone, is used as a reference and hence the simulation is terminated once 246.996 seconds of deposition time (the average time required for zone 4 to reach a thickness of 300 nm at T = 500 K and x_{SiH_3} = 7.25×10^{-5}) has elapsed. However, the concentration of radicals is allowed to vary by 1% above and below the expected values proposed by Armaou and Christofides [11] to account for uncertainties in RF

Table 2.5: Final film thickness for sinusoidally grated thin films in the presence of independent variations in x_{SiH_3} and T.

Variable	Zone	x_{SiH_3} ($\times 10^{-5}$)	T (K)	$\bar{\tau}$ (nm)
x_{SiH_3}	1	8.53	493.06	297.41
	2	8.43	495.07	306.11
	3	7.78	497.58	297.17
	4	7.32	500.00	303.25
T	1	8.62	492.56	292.39
	2	8.35	495.57	307.32
	3	7.86	498.08	303.00
	4	7.25	500.50	299.75

power. For each simulation a sinusoidally grated thin film with height H and period P = 300 nm is used. Operating parameters and resulting film thicknesses for independent variations are shown at the top of Table 2.5 (Note: values represent the maximum non-uniformity achieved within the allowed 1% fluctuation).

As expected, while maintaining the optimal temperature profile calculated previously, variations in gas-phase SiH_3 radical concentration increase final film thickness non-uniformity; however, the difference of 2.9% in the thickness of zones 2 and 3 remains relatively close to that of the initial optimized case (1.5%).

Second, the concentration of each zone is returned to the steady-state concentration gradient while the temperature is allowed to fluctuate within 0.5 K above and below the target values calculated previously using the proposed linear growth rate relations. Again, for each simulation a sinusoidally grated thin film with height H and period P = 300 nm is used. Operating parameters and resulting final film thicknesses for independent variations are shown at the bottom of Table 2.5 (Note: table values represent the maximum non-uniformity achieved within the allowed 0.5 K fluctuation).

A difference of 4.8% exists between the thickness of the zones 1 and 2. This result is expected given the linear relationship between film growth rate and surface temperature developed in previous sections. Although a 4.8% non-uniformity in thickness is significantly higher than the 2.0% non-uniformity reported for the optimal case, great improvement is still shown over the 15% non-uniformity experienced before substrate temperature regulation.

Finally, stochastic variations in the RF and heating element power are considered in tandem to account for concurrent uncertainties that may occur during operation. Independent fluctuations in SiH_3 concentration and substrate temperature that lead to maximum thickness non-uniformity are also applied here. Operating parameters and final film thicknesses are shown in Table 2.6.

Table 2.6: Final thin film thickness for sinusoidally grated wafers in the presence of concurrent variations in x_{SiH_3} and T.

Variable	Zone	x_{SiH_3} ($\times 10^{-5}$)	T (°C)	$\bar{\tau}$ (nm)
x_{SiH_3}, T	1	8.53	492.56	291.13
	2	8.43	495.57	309.67
	3	7.78	498.08	299.04
	4	7.32	500.50	301.85

Owing to contributions from both fluctuation sources, SiH_3 concentration and substrate temperature, a final film thickness non-uniformity of 6.0% is present. Again, this is a non-negligible difference in film thickness across the wafer; however, this represents the maximum non-uniformity experienced within the allowed parameter fluctuations, and a significant reduction from the initial 15% non-uniformity, validating the multiscale modeling and control strategy proposed in this work.

2.5 Conclusions

The present chapter focuses on the development of a multiscale modeling and operation framework for PECVD of thin film silicon solar cells with uniform thickness and film surface microstructure that optimizes light trapping. The macroscopic model of the gas phase is based on the hypothesis of continuum and provides the deposition rate profile across the wafer. The proposed microscopic model which utilizes a hybrid kinetic Monte Carlo algorithm that accounts for interactions amongst physisorbed radicals, chemisorption, and hydrogen abstraction, has been shown to reproduce experimentally obtained surface morphologies and growth rates. Initial simulations using flat lattices have shown that roughness is limited to a few nanometers and validated the need for grated wafer substrates in order to achieve roughness and height-height correlation length on the order of visible light wavelengths. The sinusoidal shape of grated wafers with a height and period of 300 nm has been shown to be preserved after the growth of amorphous silicon thin films up to 300 nm thickness. The retention of grating shape is attributed to the dependence of film growth on hydrogen abstraction, eliminating the need for microscale control of surface morphology. However, radially non-uniform deposition rates of the film on the wafer owing to gas-phase transport phenomena have shown that a 17% difference in SiH_3 concentration can yield a 15% difference in film thickness from the center (r = 0 cm) to the edge of the wafer (r = 10 cm). Due to the observed dependence of film growth rate on substrate temperature, the wafer surface has been separated into four concentric zones, each with an independent heating element. Extensive simulations demonstrate that the use of appropriate sinusoidal wafer grating and the regulation of substrate temperature provide a viable and effective way for the PECVD of thin film silicon solar cells with uniform thickness ($<1\%$) and film surface microstructure that optimizes light trapping, and were found to be robust with respect to model uncertainty.

Chapter 3

Multiscale Modeling and Run-to-Run Control of PECVD of Thin Film Solar Cells

3.1 Introduction

Two often neglected problems are persistent in the production of high quality amorphous silicon (*a*-Si:H) layers: the influence of reactor conditioning on the plasma chemistry [23], and the spatial non-uniformity in the thin film thickness [11] owing to gas-phase transport phenomena across the wafer. Specifically, during the initial operation of a clean PECVD reactor the plasma phase exhibits transient behavior as the interior surfaces become coated by the deposition species causing drift in the electron density profiles and in the film thickness. Second, at the reactor length scale (for example, a 20 cm wafer is used in this work) consumption and transport of deposition species across the wafer surface have been shown to cause growth rate differences greater than 19% [67, 64]. Given that the efficiency of a photovoltaic absorber layer (e.g., an *a*-Si:H thin film) is strongly dependent on the film thickness [34], reduction of growth rate non-uniformities is of paramount importance. While preconditioning prior to thin film deposition (i.e., allowing the reactor surfaces to become fouled) is a well-established practice, this represents significant waste in both valuable resources and manufacturing time. In addition, the film uniformity within a single batch cannot be

corrected via preconditioning alone, and has been shown to require advanced, in-situ processing techniques [13].

Recently much attention has been given to the development of model-based control schemes with the goal of improving solar cell performance through the production of textured surfaces (e.g., thin film grating) [29, 30]. These models typically rely on kinetic Monte Carlo (kMC) algorithms to simulate deposition processes and therefore focus on the evolution of surface microstructure in nano- to micrometer length scales. As a result, these models are unable to capture the reactor scale dynamics and cannot be applied to the problems mentioned previously which pertain to both the macroscopic and microscopic domains of batch PECVD reactor operation. Fortunately, advances in high-performance computing have made possible the modeling of multiscale processes with complex behavior and large system sizes [50, 36, 72]. In a previous work of our group [13], we developed a multiscale model which provided fundamental understanding of the dynamics involved in the PECVD of a-Si:H thin films and allowed for quantitative prediction of product quality. In the present work, we present improvements to our original model, as well as an additional simulation domain that allows for run-to-run (R2R) control of the batch process in an effort to counteract both batch-to-batch and spatial variations in the film thickness.

More specifically, this work proposes a multiscale modeling and operation framework which is capable of not only capturing the interdependence of the gas-phase and film growth phenomena, but also allows for multi-batch operation under the implementation of a run-to-run (R2R) control algorithm. Within a single batch simulation a standard gas-phase model is used; however, the microscopic model, describing the a-Si:H thin film surface evolution, has been developed from the work of Tsalikis et al. [69] to be computationally efficient and account for the four dominant microscopic processes: physisorption, surface migration, hydrogen abstraction, and chemisorption. As opposed to traditional kMC formulations, surface migration has been decoupled from the other microscopic surface processes owing to its faster rate to allow for simulations on the order of thousands of monolayers without compromising fidelity to established chemical models.

At the completion of each batch simulation, a novel R2R control algorithm is applied in order

to predict appropriate operating conditions for the upcoming batch. In other words, post-batch measurements of the film thickness at various radial positions are fed to an exponentially weighted moving average (EWMA) algorithm which in turn updates the temperature of the PECVD reactor within discrete zones. It is demonstrated that through appropriate tuning of the multiscale model, and application of the proposed R2R operation strategy, the thin film product can be driven to the desired thickness set-point regardless of radial position and drift within the PECVD reactor.

The structure of this chapter is as follows: first, a detailed description of both the macroscopic gas-phase and microscopic surface models are provided. Next, extensive simulations demonstrate strong agreement between experimentally grown *a*-Si:H films and those resulting from the multiscale model proposed in this work. A total of 40 serial batch simulations conducted using the nominal process parameters (i.e., T = 475 K and P = 1 Torr) then reveal drift in the product away from the desired film thickness of 300 nm. The proposed EWMA algorithm is then applied within a single reactor zone and shown to successfully reduce film offset to within the process noise level. Finally, four concentric reactor zones are defined, each with a corresponding R2R controller and initial gas-phase concentration. In the presence of both plasma variation caused by conditioning of the reactor and spatial non-uniformity caused by consumption of the process gas, the proposed control scheme demonstrates significantly improved thickness uniformity regardless of radial position within the reactor.

3.2 Process description and modeling

The process under consideration in this work is a parallel plate PECVD reactor utilizing two charged electrodes designed to deposit thin films onto a single wafer placed on top of the lower electrode; see Fig. 3.1 (left). We employ a showerhead arrangement to distribute the influent gas stream consisting of a 9:1 mixture of hydrogen (H_2) and silane (SiH_4) throughout the chamber. Thin film growth proceeds through the production of plasma by an radio frequency (RF) power source which generates a chemically reactive mixture of radicals. These radicals (namely, SiH_3

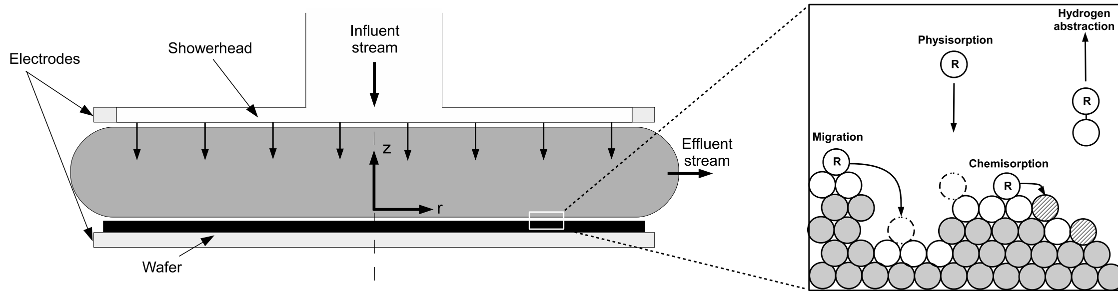

Figure 3.1: Macroscopic (left) and microscopic (right) PECVD simulation regimes.

and H) are transported to the surface via diffusion and convection where they react to form amorphous silicon (*a*-Si:H). Successful deposition requires the uniform growth of a 300 nm thick *a*-Si:H film on a wafer with a diameter of 20 cm.

Two distinct simulation regimes exist within this framework: the macroscopic gas phase which includes mass and energy balances, as well as the complex, microscopic surface interactions that dictate the structure of the silicon film of interest. Fig. 3.1 highlights the multiscale character of this process and the need to capture the dynamics at both scales due to the codepedency between the macroscopic and microscopic regimes. The following sections detail both the macroscopic gas-phase model and the microscopic surface model.

3.2.1 Gas-phase model

The twelve dominant species that lead to film growth and their corresponding thirty-four gas-phase reactions are accounted for throughout this work. A complete listing of the reactions, mechanisms and rate constants are available in Table 3.1.

The first set of results presented in this work, within the open-loop operation section, assume that the process gas is well mixed and the rate constants do not depend on temperature. For this case a differential mass balance is used to numerically integrate the species concentrations forward with time and the resulting values are used without reference to the spatial location within the PECVD reactor. The following differential equation demonstrates the possible contributions to the

Table 3.1: Reactions included in the gas-phase model. Note: Rate constants have units of cm^3/sec and have been adopted from the collection prepared by Kushner et al. [41].

Reaction	Mechanism	Rate constant
R^1	$e^- + H_2 \rightarrow 2H$	7.66×10^{12}
R^2	$e^- + SiH_4 \rightarrow SiH_3 + H$	9.57×10^{13}
R^3	$e^- + SiH_4 \rightarrow SiH_3^+ + H$	3.40×10^{12}
R^4	$e^- + SiH_4 \rightarrow SiH_2 + 2H$	1.13×10^{13}
R^5	$e^- + SiH_4 \rightarrow SiH + H_2 + H$	5.62×10^{12}
R^6	$e^- + SiH_4 \rightarrow Si + H_2 + 2H$	6.70×10^{12}
R^7	$e^- + Si_2H_6 \rightarrow SiH_3 + SiH_2 + H$	2.15×10^{13}
R^8	$e^- + Si_2H_6 \rightarrow H_3SiSiH + 2H$	7.41×10^{13}
R^9	$e^- + Si_3H_8 \rightarrow H_3SiSiH + SiH_4$	3.35×10^{14}
R^{10}	$H + SiH_2 \rightarrow SiH_3$	6.68×10^{11}
R^{11}	$H + SiH_2 \rightarrow SiH + H_2$	1.20×10^{13}
R^{12}	$H + SiH_3 \rightarrow SiH_2 + H_2$	1.20×10^{13}
R^{13}	$H + SiH_4 \rightarrow SiH_3 + H_2$	1.38×10^{12}
R^{14}	$H + H_2Si = SiH_2 \rightarrow Si_2H_5$	3.01×10^{12}
R^{15}	$H + Si_2H_6 \rightarrow SiH_4 + SiH_3$	4.03×10^{12}
R^{16}	$H + Si_2H_6 \rightarrow Si_2H_5 + H_2$	7.83×10^{12}
R^{17}	$H + Si_3H_8 \rightarrow Si_2H_5 + SiH_4$	1.19×10^{12}
R^{18}	$H_2 + SiH \rightarrow SiH_3$	1.20×10^{12}
R^{19}	$H_2 + SiH_2 \rightarrow SiH_4$	1.20×10^{11}
R^{20}	$SiH_2 + SiH_4 \rightarrow Si_2H_6$	6.02×10^{12}
R^{21}	$SiH_3 + SiH_3 \rightarrow SiH_4 + SiH_2$	4.22×10^{12}
R^{22}	$SiH_3 + SiH_3 \rightarrow Si_2H_6$	6.02×10^{12}
R^{23}	$SiH + SiH_4 \rightarrow Si_2H_5$	1.51×10^{12}
R^{24}	$SiH_2 + SiH_4 \rightarrow H_3SiSiH + H_2$	6.02×10^{12}
R^{25}	$SiH_2 + Si_2H_6 \rightarrow Si_3H_8$	7.23×10^{13}
R^{26}	$SiH_2 + SiH_3 \rightarrow Si_2H_5$	2.27×10^{11}
R^{27}	$SiH_3 + SiH_3 \rightarrow SiH_4 + SiH_2$	4.06×10^{13}
R^{28}	$SiH_3 + Si_2H_6 \rightarrow SiH_4 + Si_2H_5$	1.98×10^{13}
R^{29}	$Si_2H_5 + SiH_4 \rightarrow SiH_3 + Si_2H_6$	3.01×10^{11}
R^{30}	$SiH_3 + Si_2H_5 \rightarrow Si_3H_8$	9.03×10^{13}
R^{31}	$H_3SiSiH + SiH_4 \rightarrow Si_3H_8$	6.02×10^{12}
R^{32}	$Si_2H_5 + Si_2H_5 \rightarrow Si_3H_8 + SiH_2$	9.03×10^{13}
R^{33}	$H_3SiSiH \rightarrow H_2Si = SiH_2$	2.71×10^{13}
R^{34}	$H_2Si = SiH_2 \rightarrow H_3SiSiH$	2.29×10^{10}

mass balance for a given species:

$$\frac{dc_i}{dt} = \frac{c_i^{in}}{t_{in}} - \frac{c_i}{t_{out}} + [\sum_j \nu_i^j R^j] - \frac{1}{N_a V} r_{phys,i} + \frac{1}{N_a V} r_{abs,i}\,, \tag{3.1}$$

where c_i is the concentration in mol/cm^3 of species i, t_{in} is the inlet gas time constant defined as the reactor volume over the flow rate into the reactor, t_{out} is the outlet stream time constant defined as the reactor volume over the flow rate out of the reactor, ν_i^j is the stoichiometric coefficient for reactant i in reaction j as listed in Table 3.1, $r_{phys,i}$ is the rate of physisorption of species i, and $r_{abs,i}$ is the rate of abstraction of species i from the wafer surface.

The second set of results presented in this work, those referring to spatial non-uniformity in film growth, utilize a gas-phase model that includes energy and momentum balances in addition to the differential mass balance presented above. Under the assumptions of axisymmetric flow and continuum in the gas phase, mass, energy and momentum balances allow for the detailed modeling of the gas phase required in order to investigate spatial non-uniformities. The governing equations have been developed at length for CVD-type applications (e.g., [71, 45, 11]); however, here we apply the formulation by Armaou and Christofides [11] as radial dependence of species concentrations is needed to be accounted for due to the strong dependence of thin film thickness on photovoltaic efficiency. The mathematical model of the PECVD reactor consists of a flow velocity profile and four nonlinear dynamic diffusion-convection-reaction equations in two (radial and axial) dimensions (a set of four coupled parabolic PDEs). By treating the gas-phase as a three-dimensional stagnation flow, the evolution of the flow velocity profile within the PECVD reactor is computed from the Navier-Stokes and continuity equations. The spatio-temporal evolution of the concentration of the species throughout the reactor is obtained by applying dynamic material balances to the gas phase and accounting for diffusive and convective mass transfer, and bulk and surface reactions. Finite-difference methods are then applied in order to discretize the spatial derivative of the species concentration in the r and z directions (z is defined as the direction normal to the wafer surface; see Fig. 3.1). Finally, time integration of the resulting ordinary dif-

ferential equations is performed using the alternate direction implicit (ADI) method. More details on the model structure can be found in Armaou and Christofides [11], and calculated steady-state concentration profiles are discussed further in the spatial non-uniformity results section.

3.2.2 Surface microstructure model

The kMC methodologies applied in this work follow closely that of Crose et al. [13] and share many features common to standard kinetic Monte Carlo processes; however, simulation results generated by the multiscale model can vary widely due to discrepancies in the physical phenomena and model parameters used. As such, details of the microscopic surface interactions are presented here in full, starting with the thin film chemistry and growth kinetics.

Thin film growth chemistry

At the operating conditions of interest (T = 475 K and P = 1 Torr) two species dominate the interactions on the growing film, SiH_3 and H; the remaining species that exist in the gas-phase model are prohibited from depositing on the lattice surface and as a result are ignored for the remainder of the microscopic model. A schematic of the surface interactions is shown in Fig. 3.2, and has been verified experimentally by Perrin et al. [56] and Robertson [61]. Physisorption occurs as SiH_3 and H radicals encounter hydrogenated silicon sites ($\equiv \mathrm{Si}-\mathrm{H}$) at the film surface according to the following reactions:

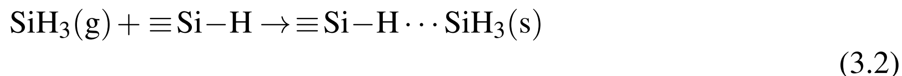

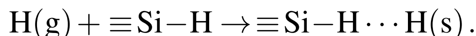

$$\begin{aligned} \mathrm{SiH_3(g)} + \equiv\mathrm{Si{-}H} &\rightarrow \equiv\mathrm{Si{-}H}\cdots\mathrm{SiH_3(s)} \\ \mathrm{H(g)} + \equiv\mathrm{Si{-}H} &\rightarrow \equiv\mathrm{Si{-}H}\cdots\mathrm{H(s)}\,. \end{aligned} \tag{3.2}$$

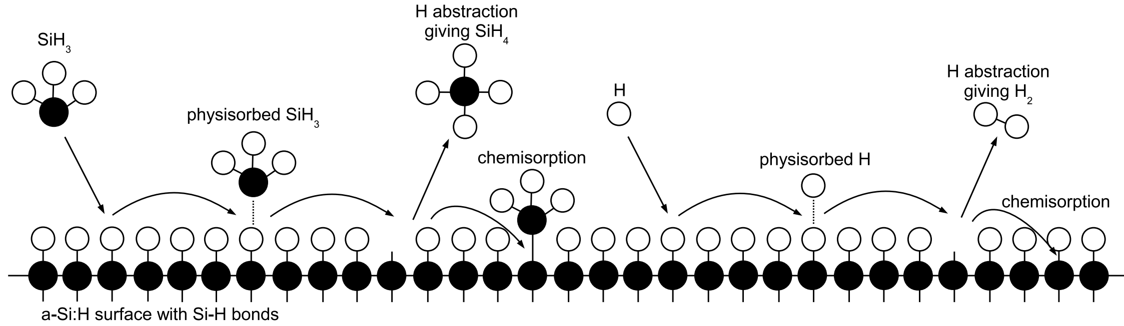

Figure 3.2: Chemical model illustration showing particle-surface interactions.

Migration involves the rapid diffusion of physisorbed radicals across the lattice surface:

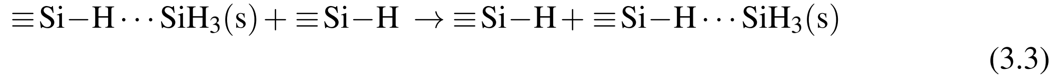
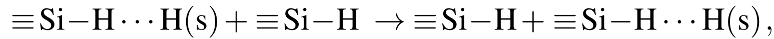

$$\begin{aligned} &\equiv\mathrm{Si{-}H}\cdots\mathrm{SiH_3(s)} + \equiv\mathrm{Si{-}H} \rightarrow \equiv\mathrm{Si{-}H} + \equiv\mathrm{Si{-}H}\cdots\mathrm{SiH_3(s)} \\ &\equiv\mathrm{Si{-}H}\cdots\mathrm{H(s)} + \equiv\mathrm{Si{-}H} \rightarrow \equiv\mathrm{Si{-}H} + \equiv\mathrm{Si{-}H}\cdots\mathrm{H(s)}\,, \end{aligned} \tag{3.3}$$

eventually contributing to either hydrogen abstraction:

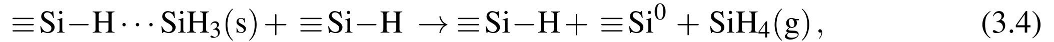

$$\equiv\mathrm{Si{-}H}\cdots\mathrm{SiH_3(s)} + \equiv\mathrm{Si{-}H} \rightarrow \equiv\mathrm{Si{-}H} + \equiv\mathrm{Si^0} + \mathrm{SiH_4(g)}\,, \tag{3.4}$$

whereby a physisorbed SiH_3 radical removes a surface hydrogen forming SiH_4 and creating a dangling bond ($\equiv Si^0$), or chemisorption at a preexisting dangling bond site according to the following reactions:

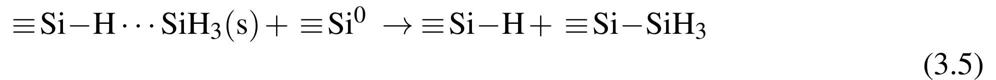
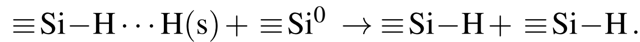

$$\begin{aligned} &\equiv\mathrm{Si{-}H}\cdots\mathrm{SiH_3(s)} + \equiv\mathrm{Si^0} \rightarrow \equiv\mathrm{Si{-}H} + \equiv\mathrm{Si{-}SiH_3} \\ &\equiv\mathrm{Si{-}H}\cdots\mathrm{H(s)} + \equiv\mathrm{Si^0} \rightarrow \equiv\mathrm{Si{-}H} + \equiv\mathrm{Si{-}H}\,. \end{aligned} \tag{3.5}$$

Chemisorption of SiH_3 at a dangling bond site permanently grows the lattice position by one (i.e., the Si atom is fixed at that location and is no longer a candidate for migration), whereas chemisorption of H results in the surface site returning to a hydrogenated state.

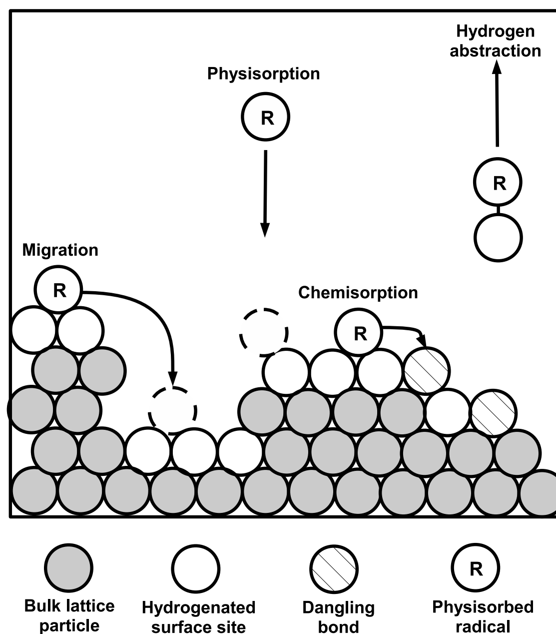

Figure 3.3: Triangular lattice representation showing four microscopic processes. Processes from left to right: migration, physisorption, chemisorption, and hydrogen abstraction.

Lattice Characterization

In our recent work [13], a solid-on-solid (SOS) lattice was implemented; specifically, particles in each successive monolayer were centered above those of the previous layer and the occupation of vacant postilions was enforced in order for the height of a given lattice column to increase. Alternatively, a two-dimensional triangular lattice is used in this work which allows for the deposition of SiH_3 and H particles (each deposited species is modeled by a single particle) without the restriction of SOS behavior. While an SOS square lattice does not allow for the creation of voids and porous structure within the film, a triangular lattice can produce overhangs that lead to voids while maintaining a minimum of two nearest neighbors per particle (see Fig. 3.3).

The size of the two-dimensional lattice is characterized by the number of lateral sites, L, and the number of monolayers, H. Using a silicon diameter of $\sim$0.25 nm, the physical length of the

lattice can be calculated as $0.25\times L$. Similarly, the thickness is calculated by:

$$\tau = 0.25 \cdot H \cdot \frac{\sqrt{3}}{2}, \tag{3.6}$$

where the factor $\sqrt{3}/2$ accounts for the reduction in thickness due to the offset monolayers (refer to Figs. 3.3 and 3.4). The number of lateral sites is chosen to be 1200 in this work as it allows for the morphology of the film to be adequately captured without being so large as to necessitate spatial variations in the gas-phase. It is important to note here that although spatial variations in the gas-phase species concentrations are introduced in later sections, they are applied at the macroscopic scale (i.e., between reactor zones) not within individual microscopic kMC simulations.

In order to enforce the restriction that all physisorbed and chemisorbed particles exist in stable, predetermined lattice locations, surface relaxation is included in the microscopic model. As shown in Fig. 3.4, an incident particle must first relax to a position that is centered within the defined triangular lattice. Additionally, each particle must meet the criteria of at least two nearest-neighbors to be considered stable. Unstable particles continue to relax down the lattice until a stable location is reached.

Relative rates formulation

A standard Arehenius-type formulation can be used to estimate the rate of thermally activated kinetic events (e.g., migration and hydrogen abstraction):

$$r_{t,i} = v_i e^{-E_i/k_B T}, \tag{3.7}$$

where v_i is the attempt frequency prefactor (s^{-1}) and E_i is the activation energy of radical i. Frequency prefactor and activation energy values are drawn from Perrin et al. [56] to correspond to the growth of a-Si:H films via the two species deposition of SiH_3 and H.

Physisorption events follow an athermal or barrierless reaction model based on the fundamental

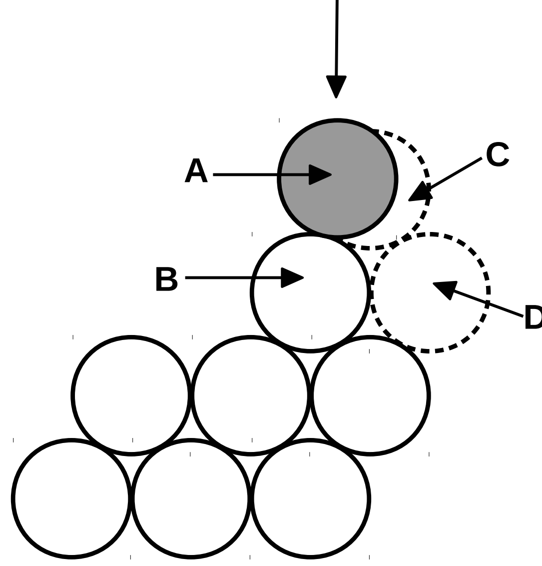

Figure 3.4: Surface relaxation for physisorbed radicals. (a) Incident particle location. (b) Surface Si particle in lattice. (c) Predefined triangular lattice site with one nearest neighbor. (d) Stable position for incident particle (two nearest neighbors).

kinetic theory of gases which yields the following rate equation:

$$r_{a,i} = J_i s_c N_a \sigma \,, \tag{3.8}$$

where J is the flux of gas-phase radicals, s_c is the local sticking coefficient, N_a is the Avogadro number, and σ is the average area per surface site. J can be calculated via the following equations:

$$J_i = \eta_i \bar{u}_i \,, \tag{3.9}$$

$$\eta_i = \frac{p_i}{RT} \,, \tag{3.10}$$

$$\bar{u_i} = \sqrt{\frac{8k_B T}{\pi m_i}} \,, \tag{3.11}$$

where η_i is the number density of radical i (here the reactive gas-phase is assumed to be ideal), $\bar{u_i}$ is the mean radical velocity, p_i is the partial pressure of i, R the gas constant, T is the temperature,

Table 3.2: Sticking coefficients and reaction rates composing the chemical model.

Thermally activated		Athermal reactions	
Reaction type	Reaction rate ($s^{-1}site^{-1}$)	Reaction type	Sticking coefficient
hydrogen abstraction	3.35×10^{5}	SiH_3 physisorption	0.5
hydrogen migration	1.58×10^{11}	hydrogen physisorption	0.8
SiH_3 migration	1.16×10^{11}		

k_B is the Boltzmann constant, and m_i is the molecular weight of radical i. Substitution of Eqs. (3.9)-(3.11) into Eq. (3.8) provides the overall reaction rate for an athermal radical i:

$$r_{a,i} = \frac{p_i}{RT}\sqrt{\frac{8k_BT}{\pi m_i}}s_cN_a\sigma\,. \tag{3.12}$$

Reaction rates and sticking coefficients for the nominal process conditions (i.e., T = 475 K and P = 1 Torr) are given in Table 3.2. Sticking coefficients are reported for athermal reactions rather than reaction rates as these are not dependent on the gas-phase composition which varies significantly from batch to batch. The microscopic surface kinetics presented in this work have been developed from the detailed work of Tsalikis et al. [69].

Kinetic Monte Carlo implementation

The time evolution of the lattice microstructure is simulated using a standard n-fold kinetic Monte Carlo algorithm. The overall reaction rate is defined as

$$r_{\text{total}} = r_a^{SiH_3} + r_a^{H} + r_t^{abs}\,, \tag{3.13}$$

where $r_a^{SiH_3}$ is the rate of physisorption of SiH_3, r_a^{H} is the rate of physisorption of H, and r_t^{abs} is the rate of hydrogen abstraction forming SiH_4. Surface migration does not factor into the overall rate as it has been decoupled in the interest of computational efficiency and will be discussed at length in the next subsection. At the beginning of each kMC event a uniform random number, $\gamma_1 \in [0,1]$ is generated. If $\gamma_1 \leq r_a^{SiH_3}/r_{\text{total}}$, then an SiH_3 physisorption event is executed. If $r_a^{SiH_3}/R_{\text{total}} <$

$\gamma_1 \leq (r_a^{SiH_3} + r_a^H)/r_{\text{total}}$, then a hydrogen radical is physisorbed. Finally, if $\gamma_1 > (r_a^H + r_t^{abs})/r_{\text{total}}$, then the abstraction of a surface hydrogen via SiH_3 occurs.

Both physisorption of SiH_3 and H start by selecting a random lattice site from a list of the available hydrogenated and dangling bond surface sites. If the chosen site contains a dangling bond, the radical becomes instantaneously chemisorbed causing the lattice to grow by one; otherwise, the radical is deposited on the lattice surface where it relaxes to a stable position (see Fig. 3.4) before becoming a candidate for migration events. Hydrogen abstraction proceeds by removing a random SiH_3 particle to form SiH_4, which is returned to the gas-phase and execution continues. Next, a second random number, γ_2, is chosen and the time step for this kMC event is calculated as

$$\delta t = \frac{-\ln(\gamma_2)}{r_{\text{total}}}, \tag{3.14}$$

where $\gamma_2 \in (0,1]$ is a uniform random number.

Decoupling surface migration

Figure 3.5 highlights the disparity in the frequency of migration events relative to other event types. As a result, more than 99% of computational resources would be spent on migration alone in a traditional brute force kMC algorithm. At the standard operating conditions of T = 475 K and P = 1 Torr, it is clear that only a small fraction of simulation time contributes to events leading to film growth; consequently, the computation of rapid particle migration is decoupled from our standard n-fold kMC implementation using a two-dimensional lattice random walk process. A kMC cycle is defined by a single physisorption or abstraction event. At the completion of each cycle, a propagator is introduced to monitor the motion of physisorbed radicals. The total number of propagation steps is $N_H + N_{SiH_3}$ where

$$N_H = \frac{r_t^H}{r_a^H + r_t^{abs} + r_a^{SiH_3}}, \quad N_{SiH_3} = \frac{r_t^{SiH_3}}{r_a^H + r_t^{abs} + r_a^{SiH_3}}, \tag{3.15}$$

and r_t^H and $r_t^{SiH_3}$ are the thermally activated migration rates of hydrogen and silane radicals,

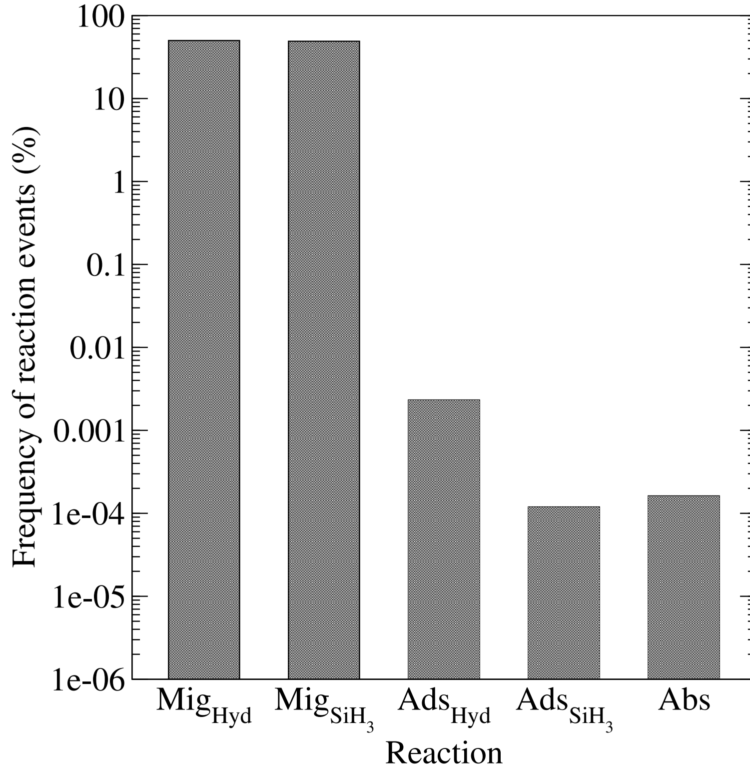

Figure 3.5: Normalized frequency of reaction events within the present kMC scheme at T = 475 K, P = 1 Torr, and a SiH_4^{in} mole fraction of 0.9.

respectively. The N_H and N_{SiH_3} propagation steps are split evenly among the n_H and n_{SiH_3} physisorbed radicals. Each radical then undergoes a two-dimensional random walk process that approximates the intricate movements of an individual particle with the bulk motion of the propagator. The procedure of the random walk process is as follows: a radical type is chosen, a random radical of the given type is selected, the weighted random walk with N_i/n_i propagation steps begins, propagation continues until either N_i/n_i steps have occurred or the radical becomes chemisorbed at a dangling bond site, the final position of the propagator is then stored as the radical's new position and this cycle continues for all $n_H + n_{SiH_3}$ physisorbed species. It is important to note that the weighting of each propagation step is such that an exponentially higher probability exists for a particle to relax down the lattice as opposed to jumping up lattice positions. In a similar manner to physisorption and hydrogen abstraction, the time increment for an individual migration step is

calculated via the following equations:

$$\delta t_H = \frac{-\ln(\gamma_i)}{r_t^H}, \quad \delta t_{SiH_3} = \frac{-\ln(\gamma_j)}{r_t^{SiH_3}}. \tag{3.16}$$

Therefore, the total time required for all migration events, δt, is determined to be

$$\Delta t = \sum_{i}^{N_H} \frac{-\ln(\gamma_i)}{r_t^H} + \sum_{j}^{N_{SiH_3}} \frac{-\ln(\gamma_j)}{r_t^{SiH_3}}. \tag{3.17}$$

Film growth continues to develop under the hybrid kMC algorithm until the time allotted for a given batch has elapsed, t_{batch}.

Our methodology of decoupling the diffusive processes from the remaining kinetic events has been validated by confirming that the underlying lattice random walk process results: (1) in surface morphologies and film porosities appropriate for the chosen process parameters, and (2) growth rates on par with experimental values. Details of our model validation strategy are given in the following sections.

3.3 Parallel computation

Due to the size of the multiscale simulations presented in this work, the computational demands are non-trivial. Specifically, deposition of a 300 nm thick film with a horizontal dimension of 300 nm requires a simulation time on the order of days when using a single processor. The results presented in this work represent many successive batches, as well as data that has been averaged over several repeated simulations in an effort to reduce noise that occurs due to the stochastic nature of the kMC model. Consequently, computation on a single processor represents an impractical task; however, we present parallel computation here as a viable solution.

The motivations behind the use of parallel computation are threefold. As mentioned previously, the reduction in simulation time for a serial task is significant through the use of multiple processors. Second, kMC simulations inherently exhibit noise due to the stochastic nature of the

model. By repeating a simulation with the same parameters numerous times we can reduce the noise and obtain more accurate, averaged values. Finally, one might want to perform many simulations at different conditions (e.g., to find suitable model parameters by testing various deposition conditions and calibrating with known experimental data).

As a brief outline, the process of creating a parallel program can be broken down into three elementary steps: (1) the original serial task is decomposed into small computational elements, (2) tasks are then distributed across multiple processors, and (3) communication between processors is orchestrated at the completion of each batch simulation. Here decomposition of the original program is achieved by separating duplicate batch simulations only, as single batch operations cannot be parallelized. The maximum achievable speedup can then be calculated as follows:

$$S(N) = \frac{1}{(1-P)+\frac{P}{N}}, \tag{3.18}$$

where S is the maximum speedup, P is the fraction of the program which is available for parallelization (i.e., the fraction of the serial task which involves repeated batch simulations), and N is the number of processors utilized [17].

There are two general modes used in the assignment of tasks: synchronous and asynchronous. Given the need for averaged data to be available before the next batch can be initiated, a synchronous scheme is necessary despite a slight loss in performance as compared to an asynchronous workflow in which processors are not required to wait for a batch competition before starting the next task. In other words, if it is desired to simulate n batches of PECVD reactor with ten redundant computations per batch, all ten redundant tasks must complete before the next batch in line can be initiated.

Orchestration of the assigned tasks and communication between processors is achieved using a standard message-passing interface (MPI) structure and therefore will not be discussed at this time. Further details of the parallel computation strategy employed here can be found in the recent publication of Kwon et al. [42] on which the parallel computation is based.

To demonstrate the reduction in computational time, a sample batch-to-batch simulation is run which includes 40 successive batches of PECVD of a 300 nm thick film with 10 redundant calculations per batch. The resulting computational requirements are shown in Table 3.3. It is clear that significant time savings are achieved as the number of cores utilized is increased. Increasing the number of cores also generates additional overhead costs due to the communication between cores and the requirement that all cores wait for the completion of the slowest redundant calculation; this is evident in the difference between the true and ideal speedup times when $n_{cores} > 1$.

Table 3.3: Required time to complete a sample batch-to-batch simulation and the speedup time achieved.

n_{cores}	time (hours)	speedup (times)	ideal speedup (times)
1	73.83	1.00	1
2	38.11	1.94	2
4	19.45	3.80	4
10	8.32	8.87	10

3.4 Open-loop results

Throughout this work, simulations are conducted using a 1200 particle length (L = 1200) lattice with a surface that is roughened using 2400 randomly distributed deposition events to ensure that the results are not impacted by the initial configuration of the lattice. The inlet gas composition, temperature and pressure are chosen to represent industrially used PECVD parameters and to correspond to conditions for which reliable experimental data exist. In the following two sections, simulations at the center of the PECVD reactor are used to determine the fidelity of the hybrid kMC formulation with respect to experimentally obtained film characteristics; later results will discuss operation in other reactor zones in order to highlight the importance of thickness uniformity on the efficiency of the thin film.

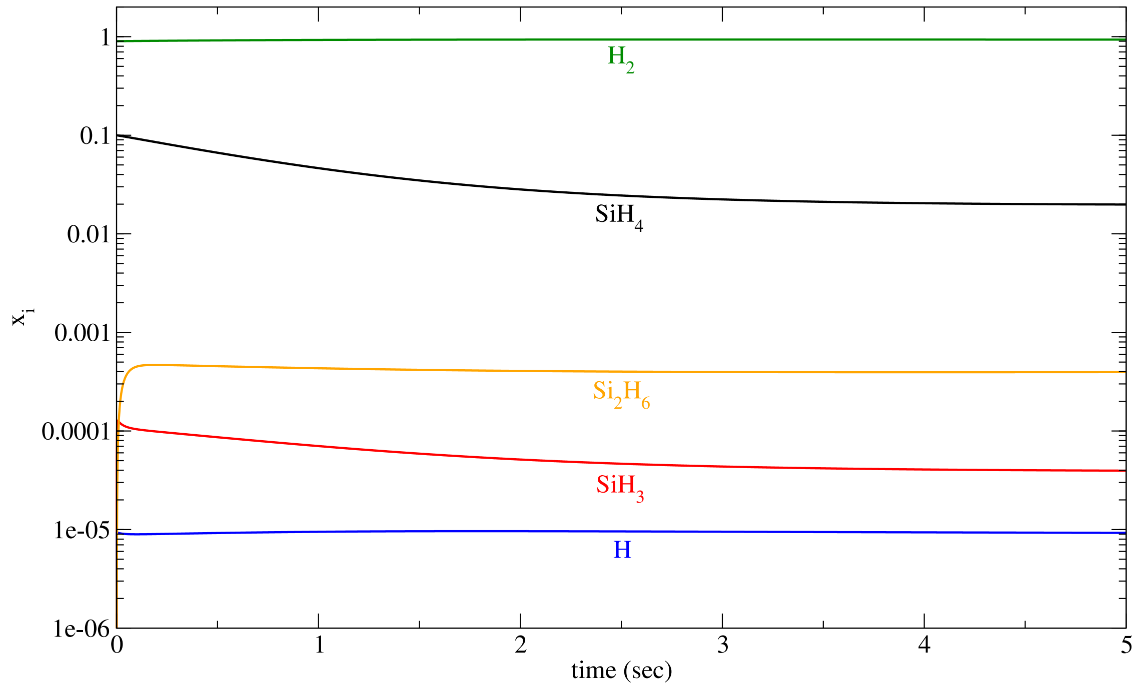

Figure 3.6: Time evolution of dominant gas-phase species at T = 475 K and P = 1 Torr.

3.4.1 Plasma composition, film roughness and hydrogen content

The temporal profiles for the five species with leading concentration are shown in Fig. 3.6 (Note: this plot represents operation using typical process parameters, T = 475 K and P = 1 Torr). Here the inlet gas stream is maintained at 9:1 ratio of hydrogen to silane with a flow rate of 75 cm^3/s. When compared to the time scale of a complete batch ($t_{batch} \approx 285$ sec), the dynamics of the species within the plasma are relatively short lived: within the first few seconds of operation all five species quickly approach their respective steady state values. Detailed plasma models have been developed by Amanatides et al. [1] and Kushner, M. [41] which predict similar behavior for the dominant species considered here and yields confidence in the plasma composition obtained in this work.

Scanning tunneling microscopy has been used by Tanenbaum et al. [68] to accurately map the surface morphology during the growth of a 50 nm thick amorphous silicon layer deposited at 523 K and 0.54 Torr. A 1200 particle wide lattice is grown under identical conditions and the root mean

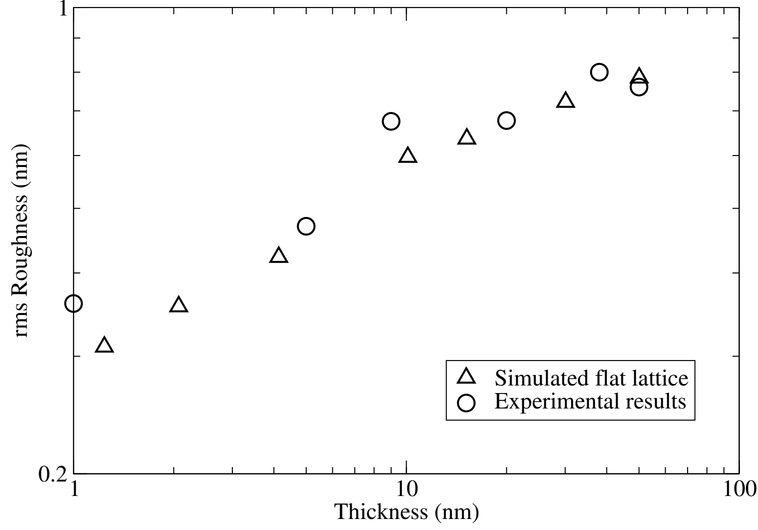

Figure 3.7: Comparison of experimental and simulated rms roughness at various film thicknesses.

square (RMS) roughness sampled at various thicknesses. The RMS roughness is calculated via the following equation:

$$R_{rms} = \sqrt{\frac{1}{L}\sum_{i=1}^{L}\left(h_i - \bar{h}\right)^2}, \tag{3.19}$$

where h_i is the height of the lattice at position i and $\bar{h}$ is the mean height of the lattice. As noted previously, due to the triangular arrangement of Si atoms, the height at a given position is calculated to be $\sqrt{3}/2 \cdot n$ where n is the number of layers. The results in Fig. 3.7 represent considerable consistency between the experimental work of Tanenbaum et al. [68] and the prediction of the multiscale model, owing further confidence to the hybrid kMC methodology used here.

Calibration of the hydrogen content within the film is accomplished by varying the deposition temperature in successive batches before postprocessing the film to determine the atomic hydrogen fraction. Comparing these values to those reported in literature [2, 7, 39] reveals three deposition regions with distinct behavior: (1) below 500 K the hydrogen content decreases linearly with increasing deposition temperature, (2) between 500 K and 575 K atomic hydrogen fraction remains relatively unchanged and (3) above 575 K the hydrogen capacity of the film begins to increase (see Fig. 3.8). While the observed range for the atomic hydrogen fraction falls within the accepted experimental region, the upturn above 575 K contradicts the expected behavior. The shift in hydro-

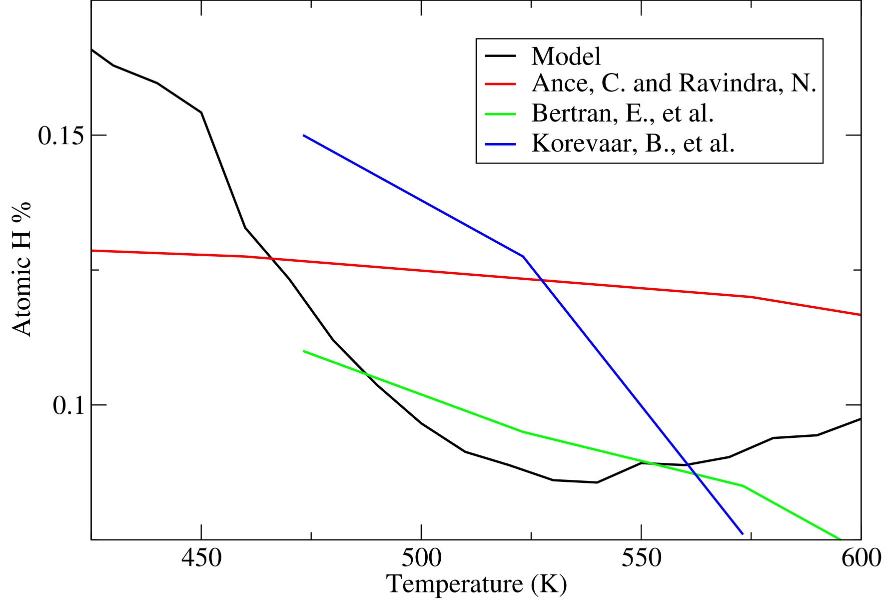

Figure 3.8: Hydrogen content dependence on deposition temperature.

gen content at high deposition temperatures is believed to be due to competition between migration and hydrogen abstraction. When operating below 550 K, an increase in temperature will boost the migration rate for surface radicals resulting in a more dense lattice; however, at high temperatures migration down the lattice cannot overcome the rapid creation of dangling bonds leading to a porous film with increased hydrogen content. In this work the operating conditions of interest call for T = 475 K which lies within the linear region in which the model captures well the available experimental data.

Due to the complexity of the thin film microstructure, the hydrogen content alone cannot be used to determine the validity of the multiscale model developed here. Instead, the criteria of interest is the relationship between the porosity of the film and the hydrogen content. In this work, the site occupancy ratio (SOR) is used as a measure of porosity:

$$SOR = \frac{n}{LH}, \tag{3.20}$$

where n is the number of occupied lattice sites and LH is the total number of sites within the

lattice. Given that hydrogen persists on the interior surfaces of the film it is expected that a strong correlation exists between the hydrogen content and SOR.

Fig. 3.9 shows the details of the film microstructure produced by the model at T = 475 K and P = 1 Torr. The scale of the lattice has been reduced here in order to demonstrate the porosity of the film, a typical simulation used in this work produces a lattice with dimensions L = 1200 and $H \sim 1400$ particles. The lattice shown has an SOR of 86% and an f_H of 13.8%. While Fig. 3.9 provides insight into the morphology of the amorphous thin film, further simulation is necessary in order to determine the accuracy of the multiscale model. Consequently, the deposition temperature is again varied and the hydrogen content of the resulting films calculated; however, in this case the hydrogen content is plotted against the SOR as experimental data is readily available for comparison. In Fig. 3.10 it is clear that regardless of the SOR (i.e., porosity) of a given thin film, the multiscale model developed in this work accurately reproduces the hydrogen content. In the interest of clarity, consider two simulated thin films: the first contains a distribution of small (e.g., mono- and di-) vacancies as well as less frequent, long range voids. The second simulated film may contain only a single, large pore. While the SOR of both films may be calculated to be 86%, the hydrogen content would vastly differ due to the degree of interior surface area available in each case. As such, the strong agreement in the relationship between the film SOR and hydrogen content yields confidence is the ability of the multiscale model developed in this work to reproduce the deposition of a-Si:H thin films with accurate structure and composition.

3.4.2 Batch-to-batch variability

Successive deposition sequences lead to fouling on the interior surfaces of the PECVD reactor causing rapid drift in the electron density of the plasma during the first several batches. The resulting drop in the concentration of SiH_3 causes the growth of the a-Si:H layer to slow yielding thin films which deviate significantly from the target thickness. This effect is demonstrated in Fig. 3.11 where the film thickness after 284 seconds of deposition is reported for 40 successive batches. By batch number 40, the reactor is considered to be fully conditioned and the electron density of

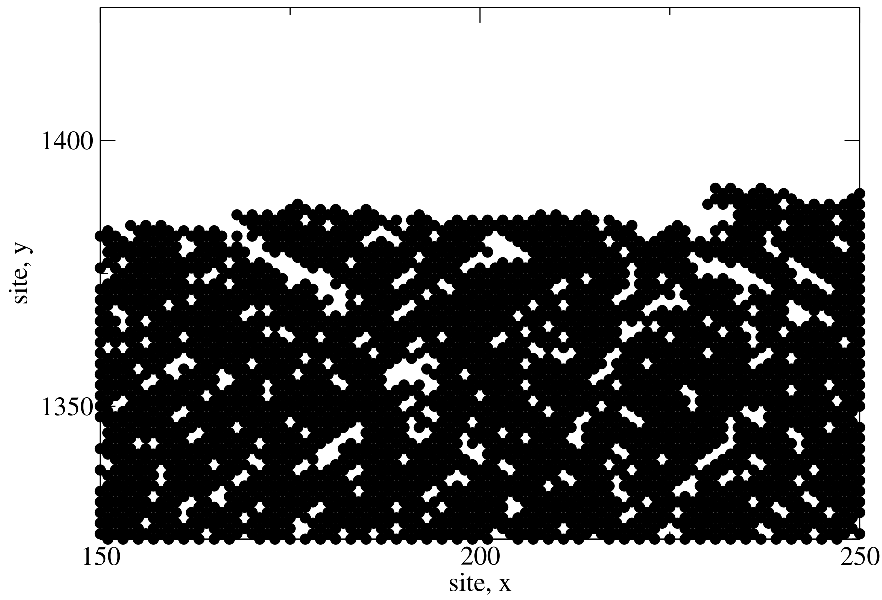

Figure 3.9: Representation of voids within a typical simulated lattice. (Note: Only a fraction of the full size lattice is shown in order to highlight porosity.)

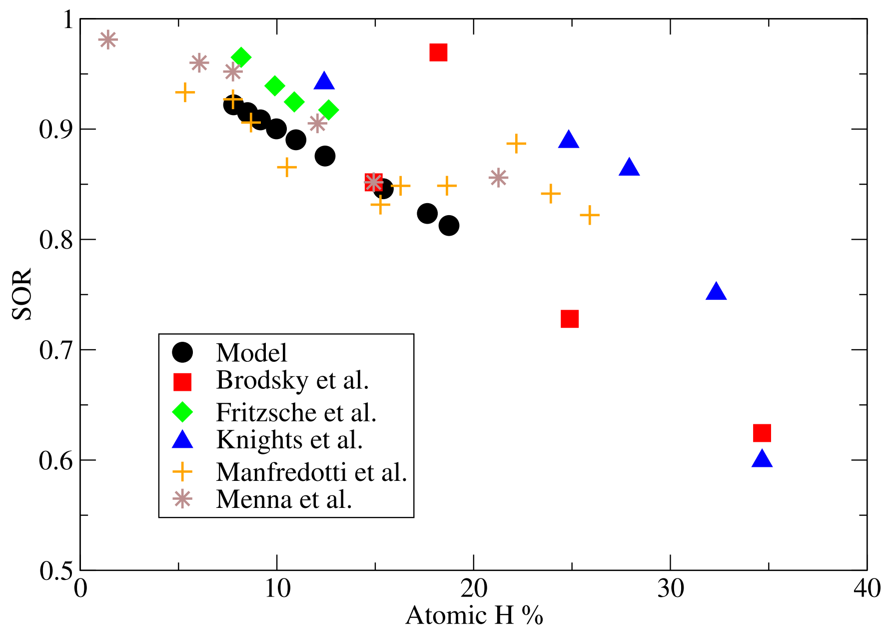

Figure 3.10: Relationship between film SOR and hydrogen content.

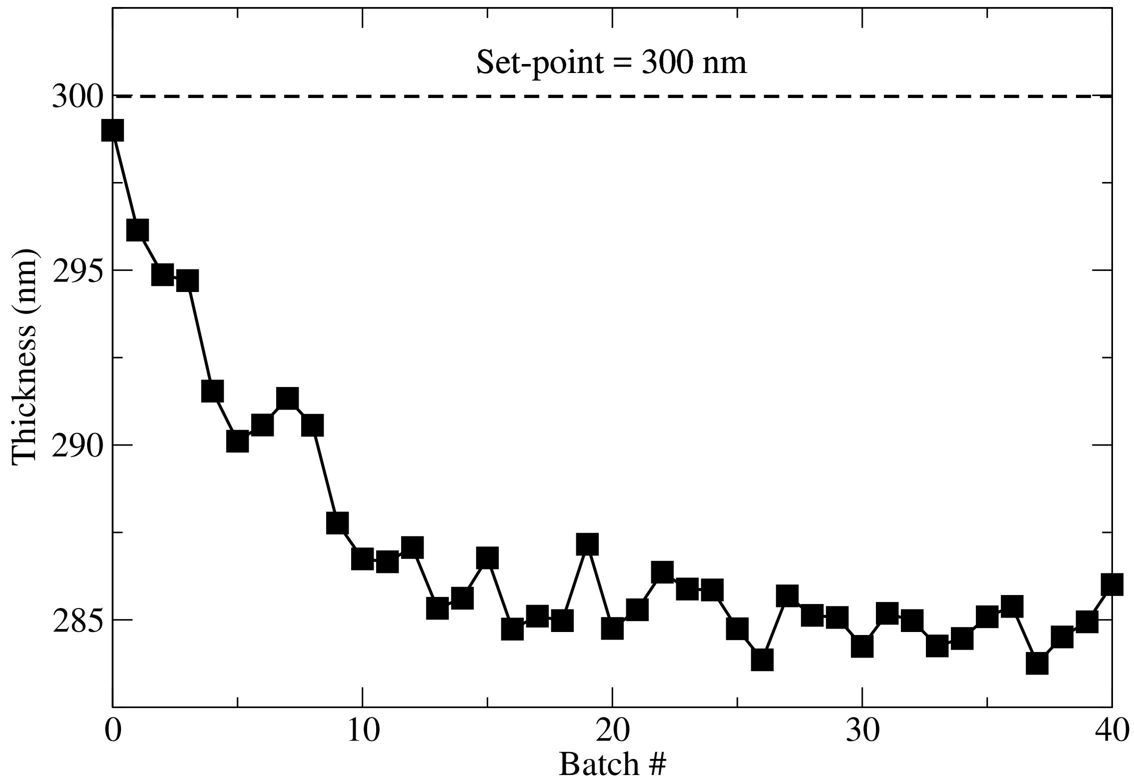

Figure 3.11: Batch-to-batch drift in the film thickness.

the plasma is held constant thereafter. A deposition time of 284 seconds is utilized here as this represents the average time required for an *a*-Si:H layer to reach 300 nm thickness when simulated using the nominal process parameters discussed previously.

Films deposited in later batches show an offset of up to 5% from the target thickness of 300 nm. Due to a need for nanometer scale resolution in silicon processing industries, an offset of $\sim$15 nm represents an unacceptable margin and has been shown to adversely affect the photovoltaic efficiency of the thin film [34]. Although the loss in efficiency due to batch-to-batch variations is relatively minor (e.g., on the order of 1%), the effect becomes greatly exaggerated when spatial variations within the PECVD reactor are accounted for. The following sections detail our efforts to reduce offset in the film thickness using a run-to-run control algorithm and spatially distributed operating temperatures.

3.5 R2R control of film thickness

Recently Crose et al. [13] demonstrated that the deposition rate of *a*-Si:H can be regulated by adjusting the temperature of the parallel plate reactor to values determined a priori by a non-linear growth rate equation. They have shown that through the use of an appropriate open-loop operation strategy, films can be deposited with uniform thickness in order to optimize photovoltaic efficiency; however, this strategy is limited to a single batch and therefore cannot account for efficiency loss due to batch-to-batch variability in the product thickness. In this work, we build upon the concept of regulated deposition temperatures in order to develop an operation strategy which can drive the thickness of the film to the desired set-point of 300 nm in the presence of drift in the electron density of the plasma. As a result, it is first necessary to develop a relationship between the thin film growth rate and the deposition temperature within the multiscale model.

The growth rate of the film is plotted against deposition temperature in Fig. 3.12. The nominal process parameters call for a deposition temperature of 475 K. In the vicinity of chosen operating conditions the growth rate is shown to be proportional to the deposition temperature; consequently, a linear growth rate equation is derived using standard least squares methods:

$$G(T) = 0.0365\,T - 6.56\ (nm \cdot K^{-1}s^{-1})\,. \tag{3.21}$$

Due to the brief startup time for the reactor, the thickness (τ) of a deposited layer can be approximated as follows:

$$\tau = G(T) \cdot t_{batch}\,. \tag{3.22}$$

Together Eqs. 3.21 and 3.22 allow for the conversion between thickness measurements and temperature units required for closed-loop operation. A detailed closed-loop calculation is provided in the following section.

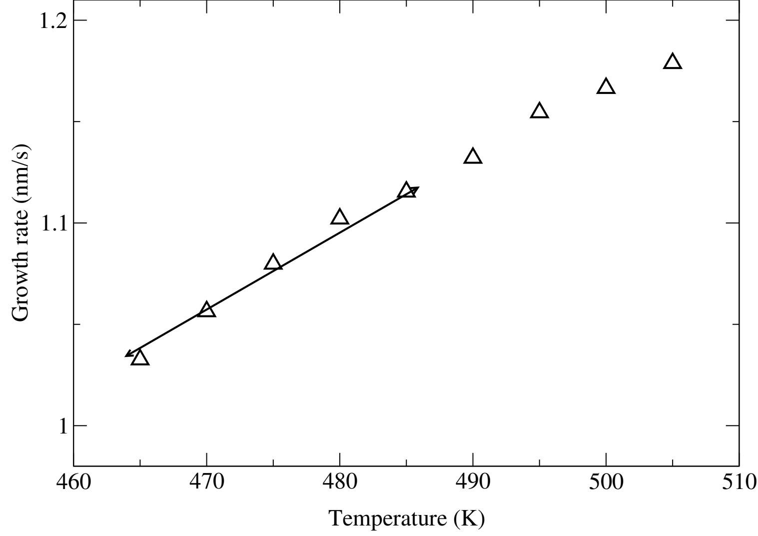

Figure 3.12: Relationships between growth rate and temperature for the nominal operation parameters.

3.5.1 EWMA formulation

Given the difficulty of continuous time measurement within a PECVD reactor, a run-to-run control strategy is utilized in this work which requires only post-batch measurement [43, 44]. Specifically, at the completion of a batch deposition process (i.e., after 284 seconds of simulation time) the thickness of the amorphous silicon layer is measured and fed into an EWMA (exponentially weighted moving average) algorithm which updates the temperature of the reactor for the next batch in an effort to overcome the aforementioned thickness non-uniformity. A schematic of the closed-loop operation strategy is shown in Fig. 3.13. Details of the EWMA algorithm (i.e., the post-batch simulation regime) are provided below:

$$\begin{aligned} \varepsilon_{k+1} &= (1-\lambda)\varepsilon_k + \lambda(T_{sp} - T_{model}) \\ T_{k+1} &= T_k + \varepsilon_{k+1}\,, \end{aligned} \tag{3.23}$$

where ε_{k+1} is the parameter correction for the $k+1$ batch, λ is the learning factor, T_{sp} is the temperature that the model predicts will be necessary to reach the set-point given t_{batch} seconds of

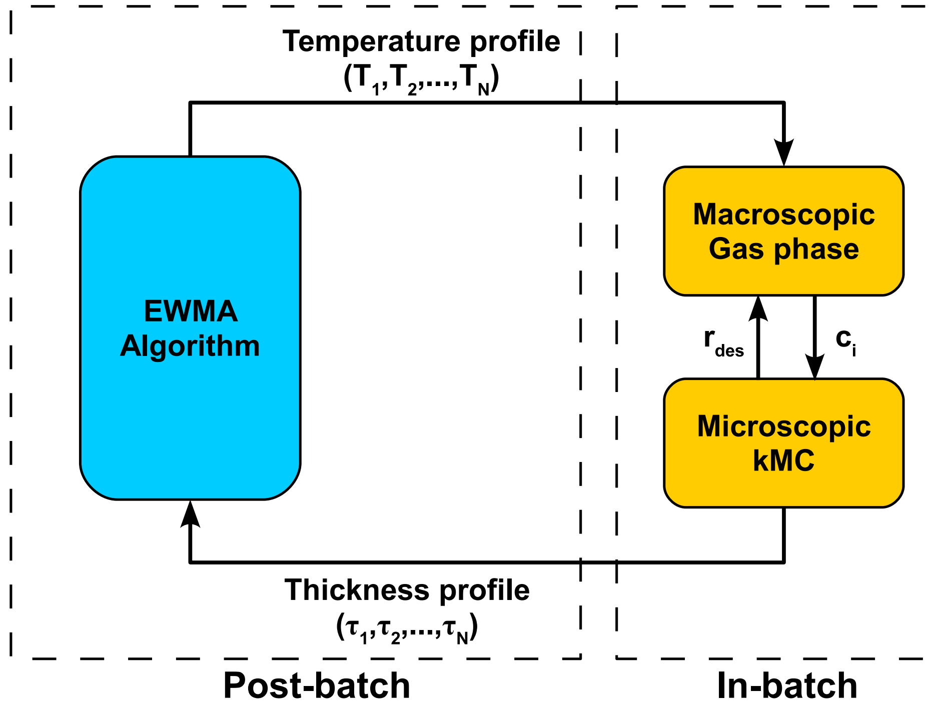

Figure 3.13: Run-to-run operation of PECVD reactor.

deposition, T_{model} is the temperature that the model predicts should lead to the measured thickness, and T_{k+1} is the updated deposition temperature for the $k+1$ batch based on the previous deposition temperature and the parameter correction value, ε_{k+1}.

3.5.2 Closed-loop operation

Three data sets are shown in Fig. 3.14; the square data points represent successive batch operation without the application of the EWMA control algorithm. As stated previously, after 40 batches the product is roughly 5% below the desired set-point of 300 nm. The spherical data points represent repeated simulation using the nominal process parameters (i.e., no drift in the electron density and no control strategy applied). This provides some insight into the level of process noise and represents the threshold for perfect operation of the controller. Finally, the triangular data points represent the simulated reactor under the influence of the proposed EWMA control algorithm. Similar to the case with no control, we see that the thickness of the product initially moves away

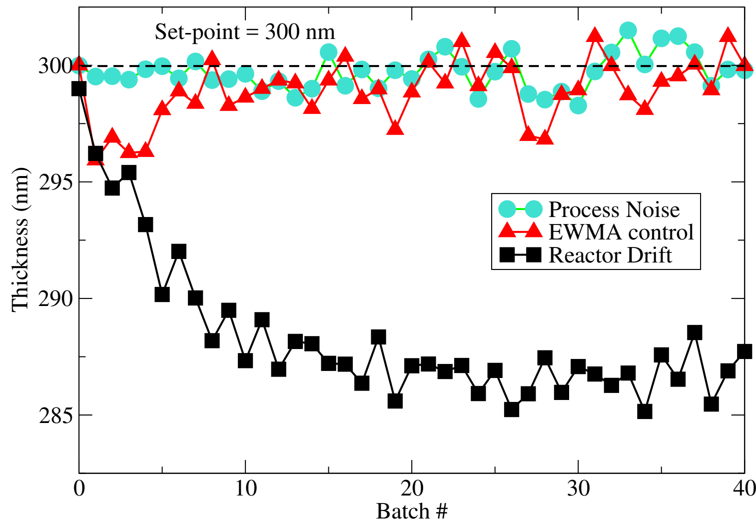

Figure 3.14: Drift cancellation via a R2R controller.

from the set-point (batches 1-3). However, in the following batches the parameter error correction, ε, begins to counteract the effect of drift in the electron density. By batch 10 the controller has driven the product to the desired set-point and then holds the product thickness within the process noise level for all remaining batches.

As demonstrated in Fig. 3.15, the value of the learning factor affects the number of batches required for the thin film product to approach close to the desired set-point of 300 nm, however, in both cases (λ = 0.75 and λ = 0.25), the thickness value approaches the set-point after about 10 batches.

It is important to note here that each batch simulation treats the PECVD reactor as a single zone. In other words, the reported thickness measurements are for the entire thin film and the temperature parameters are applied equally throughout the reactor. In the following section we report an extension of the EWMA controller to multiple reactor zones in an effort to address the problem of spatial non-uniformity within a batch deposition process.

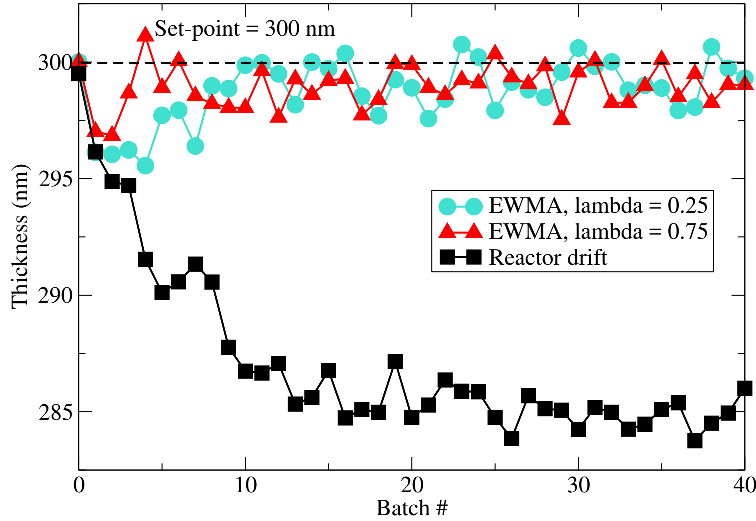

Figure 3.15: Comparison of different learning factor values.

3.6 Spatial non-uniformity in PECVD systems

In the previous section, the discussion was focused on drift in the electron density in a batch-to-batch manufacturing process; in other words, the non-uniformity in plasma composition occurred between successive deposition sequences. Here, we address the additional problem of in-batch spatial variations (e.g., non-uniform steady-state concentration profiles in SiH_3).

As discussed in the gas-phase model, a steady-state concentration gradient for SiH_3 above the wafer surface has been calculated [11] using finite differences methods. For a 20 cm diameter wafer, a radial non-uniformity of up to 17% in the [SiH_3] is observed from the center to the edge of the silicon wafer which is expected to cause an efficiency loss of roughly 5.4% [34]; Fig. 3.16 demonstrates this effect for the nominal process parameters (i.e., T = 475 K and P = 1 Torr) at four distinct locations across the wafer surface.

This 5.4% level of efficiency drop corresponds to roughly the same level of thin film solar cell power output loss, as can be concluded from the dependence of voltage and current on thin film thickness reported in [34]. Carrying out a rough engineering estimate, for a typical utility-scale thin film solar cell system of 100 MW, a total installation cost of \$1.49/W–\$1.84/W is projected [22]; this cost includes not only the photovoltaic modules themselves, but also infrastructure, labor,

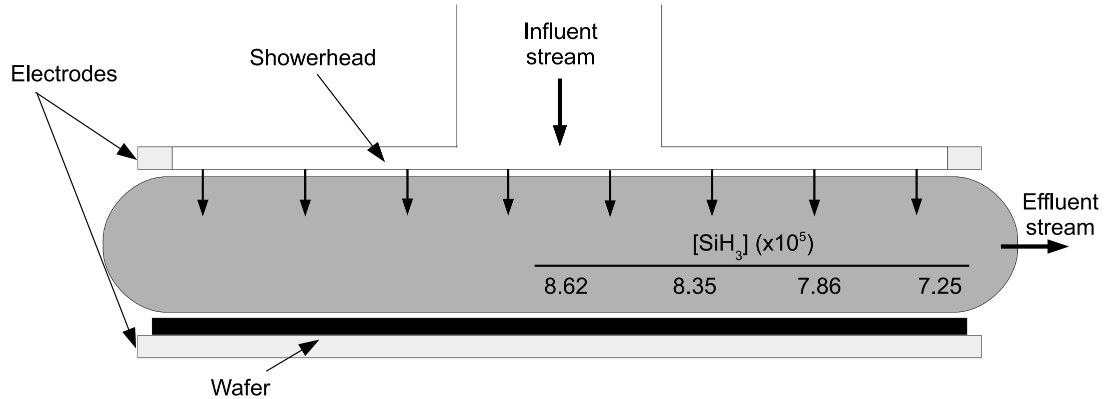

Figure 3.16: Radial non-uniformity in [SiH_3] at T = 475 K and P = 1 Torr.

environmental permits and other costs. Given an efficiency loss due to non-uniform deposition of thin film layers, as described above, more modules will be required in order to meet the client specification of 100 MW of power production. Assuming that the most economical features are chosen (i.e., using the lower bound for installation cost of $1.49/W), and ignoring fixed costs, the additional photovoltaic modules (resulting from non-uniform thin film thickness) are expected to contribute on the order of $8 million to the total plant cost of roughly $150 million [22]. As such, significant economic benefits are available through the use of controlled operation of the PECVD reactor.

Similar to the case of batch-to-batch drift, the concentration of the deposition species of interest ([SiH_3]) is tied directly to the electron density. The resulting effect on the uniformity of the film thickness can be seen in Fig. 3.17 by simulating the deposition of 40 successive batches in which both batch-to-batch variation in the electron density is allowed to occur, as well as spatial non-uniformity in the steady-state concentration profiles.

The four curves in Fig. 3.17 represent batch-to-batch operation at four zones within the reactor without the application of an EWMA control algorithm (Note: each zone is simulated using a single lattice of length L = 1200). The effect of spatial non-uniformity in the concentration of SiH_3 is evident in both the initial thickness (i.e., thickness of batch 0) of each zone, as well as the total offset after 40 batches. While the product in zone 1 maintains the same 5% offset discussed

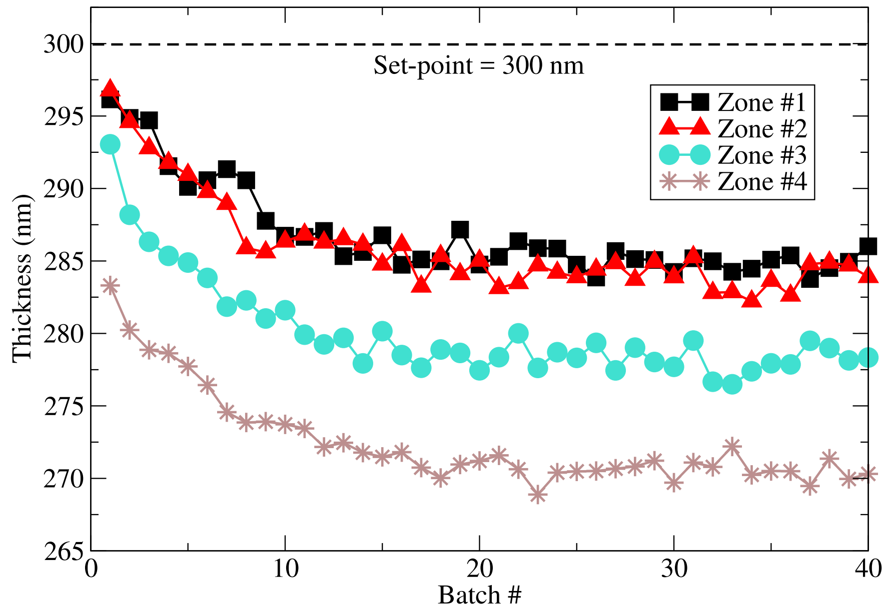

Figure 3.17: Open-loop drift and spatial non-uniformity in the four radial wafer zones.

earlier, zones 2-4 exhibit increased offset. After 40 batches zone 4 has drifted roughly 15% from the desired set-point of 300 nm despite the same drift in electron density being applied.

3.6.1 EWMA extension to concentric reactor zones

Crose et al. [13] have shown that four concentric zones can be defined within the PECVD reactor as shown in Fig. 3.18 each with an associated heating element. Thus, the temperature in every zone can be adjusted independently in order to modulate the growth rate of the thin film. However, accurate prediction of the deposition temperature in each zone requires a corresponding growth rate relation.

Consequently, simulated films are deposited at various temperatures and the corresponding growth rates are plotted in Fig. 3.19. Each data set represents a different reactor zone in which the concentration of SiH_3 has been adjusted to account for the aforementioned spatial non-uniformity. The uppermost curve corresponds to the first zone and is therefore identical to the growth rate data presented in the previous section. The remaining curves demonstrate the reduction in film growth rate that occurs due to the consumption of deposition species as process gas travels radially

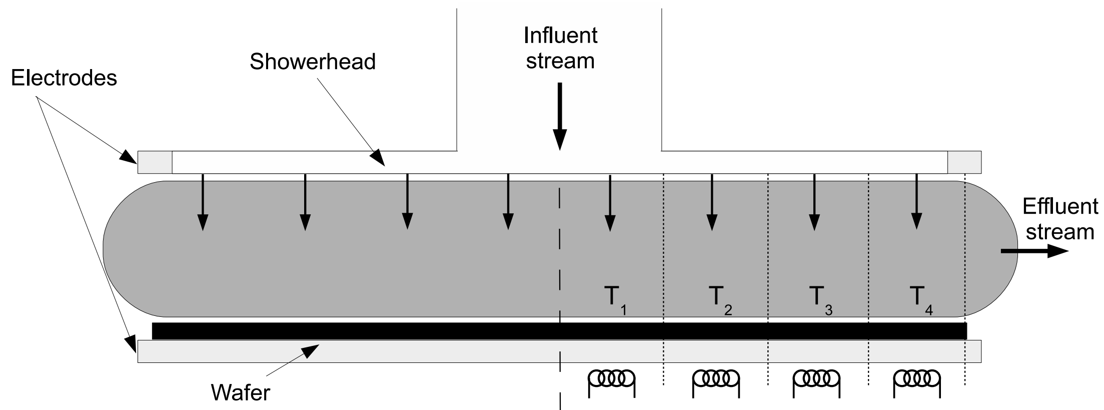

Figure 3.18: Discrete PECVD reactor schematic showing four independent, concentric substrate temperature control zones.

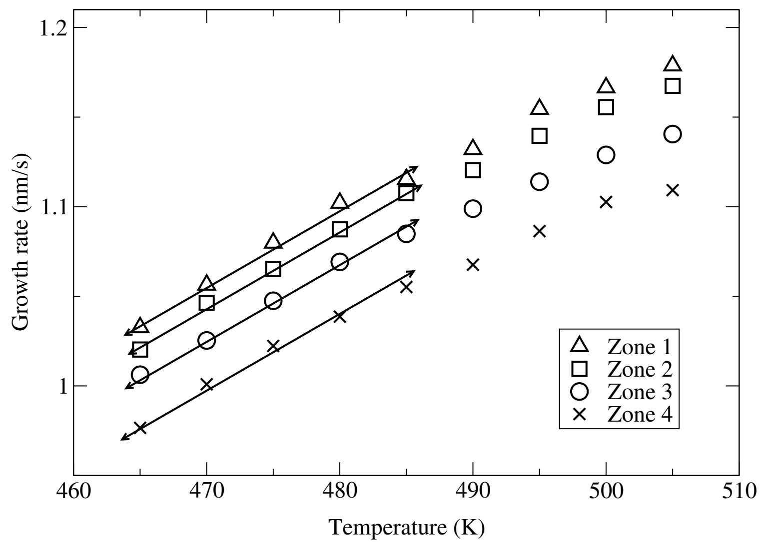

Figure 3.19: Relationships between growth rate and temperature for each reactor zone.

outward toward the edge of the wafer. Linear relations are developed for each zone using standard least squares methods:

$$
\begin{aligned}
G(T)^1 &= 0.0365\,T - 6.56\;(nm \cdot K^{-1}s^{-1}),\\
G(T)^2 &= 0.0366\,T - 6.74\;(nm \cdot K^{-1}s^{-1}),\\
G(T)^3 &= 0.0337\,T - 5.54\;(nm \cdot K^{-1}s^{-1}),\\
G(T)^4 &= 0.0331\,T - 5.54\;(nm \cdot K^{-1}s^{-1}).
\end{aligned}
\tag{3.24}
$$

$G(T)^1$ through $G(T)^4$ correspond to zones 1-4, respectively.

At this point, we can define a set of EWMA algorithms using the developed growth rate relations:

$$
\begin{aligned}
\varepsilon^i_{k+1} &= (1-\lambda)\varepsilon^i_k + \lambda(T^i_{sp} - T^i_{model})\\
T^i_{k+1} &= T^i_k + \varepsilon^i_{k+1}\,.
\end{aligned}
\tag{3.25}
$$

Recall, through the assumption of time invariant growth rates we can write the thickness as $\tau^i = G(T)^i \cdot t_{batch}$ to allow for conversion between post-batch measurements and temperature values necessary for the controlled input.

In the interest of clarity, Fig. 3.20a is provided which details the paths of the controlled inputs, T^i. In each zone, the deposition temperature increases from batch to batch to overcome the reduction in electron density that occurs as the reactor becomes conditioned. As expected, a significantly higher temperature must be applied in the outermost zones in order to accommodate for the reduced growth rate due to consumption of SiH_3. The four matching curves in Fig. 3.20b show the performance of the extended EWMA control algorithm. By batch number 10, the thin film thickness in each reactor zone is driven to the desired set-point and then maintained within the process noise level for all successive batches.

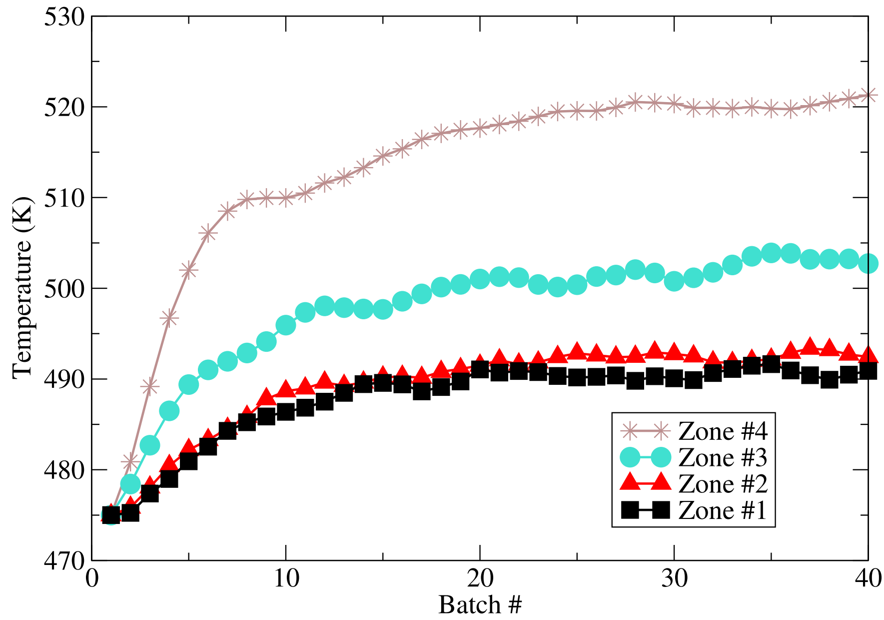

(a) Control action computed by EWMA algorithm.

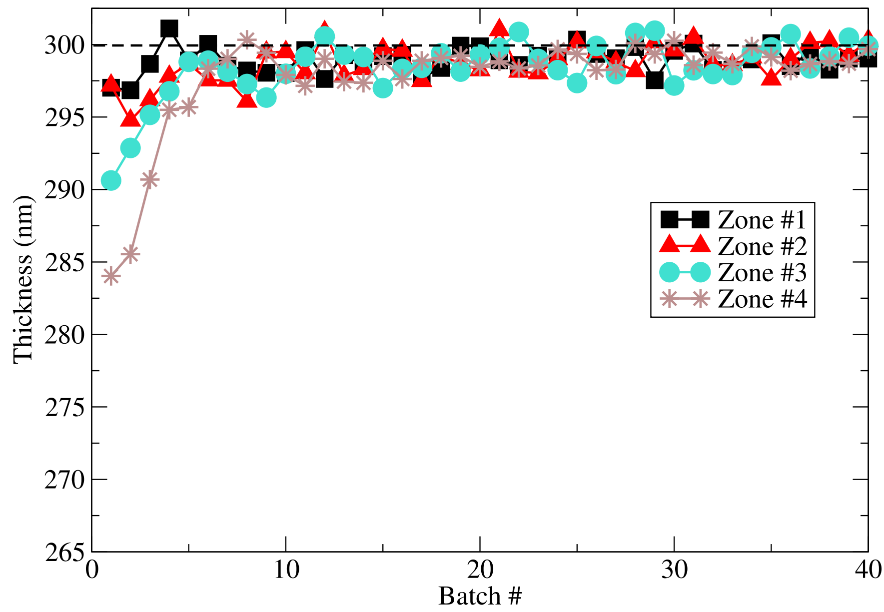

(b) Closed-loop operation via EWMA control algorithm.

Figure 3.20: R2R control of four independent wafer zones.

3.7 Conclusions

In this chapter, a multiscale modeling and run-to-run framework for the PECVD of thin film solar cells with uniform thickness and reduced batch-to-batch variability was proposed. The macroscopic gas-phase utilizes mass, momentum and energy balances, under the assumption of continuum to provide the plasma composition necessary in the calculation of deposition rate profiles. Additionally, the proposed microscopic model is based on a novel hybrid kinetic Monte Carlo algorithm that has been shown to be both computationally efficient and to reproduce thin film morphologies on par with experimental observations. Together the macroscopic and microscopic simulation have yielded insights and data that have been used to develop a closed-loop operation strategy which has been shown to improve film quality and to reduce batch-to-batch variability caused by drift during the conditioning phase of reactor operation. Specifically, an EWMA (exponentially weighted moving average) algorithm has been introduced which calculates substrate temperatures that mitigate the effect of batch-to-batch reactor variability. Simulations of open-loop operation suggest an offset of 5% from the desired set-point of 300 nm film thickness due to reactor variability. The proposed EWMA control strategy was applied first to a PECVD reactor with a single heating control element which allowed for the temperature to be adjusted post-batch to counteract drift in the electron density, thereby reducing the product offset to $<1\%$. Lastly, an extension of the proposed EWMA control algorithm was demonstrated which allows for in batch variation in the deposition temperature within concentric reactor zones in an effort to reduce spatial non-uniformity in the thin film thickness. Simulations demonstrate both a reduction in the product offset to less than 1% as well as radially uniform films within 10 batches of closed-loop operation.

Chapter 4

Multiscale Computational Fluid Dynamics: Methodology and Application to PECVD of Thin Film Solar Cells

4.1 Introduction

Due to low production costs and decreased operating temperatures, plasma enhanced chemical vapor deposition (PECVD) remains the dominant processing method for the manufacture of silicon thin films in both the solar cell and microelectronic industries [35, 40, 73]. Given the difficulty of in-situ measurements during the deposition of amorphous silicon thin films, numerous groups have developed models to characterize the behavior of PECVD systems. Specifically, gas flow and volumetric chemical reactions within PECVD reactors have been investigated using computational fluid dynamics (CFD) models of varying complexities [12, 37, 18]. Additionally, the complex chemistry and surface interactions that define the microscopic growth of thin film layers have been modeled [13, 50, 36, 72] using kinetic Monte Carlo models and such models have been demonstrated to reproduce amorphous silicon films with accurate growth rates and morphologies. Furthermore, significant efforts have been made in linking macroscopic first-principals models of

gas phase species concentrations and temperature employing approximate flow field equations with microscopic surface models (e.g., Rodgers S. and Jensen K., 1998, Lou Y. and Christofides P.D., 2003 and Aviziotis et al., 2016 [62, 48, 4]). However, macroscopic CFD models that develop an accurate flow field solution without approximation and microscopic surface models have not been linked in the context of PECVD.

Unfortunately, potentially decoupled CFD and surface interaction models are unable to capture phenomena which occur at the boundary (thin film surface) between the two PECVD simulation domains. One such phenomenon which remains a persistent issue during the manufacture of amorphous silicon thin films, is non-uniformities which develop in the thickness and morphology of deposited layers across the radius of the wafer. Spatially non-uniform deposition has been well characterized [11, 67, 64] and shown to affect the efficiency of solar cell products [34], resulting in poor device quality and increased costs [14]. As such, there exists a need for accurate PECVD reactor models which are capable of predicting the codependent behavior of the macroscopic gas phase and microscopic thin film growth. Multiscale models of this type may provide insight into the root cause of spatial non-uniformities present in the deposition of silicon layers, as well as allow for improved reactor geometries and optimal operating strategies to be developed.

To this end, a multiscale CFD model is proposed in this chapter which captures the interconnection between the macroscopic and microscopic domains in PECVD systems. This model is applied to the PECVD of a-Si:H thin films at industrially relevant conditions of T = 475 K, P = 1 Torr and a 9:1 ratio of hydrogen to silane gas in the feed. At the macroscopic scale, a structured mesh containing 120,000 cells is used to discretize the chambered reactor geometry. ANSYS Fluent software is used as a framework to solve the governing momentum, mass and energy equations which define the dynamics of the process gas inside the parallel plate PECVD reactor, and to orchestrate the communication between simulation domains. Three user defined functions (UDFs) are implemented in order to tailor the Fluent architecture to the specific application of the deposition of amorphous silicon thin films. The first accounts for the 34 prevalent gas phase reactions, including nine ionization reactions which produce the plasma. A second UDF provides an accurate

electron density profile based on the work of Park et al. [55]. The final and most computationally demanding function comprises a hybrid kinetic Monte Carlo algorithm used to model the complex surface phenomena which characterize the microscopic domain. Additionally, given the significant computational requirements of this work, a novel parallelization strategy is developed and applied to both the reactor mesh and the individual microscopic thin film simulations.

The model described above is applied to the batch deposition of a 300 nm thick *a*-Si:H thin film. Spatial gradients are shown to develop in the concentration of SiH_3 and H near the surface of the silicon wafer. Consequently, non-uniformities in the thin film thickness and hydrogen content are predicted to exceed 20% and 3%, respectively. These results represent an unacceptable margin from a manufacturing standpoint and highlight the importance of multiscale models in predicting and characterizing the behavior of PECVD reactors such that improved reactor geometries and operating conditions may be achieved.

4.2 Process description and modeling

The PECVD reactor utilized in this work belongs to the widely used subclass of CVD reactors known as chambered, parallel-plate reactors. The specific geometry used in this investigation is a cylindrical reaction chamber with a 20 cm wafer capacity and 3 cm showerhead spacing (Figs. 4.1 and 4.2). Process gases are pumped into the inlet at the top of the reactor before being distributed through circular showerhead holes into the reaction zone (light grey region in Fig 4.1). Within the reaction zone plasma is produced via a radio frequency (RF) power source across the parallel plate structure. The resulting plasma phase species flow radially outward across the wafer surface, eventually exiting the reactor through outlets near the bottom. The specifics of the plasma chemistry will be provided in the macroscopic modeling section (section 2.2 and Table 4.1 below).

Two distinct simulation regimes may be specified within the PECVD process: the macroscopic gas phase which can be described by momentum, mass and energy balances, as well as the complex, microscopic surface interactions that dictate the structure of the silicon thin film of interest.

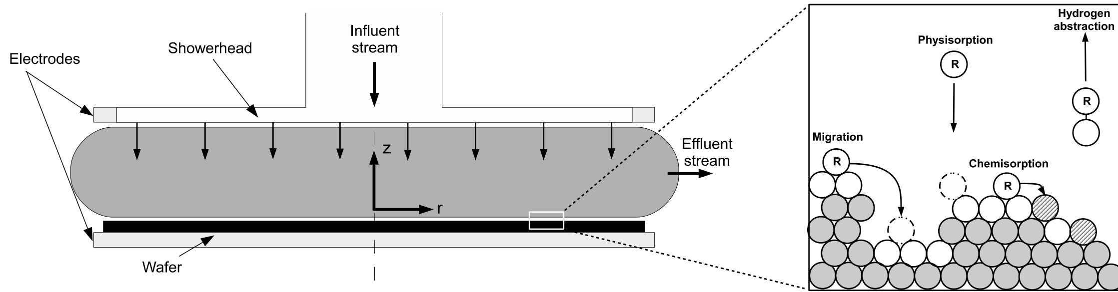

Figure 4.1: Macroscopic (left) and microscopic (right) PECVD simulation regimes.

Fig. 4.1 highlights the multiscale character of this process and the need to capture the dynamics at both scales due to the codepedency between the macroscopic and microscopic regimes. The following sections detail both the macroscopic gas-phase model and the microscopic surface model.

4.2.1 CFD geometry and meshing

Throughout this work ANSYS Fluent software is utilized for the creation of the geometric mesh (specifically, ICEM meshing) and as a solver for the partial differential equations presented in the following sections (FLUENT version 15.07). As mentioned previously, the chambered PECVD reactor is approximated using a 2D axisymmetric geometry (Fig. 4.2). Given the difficulty of translating three dimensional showerhead holes into a two dimensional axisymmetric representation, 1 cm gaps are chosen as a simple means by which the inlet gases may flow into the plasma chamber. The results presented in the latter half of this work suggest a good agreement between the observed plasma characteristics and those reported experimentally; consequently, no additional showerhead hole arrangements are explored.

Two general meshing strategies exist for the discretization of a given geometry: (1) structured meshes contain a collection of quadrilateral cells in a specific, repeating pattern, and (2) unstructured meshes are composed of a collection of polygons in an irregular pattern. Simple geometries (i.e., geometries lacking curvature and complex shapes) benefit from the use of a structured mesh as they can provide higher quality, in terms of orthogonality and aspect ratio, while remaining computationally efficient. Given the rectangular character of the 2D axisymmetric PECVD geometry,

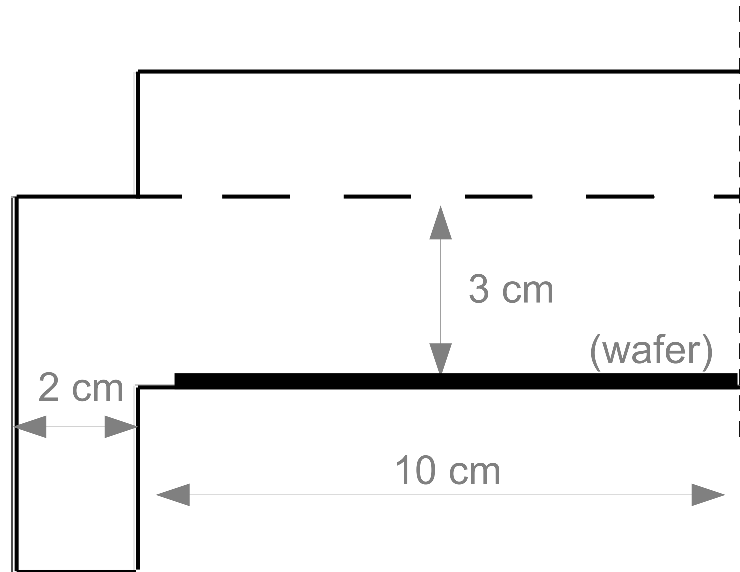

Figure 4.2: 2D axisymmetric PECVD geometry.

a structured mesh composed of 120,000 cells is employed. The specific number of cells within the mesh is determined using a mesh-independent study whereby the number of cells is increased until identical results are recorded. Thus, the use of a finer mesh (above 120,000 cells) would provide no benefit to the PECVD model developed here while requiring greater computational resources.

Fig. 4.3 demonstrates the non-uniform cell density within the proposed mesh. Regions in which significant gradients are expected (e.g., gradients in the temperature, species concentration, flow velocity, etc.) contain a higher mesh density. This is of special importance near the showerhead holes and along the surface of the wafer. Accurate flow modeling of the process gas into the reaction zone is crucial in order to obtain plasma distributions which are industrially relevant and which yield representative growth of thin film layers.

Due to the relatively low flow rate of process gas (75 cm^3/min) and low chamber pressure (1 Torr), the flow along the surface of the wafer is expected to be laminar (note: preliminary flow characteristics from the macroscopic model suggest a Reynold's number of $Re = 2.28 \times 10^{-4}$). As a result, the mesh density directly above the wafer surface has been increased such that the boundary layer can be adequately captured.

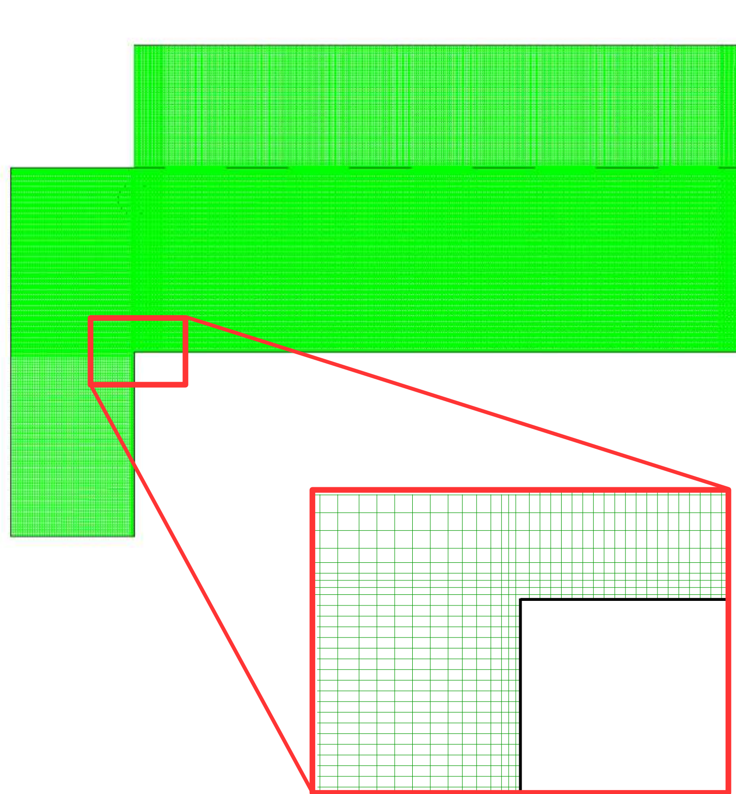

Figure 4.3: Structured mesh containing 120,000 cells.

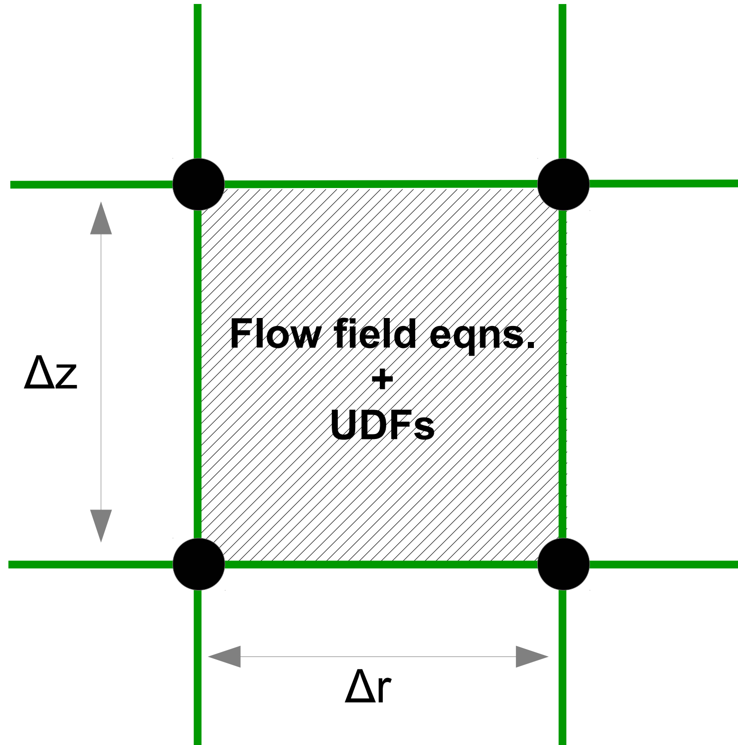

Figure 4.4: Individual unit cell for structured mesh.

4.2.2 Gas-phase model

At the macroscopic level, the physio-chemical phenomena that govern the behavior of the gas-phase species are complex in nature. Mass, momentum and energy balances each play a key role in determining the growth of amorphous silicon layers within the PECVD reactor. Consequently, analytic solutions to the gas-phase model are viable only for simplified systems which fail to yield meaningful results. Instead, we employ numerical methods here which are capable of solving the complex fluid dynamics equations with high accuracy within the mesh structure presented in the previous section. At every time step, and for each cell of the mesh (e.g., Fig. 4.4), the governing equations are discretized using the ANSYS Fluent solver via finite difference methods. Additionally, user defined functions (UDFs) are applied to each cell which allow for extended functionality of the Fluent framework. The continuity, energy and momentum equations employed in this work are standard and as such will be presented only briefly. For a more detailed description

of the flow field equations, please refer to the Fluent user manual [3, **?**]. In a generalized vector form, the governing equations are given by the following system:

$$\frac{\partial}{\partial t}(\rho\vec{v}) + \nabla(\rho\vec{v}\vec{v}) = -\nabla p + \nabla\bar{\bar{\tau}} + \rho\vec{g} + \vec{F} \tag{4.1}$$

$$\bar{\bar{\tau}} = \mu[(\nabla\vec{v} + \nabla\vec{v}^T) - \frac{2}{3}\nabla\vec{v}I] \tag{4.2}$$

$$\nabla\vec{v} = \frac{\partial v_z}{\partial z} + \frac{\partial v_r}{\partial r} + \frac{v_r}{r} \tag{4.3}$$

$$\frac{\partial}{\partial t}(\rho E) + \nabla(\vec{v}(\rho E + p)) = \nabla(k\nabla T - \Sigma h\vec{J} + (\bar{\bar{\tau}}\vec{v})) + S_h \tag{4.4}$$

$$\frac{\partial}{\partial t}(\rho Y_i) + \nabla\cdot(\rho\vec{v}Y_i) = -\nabla\cdot\vec{J}_i + R_i + S_i \tag{4.5}$$

$$\vec{J}_i = -\rho D_{i,m}\nabla Y_i - D_{T,i}\frac{\nabla T}{T} \tag{4.6}$$

where ρ is the density of the gas, $\vec{v}$ is the physical velocity vector, p is the static pressure, $\bar{\bar{\tau}}$ and I are the stress and unit tensors, J is the diffusive flux, Y_i is the mass fraction of species i, D_i is the diffusion coefficient of species i, and S_h, R_i and S_i are user defined terms which will be defined below.

In order to tailor the functionality of the Fluent solver to the specific application of silicon processing via PECVD, three predominant user defined functions are utilized, the first of which accounts for the volumetric reactions occurring within the plasma. The twelve dominant species that lead to film growth and their corresponding thirty-four gas-phase reactions are accounted for throughout this work. A complete listing of the reactions, mechanisms and rate constants are available in Table 4.1. Thus, the R_i terms in the mass balance presented above are a product of this reaction set and are updated by the UDF at the completion of each time step.

Special consideration must be taken when modeling cells that lie along the surface of the wafer (e.g., Fig. 4.5). In addition to the previously detailed transport and reaction phenomena, the cells bordering the surface share mass and energy with the growing thin film layer. Specifically, SiH_3 and H radicals deposit on the thin film causing a mass sink, while SiH_4 and H_2 desorb from the

Table 4.1: Reactions included in the gas-phase model. Note: Rate constants have units of cm^3/sec and have been adopted from the collection prepared by Kushner et al. [41].

Reaction	Mechanism	Rate constant
R^1	$e^- + H_2 \rightarrow 2H$	7.66×10^{12}
R^2	$e^- + SiH_4 \rightarrow SiH_3 + H$	9.57×10^{13}
R^3	$e^- + SiH_4 \rightarrow SiH_3^+ + H$	3.40×10^{12}
R^4	$e^- + SiH_4 \rightarrow SiH_2 + 2H$	1.13×10^{13}
R^5	$e^- + SiH_4 \rightarrow SiH + H_2 + H$	5.62×10^{12}
R^6	$e^- + SiH_4 \rightarrow Si + H_2 + 2H$	6.70×10^{12}
R^7	$e^- + Si_2H_6 \rightarrow SiH_3 + SiH_2 + H$	2.15×10^{13}
R^8	$e^- + Si_2H_6 \rightarrow H_3SiSiH + 2H$	7.41×10^{13}
R^9	$e^- + Si_3H_8 \rightarrow H_3SiSiH + SiH_4$	3.35×10^{14}
R^{10}	$H + SiH_2 \rightarrow SiH_3$	6.68×10^{11}
R^{11}	$H + SiH_2 \rightarrow SiH + H_2$	1.20×10^{13}
R^{12}	$H + SiH_3 \rightarrow SiH_2 + H_2$	1.20×10^{13}
R^{13}	$H + SiH_4 \rightarrow SiH_3 + H_2$	1.38×10^{12}
R^{14}	$H + H_2Si = SiH_2 \rightarrow Si_2H_5$	3.01×10^{12}
R^{15}	$H + Si_2H_6 \rightarrow SiH_4 + SiH_3$	4.03×10^{12}
R^{16}	$H + Si_2H_6 \rightarrow Si_2H_5 + H_2$	7.83×10^{12}
R^{17}	$H + Si_3H_8 \rightarrow Si_2H_5 + SiH_4$	1.19×10^{12}
R^{18}	$H_2 + SiH \rightarrow SiH_3$	1.20×10^{12}
R^{19}	$H_2 + SiH_2 \rightarrow SiH_4$	1.20×10^{11}
R^{20}	$SiH_2 + SiH_4 \rightarrow Si_2H_6$	6.02×10^{12}
R^{21}	$SiH_3 + SiH_3 \rightarrow SiH_4 + SiH_2$	4.22×10^{12}
R^{22}	$SiH_3 + SiH_3 \rightarrow Si_2H_6$	6.02×10^{12}
R^{23}	$SiH + SiH_4 \rightarrow Si_2H_5$	1.51×10^{12}
R^{24}	$SiH_2 + SiH_4 \rightarrow H_3SiSiH + H_2$	6.02×10^{12}
R^{25}	$SiH_2 + Si_2H_6 \rightarrow Si_3H_8$	7.23×10^{13}
R^{26}	$SiH_2 + SiH_3 \rightarrow Si_2H_5$	2.27×10^{11}
R^{27}	$SiH_3 + SiH_3 \rightarrow SiH_4 + SiH_2$	4.06×10^{13}
R^{28}	$SiH_3 + Si_2H_6 \rightarrow SiH_4 + Si_2H_5$	1.98×10^{13}
R^{29}	$Si_2H_5 + SiH_4 \rightarrow SiH_3 + Si_2H_6$	3.01×10^{11}
R^{30}	$SiH_3 + Si_2H_5 \rightarrow Si_3H_8$	9.03×10^{13}
R^{31}	$H_3SiSiH + SiH_4 \rightarrow Si_3H_8$	6.02×10^{12}
R^{32}	$Si_2H_5 + Si_2H_5 \rightarrow Si_3H_8 + SiH_2$	9.03×10^{13}
R^{33}	$H_3SiSiH \rightarrow H_2Si = SiH_2$	2.71×10^{13}
R^{34}	$H_2Si = SiH_2 \rightarrow H_3SiSiH$	2.29×10^{10}

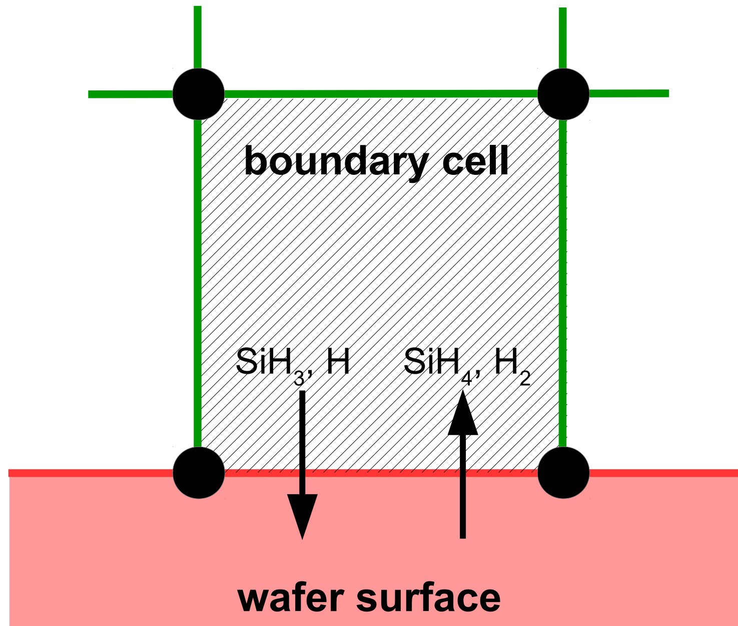

Figure 4.5: Boundary cell adjacent to wafer surface.

surface representing a mass source. Additionally, energy is consumed and released through the breaking and formation of covalent bonds during the chemisorption process. As a result, S_h and S_i terms have been added to the energy and mass balances, respectively. The values of these user defined terms are updated after each time step of the microscopic model to reflect the growth events that have occurred. In the interest of clarity, it is important to note here that microscopic simulations are not conducted within every boundary cell. Instead, microscopic simulations occur at discrete locations across the wafer surface (e.g., ten discrete locations from $r = 0.0$ to 10.0 cm are used in this work), and the appropriate mass and energy consumption for the remaining boundary cells are found via linear interpolation. After each boundary cell has been resolved, calculation of the next time step can commence.

Electron density profile

The first nine reactions in Table 4.1 involve the creation of radicals via collision with free electrons; therefore, the second user defined function which is key to the accuracy of the plasma phase, is

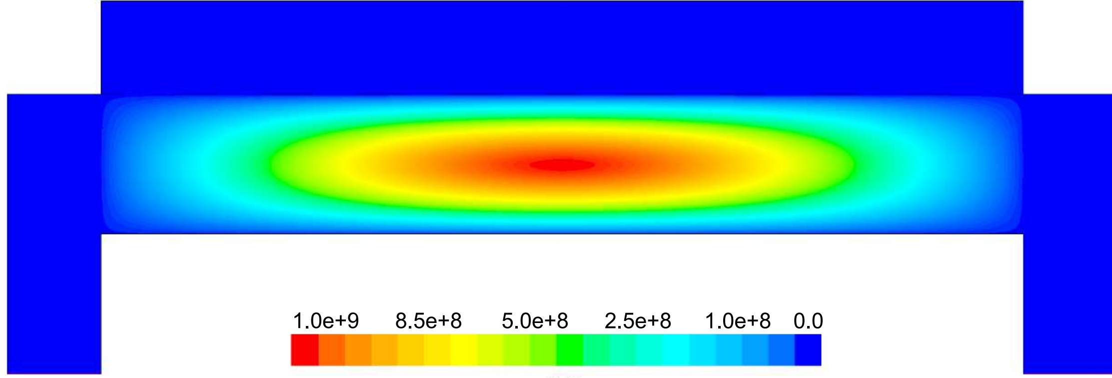

Figure 4.6: Electron density within 2D axisymmetric PE-ALD geometry (cm^{-3}).

that which accounts for the electron density profile. For plasmas propagating within cylindrical geometries, the electron density can accurately be modeled by the product of the zero order Bessel function and a sine function whose period is twice the parallel plate spacing [55]. This is described by the following equation:

$$n_e(r,z) = n_{eo} \cdot J_0(2.405\frac{r}{r_t}) \cdot sin(\frac{\pi z}{D}), \tag{4.7}$$

where n_{eo} is the maximum electron density, J_0 is the zero order Bessel function of the first kind, r_t is the radius of the reactor, and D is the distance between the showerhead and wafer (i.e., the parallel plate spacing). When applied to the PECVD geometry discussed previously, the resulting electron distribution can be seen in Fig. 4.6. The electron cloud is bounded by the charged region between the parallel plates and demonstrates a maximum, as expected, in the center of the reactor.

4.2.3 Surface microstructure model

The final UDF utilized in the multiscale model is of the greatest complexity as it is responsible for computation of the microscopic domain in its entirety (i.e., the hybrid kinetic Monte Carlo algorithm and communication between boundary cells). Details of the microscopic surface model

are presented here in an abbreviated form; however, since simulation results can vary widely based on minor discrepancies in physical phenomena and model parameters, an in-depth discussion of kinetic Monte Carlo processes and complex surface interaction models can be found in the earlier works of Crose et. al [13] and Tsalikis et al. [69]. The following subsection provides a brief introduction to the chemistry involved in amorphous silicon deposition as a foundation for the 2D triangular lattice approximation presented later in this work.

Thin film growth chemistry

Throughout this work deposition within the microscopic model excludes higher order species and aggregates as Perrin et al. [56] and Robertson [61] have verified experimentally that $>98\%$ of deposition can be attributed to SiH_3 and H radicals alone. In the neighborhood of the parameter space of interest, namely T = 475 K and P = 1 Torr, all other species remain trapped within the macroscopic gas-phase model. As such, the surface interactions for the microscopic domain can be described by the following chemistry.

Upon striking the surface of the growing a-Si:H layer, physisorption occurs as SiH_3 and H radicals contact hydrogenated silicon sites ($\equiv \mathrm{Si}-\mathrm{H}$) according to the following reaction set:

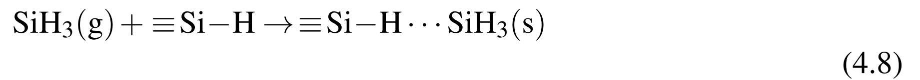
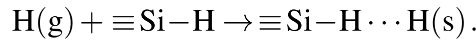

$$\begin{gathered}\mathrm{SiH_3(g)} + \equiv\mathrm{Si{-}H} \rightarrow \equiv\mathrm{Si{-}H\cdots SiH_3(s)} \\ \mathrm{H(g)} + \equiv\mathrm{Si{-}H} \rightarrow \equiv\mathrm{Si{-}H\cdots H(s)}\,.\end{gathered} \tag{4.8}$$

Once a weak hydrogen bond has been formed, rapid diffusion of physisorbed radicals across the lattice surface defines migration events:

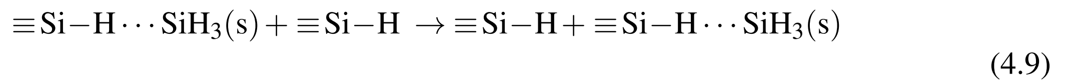
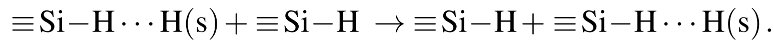

$$\begin{gathered}\equiv\mathrm{Si{-}H\cdots SiH_3(s)} + \equiv\mathrm{Si{-}H} \rightarrow \equiv\mathrm{Si{-}H} + \equiv\mathrm{Si{-}H\cdots SiH_3(s)} \\ \equiv\mathrm{Si{-}H\cdots H(s)} + \equiv\mathrm{Si{-}H} \rightarrow \equiv\mathrm{Si{-}H} + \equiv\mathrm{Si{-}H\cdots H(s)}\,.\end{gathered} \tag{4.9}$$

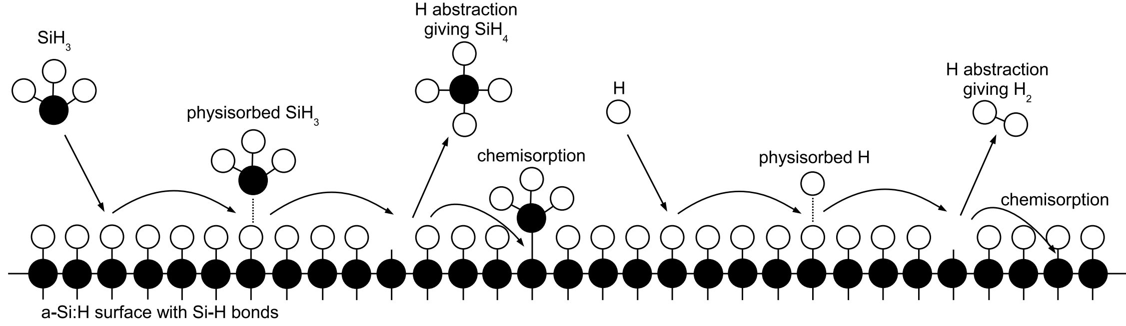

Figure 4.7: Chemical model illustration showing particle-surface interactions.

The termination of a given migration path falls into one of two categories: hydrogen abstraction,

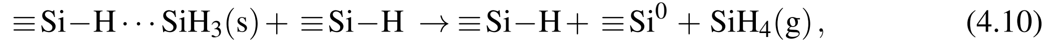

$$\equiv\mathrm{Si{-}H}\cdots\mathrm{SiH_3(s)} + \equiv\mathrm{Si{-}H} \;\rightarrow \equiv\mathrm{Si{-}H} + \equiv\mathrm{Si}^0 + \mathrm{SiH_4(g)}\,, \tag{4.10}$$

whereby a physisorbed radical removes a surface hydrogen reforming the stable species (SiH_4 or H_2) and creating a dangling bond ($\equiv Si^0$) in the process, or chemisorption at a preexisting dangling bond site according to the following reactions:

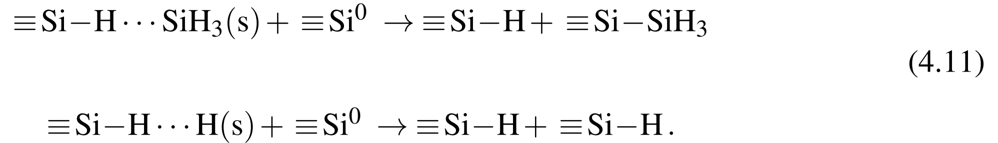

$$\begin{aligned} &\equiv\mathrm{Si{-}H}\cdots\mathrm{SiH_3(s)} + \equiv\mathrm{Si}^0 \;\rightarrow \equiv\mathrm{Si{-}H} + \equiv\mathrm{Si{-}SiH_3} \\ &\equiv\mathrm{Si{-}H}\cdots\mathrm{H(s)} + \equiv\mathrm{Si}^0 \;\rightarrow \equiv\mathrm{Si{-}H} + \equiv\mathrm{Si{-}H}\,. \end{aligned} \tag{4.11}$$

Growth of the lattice proceeds unit by unit via chemisorption of SiH_3 at dangling bond sites (i.e., the Si atom forms a covalent bond, permanently fixing its location within the amorphous structure). Conversely, chemisorption of H only results in a return of the surface to its original, hydrogenated state. A simplified illustration of the surface chemistry can be seen in Fig. 4.7.

Lattice Characterization

In our recent works [13, 14], two typical lattice implementations have been explored. The first, a solid-on-solid (SOS) lattice, is composed of a simple square structure in which particles in each

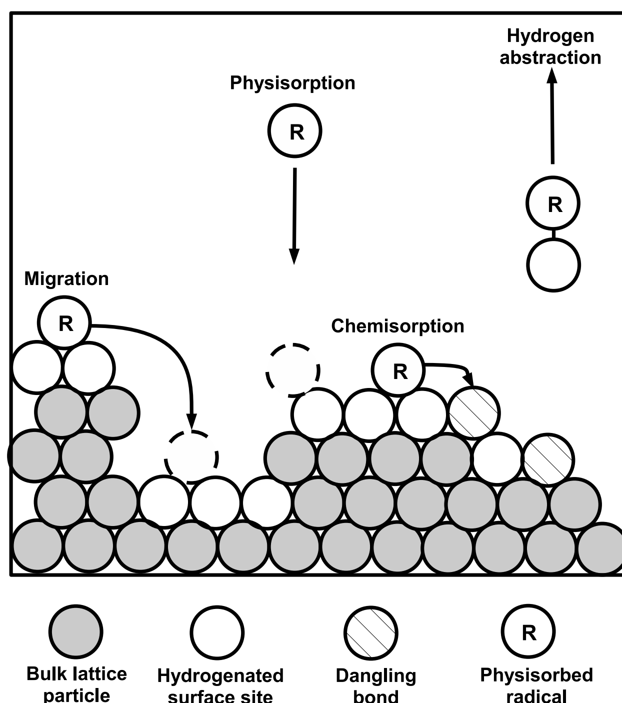

Figure 4.8: Triangular lattice representation showing four microscopic processes. Processes from left to right: migration, physisorption, chemisorption, and hydrogen abstraction.

successive monolayer are centered directly above those that define the previous layer. Thus, no vacancies are permitted within the bulk of the lattice. Alternatively, the lattice was given a two-dimensional triangular framework without the restriction of SOS behavior. Specifically, adjacent layers form close-packed groups which allow for the creation of porous structure within the growing film. By enforcing a minimum of two nearest neighbors per particle, overhangs may develop which in turn lead to voids in the triangular lattice. This effect can be seen in the 2D triangular surface representation of Fig. 4.8. Given that experimentally grown *a*-Si:H layers have been observed to have void fractions in the range of 10-20%, the triangular lattice allows for the development of a more representative microscopic model, and is therefore used throughout the remainder of this work.

For each individual microscopic simulation (i.e., for each location along the radius of the wafer), the size of the two-dimensional lattice can be characterized by the product of the length and

thickness. The number of lateral sites is denoted by L and is proportional to the physical length by $0.25\times L$, given a hard-sphere silicon diameter of $\sim$0.25 nm. The thickness can be calculated from the number of monolayers, H, using the following equation:

$$\tau = 0.25 \cdot H \cdot \frac{\sqrt{3}}{2}, \tag{4.12}$$

where the factor $\sqrt{3}/2$ accounts for the reduction in thickness due to the offset monolayers which result from the close-packed, hard-sphere structure defined by the triangular lattice (refer to Figs. 4.8 and 4.9). Throughout this work, the number of lateral sites remains fixed at $L = 1200$ in order to provide a lattice with enough area for the morphology of the *a*-Si:H thin film to be adequately captured without being so large as to pose additional computational challenges and to necessitate the inclusion of spatial variations within the microscopic model. In other words, while significant gradients exist in the concentration of SiH_3 and H within the PECVD reactor, finite microscopic zones of length $\sim$300 nm can be assumed to experience uniform deposition rates without the need for spatial considerations.

Relative rates formulation

Migration and hydrogen abstraction involve species which exist on the surface of the thin film; as a result, these reactions are thermally activated events and follow a standard Arrhenius-type formulation:

$$r_{t,i} = v_i e^{-E_i/k_B T}, \tag{4.13}$$

where v_i is the attempt frequency prefactor (s^{-1}) and E_i is the activation energy of radical i. Frequency prefactor and activation energy values are drawn from Bakos et al. [5, 6] to correspond to the growth of *a*-Si:H films via the two species deposition of SiH_3 and H.

Physisorption events originate within the gas-phase and can be described by an athermal or barrierless reaction model based on the fundamental kinetic theory of gases which yields the following

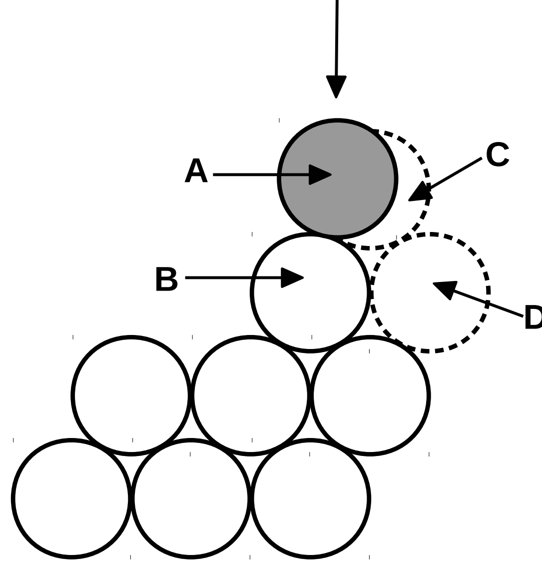

Figure 4.9: Surface relaxation for physisorbed radicals. (a) Incident particle location. (b) Surface Si particle in lattice. (c) Predefined triangular lattice site with one nearest neighbor. (d) Stable position for incident particle (two nearest neighbors).

rate equation:

$$r_{a,i} = J_i s_c N_a \sigma \,, \tag{4.14}$$

where J is the flux of gas-phase radicals, s_c is the local sticking coefficient (i.e., the probability that a particle which strikes the surface will 'stick' rather than bouncing off), N_a is the Avogadro number, and σ is the average area per surface site. Eqs. (4.15)-(4.17) can be used to calculate the flux, J:

$$J_i = \eta_i \bar{u}_i \,, \tag{4.15}$$

$$\eta_i = \frac{p_i}{RT} \,, \tag{4.16}$$

$$\bar{u}_i = \sqrt{\frac{8 k_B T}{\pi m_i}} \,, \tag{4.17}$$

where η_i is the number density of radical i (here the reactive gas-phase is assumed to be ideal), $\bar{u}_i$ is the mean radical velocity, p_i is the partial pressure of i, R the gas constant, T is the temperature, k_B is the Boltzmann constant, and m_i is the molecular weight of radical i. By substitution of the

expression for J into Eq. (4.14), the overall reaction rate for an athermal radical i becomes:

$$r_{a,i} = \frac{p_i}{RT}\sqrt{\frac{8k_BT}{\pi m_i}} s_c N_a \sigma \,. \tag{4.18}$$

Kinetic Monte Carlo implementation

Evolution of the lattice microstructure is achieved using a hybrid n-fold kinetic Monte Carlo algorithm for which the overall reaction rate is defined by

$$r_{\text{total}} = r_a^{SiH_3} + r_a^H + r_t^{abs} \,, \tag{4.19}$$

where $r_a^{SiH_3}$ is the rate of physisorption of SiH_3, r_a^H is the rate of physisorption of H, and r_t^{abs} is the rate of hydrogen abstraction forming SiH_4 (note: the subscripts a and t denote athermal and thermally activated reactions, respectively). In the interest of computational efficiency, surface migration is decoupled and does not contribute to the overall rate. The details and motivations behind decoupling migration events will be discussed at length in the next subsection.

Each kMC cycle begins through generating a uniform random number, $\gamma_1 \in [0,1]$. If $\gamma_1 \leq r_a^{SiH_3}/r_{\text{total}}$, then an SiH_3 physisorption event is executed. If $r_a^{SiH_3}/R_{\text{total}} < \gamma_1 \leq (r_a^{SiH_3} + r_a^H)/r_{\text{total}}$, then a hydrogen radical is physisorbed. Lastly, if $\gamma_1 > (r_a^H + r_t^{abs})/r_{\text{total}}$, then a surface hydrogen is abstracted via SiH_3.

Physisorption events for each radical type, SiH_3 or H, proceed through selecting a random site on the surface of the lattice from a list of candidate sites. Acceptable candidate sites are limited to those which exist in either their original, hydrogenated state, or which contain a dangling bond; sites which currently host a physisorbed radical cannot accept additional physisorption events. If the chosen site contains a dangling bond, the particle is instantaneously chemisorbed causing the lattice to grow by one. Hydrogen abstraction occurs by selecting a random SiH_3 particle from the surface of the lattice and returning it to the gas-phase as the stable species, SiH_4. In other words, a migrating SiH_3 radical removes a hydrogen atom from the surface of the film leaving behind a

dangling bond in its place. A second random number, γ_2 is now drawn in order to calculate the time required for the completed kMC event:

$$\delta t = \frac{-\ln(\gamma_2)}{r_{\text{total}}}, \tag{4.20}$$

where $\gamma_2 \in (0,1]$ is a uniform random number.

Deposition and movement of particles on the triangular lattice are also governed by what's known as surface relaxation whereby a minimum of two nearest neighbors is enforced in order to consider a particle location as stable. As an example, if a radical were to physisorb at location (A) in Fig. 4.9, it would first have to relax to position (C) such that it fits into the predetermined triangular lattice structure. However, at position (C) the incident particle has only a single nearest neighbor and is therefore only quasi-stable. Full stability is achieved by the particle further relaxing to position (D), at which point execution of the kMC algorithm can continue.

Decoupling surface migration

The frequency of reaction events listed in Fig. 4.10 motivate the choice to decouple migration from other kMC event types. Brute force kMC methods (in which all event types are available for execution) require more than 99% of computational resources to be spent on migration alone (note: the results in Fig. 4.10 are typical for *a*-Si:H systems operating near T = 475 K and P = 1 Torr). Consequently, only a small fraction of simulation time contributes to events leading to film growth while the vast majority is spent on updating the locations of rapidly moving particles. In an effort to reduce the computational demands of the microscopic model, a Markovian random-walk process has been introduced which decouples particle migration from the standard kMC algorithm.

A kMC cycle is typically defined by the execution of single event which moves forward the physical time of the system. In this work the completion of each cycle involves two steps: first, a kMC event is executed according to the relative rates of $r_a^{SiH_3}$, r_a^H and r_t^{abs}, second a propagator is

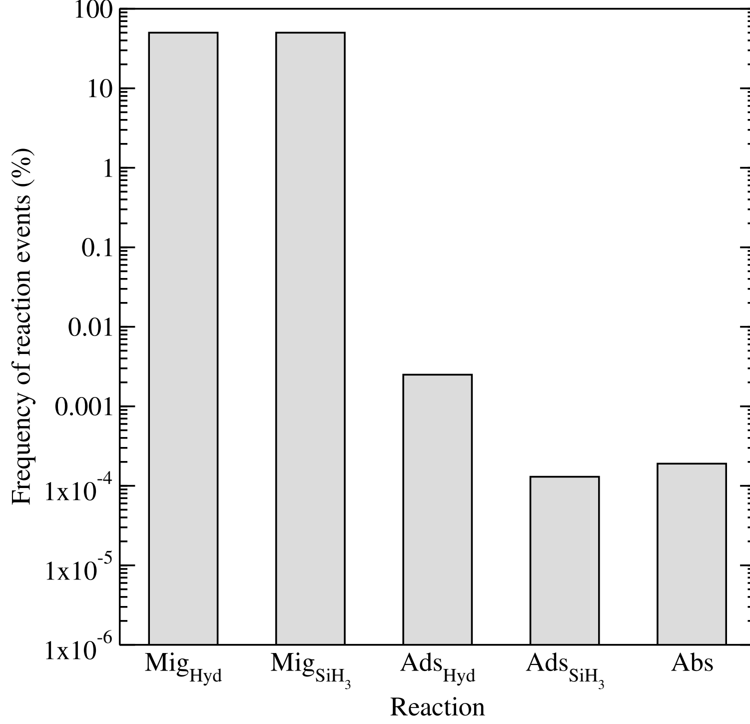

Figure 4.10: Normalized frequency of reaction events within the present kMC scheme at T = 475 K, P = 1 Torr, and a SiH_4^{in} mole fraction of 0.9.

introduced to monitor the motion of physisorbed radicals. The total number of propagation steps is $N_H + N_{SiH_3}$ where

$$N_H = \frac{r_t^H}{r_a^H + r_t^{abs} + r_a^{SiH_3}}, \quad N_{SiH_3} = \frac{r_t^{SiH_3}}{r_a^H + r_t^{abs} + r_a^{SiH_3}}, \tag{4.21}$$

and r_t^H and $r_t^{SiH_3}$ are the thermally activated migration rates of hydrogen and silane radicals, respectively. Each set of propagation steps, N_H and N_{SiH_3}, are split evenly among the current number of physisorbed radicals, n_H and n_{SiH_3}. The radicals then initiate a two-dimensional random walk process according to the number of assigned propagation steps. Thus, the intricate movements of an individual particle are approximated via the bulk motion of the propagator. For clarity, the procedure of the random walk process is as follows: a radical type is chosen, a random physisorbed radical of the given type is selected, the weighted random walk with N_i/n_i propagation steps begins,

propagation continues until either N_i/n_i steps have occurred or the radical becomes chemisorbed at a dangling bond site, the final position of the propagator is then stored as the radical's new position and this cycle continues for all $n_H + n_{SiH_3}$ physisorbed species. The weighting of each propagation step is designed such that the probability for a particle to relax down the lattice is exponentially higher than jumping up lattice positions (i.e., migration down the lattice is favored). Thus, relaxation and particle tracking are only required to be updated once per particle rather than after each individual particle movement as in brute force methods. In much the same way as physisorption and hydrogen abstraction, the time required for an individual migration step is calculated via the following equations:

$$\delta t_H = \frac{-\ln(\gamma_i)}{r_t^H}, \quad \delta t_{SiH_3} = \frac{-\ln(\gamma_j)}{r_t^{SiH_3}}. \tag{4.22}$$

Thus, the total time elapsed for all migration events, Δt, is determined by summation over the number of propagation steps,

$$\Delta t = \sum_i^{N_H} \frac{-\ln(\gamma_i)}{r_t^H} + \sum_j^{N_{SiH_3}} \frac{-\ln(\gamma_j)}{r_t^{SiH_3}}. \tag{4.23}$$

Our methodology of decoupling the diffusive processes from the remaining kinetic events has been validated by confirming that the underlying lattice random walk process results: (1) in surface morphologies and film porosities appropriate for the chosen process parameters, and (2) growth rates on par with experimental values. Detailed model validation can be found in the latter half of this paper. It is important to note that film growth continues in this cyclic manner until the kMC algorithm has reached the alloted time step (i.e., until the microscopic model has caught up with the macroscopic, CFD solver). For a more in-depth discussion of the transient operation of the multiscale model, please refer to the following section.

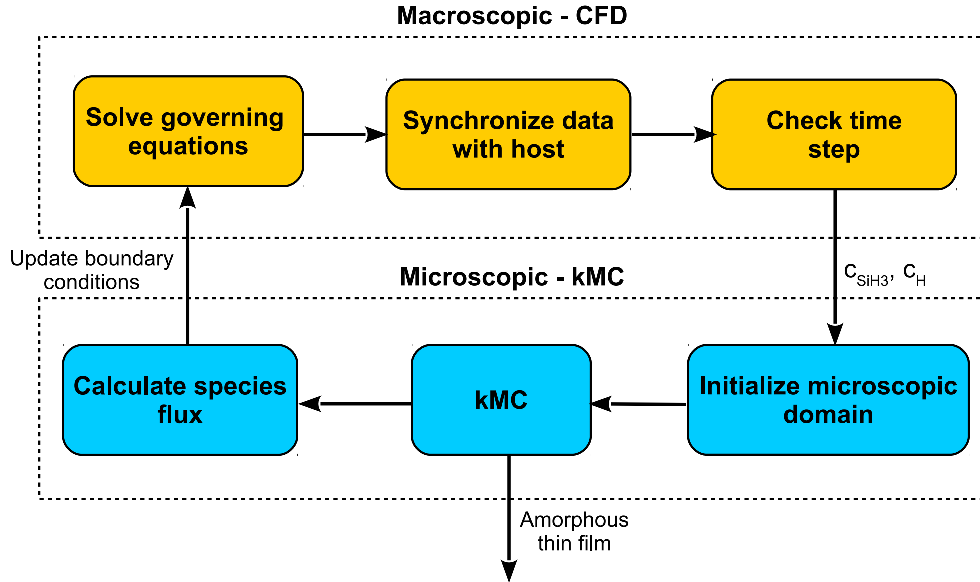

Figure 4.11: Multiscale simulation workflow detailing the coordination between the macroscopic and microscopic events.

4.3 Simulation workflow

At each time step, every cell of the mesh will first solve the governing equations with respect to their reduced spatial coordinates using finite difference methods, then the boundaries along adjacent cells are resolved iteratively. In order to move from one time step to the next, an Implicit Euler scheme is utilized. The result of this method is accurate predictions of the concentrations of each deposition species at all locations within the geometry for a particular time, t. Given the complete characterization of the plasma for all times, the microscopic model described throughout this work can once again be simulated in parallel such that the resulting thin film layers will be a product of accurate plasma chemistry. Fig. 4.11 clarifies the proposed multiscale workflow including the communication between domains at each time step.

At a given time, t, the governing equations are solved within each cell of the reactor mesh. The concentrations of the deposition species of interest, SiH_3 and H, are fed to the microscopic domain at which point the kMC model presented earlier can grow the thin film until time t is reached. The boundary cells (i.e., cells which are adjacent to the wafer surface) then receive

updated boundary conditions based the the transfer of mass and energy to the microscopic domain. This cycle continues through the completion of the PECVD batch deposition. Please note, the "initialization" of the microscopic domain refers to non-trivial startup costs associated with loading the lattice from the previous cycle (i.e., initialization must be run at every time step).

4.4 Parallel computation

Transient operation of the multiscale model presented in this work represents non-trivial computational demands. The simulated deposition of a 300 nm thick *a*-Si:H thin film alone requires two to three days of computation when using a single processor, and close to a day when utilizing a multi-core personal workstation. Addition of the CFD model increases the computational time of a single batch simulation to greater than a week of continuous processing (thus, for the given system with 120,000 cells in the mesh, the computational demands of the micro- and macroscopic scales are on the same order of magnitude). The results presented in the following sections represent not only the culmination of many test batches during the development of the multiscale model, but also data that has been averaged across several repeated simulations; therefore, serial computation on a single processor corresponds to an impractical task. We present a parallel computation strategy here as a viable solution to mitigate the aforementioned computational demands.

The motivations behind the use of parallel computation are threefold. As mentioned previously, the reduction in simulation time for a serial task is significant through the use of multiple processors. Second, kMC simulations inherently exhibit noise due to the stochastic nature of the model. By repeating a simulation with the same parameters numerous times, we can reduce the noise and obtain more accurate, averaged values. Finally, one might want to perform many simulations at different conditions (e.g., to find suitable model parameters by testing various deposition conditions and calibrating with known experimental data).

The details of the parallel algorithm and message-passing interface (MPI) are standard and therefore will not be discussed at this time. The recent publication of Kwon et al. [42] provides

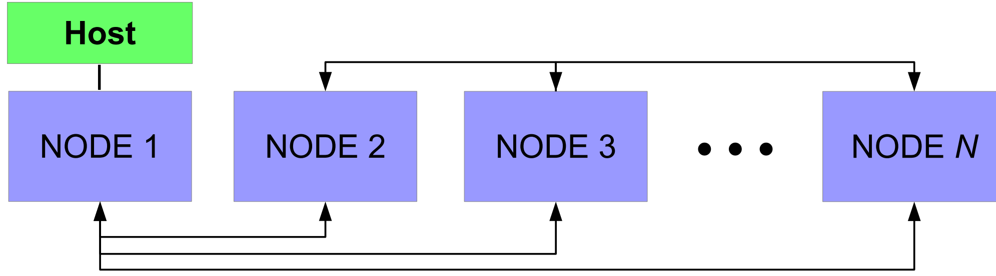

Figure 4.12: Communication between host and nodes within the MPI architecture.

further information on the parallelization strategies on which this work is based; additionally, in-depth studies of parallel processing with applications to microscopic simulations have been made by Nakano et al. and Cheimarios et al. [52, 10]. However, as a brief outline, the process of creating a parallel program can be understood through three elementary steps: (1) the original serial task is decomposed into small computational elements, (2) tasks are then distributed across multiple processors, and (3) communication between processors is orchestrated at the completion of each time step. Here decomposition of the serial program is achieved through two separate mechanisms. First, the mesh that defines the 2D axisymmetric geometry can be discretized into a number of smaller mesh regions in which a reduced number of cells reside. For example, in the case of a typical personal computer with 4 cores, each core would be assigned roughly 1/4 of the original 120,000 cell mesh. By utilizing UCLA's Hoffman2 computation cluster, up to 80 cores are available for parallel operation resulting in each core containing less than 2,000 cells. The maximum achievable speedup given the aforementioned parallel programming strategy can be defined by:

$$S(N) = \frac{1}{(1-P)+\frac{P}{N}}, \tag{4.24}$$

where S is the maximum speedup, P is the fraction of the program which is available for parallelization (i.e., the fraction of the original serial task which may be discretized), and N is the number of processors utilized [17].

4.5 Steady-state behavior

Before the results of the multiscale CFD model can be discussed, we must first validate each domain with available experimental data. To that end, a number of batch simulations have been conducted using an inlet gas composition, reactor temperature and pressure chosen to represent industrially relevant PECVD conditions. Namely, the inlet gas is composed of a 9:1 mixture of hydrogen to silane, the parallel plates are maintained at T = 475 K and a chamber pressure of P = 1 Torr is used. In the following section three criteria have been evaluated in order to determine the fidelity of the proposed model to experimentally grown *a*-Si:H thin films. It is important to note that although the results presented in the following sections have been collected after the reactor has reached steady-state, the multiscale model maintains transient operation. Startup of the PECVD reactor may affect the hydrogen content and porosity of the thin film layer, and therefore cannot be excluded.

4.5.1 Plasma composition, porosity and hydrogen content

Figs. 4.13 and 4.14 detail the distribution of the process gases within the PECVD reactor at steady-state. As one might expect, before reaching the showerhead holes, both SiH_4 and H_2 appear in similar concentrations to the inlet gas. Once entering the plasma region the silane gas is quickly consumed and continues to decrease in concentration towards the surface of the wafer. Due to the reaction set presented previously, the behavior of H_2 within the plasma is more complex. Hydrogen is primarily a product of the dominant gas-phase reactions (see Table 4.1), and this effect is reflected in the maximum concentration occurring near the outlets of the chamber.

Since growth of the thin film is dependent on the concentration and distribution of SiH_3 and H within the reactor, the steady-state profiles of these two species are of particular importance. Silane radicals (SiH_3) are observed to have a maximum mole fraction at the center of the PECVD reactor with significant gradients in both the r and z directions. Specifically, Figs. 4.15 and 4.16 demonstrate that the concentration of the deposition species track closely with the electron density

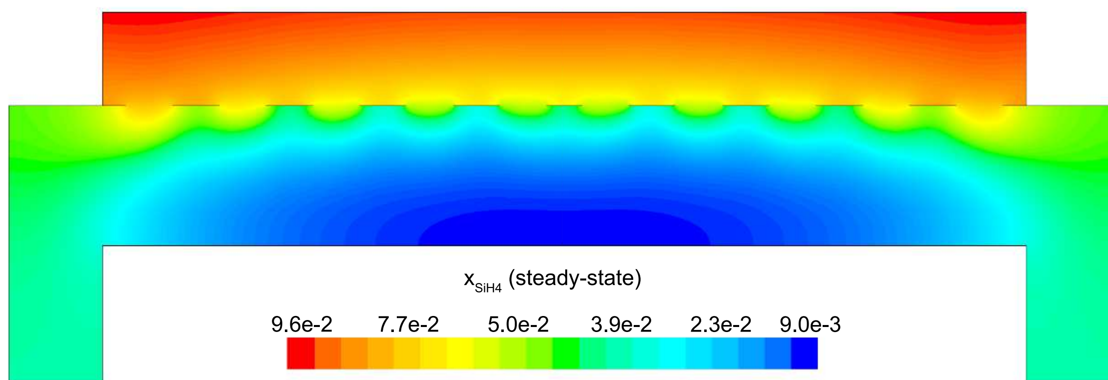

Figure 4.13: Steady-state profile of x_{SiH_4} at T = 475 K and P = 1 Torr.

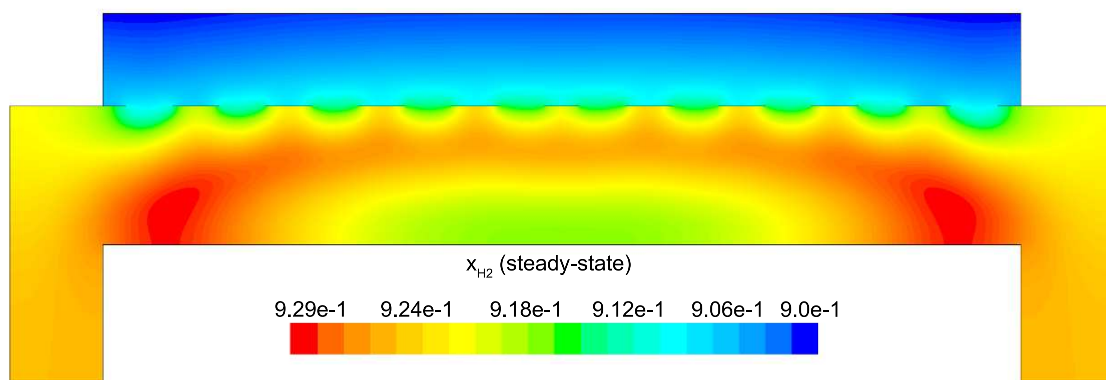

Figure 4.14: Steady-state profile of x_{H_2} at T = 475 K and P = 1 Torr.

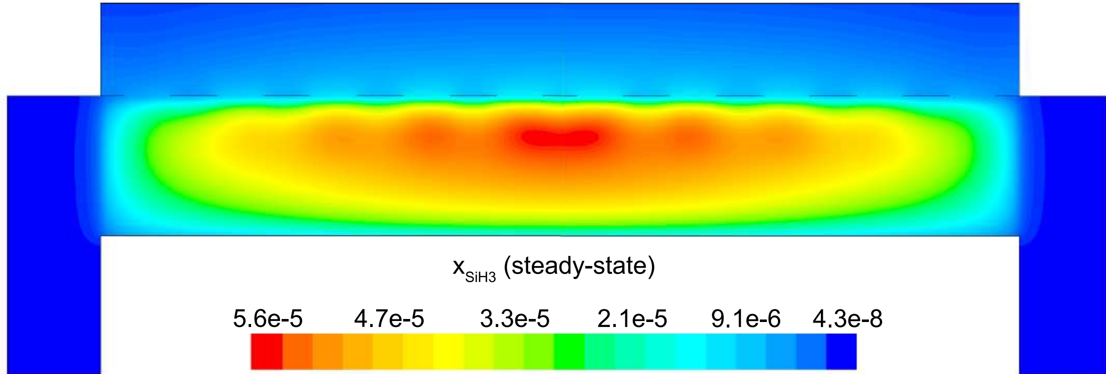

Figure 4.15: Steady-state profile of x_{SiH_3} at T = 475 K and P = 1 Torr.

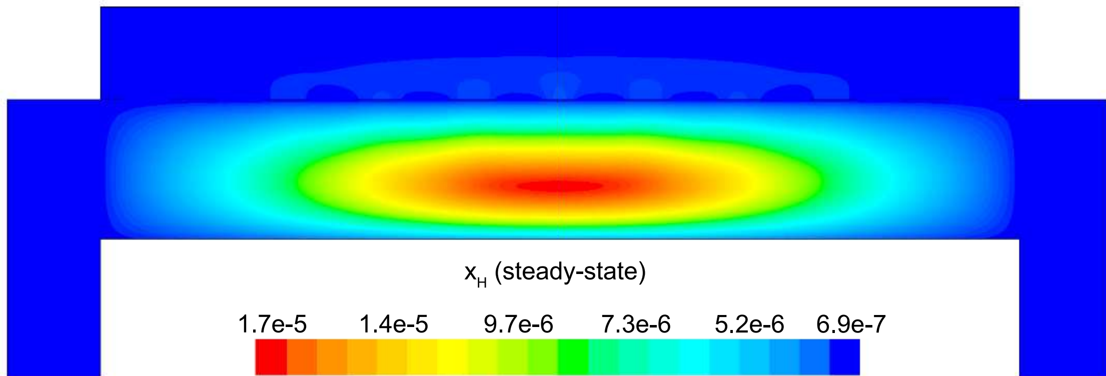

Figure 4.16: Steady-state profile of x_H at T = 475 K and P = 1 Torr.

(recall, Fig. 4.6). Due to the relatively short lifespan of radicals within a plasma, it is reasonable that the concentration of SiH_3 and H will be tied to the distribution of electrons rather than to convective and diffusive effects. Additionally, consumption of radicals during the growth of the thin film would suggest that depleted concentrations would be observed near the wafer surface; as expected, regardless of radial position, at $z = 0$ (along the wafer surface) a boundary layer can be clearly seen in x_{SiH_3} and x_H. Similar behavior has been predicted for the dominant deposition species in the detailed work of Amanatides et al. [1] and Kushner, M. [41], which yields confidence in the plasma composition obtained here.

The next criteria of interest is the hydrogen content of the thin film as predicted by the microscopic model. In the earlier discussion of the lattice character, the development of porosity

within the amorphous structure was highlighted. Hydrogen remains bonded to the interior surfaces of mono- and di-vacancies, as well as within much larger, long range voids. Fig. 4.17 shows a portion of a completed *a*-Si:H thin film which demonstrates the porous nature and the various void shapes produced. In an effort to calibrate the hydrogen content with experimentally obtained data, a number of batch PECVD processes are conducted using varying deposition parameters; specifically, the deposition temperature in successive batches is varied which yields thin film layers with different morphologies and degrees of bonded hydrogen. Comparing the recorded values to those reported in literature [2, 7, 39] reveals three distinct regions of interest: (1) below 500 K the hydrogen content of the *a*-Si:H thin film decreases linearly with increasing deposition temperature, (2) between 500 and 575 K atomic hydrogen fractions remain relatively constant ($\sim$9%) and (3) above 575 K the hydrogen capacity of the porous film begins to increase (see Fig. 4.18). While the observed atomic hydrogen falls within the accepted experimental range regardless of deposition temperature, the gradual upturn of hydrogen fractions above 575 K contradicts the expected behavior. Increasing the temperature of the film allows for more rapid migration of physisorbed species along the surface of the lattice, resulting in a more stable, less porous structure with reduced interior surface area available for hydrogen bonding. Consequently, a linear decrease in atomic hydrogen is observed in all four data sets as the deposition temperature is increased below the 575 K threshold. Deviation in the microscopic model's behavior above 575 K is believed to be due to competition between surface events. At high temperatures the frequency of hydrogen abstraction continues to grow which allows for premature chemisorption of migrating SiH_3 radicals. In other words, covalent bonds are formed in unfavorable locations before a more stable, close-packed structure can be achieved. Nonetheless, the operating conditions within this work call for a temperature of 475 K which lies well within the linear region.

Given the high complexity of the thin film morphology and near limitless distributions of voids which can lead to a specific hydrogen fraction, the validity of the microscopic model cannot be determined from the hydrogen content alone. As an example, two films could be deposited with identical degrees of porosity; the first may have scattered small vacancies while the second could

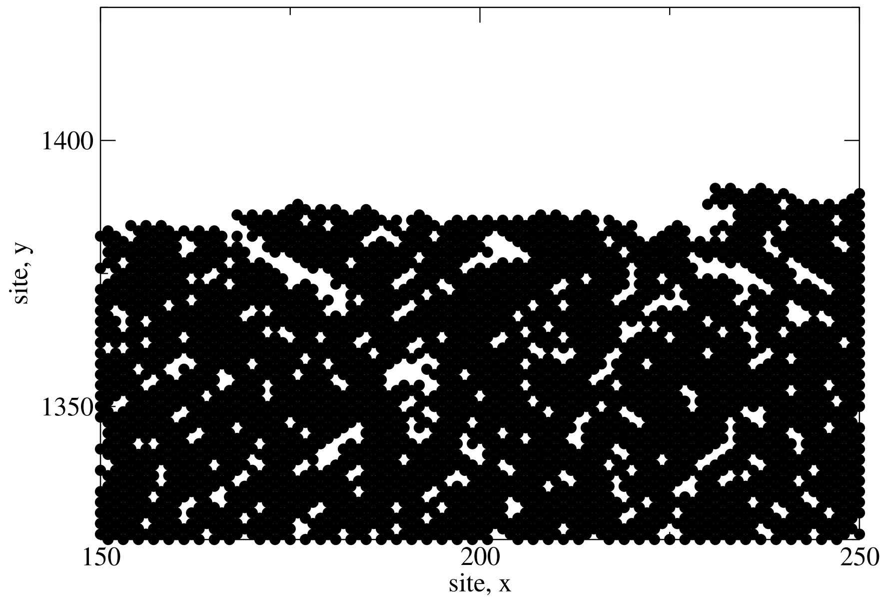

Figure 4.17: Representation of voids within a typical simulated lattice. (Note: Only a fraction of the full size lattice is shown in order to highlight porosity.)

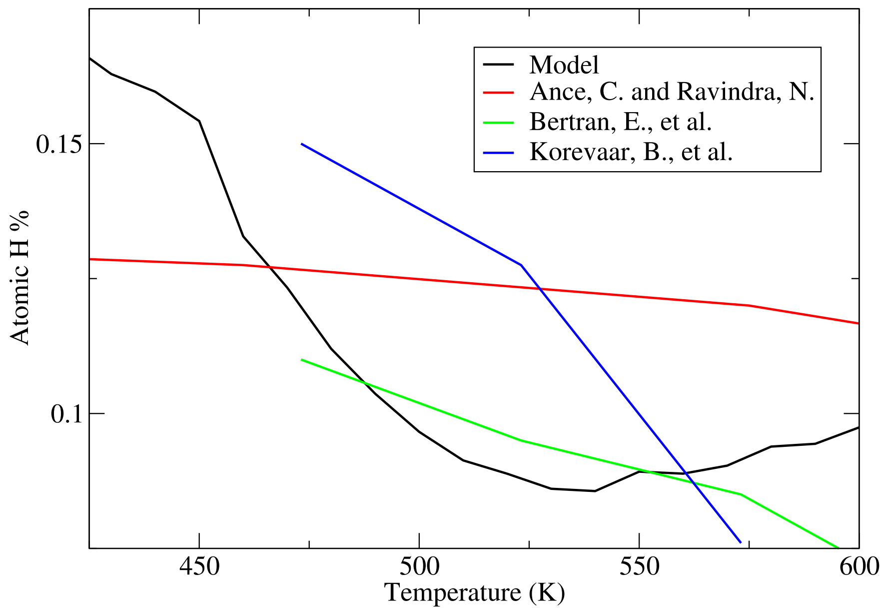

Figure 4.18: Hydrogen content dependence on deposition temperature.

contain a single large pore. While both films maintain the same overall porosity, the amount of bonded hydrogen will vary widely due to differences in interior surface area. As a result, an additional criteria is defined here, the relationship between the porosity of the film and the associated hydrogen content. For consistency with data obtained from literature, the site occupancy ratio (SOR) is used as a measure of porosity:

$$SOR = \frac{n}{LH}, \tag{4.25}$$

where n is the number of occupied lattice sites and LH is the total number of sites within the lattice. Again, given that hydrogen persists on the interior surfaces of the film, it is expected that a strong correlation exists between the hydrogen content and SOR which will allow for a more detailed evaluation of the accuracy of the microscopic model.

Another set of batch deposition processes were performed in which the pressure was maintained at P = 1 Torr and the inlet gas compositions at a 9:1 ratio of hydrogen to silane. The temperature of the wafer was increased incrementally from 450 K to 500 K and at the completion of each batch the SOR and atomic hydrogen fraction was recorded. In Fig. 4.19, this data has been plotted alongside experimentally grown films obtained from five different literature sources [8, 21, 38, 49, 51]. As expected from the bonding of hydrogen on the interior surfaces of amorphous silicon films, all six data sets demonstrate a similar trend of increasing hydrogen fractions with decreasing site occupancy ratios. Additionally, regardless of SOR the microscopic model predicts a hydrogen content value consistent with the range observed experimentally. These results yield confidence in the ability of the multiscale model presented here to reproduce thin film layers with not only the correct amount of bonded hydrogen, but also with lattice morphologies with high fidelity to those produced via commercially available PECVD systems.

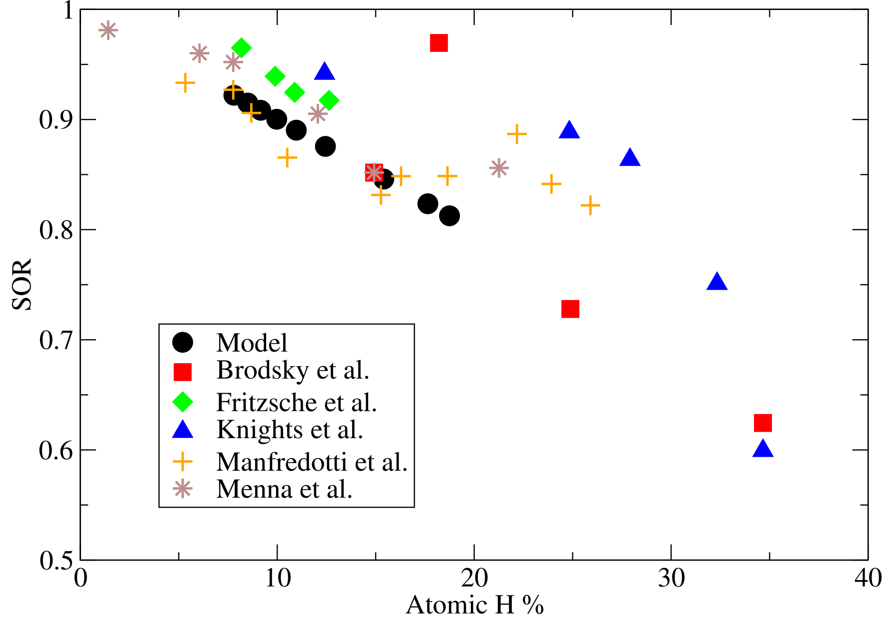

Figure 4.19: Relationship between film SOR and hydrogen content.

4.6 Multiscale CFD analysis

The primary motivation for the development of a multiscale CFD model for the PECVD of silicon thin films is to explore complex phenomena otherwise unobservable by a macroscopic or microscopic simulation alone. To that end, we now comment on the interconnection between these two domains. Specifically, at the macroscopic scale significant gradients exist in the concentration of the deposition species of interest, SiH_3 and H. Meaning, microscopic simulations at various points along the surface of the wafer should yield non-uniform thin film character due to receiving spatially varying input parameters from the CFD model. This effect can be readily seen in Figs. 4.20 and 4.21 by narrowing our focus to the region just above the surface of the wafer. As discussed in the steady-state analysis, radial dependence of x_{SiH_3} and x_H develops due to consumption of the gas as it flows radially outward through the electron cloud and across the wafer. Given that growth of *a*-Si:H films is dependent on SiH_3 radicals reaching the surface, it is likely that at the completion of a batch, the thickness of the thin film layer will not be uniform (further discussion of thickness non-uniformities can be found in the works of Armaou et al. [11] and Sansonnens et al. [64]).

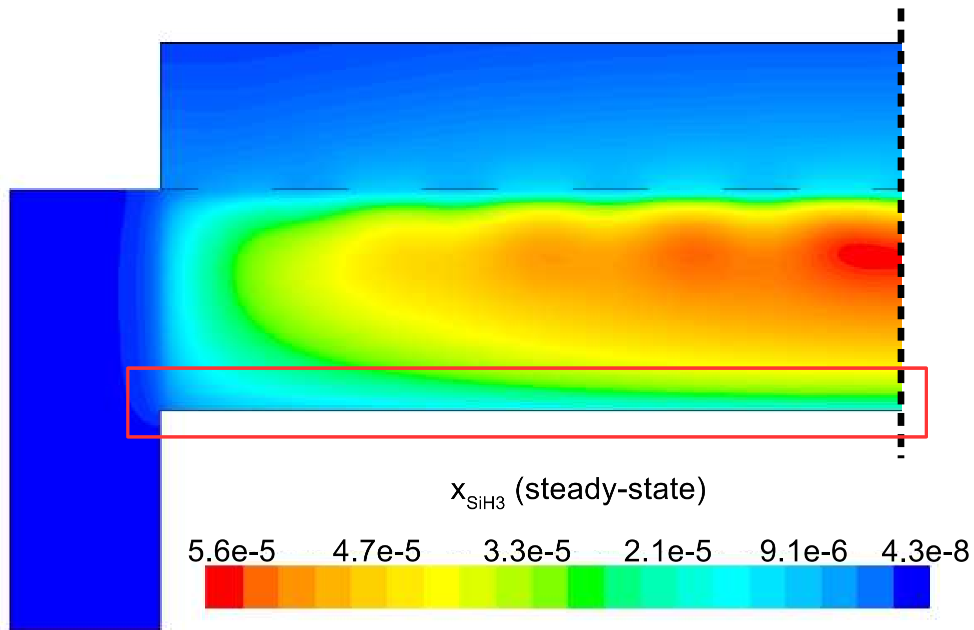

Figure 4.20: Radial gradient in the concentration of SiH_3 above the wafer surface.

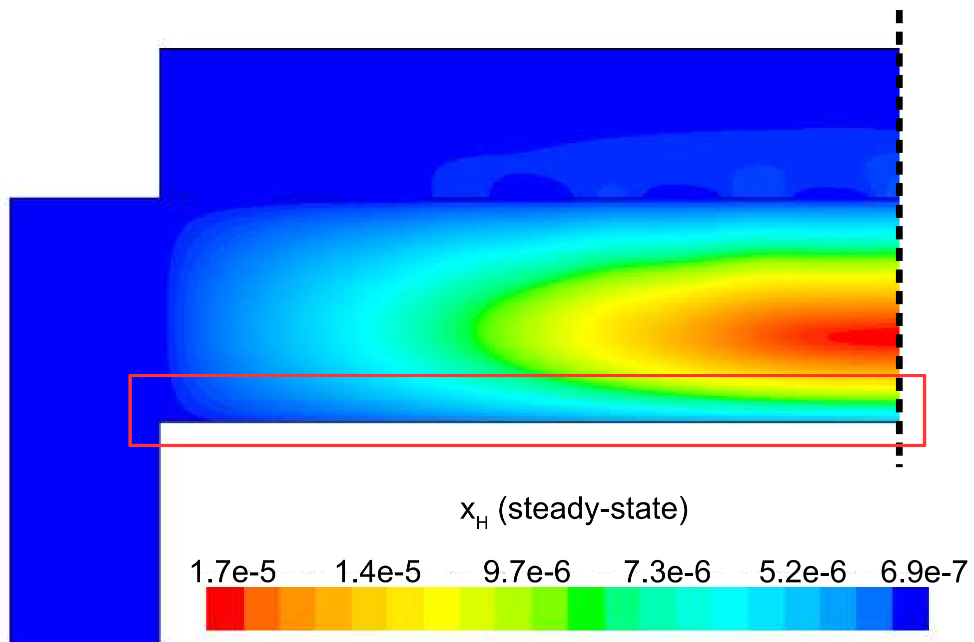

Figure 4.21: Radial gradient in the concentration of H above the wafer surface.

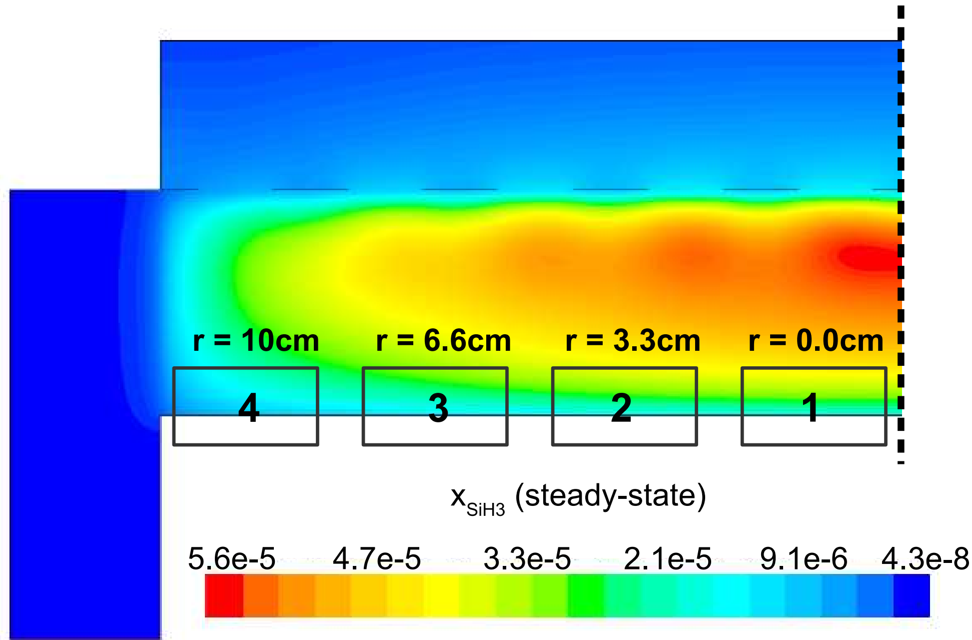

Figure 4.22: Four discrete locations across the wafer surface in which a representative thin film layer will be grown in order to investigate non-uniformities in the amorphous product.

In an effort to quantify the non-uniformities predicted above, four distinct locations across the wafer surface are defined. During the operation of the multiscale model the output from the microscopic domain at each location is recorded (i.e., thin film samples from r = 0.0, r = 3.3, r = 6.6 and r = 10 cm are collected). Analysis of each thin film sample may yield insight into the performance of the PECVD reactor as well as the character of the amorphous product.

Fig. 4.23 shows the growth rate of the thin film at each radial location averaged over 10 independent batch simulations. A clear dependence on radial position can be seen with >20% difference between the growth rates of the film at r = 0.0 cm and r = 10 cm. Given that the goal of PECVD processing of *a*-Si:H is to deposit thin films with uniform thickness and photovoltaic properties, a 20% non-uniformity in product thickness represents an unacceptable margin. In terms of photovoltaic properties, Staebler and Wronski [66] and Smets et al. [65] have demonstrated that the hydrogen content and porosity of amorphous silicon thin films are tied directly to the efficiency of the solar cell produced. Therefore, the uniformity of bonded hydrogen and porous structure

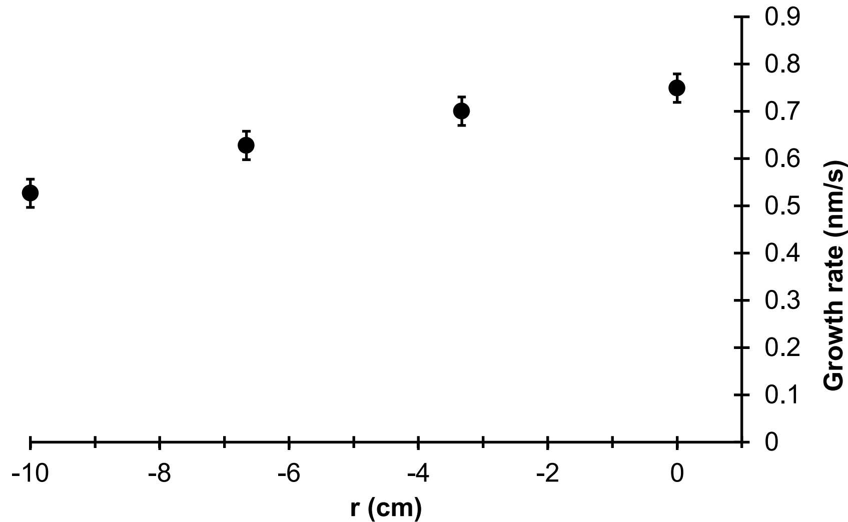

Figure 4.23: Open-loop drift and spatial non-uniformity in the four radial wafer zones.

across the film is of great interest.

To that end, Fig. 4.24 lists the SOR and atomic hydrogen % averaged over 10 independent batch simulations for the same four radial locations described previously. The SOR from the center to the edge of the thin film layer remains relatively unchanged (i.e., the difference between each data point lies within the standard deviation of the data set). This is likely due to the fact that all four radial locations experience the same deposition temperature; recall from the earlier discussion of validation criteria that the morphology of the film is dependent on the temperature of the wafer. However, non-trivial differences in the hydrogen content of the film can be seen between r = 0.0 cm and r = 10 cm. Due to the significant gradient of x_H observed in the steady-state concentration profile (see Fig. 4.21), the radial non-uniformity in the film's hydrogen content is expected. It is important to note that while the two data sets presented here are unrelated to the thickness non-uniformity, the hydrogen content and SOR remain industrially relevant parameters due to the Staebler-Wronski effect.

The results presented here highlight the importance of accurate reactor modeling; specifically, the importance of utilizing multiscale models which capture the behavior of the reactor as a whole. Information on film non-uniformities obtained via the multiscale PECVD model developed here

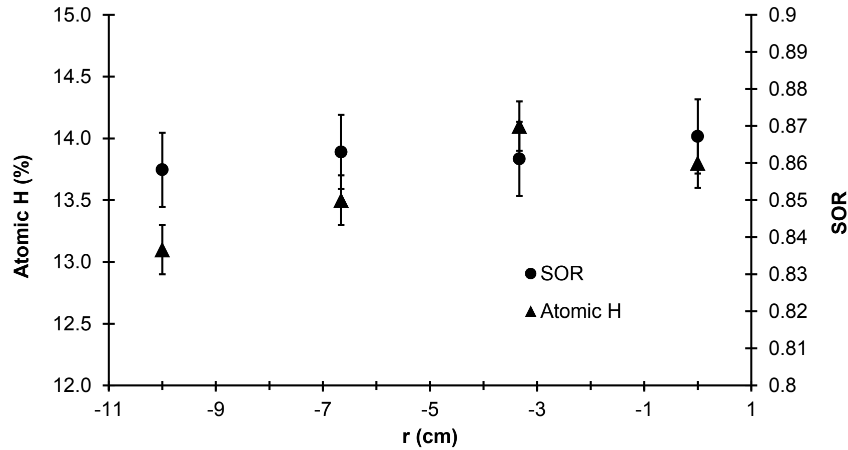

Figure 4.24: Open-loop drift and spatial non-uniformity in the four radial wafer zones.

may provide insight into the design of improved reactor geometries and operational strategies otherwise unavailable using traditional modeling approaches.

4.7 Conclusions

A multiscale CFD simulation framework, including both a macroscopic CFD model and a microscopic surface interaction model, has been presented here with applications to silicon processing via PECVD. Within the macroscopic domain, mass, momentum and energy balances have been solved by discretization of the PECVD geometry using a 2D axisymmetric mesh and finite difference methods. Along the boundary of the 20 cm diameter wafer, a hybrid kinetic Monte Carlo algorithm has been proposed to account for complex phenomena within the microscopic domain describing thin film growth. A parallel operation strategy has been implemented and demonstrated to reduce the computational demands of the multiscale CFD model and allow for the operation of an otherwise computationally prohibitive model. Together the macroscopic and microscopic simulations have yielded insight into the operation of PECVD systems; specifically, observed non-uniformities in the growth rate (>20%) and hydrogen content of the thin film product suggest that detailed modeling offers the capacity for improved reactor geometries and flow characteristics.

Chapter 5

Multiscale Three-Dimensional CFD Modeling for PECVD of Amorphous Silicon Thin Films

5.1 Introduction

The past two decades have seen continual development in the multiscale modeling of plasma-enhanced chemical vapor deposition (PECVD) with specific applications to the manufacturing of silicon thin films for use in the photovoltaic and microelectronics industries (e.g., [58, 12, 18]). Accurate modeling of thin film deposition remains a key element in the effort to improve product quality and to cut down on manufacturing costs due to the difficulties associated with continuous and/or in situ measurements during chambered deposition processes [58, 57, 19]. Recently, Crose et al. [15] demonstrated a novel multiscale computational fluid dynamics (CFD) model, which combined a macroscopic CFD domain with a microscopic surface domain through a common boundary which lies on the surface of the silicon wafer. Although advanced modeling of chemical reactors via CFD has existed for some time [26], the work of Crose et al. was the first to capture the link between PECVD reactor behavior and the microscopic domain. In particular,

non-uniform deposition of a-Si:H (amorphous silicon) films was studied and provided a basis for future multiscale CFD modeling endeavors. Nonetheless, the two-dimensional axisymmetric nature of the model limits the exploration of some phenomena which exist in the three-dimensional in space process. Specifically, two-dimensional (2D) axisymmetric models cannot represent the full geometry of showerhead holes that provide reactant gases to the plasma region – a key feature when considering the uniformity of thin film products.

Given the aforementioned motivations, the framework previously developed for use in 2D applications is extended to the three dimensional in space domain. Using a three-dimensional (3D) rendering which captures the typical geometry of chambered, parallel-plate PECVD reactors, a CFD model is proposed in the present work which is capable of reproducing accurately both plasma chemistry and fluid flow into the reaction zone through the showerhead region. With regard to the microscopic domain (i.e., the surface of the silicon wafer), a detailed kinetic Monte Carlo (kMC) algorithm developed previously by Crose et al. [15] is applied in order to capture both the exchange of mass and energy, as well as the microstructure of the a-Si:H thin film. Given that the startup and operation of PECVD reactors are inherently dynamic, the proposed simulations cannot derive accurate reactor behavior from steady-state solutions; however, the computationally demanding nature of the transient simulations necessitates the use of a parallel computation strategy as well as taking advantage of multiple-time-scale phenomena occurring in the process. In this chapter, a Message Passing Interface (MPI) structure is adopted which allows for the discretization of both the macroscopic CFD volume and the microscopic kMC algorithm. The outlined multiscale model including its parallel implementation is applied to the deposition of 300 nm thick a-Si:H thin films revealing significant non-uniformities in the thickness of the thin film product. An improved reactor geometry is proposed which utilizes a polar showerhead arrangement and a radially-adjusted showerhead hole diameter. This geometry is shown to reduce thickness non-uniformity in the a-Si:H thin film product from $\sim$8% to less than 4%, representing significant product quality improvement and financial savings.

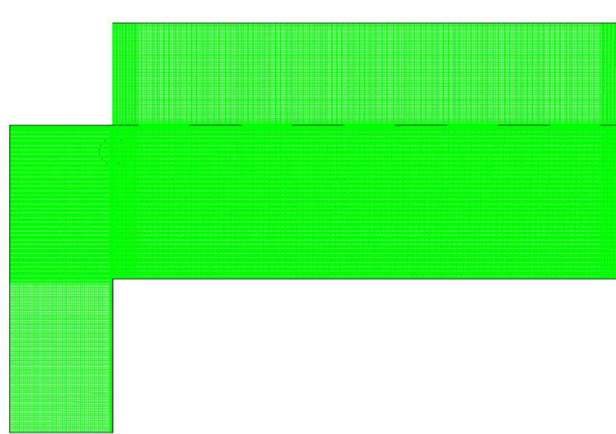

(a) Structured mesh

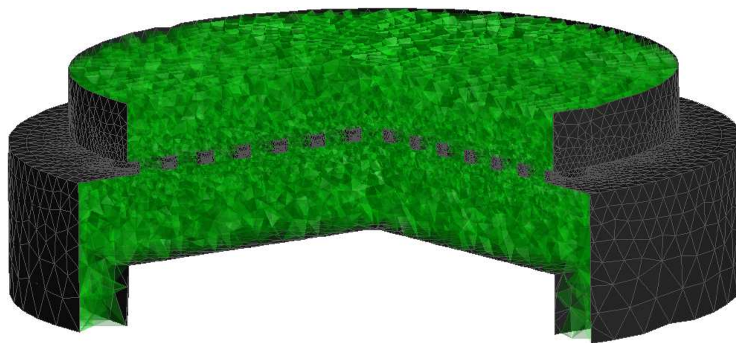

(b) Unstructured mesh

Figure 5.1: (a) 2D axisymmetric geometry after discretization using a structured mesh containing 120,000 cells. (b) Collection of 1.5 million polygons which define the unstructured, 3D mesh.

5.2 Three-dimensional modeling

Recently, Crose et al. [15] demonstrated the need for multiscale modeling in the PECVD process due to the interconnection between the macroscopic, reactor scale and the microscopic, thin film growth domains. Specifically, a two-dimensional (2D) axisymmetric geometry was used in the creation of the reactor mesh and a hybrid kinetic Monte Carlo (kMC) algorithm was applied to capture the growth of amorphous silicon (*a*-Si:H) thin film layers. The common boundary between the reactor mesh and microscopic model is of key importance as it allows for the distinct domains to remain linked throughout the course of transient simulations, and will be discussed at length in the multiscale workflow section. Although this model has proved useful in designing optimized reactor operational strategies, some features of the PECVD reactor are lost when using 2D representations. In looking at Figs. 5.1a and 5.1b, the difference between showerhead geometries becomes clear: the cylindrical showerhead holes and their associated spatial arrangement of the 3D system cannot be directly translated to 2D models. Given the primary motivation of addressing *a*-Si:H thin film product quality (in particular, thin film spatial non-uniformity) through improved PECVD reactor design, in this work the development of a 3D multiscale CFD model will be presented including both the macroscopic and microscopic domains, as well as the associated dynamic boundary conditions and parallel computing implementation.

5.2.1 CFD geometry and meshing

As discussed previously, we utilize a 3D, cylindrical PECVD reactor geometry (see Fig. 5.1b) with dimensions typical of those used in industry. The showerhead holes, visible in Figs. 5.1b and 5.14a, have a diameter of 1 cm and are evenly spaced in a rectangular array throughout the inlet region. In order to solve the partial differential equations which capture the gas phase mass, momentum and energy balances, the reactor geometry is discretized using an unstructured mesh containing $\sim$1.5 million tetrahedral cells. While previous efforts in modeling PECVD systems have relied on structured meshing (e.g., Crose et al. [15]) due to the possibility for higher mesh

quality, in terms of orthogonality and aspect ratio, these models were based on 2D geometries with rectangular structures; however, in this work the curvature of the cylindrical reactor shell and showerhead holes favor the use of unstructured mesh compositions.

Specifically, the reactor mesh is built from a collection of tetrahedral cells with non-uniform cell density. Regions in which significant gradients are expected in temperature, species concentration, flow velocity, etc. (i.e., near walls, corners and highly curved surfaces) have been given higher cell density as opposed to the bulk fluid regions, see Fig. 5.1b. In order to obtain industrially relevant plasma distributions and thin film growth, accurate flow modeling of the process gas throughout the chamber is paramount. As an additional consideration, the cell density near surfaces is directly correlated to the flow characteristics of the gas, and in particular, the boundary layer which is formed at the interface of the fluid and solid phases. Given the relatively low flow rate of process gas (75 SCCM) and low chamber pressure (1 Torr), flow along the surface of the wafer is expected to be laminar (note: preliminary results from the macroscopic model and earlier work suggest a Reynold's number of Re = 2.28×10^{-4}). As a result, the mesh density directly above the substrate surface has been tuned such that the boundary layer may be captured within one cell 'layer' to provide accurate predictions necessary for the linked microscopic model. Although the choice to use an unstructured mesh in this manner rather than a simplified structured mesh comes at the cost of computational efficiency, the ease in designing new reactor geometries without constraints for showerhead hole size and curvature necessitates its use and the associated computational demands will be discussed at length in the parallel programming section below.

It is important to note that throughout this work ANSYS software is applied to the creation of the geometric mesh (specifically, ICEM meshing) and as a solver for the PDEs describing transport phenomena and chemical reactions [3]. The ANSYS Fluent software alone cannot yield a multiscale model for the PECVD process of interest; consequently, three user defined functions (UDFs) have been developed to tailor the solver to the deposition of *a*-Si:H thin films. More specifically, the thirty four most dominant gas phase reactions have been accounted for via a volumetric reaction scheme which includes terms for the nine primary plasma reactions which lead to thin film

growth. The necessary electron density within the plasma region is calculated using a product of the zero-order Bessel function and a sine function which account for the spatial dependencies within the cylindrical reaction zone. The third UDF necessary to the multiscale nature of the model simulates the growth of *a*-Si:H thin films along the surface of the wafer substrate. The details of these UDFs, in particular the kinetic Monte Carlo (kMC) algorithm which defines the microscopic domain, are expanded upon at length in the following sections.

5.2.2 Gas-phase model

Growth of amorphous silicon layers within a PECVD reactor is intimately tied to the physio-chemical phenomena that govern the gas phase. Mass, momentum and energy balances each play a key role in predicting the conditions at the shared boundary between the macroscopic and microscopic domains. To that end, traditional analytic solutions to the gas-phase model are viable only for simplified geometries or systems which fail to provide meaningful results that can be applied to industrially used PECVD systems. By defining the mesh structure as described in the previous section, numerical methods may be introduced which are capable of solving the complex computational fluid dynamics equations with high resolution. Specifically, at every time step, the governing equations are discretized in alignment with the cell distribution presented in Fig. 5.1b, allowing for the ANSYS Fluent solver to implement finite volume methods. Extended functionality of the Fluent solver (i.e., a tailored solution specific to deposition via PECVD) is achieved using the aforementioned user defined functions (see Fig. 5.2 for an example tetrahedral cell element as viewed by the solver).

The continuity, energy and momentum equations employed in this work are standard and as such will be presented only briefly without rigorous derivation. An in-depth description of the flow field equations can be found in the Fluent user manual [3]. In a generalized vector form, the governing equations are given by the following system:

$$\frac{\partial}{\partial t}(\rho\vec{v})+\nabla(\rho\vec{v}\vec{v})=-\nabla p+\nabla\bar{\bar{\tau}}+\rho\vec{g}+\vec{F} \tag{5.1}$$

$$\bar{\bar{\tau}} = \mu[(\nabla\vec{v} + \nabla\vec{v}^T) - \frac{2}{3}\nabla\vec{v}I] \tag{5.2}$$

$$\frac{\partial}{\partial t}(\rho E) + \nabla(\vec{v}(\rho E + p)) = \nabla(k\nabla T - \Sigma h\vec{J} + (\bar{\bar{\tau}}\vec{v})) + S_h \tag{5.3}$$

$$\frac{\partial}{\partial t}(\rho Y_i) + \nabla \cdot (\rho\vec{v}Y_i) = -\nabla \cdot \vec{J}_i + R_i + S_i \tag{5.4}$$

$$\vec{J}_i = -\rho D_{i,m}\nabla Y_i - D_{T,i}\frac{\nabla T}{T} \tag{5.5}$$

where ρ is the density of the gas, $\vec{v}$ is the physical velocity vector, p is the static pressure, $\bar{\bar{\tau}}$ and I are the stress and unit tensors, J is the diffusive flux, Y_i is the mass fraction of species i, D_i is the diffusion coefficient of species i, and S_h, R_i and S_i are terms specific to the UDFs utilized in this work and will be defined below.

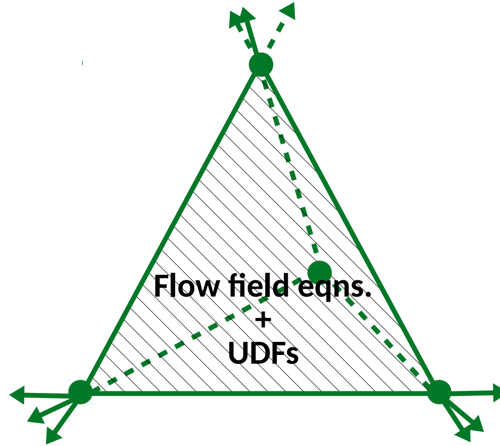

Figure 5.2: Individual unit cell within the unstructured mesh.

As mentioned in the previous subsection, three predominant UDFs are used to tailor the functionality of the generalized Fluent solver to the problem of interest in this work, the first of which accounts for the volumetric reactions occurring above the substrate surface. Although extensive reaction sets have been proposed which detail all possible intermediate and aggregate species involved in the deposition of *a*-Si:H films (e.g., [41]), here we limit the scope to the twelve most dominant species and their associated thirty-four gas-phase reactions. A complete listing of the reactions, mechanisms and rate constants are given in Table 5.1. Thus, the R_i terms in the mass

balance presented above are a product of this reaction set and are updated by the UDF during each time step.

The terms S_h and S_i appearing in Eqs. 5.3 and 5.4, respectively, refer to user defined sources or sinks. During the deposition of amorphous silicon, mass is drawn from the gas phase in the form of SiH_3 and H radicals, and mass is likewise reintroduced to the macroscopic domain due to hydrogen abstraction from the substrate surface via the formation of the stable species, SiH_4 (note: this phenomena is visible in Fig. 5.4a). The S_i term acts as a dynamic boundary condition which is updated based on the transfer of mass during the previous microscopic simulation cycle, with units of kg $s^{-1}m^{-2}$. In other words, at the end of a time step the amount of mass (for each species) withdrawn from, or introduced to, the macroscopic domain is reported from the individual microscopic calculations. Subsequently, the boundary conditions for the two-dimensional areas which define the interfaces of the kMC regions are updated before the next time step commences. Additionally, the formation and breaking of chemical bonds along the amorphous surface causes an exchange of energy between the substrate and the continuous gas phase which is tracked through the S_h term. For clarification on the dynamic boundary conditions and their role in the overall multiscale model, please refer to the multiscale workflow section below.

Electron density profile

In looking at Table 5.1, reactions R^1 through R^9 involve the interaction of free electrons and stable species; these nine reactions define the plasma chemistry necessary for the deposition of SiH_3 and H. As such, the electron density is key to the accuracy of the plasma phase and the corresponding growth of thin film layers. For plasmas generated from radio frequency (RF) discharges within cylindrical geometries, literature has shown that the electron density can be accurately estimated from the product of the zero order Bessel function and a sine function whose period is twice the distance between the showerhead and wafer substrate [55]. This is described by the following equation:

$$n_e(r,z) = n_{eo} \cdot J_0(2.405\frac{r}{r_t}) \cdot sin(\frac{\pi z}{D}), \tag{5.6}$$

Table 5.1: Macroscopic reaction set. Note: Rate constants have units of cm^3/sec and have been adopted from the collection prepared by Kushner et al. [41].

Reaction	Mechanism	Rate constant
R^1	$e^- + H_2 \rightarrow 2H$	7.66×10^{12}
R^2	$e^- + SiH_4 \rightarrow SiH_3 + H$	9.57×10^{13}
R^3	$e^- + SiH_4 \rightarrow SiH_3^+ + H$	3.40×10^{12}
R^4	$e^- + SiH_4 \rightarrow SiH_2 + 2H$	1.13×10^{13}
R^5	$e^- + SiH_4 \rightarrow SiH + H_2 + H$	5.62×10^{12}
R^6	$e^- + SiH_4 \rightarrow Si + H_2 + 2H$	6.70×10^{12}
R^7	$e^- + Si_2H_6 \rightarrow SiH_3 + SiH_2 + H$	2.15×10^{13}
R^8	$e^- + Si_2H_6 \rightarrow H_3SiSiH + 2H$	7.41×10^{13}
R^9	$e^- + Si_3H_8 \rightarrow H_3SiSiH + SiH_4$	3.35×10^{14}
R^{10}	$H + SiH_2 \rightarrow SiH_3$	6.68×10^{11}
R^{11}	$H + SiH_2 \rightarrow SiH + H_2$	1.20×10^{13}
R^{12}	$H + SiH_3 \rightarrow SiH_2 + H_2$	1.20×10^{13}
R^{13}	$H + SiH_4 \rightarrow SiH_3 + H_2$	1.38×10^{12}
R^{14}	$H + H_2Si = SiH_2 \rightarrow Si_2H_5$	3.01×10^{12}
R^{15}	$H + Si_2H_6 \rightarrow SiH_4 + SiH_3$	4.03×10^{12}
R^{16}	$H + Si_2H_6 \rightarrow Si_2H_5 + H_2$	7.83×10^{12}
R^{17}	$H + Si_3H_8 \rightarrow Si_2H_5 + SiH_4$	1.19×10^{12}
R^{18}	$H_2 + SiH \rightarrow SiH_3$	1.20×10^{12}
R^{19}	$H_2 + SiH_2 \rightarrow SiH_4$	1.20×10^{11}
R^{20}	$SiH_2 + SiH_4 \rightarrow Si_2H_6$	6.02×10^{12}
R^{21}	$SiH_3 + SiH_3 \rightarrow SiH_4 + SiH_2$	4.22×10^{12}
R^{22}	$SiH_3 + SiH_3 \rightarrow Si_2H_6$	6.02×10^{12}
R^{23}	$SiH + SiH_4 \rightarrow Si_2H_5$	1.51×10^{12}
R^{24}	$SiH_2 + SiH_4 \rightarrow H_3SiSiH + H_2$	6.02×10^{12}
R^{25}	$SiH_2 + Si_2H_6 \rightarrow Si_3H_8$	7.23×10^{13}
R^{26}	$SiH_2 + SiH_3 \rightarrow Si_2H_5$	2.27×10^{11}
R^{27}	$SiH_3 + SiH_3 \rightarrow SiH_4 + SiH_2$	4.06×10^{13}
R^{28}	$SiH_3 + Si_2H_6 \rightarrow SiH_4 + Si_2H_5$	1.98×10^{13}
R^{29}	$Si_2H_5 + SiH_4 \rightarrow SiH_3 + Si_2H_6$	3.01×10^{11}
R^{30}	$SiH_3 + Si_2H_5 \rightarrow Si_3H_8$	9.03×10^{13}
R^{31}	$H_3SiSiH + SiH_4 \rightarrow Si_3H_8$	6.02×10^{12}
R^{32}	$Si_2H_5 + Si_2H_5 \rightarrow Si_3H_8 + SiH_2$	9.03×10^{13}
R^{33}	$H_3SiSiH \rightarrow H_2Si = SiH_2$	2.71×10^{13}
R^{34}	$H_2Si = SiH_2 \rightarrow H_3SiSiH$	2.29×10^{10}

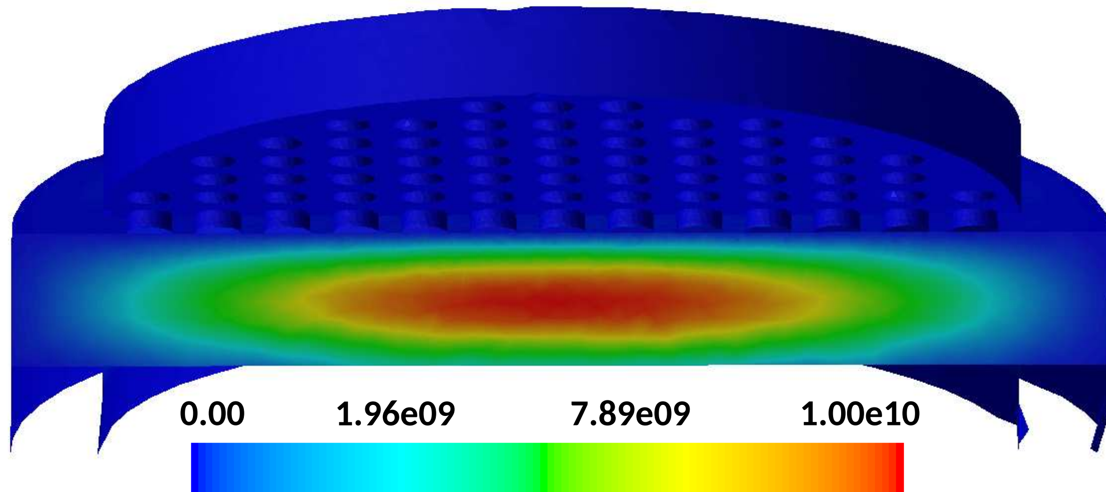

Figure 5.3: Electron density within 3D axisymmetric PECVD geometry (cm^{-3}).

where n_{eo} is the maximum electron density, J_0 is the zero order Bessel function of the first kind, r_t is the radius of the reactor, and D is the distance between the showerhead and wafer (i.e., the parallel plate spacing). The distribution seen in Fig. 5.3 is the result of applying the aforementioned electron density to the three-dimensional PECVD geometry presented earlier. The free electron 'cloud' remains bounded by the charged region between the cylindrical walls of the reaction chamber and the parallel plates which make up the showerhead and substrate platform. As expected, the zero order Bessel function enforces a maximum density in the center of the reactor which trails off near the exit ports along the edge.

5.2.3 Microscopic domain

While the CFD model itself, along with the UDFs for the gas phase reactions and electron density, define the macroscopic domain, the microscopic domain is contained entirely within the third and final UDF; specifically, as radicals diffuse from the gas phase down to the substrate surface, they enter the microscopic domain. In looking at Fig. 5.4a, finite elements (i.e., mesh cells) which share a boundary with the substrate surface allow for the exchange of SiH_3 and H radicals. This mechanism makes possible the interconnection between the two distinct simulation domains. While

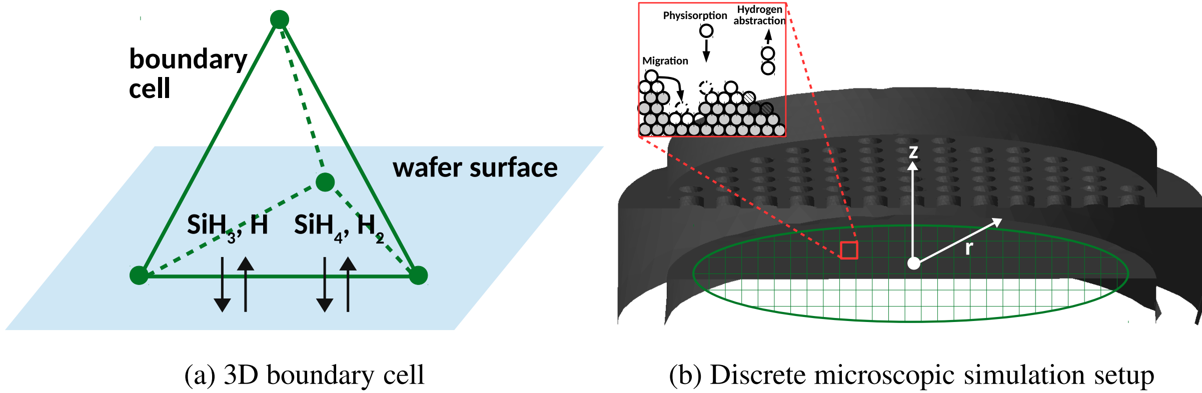

(a) 3D boundary cell

(b) Discrete microscopic simulation setup

Figure 5.4: (a) Finite element adjacent to the substrate surface with dynamic boundary condition calculated via microscopic simulation domain. (b) Kinetic Monte Carlo setup within overall multiscale simulation. Wafer substrate discretized in both the x and y directions forming a 'grid' structure.

tracking of each individual particle remains a computationally infeasible task, growth of *a*-Si:H thin film layers may still be achieved using a network of parallel kinetic Monte Carlo (kMC) algorithms. Specifically, the substrate surface is broken down into discrete regions along the x-y plane as shown in Fig. 5.4b, and within each region an independent kMC simulation is executed. Each simulation consists of a lattice of width 1200 particles which captures the growth of a representative *a*-Si:H layer within the associated region. The tetrahedral cells bordering each region are assigned dynamic boundary conditions corresponding to the exchange of mass and energy due to thin film growth at each time step (see Fig. 5.4a). Details concerning the development of the microscopic UDF, including both the parallel kMC structure and dynamic boundary conditions, will be discussed in detail in the following subsections.

Thin-film growth chemistry

Before the microscopic model is presented, it is important to detail the chemical phenomena which occur along the surface of the growing thin film layer. Only SiH_3 and H appear in this text as deposition species due to experimental results from Perrin et al. [56] and Robertson [61] which indicate that greater than 98% of amorphous silicon deposition can be attributed to these species

alone.

In order for growth of the *a*-Si:H thin film to occur, particles must diffuse from the gas phase to the wafer substrate, and subsequently stick to the hydrogenated surface. Upon striking the surface, SiH_3 and H radicals may either be deflected back into the gas phase or physisorption may occur at hydrogenated silicon sites ($\equiv Si-H$) as evidenced by the following reaction set:

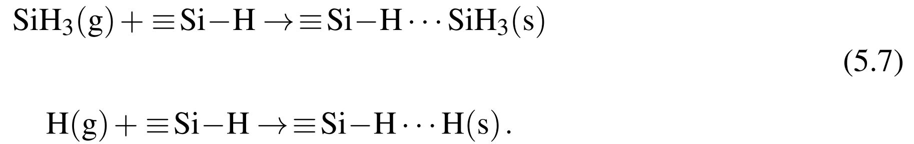

$$\begin{gathered} SiH_3(g) + \equiv Si-H \rightarrow \equiv Si-H \cdots SiH_3(s) \\ H(g) + \equiv Si-H \rightarrow \equiv Si-H \cdots H(s)\,. \end{gathered} \tag{5.7}$$

The probability for a particle which strikes the surface to remain on the surface is known as the sticking coefficient and will be considered in the kinetic Monte Carlo section to follow. Once a weak hydrogen bond has been formed, physisorbed radicals may follow one of two distinct mechanisms; the first and most dominant of which is rapid diffusion across the surface of the lattice via migration:

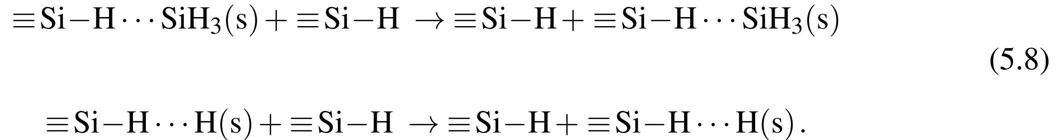

$$\begin{gathered} \equiv Si-H \cdots SiH_3(s) + \equiv Si-H \rightarrow \equiv Si-H + \equiv Si-H \cdots SiH_3(s) \\ \equiv Si-H \cdots H(s) + \equiv Si-H \rightarrow \equiv Si-H + \equiv Si-H \cdots H(s)\,. \end{gathered} \tag{5.8}$$

Alternatively, a particle may return to the gas phase through the abstraction of a surface hydrogen,

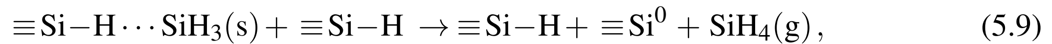

$$\equiv Si-H \cdots SiH_3(s) + \equiv Si-H \rightarrow \equiv Si-H + \equiv Si^0 + SiH_4(g)\,, \tag{5.9}$$

whereby a physisorbed radical removes a neighboring hydrogen atom and reforms the stable species (e.g., SiH_4 or H_2 in the case of two species deposition). This process leaves behind dangling bonds ($\equiv Si^0$) which are crucial to the growth of the amorphous silicon film. Growth of the lattice proceeds unit by unit via chemisorption of SiH_3 at dangling bond sites (i.e., the Si atom forms a covalent bond, permanently fixing its location within the amorphous structure) as shown

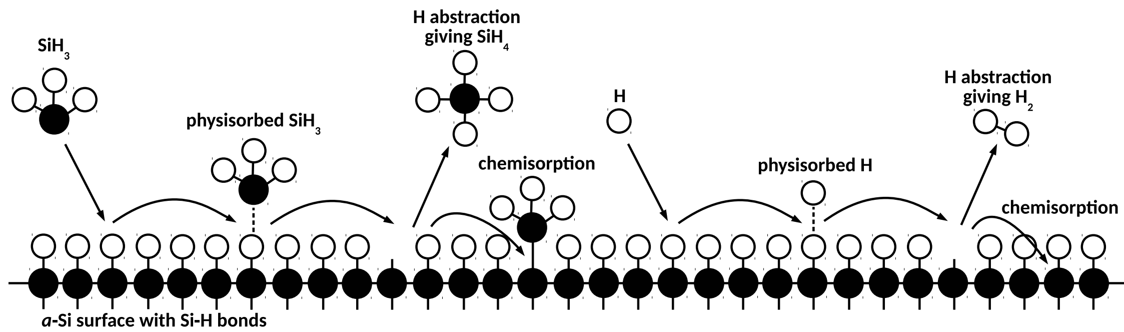

Figure 5.5: Chemical model illustration showing particle-surface interactions.

in the following reactions:

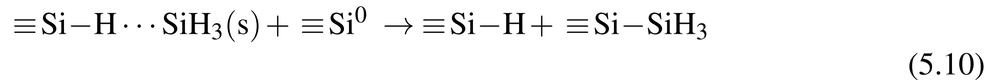
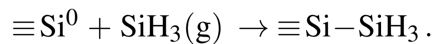

$$
\begin{gathered}
\equiv \mathrm{Si-H} \cdots \mathrm{SiH_3(s)} + \equiv \mathrm{Si}^0 \rightarrow \equiv \mathrm{Si-H} + \equiv \mathrm{Si-SiH_3} \\
\equiv \mathrm{Si}^0 + \mathrm{SiH_3(g)} \rightarrow \equiv \mathrm{Si-SiH_3}\,.
\end{gathered}
\tag{5.10}
$$

The second reaction listed above suggests a gas phase radical may directly chemisorb at an existing dangling bond site without first migrating around the hydrogenated surface. While these events are unlikely due to the relative infrequency of dangling bonds across the surface area of the *a*-Si:H film, they are not strictly forbidden and must be considered in the development of the microscopic model. It is important to note that chemisorption of H only results in a return of the surface to its original, hydrogenated state:

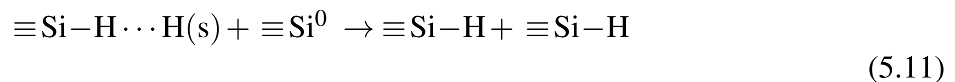
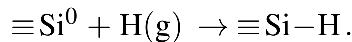

$$
\begin{gathered}
\equiv \mathrm{Si-H} \cdots \mathrm{H(s)} + \equiv \mathrm{Si}^0 \rightarrow \equiv \mathrm{Si-H} + \equiv \mathrm{Si-H} \\
\equiv \mathrm{Si}^0 + \mathrm{H(g)} \rightarrow \equiv \mathrm{Si-H}\,.
\end{gathered}
\tag{5.11}
$$

A simplified illustration of the surface chemistry can be seen in Fig. 5.5.

Lattice characterization and relative rates

In our early work on modeling PECVD systems [?], a solid-on-solid (SOS) lattice was used to represent the microscopic structure of the growing *a*-Si:H thin film. Although a two-dimensional SOS lattice remains the most efficient lattice structure from a computational standpoint, no vacancies or voids are permitted within the bulk material. Given that experimentally grown *a*-Si:H layers are observed to have void fractions in the range of 10-20%, our recent works have alternatively utilized a triangular framework [14, 15]. By eliminating the restriction of SOS behavior and introducing close-packed groups with a minimum of two nearest neighbors, overhangs may develop which in turn lead to voids in the triangular lattice (see Fig. 5.6). It is important to note that while the overall multiscale model operates in three dimensional space, the lattice which defines the microscopic domain remains two dimensional. Although the effort required to expand the lattice structure into a third coordinate is relatively minimal, the computational cost of doing so would be non-trivial. Given that the goal of the microscopic model (i.e., the lattice structure and associated kinetic Monte Carlo algorithm), is to capture the growth rate of amorphous silicon deposition, nothing would be gained from a three dimensional lattice; particle interactions, void formation and steric hindrance are accurately expressed in the proposed triangular lattice model.

Each grid location defined in Fig. 5.7 represents an independent microscopic simulation. Within these discrete grid cells exists a representative triangular lattice whose size can be characterized by the product of the length and thickness. The number of lateral sites is denoted by L and is proportional to the physical lattice length by $0.25 \times L$, given a hard-sphere silicon diameter of $\sim$0.25 nm. The thickness, τ, may be calculated from the number of monolayers, H, by the following equation:

$$\tau = 0.25 \cdot H \cdot \frac{\sqrt{3}}{2}, \tag{5.12}$$

where the factor 0.25 accounts for the diameter of individual silicon atoms and $\sqrt{3}/2$ accounts for the reduction in thickness due to the offset monolayers which result from the close-packed structure of the triangular lattice (refer to Fig. 5.6). The number of lateral sites remains fixed at $L = 1200$ for

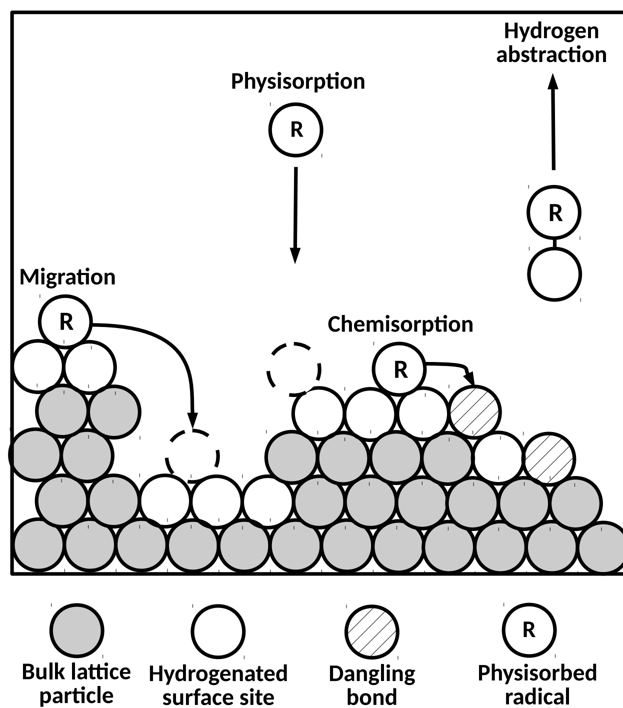

Figure 5.6: Triangular lattice representation showing four microscopic processes. Processes from left to right: migration, physisorption, chemisorption, and hydrogen abstraction.

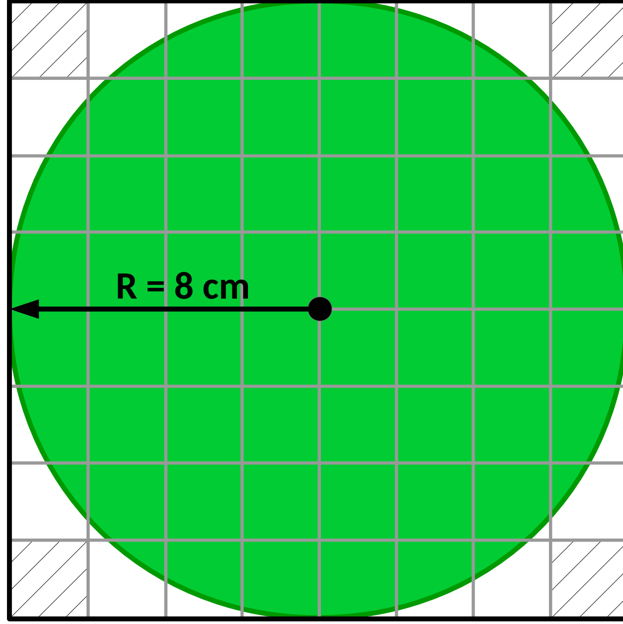

Figure 5.7: Spatial distribution of kinetic Monte Carlo simulations. One representative microscopic simulation (i.e., a 1200 particle wide lattice) is executed within each overlapping grid location. The hashed corners represent regions which do not overlap the substrate surface.

each discrete microscopic simulation zone. This length allows for adequate development of thin film morphology and reduces wall effects without being so large as to necessitate the inclusion of spatial variations across individual lattices. To be clear, while significant gradients exist in the species concentrations within the PECVD reactor and from one grid location to another (e.g., Figs. 5.4b and 5.7), finite microscopic simulations of length ∼300 nm can be assumed to experience uniform deposition.

Migration and hydrogen abstraction involve species which exist on the surface of the thin film; as a result, these reactions are thermally activated events and follow a standard Arrhenius-type formulation:

$$r_{t,i} = v_i e^{-E_i/k_B T}\,, \tag{5.13}$$

where v_i is the attempt frequency prefactor (s^{-1}) and E_i is the activation energy of radical i. Frequency prefactor and activation energy values are drawn from Bakos et al. [5, 6] to correspond to

the growth of *a*-Si:H films via the two species deposition of SiH_3 and H.

Physisorption events originate within the gas-phase and can be described by an athermal or barrierless reaction model based on the fundamental kinetic theory of gases which yields the following rate equation:

$$r_{a,i} = J_i s_c N_a \sigma \,, \tag{5.14}$$

where J is the flux of gas-phase radicals, s_c is the local sticking coefficient (i.e., the probability that a particle which strikes the surface will 'stick' rather than bouncing off), N_a is the Avogadro number, and σ is the average area per surface site. Eqs. (5.15)-(5.17) can be used to calculate the flux, J:

$$J_i = \eta_i \bar{u}_i \,, \tag{5.15}$$

$$\eta_i = \frac{p_i}{RT} \,, \tag{5.16}$$

$$\bar{u}_i = \sqrt{\frac{8k_B T}{\pi m_i}} \,, \tag{5.17}$$

where η_i is the number density of radical i (here the reactive gas-phase is assumed to be ideal), $\bar{u}_i$ is the mean radical velocity, p_i is the partial pressure of i, R the gas constant, T is the temperature, k_B is the Boltzmann constant, and m_i is the molecular weight of radical i. By substitution of the expression for J into Eq. (5.14), the overall reaction rate for an athermal radical i becomes:

$$r_{a,i} = \frac{p_i}{RT} \sqrt{\frac{8k_B T}{\pi m_i}} s_c N_a \sigma \,. \tag{5.18}$$

The relative magnitude of these reaction rates determines their frequency within the microscopic simulation, as will be discussed at length in the following subsection.

Kinetic Monte Carlo algorithm

The aforementioned lattice structure defines the scope and interaction of particles within the microscopic domain; however, the evolution of the lattice microstructure (i.e., growth of thin film

layers on the wafer substrate) is achieved using a hybrid n-fold kinetic Monte Carlo algorithm for which the overall reaction rate is defined by

$$r_{\text{total}} = r_a^{SiH_3} + r_a^H + r_t^{abs}, \tag{5.19}$$

where $r_a^{SiH_3}$ is the rate of physisorption of SiH_3, r_a^H is the rate of physisorption of H, and r_t^{abs} is the rate of hydrogen abstraction forming SiH_4 (note: the subscripts a and t denote athermal and thermally activated reactions, respectively). In the interest of computational efficiency, surface migration is decoupled and does not contribute to the overall rate. Specific details regarding the motivation for decoupling migration events and the associated procedure for doing so are provided at the end of this section.

Each kMC cycle begins through generating a uniform random number, $\gamma_1 \in [0,1]$. If $\gamma_1 \leq r_a^{SiH_3}/r_{\text{total}}$, then an SiH_3 physisorption event is executed. If $r_a^{SiH_3}/r_{\text{total}} < \gamma_1 \leq (r_a^{SiH_3} + r_a^H)/r_{\text{total}}$, then a hydrogen radical is physisorbed. Lastly, if $\gamma_1 > (r_a^H + r_t^{abs})/r_{\text{total}}$, then a surface hydrogen is abstracted via SiH_3.

Execution of physisorption events, regardless of radical type, proceed through selecting a random site on the surface of the triangular lattice from a list of candidate sites. Acceptable candidate sites consist of those which exist in their standard, hydrogenated state, or which contain a dangling bond left behind from a hydrogen abstraction event; sites which currently host a physisorbed radical cannot accept additional physisorption events. If the chosen site contains a dangling bond, the particle is instantaneously chemisorbed, and in the case of SiH_3 radicals the lattice to grows by one. Hydrogen abstraction occurs by selecting a random SiH_3 particle from the surface of the lattice and returning it to the gas-phase as the stable species, SiH_4. In other words, a migrating SiH_3 radical removes a hydrogen atom from the surface of the film leaving behind a dangling bond in its place. Although physisorbed hydrogen radicals may also abstract a hydrogen atom to reform the diatomic species, the high activation energy required causes these events to be infrequent at the deposition conditions of interest. A second random number, γ_2 is now sampled in order to calculate

the time required for the completed kMC event:

$$\delta t = \frac{-\ln(\gamma_2)}{r_{\text{total}}}, \tag{5.20}$$

where $\gamma_2 \in (0,1]$ is a uniform random number.

Up to this point, migration has been excluded from the discussion of kMC events. In looking at Fig. 5.8, it is clear that migration is the dominant interaction mechanism within the growing lattice structure. Brute force kMC methods (in which all event types are available for execution) require more than 99% of computational resources to be spent on migration alone (note: the results in Fig. 5.8 are typical for *a*-Si:H systems operating near T = 475 K and P = 1 Torr). Consequently, only a small fraction of simulation time contributes to events leading directly to film growth while the vast majority is spent on updating the locations of rapidly moving particles. In a continual effort to reduce the computational demands of the overall multiscale model, any savings that result from the microscopic domain are of great interest. To that end, a Markovian random-walk process has been introduced which successfully decouples particle migration from classic kMC algorithms.

Traditionally, a kMC cycle is defined by the execution of single event which moves forward the physical time of the system. The hybrid kinetic Monte Carlo scheme presented here requires two successive steps per cycle: first, a kMC event is executed according to the relative rates of $r_a^{SiH_3}$, r_a^H and r_t^{abs} as presented above; second, a propagator is introduced to capture the motion of physisorbed radicals. The total number of propagation steps is $N_H + N_{SiH_3}$ where

$$N_H = \frac{r_t^H}{r_a^H + r_t^{abs} + r_a^{SiH_3}}, \quad N_{SiH_3} = \frac{r_t^{SiH_3}}{r_a^H + r_t^{abs} + r_a^{SiH_3}}, \tag{5.21}$$

and r_t^H and $r_t^{SiH_3}$ are the thermally activated migration rates of hydrogen and silane radicals, respectively. In other words, the total number of random walk steps is in proportion to the magnitude of the migration rates, and each set of propagation steps, N_H and N_{SiH_3}, are split evenly among the current number of physisorbed radicals, n_H and n_{SiH_3}. The radicals then initiate a series of two-dimensional random walk processes according to the number of assigned propagation steps.

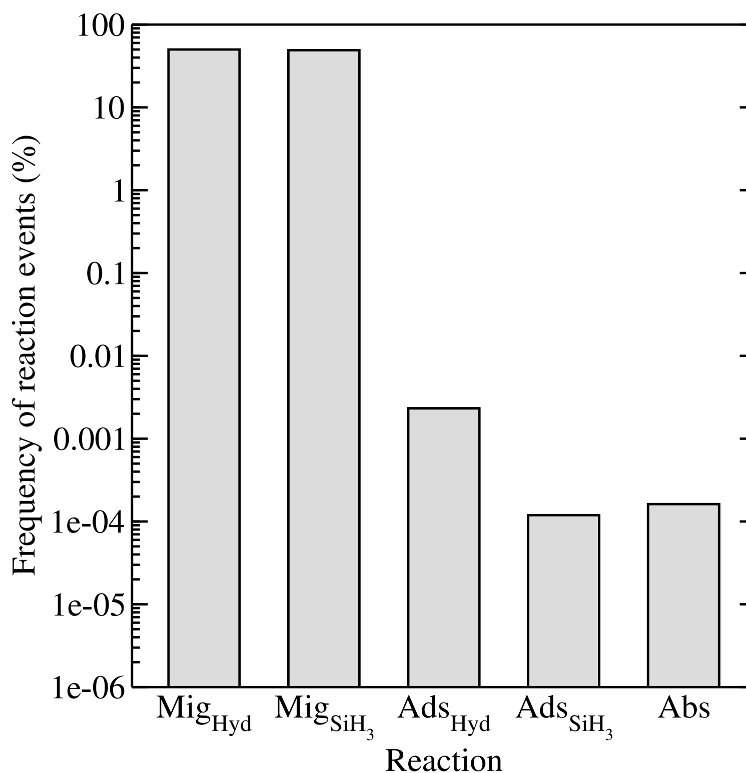

Figure 5.8: Normalized frequency of reaction events within the present kMC scheme at T = 475 K, P = 1 Torr, and a SiH_4^{in} mole fraction of 0.9.

Thus, the bulk motion of the propagator approximates the intricate movements of a given particle. In the interest of clarity, the procedure for the random walk process is as follows: a radical species is chosen, a random physisorbed radical of the given species is selected, the weighted random walk consisting of N_i/n_i propagation steps begins, propagation continues until either N_i/n_i steps have been executed or the movement terminates prematurely when a radical becomes chemisorbed at a dangling bond site, the final position of the propagator is then stored as the radical's new position and this cycle continues until all $n_H + n_{SiH_3}$ physisorbed species have migrated. The weighting of each propagation step is designed such that the probability for a particle to relax down the lattice is exponentially higher than 'jumping' up lattice positions (i.e., migration down the lattice is favored), and likewise, the probability of 'jumping' to nearby locations is higher than distant ones. The net result of this method is relaxation and particle tracking are only required to be updated once per particle rather than after each individual particle movement, as in brute force methods. The time

required for an individual migration step is calculated in much the same way as physisorption or hydrogen abstraction:

$$\delta t_H = \frac{-\ln(\gamma_i)}{r_t^H}, \quad \delta t_{SiH_3} = \frac{-\ln(\gamma_j)}{r_t^{SiH_3}}. \tag{5.22}$$

Thus, the total time elapsed for all migration events, Δt, is determined by summation over the number of propagation steps per radical type,

$$\Delta t = \sum_i^{N_H} \frac{-\ln(\gamma_i)}{r_t^H} + \sum_j^{N_{SiH_3}} \frac{-\ln(\gamma_j)}{r_t^{SiH_3}}. \tag{5.23}$$

In this manner, the elapsed time for the microscopic domain moves forward towards the completion of the time step set by the macroscopic, CFD solver.

Although our methodology of decoupling the diffusive processes from the remaining kinetic events represents significant computational savings, we must validate that doing so does not alter the overall morphology or characteristics of the resulting *a*-Si:H thin film. Validation of the Markovian random walk approximation is achieved via two mechanisms: (1) ensuring that surface morphologies and film porosities observed are appropriate for the chosen process parameters, and (2) that growth rates remain on par with experimental values. Detailed model validation can be found in the earlier works of Crose et al. [15]. It is important to note that film growth continues in this cyclic manner until the kMC algorithm has reached the alloted time step (i.e., until the microscopic model has caught up with the macroscopic, CFD solver). For a more in-depth discussion of the transient operation of the multiscale model, please refer to the following section.

5.2.4 Multiscale workflow

The methodology for connecting the the macro- and microscopic domains is of particular importance to the function of the multiscale model; consequently, the simulation workflow must be examined here. In Fig. 5.9, the top and bottom regions denote execution of macroscopic and microscopic events, respectively. At the start of each transient batch simulation, $t = 0$, every cell of the mesh will first solve the governing equations with respect to their reduced spatial coordinates

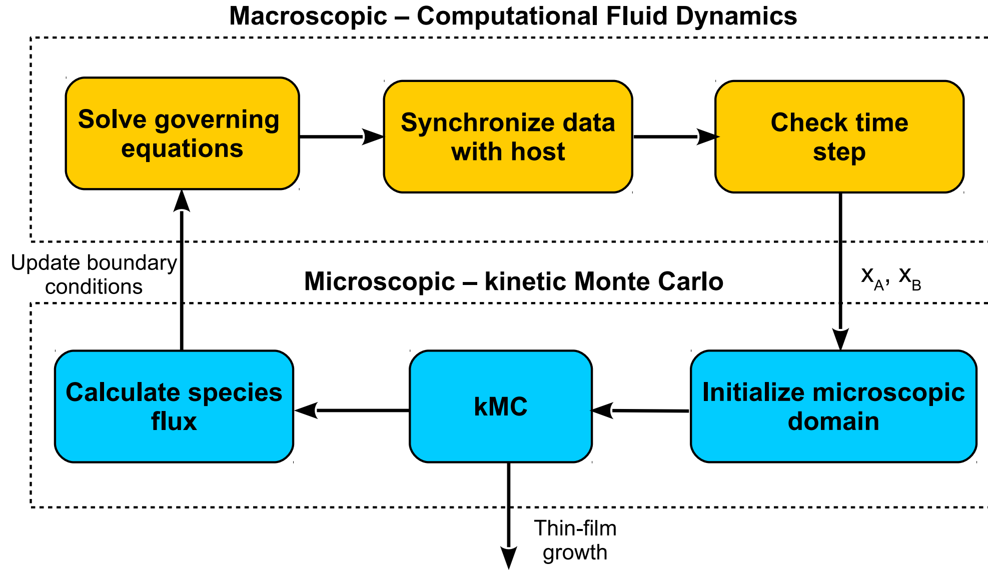

Figure 5.9: Multiscale simulation workflow detailing the coordination between the macroscopic and microscopic events.

using finite volume methods, then the boundaries along adjacent cells are resolved iteratively. In order to move forward in time, an Implicit Euler scheme is utilized (note: a detailed methodology is available in the Fluent user manual, [3]). Additionally, the first two UDFs (e.g., the volumetric reaction and electron density scripts) are executed and the results of which are fed into Fluent's PDEs. Once a time step has been completed, $t = t_1$, the species concentration, the temperature and the pressure along the boundary of the wafer substrate are transferred to the microscopic domain (e.g., Fig. 5.4a and and the right-hand side of Fig. 5.9). The discrete kMC simulations discussed in the previous section are then initialized using this information allowing for growth of *a*-Si:H thin film layers to begin. Once all of the microscopic simulations have reached t_1, the dynamic boundary conditions for cells bordering the wafer surface are updated based on the mass and energy transfer within the associated region (e.g., Figs. 5.4 and 5.9, left). Again, the macroscopic PDEs are solved such that the time moves forward to t_2 and the cycle continues. In this way, the multiscale model progresses until the end of the batch deposition process is reached (i.e., until $t = t_{batch}$).

Given that the kinetic Monte Carlo algorithm is unable to span the entire substrate surface in a single microscopic simulation (refer to Figs. 5.4b and 5.7), it is necessary to interpolate between known data points when updating the boundary conditions. Specifically, boundary cells which lie between kMC simulation locations are assigned mass and energy transfer values based on interpolation between the three nearest data points. In other words, every set of three nearest data points forms a triangular surface which provides boundary condition data for all mesh cells contained within that region. Further details concerning the execution of the discrete kMC simulations will be provided in the following section. As a final note, it is important to clarify the relative differences in the time constants for each domain. The gas-phase reactions reach equilibrium within the first few seconds of reactor operation. Conversely, while the individual surface interactions on the silicon thin film are rapid, growth of the thin film layer is continuous throughout the batch cycle. As a result, for the specific reactor geometry and reaction set used in this work it would be feasible to switch off calculations of the macroscopic domain after the initial transience dies out. This would improve the computational speed of the model in some cases at the cost of generality and with a loss in accuracy at the boundary between the two domains. More importantly, applicability of the model to other reactor designs, multiscale systems and deposition methods would be lost (e.g., atomic layer deposition studies).

5.2.5 Parallel computation

The move from 2D to 3D PECVD reactor models comes at the cost of computational efficiency. In the recent work of Crose et al. [15], the 2D axisymmetric CFD simulations required the use of a message passing interface (MPI) structure in order to parallelize the domain and to achieve feasible computation times (e.g., $<$1 day per batch simulation), as is common practice in systems with non-trivial computational requirements [31, 42]. In this work, the computational demands are further increased due to the mesh containing $\sim$1.5 million cells (as opposed to 120,000 for the 2D model), tetrahedral cell shape and far more discrete kMC simulations required to span the substrate surface. It is important to keep in mind that the results presented in the following

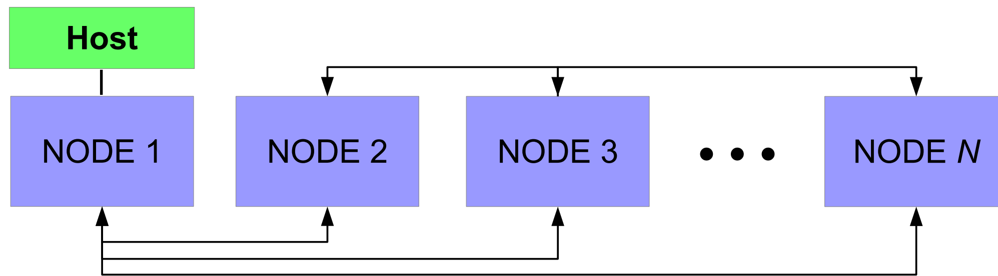

Figure 5.10: Communication between host and nodes within the MPI architecture.

sections represent not only the culmination of several test batches necessary to the development of the multiscale model, but also data that has been averaged across several redundant simulations; therefore, serial computation on a single processor or workstation corresponds to an infeasible task. As a result, the parallel computation strategy detailed here remains crucial to operation of transient simulations in order to mitigate the aforementioned computational demands.

In addition to the primary motivation of reducing simulation time, two other key benefits motivate the extra effort necessary in utilizing parallel programming. First, kMC simulations inherently exhibit noise due to the stochastic nature of event selection and particle movement. By maintaining constant deposition parameters and repeating simulations numerous times, we can reduce the noise level and obtain more accurate, averaged values. Second, it is often useful to perform many simulations at different conditions (e.g., when searching for suitable model parameters) without having to schedule several serial batch runs.

The details of the parallel algorithm itself, as well as the associated message-passing interface (MPI) structure, are standard and therefore will not be expanded upon at this time. In-depth studies of parallel processing with applications to microscopic simulations have been made by Nakano et al. and Cheimarios et al. [52, 10], and the recent work of Kwon et al. [42] provides the basis on which this work is built upon. That being said, a brief outline of parallel programming structure and its application to this work is useful in clarifying the simulation workflow and will be provided below.

The process for creating a parallel program can be understood through three elementary steps:

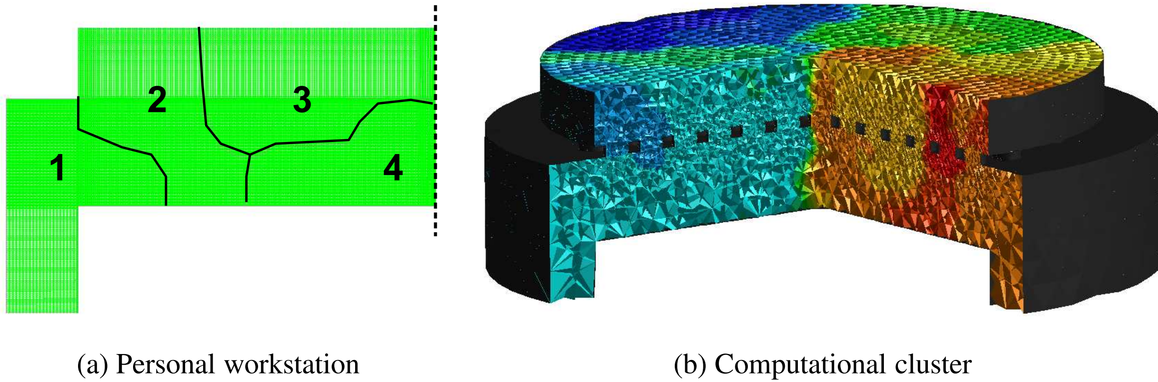

(a) Personal workstation (b) Computational cluster

Figure 5.11: (a) Distribution of 2D structured mesh across computational cores on a typical personal workstation with a quad-core CPU. (b) Unstructured mesh containing 1.5 million cells distributed across 128 computational cores (note: the colored regions denote different assignments).

(1) the original serial task is decomposed into small computational elements; (2) tasks are distributed across multiple processors; and (3) a host node orchestrates communication between processors at the completion of each time step. As shown in Fig. 5.10, nodes 2 through N pass information to node 1 which in turn forwards information to the host node. The number of available nodes is dependent on the architecture of the workstation or computational cluster used, and often a node on a computational cluster may contain multiple computing cores. In an effort to generalize the discussion, nodes and cores will be used interchangeably throughout this work, as would be the case on a cluster with one core per node. Fig. 5.11a provides an example for distributing the cells of a 2D mesh across 4 cores of a personal workstation; similarly, Fig. 5.11b shows the distribution of mesh elements across 64 cores as used in this work. The maximum achievable speedup given the aforementioned parallel programming strategy can be defined by:

$$M(N) = \frac{1}{(1+P)+\frac{P}{N}}, \tag{5.24}$$

where M is the maximum achievable speedup, P is the fraction of the program which is available for parallelization (i.e., the fraction of the original task which may be discretized), and N is the number of processors utilized [17].

In reality, the maximum speedup (i.e., execution speed multiplier) deviates from this formu-

lation for two reasons. First, as the number of cores increases, so does the overhead time for communication between cores and the host node. Second, only the serial computations defining the macroscopic (CFD) domain may be strictly decomposed into smaller tasks. As discussed, the PECVD reactor mesh can be distributed across the 64 cores utilized in this work; however, the microscopic kMC simulations are unable to be decomposed. Given the relatively small lattice size (1200 nm) as compared to the overall dimension of the reactor, decomposition of a single lattice would provide little benefit while introducing significant computational overhead necessary for resolving the shared lattice boundaries. Instead, we can exploit the fact that the kMC simulations across the substrate surface are independent of one another and may be distributed among the available nodes. In other words, while a single kMC simulation should not be decomposed, the many independent kMC simulations necessary for spanning the substrate surface can be distributed to speedup the overall multiscale simulation. The resulting speedup due to the combination of these methods can be seen in Fig. 5.12. The linear 1:1 speedup is never achievable due to the communication overhead but provides a benchmark for comparison. The continuous grey curve represents the theoretical speedup if the multiscale simulation was strictly decomposable. Finally, the actual multiplier curve exhibits a sharp jump between 59 and 60 cores. Given that the parallel simulations used in this work are synchronized (i.e., faster nodes must wait for slower nodes to complete a time step before execution continues), if even one node is forced to run two microscopic kMC simulations, the remaining $N-1$ nodes must sit idle. Since 60 kMC locations are used to span the substrate surface (see the microscopic modeling section), the number of nodes, N, is recommended to be greater than 60.

5.3 Results

The results presented in the following subsections represent the long-time behavior of the PECVD reactor at operating conditions of T = 475 K, P = 1 Torr and an inlet gas flow rate of 75 SCCM at a 10:1 ratio of hydrogen to silane. Although the simulations presented in this work are entirely

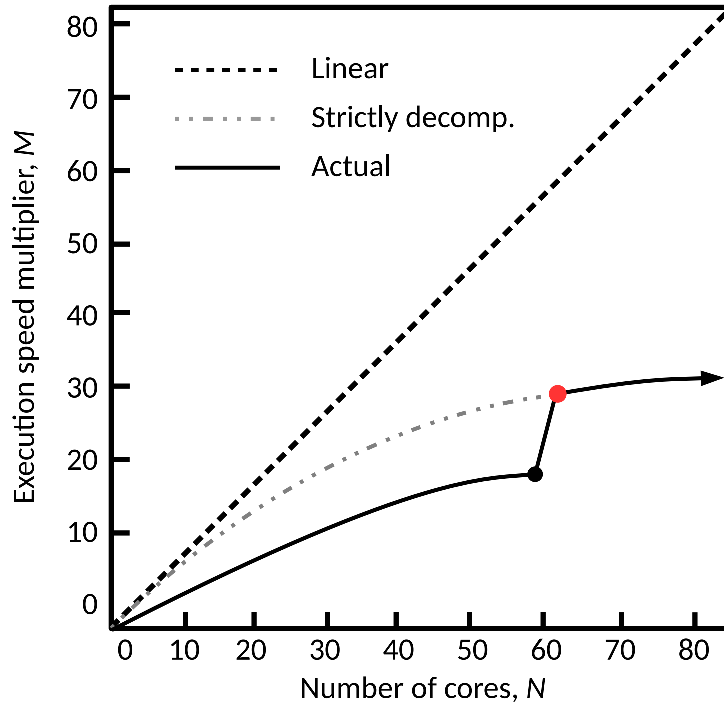

Figure 5.12: Expected speed-up due to parallelization across N nodes.

transient in nature, the startup period of the reactor is relatively brief and therefore will not be discussed at this time. Instead, the three dimensional contour maps shown below have been drawn from t = 320 seconds, roughly half way through the thin film growth period after the transient dynamics in the gas phase have largely died out. Note, the reactor never reaches a steady-state due to the continual particle interactions and growth within the microscopic domain. Given that the deposition of *a*-Si:H layers via PECVD is a batch process, the thickness measurements reported have been drawn at the completion of a batch, t_{batch} = 640 seconds, the time required to complete deposition of a 300 nm thick film. Additionally, thickness measurements have been averaged across 10 redundant batch simulations to minimize stochastic effects due to the kinetic Monte Carlo model.

5.3.1 Non-uniform deposition

Fig. 5.13a shows the resulting velocity profile of the gas phase species in the PECVD reactor after the brief startup period. According to the flow field, the gas phase reaches maximal velocity when flowing through the showerhead. Below the showerhead level, the flow velocity is increased near the narrow outlet regions, while at the center the gas flow stagnates in an apparent 'dead zone.' The velocity distribution suggests that a change of shape or frequency of showerhead holes might influence the flow profile and resulting species distribution. The relationship between flow field and distribution of deposition species is more evident through a direct comparison between Figs. 5.13a and 5.13b. Fig. 5.13b shows that the concentration of SiH_3, the deposition species responsible for thin film growth, reaches its maximum at the center of the reactor and diminishes in the radial direction. This is consistent with the flow velocity profile in Fig. 5.13a as species in regions with a lower flow rate will experience higher residence times (i.e., more time to react and produce silane radicals). This effect is magnified by the electron density profile which defines a maximum electron density, n_{eo} at the center of the cylindrical reaction chamber. In addition, variation in the concentration of SiH_3 along the azimuthal, θ, direction is observed. Fig. 5.14a shows that for a fixed radial position and height, the concentration of SiH_3 is non-uniform. A quantitative report of the azimuthal variation in x_{SiH_3} is given in Fig. 5.15, where the triangular data points represent the SiH_3 concentration profile which results from the original showerhead design (i.e., the showerhead design shown in Figs. 5.13 and 5.14a).

Due to the interconnection between the macroscopic reactor scale and microscopic thin film domain, it is expected that variations in the deposition species concentration, in particular variations near the substrate surface, will result in thin film products with non-uniform thickness. This effect has been well characterized and is known to cause device quality issues and poor solar conversion in the case of photo-voltaic cells [18, 14, 15]. As shown by the upward triangles in Fig. 5.15b, for the PECVD system described in this work, the multiscale model suggests that variations in the concentration of SiH_3 and H lead to a thickness offset of 25 nm from the desired set-point of 300 nm near the edge of the wafer substrate. Between $r = 0$ and 4 cm, the thickness offset is

relatively minor, within 5 nm of the set-point.

5.3.2 Adjusted reactor geometry

Compared with simplified 2D multiscale models, the 3D multiscale CFD model presented in this work is able to capture detailed showerhead geometries, and is therefore capable of evaluating alternative PECVD reactor designs. As mentioned in the motivations for this work, improvement to the thickness uniformity of amorphous silicon thin films is of significant interest from a manufacturing perspective. To this end, a modified showerhead design that reduces the spatial non-uniformity of deposition species is proposed here. The original showerhead geometry consists of circular holes with equal diameter, which are distributed in a rectangular array (e.g., Fig. 5.14a). In the new showerhead design, showerhead holes are arranged in a polar array, and the diameter of the showerhead holes increases in the radial direction from 0.5 to 1 cm, as shown in Fig. 5.14b.

Computational constraints limit the number of incremental design changes which may be evaluated. Consequently, the proposed showerhead design cannot be claimed to be optimal; instead, adjustments have been made based on the observed results in the previous section. Specifically, larger showerhead hole area near the edge of the reactor allows for more gas flow above the rim of the substrate, which helps diminish the radial variation of SiH_3 concentration. The overall showerhead hole area has been reduced causing the reactant gases to pass more quickly through the holes and over the substrate surface. Although this change is expected to lead to slower growth of the thin film product, the thickness uniformity should nonetheless improve. In addition, the polar array of showerhead holes is symmetrical with respect to any θ direction, and therefore is beneficial to the elimination of azimuthal non-uniformity. It is important to note that, the geometries discussed in this work represent typical dimensions used in industry and may be considered as a base case. The multiscale model developed here may be easily modified to fit specific PECVD reactor schematics provided by a given manufacturer.

The net effect of the adjusted showerhead geometry on spatial uniformity is reflected in Fig. 5.14b, where the concentration of SiH_3 in cells bordering the substrate surface show significantly

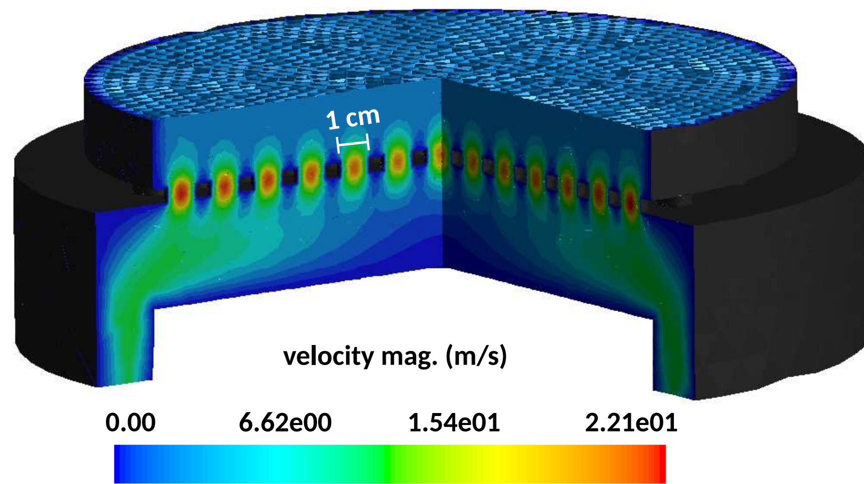

(a) Flow field

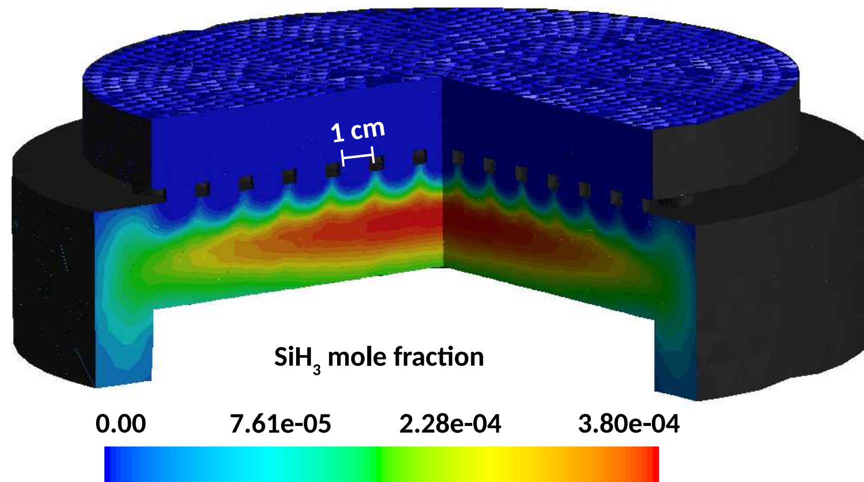

(b) SiH_3 mole fraction

Figure 5.13: (a) Velocity magnitude within 3D PECVD reactor showing dead-zone near substrate center. (b) Non-uniform, steady-state SiH_3 concentration.

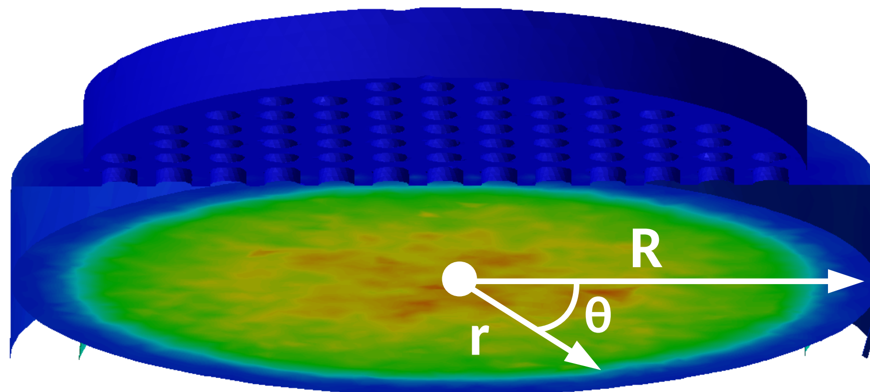

(a) Nominal PECVD geometry

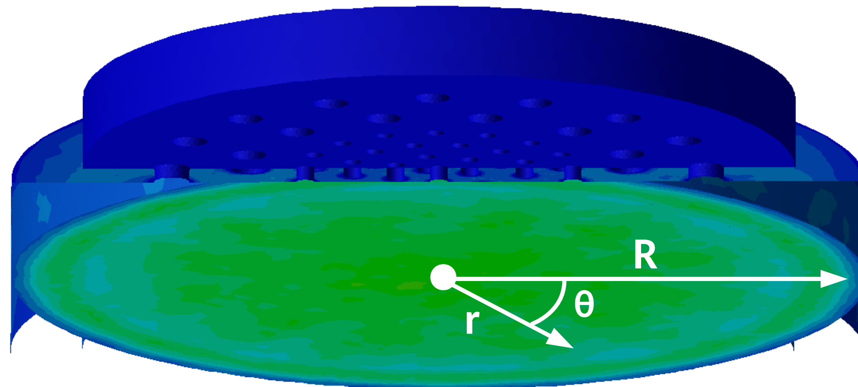

(b) Adjusted showerhead geometry

Figure 5.14: (a) Cross section of SiH_3 concentration taken just above the surface of the wafer substrate (b) SiH_3 concentration above the wafer surface for the adjusted reactor geometry.

improved uniformity. When compared to the cross section in Fig. 5.14a, the adjusted reactor design has virtually eliminated 'hot spots' or regions of high SiH_3 concentration. More specifically, in Fig. 5.15a the reduction in x_{SiH_3} variation for fixed radial positions is obvious (i.e., the black circles as compared to the red triangles). As discussed previously, uniformity of the thin film product thickness is of greater interest than species concentration alone. To that end, the circular and triangular data points in Fig. 5.15b demonstrate that the *a*-Si:H thickness offset has been reduced from $\sim$25 nm to less than 13 nm near the edge of the substrate at the completion of the batch deposition process. The regions beyond r = 8 cm in Fig. 5.15 denote the exit port of the PECVD reactor. As shown in Figs. 5.1 and 5.13, these regions lie beyond the wafer substrate and therefore no film thickness data exits and the slight increase in SiH_3 concentration cannot affect film growth.

5.4 Conclusions

An alternative PECVD reactor design has been evaluated using a three-dimensional multiscale CFD model which coordinates communication between the macroscopic reactor scale and the microscopic thin film growth domain. Application of this model to two representative PECVD reactor geometries has shown that thickness non-uniformity in the *a*-Si:H product can be minimized by adjusting the positions and size of the showerhead holes. As a result, the 3D CFD model presented holds promise for not only improving product quality in PECVD processing, but also for significant savings in time and resources otherwise spent on the testing and manufacture of physical reaction chambers.

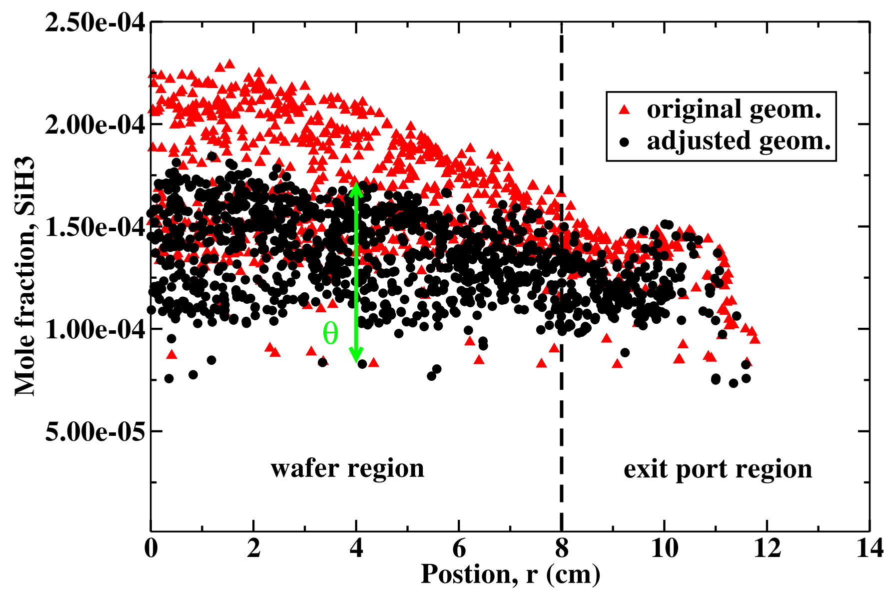

(a) Axial SiH_3 variance

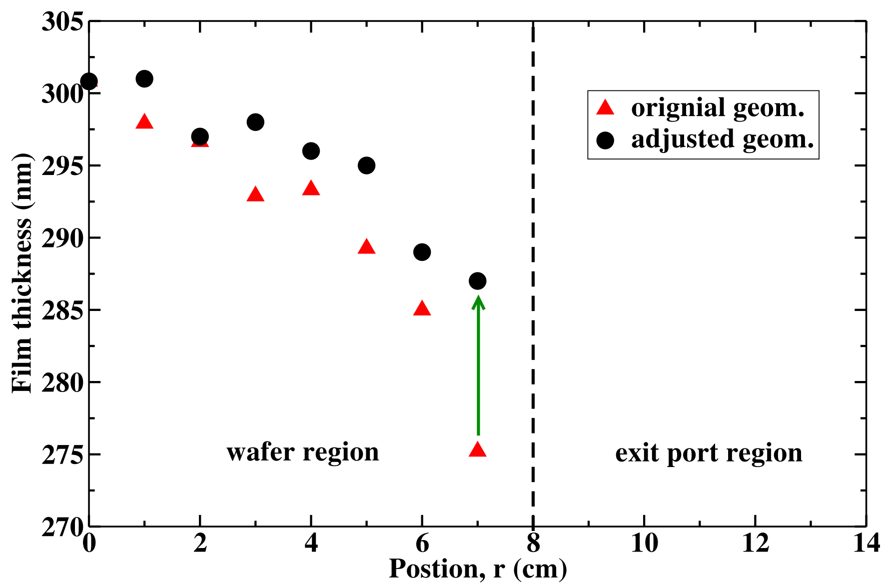

(b) Improved thickness uniformity

Figure 5.15: (a) SiH_3 mole fraction as a function of radial position, r, and azimuthal position, θ. (b) Radial *a*-Si:H product thickness for both the original and adjusted reactor geometries.

Chapter 6

Run-to-Run Control of PECVD Systems: Application to a Multiscale Three-Dimensional CFD Model of Thin Film Silicon Solar Cell Deposition

6.1 Introduction

Continual efforts are being made to increase the density of semiconductor products while maintaining high production quality. Due to the high cost associated with collecting experimental data and re-tooling production machinery (e.g., deposition chambers), the push for accurate modeling of chemical vapor deposition (CVD) is greater than ever [12, 18, 26]. Recently Crose et al. developed a three-dimensional multiscale model for plasma-enhanced chemical vapor deposition (PECVD), with specific focus on capturing the deposition of amorphous silicon thin films. The model proved successful in capturing both the macroscopic, reactor scale behavior, as well as the microscopic surface interactions associated with thin film growth. While Crose et al. further demonstrated that models of this type may be used in the design of improved reactor geometries (i.e., geometries that

reduce thickness non-uniformities in thin film products), there is room for further improvement. Specifically, in altering the PECVD reactor geometry the product thickness non-uniformity was reduced from 8% to less than 4%; however, demand in the semiconductor industry for microelectronic devices of high quality requires products with tighter uniformity still [19, 57, 58]. To that end, in this work we propose the addition of operational control within successive batch deposition cycles using an exponentially-weighted moving average (EWMA) algorithm. The goal of which is to drive the thickness of the amorphous silicon product to the desired set-point of 300 nm by adjusting the temperature of the wafer substrate between deposition cycles. The 3D multiscale CFD model is used to demonstrate the effectiveness of the algorithm in driving the product to within 1% of the set-point and maintaining it there for all batches thereafter.

The structure of this chapter is as follows: first, details concerning the development of each modeling domain are provided, including the dynamic boundary condition which connects the two simulation regimes. Next, a parallel programming approach is explored which is shown to reduce the computational time to within reasonable limits while maintaining a model with high fidelity to the physical system. Steady-state results then yield evidence of significant non-uniformity in the gas-phase species concentrations, as well as the resulting thickness of the *a*-Si:H product. Finally, the EWMA algorithm is defined and 10 transient batch simulations are conducted for each of two common PECVD geometries; manipulation of the substrate temperature shows success in driving the product to the 300 nm thickness set-point.

6.2 Three-dimensional modeling

In the recent publications of Crose et al. [15, 16], the usefulness of three dimensional reactor modeling in capturing the complex geometry of PECVD systems was demonstrated. The 3D geometry used was able to account for not only the showerhead layout which plays a key role in the distribution of process gas into the reactor, but also the spatial dependency of the wafer substrate. As such, the framework developed in Crose et al. [16] will provide the foundation for

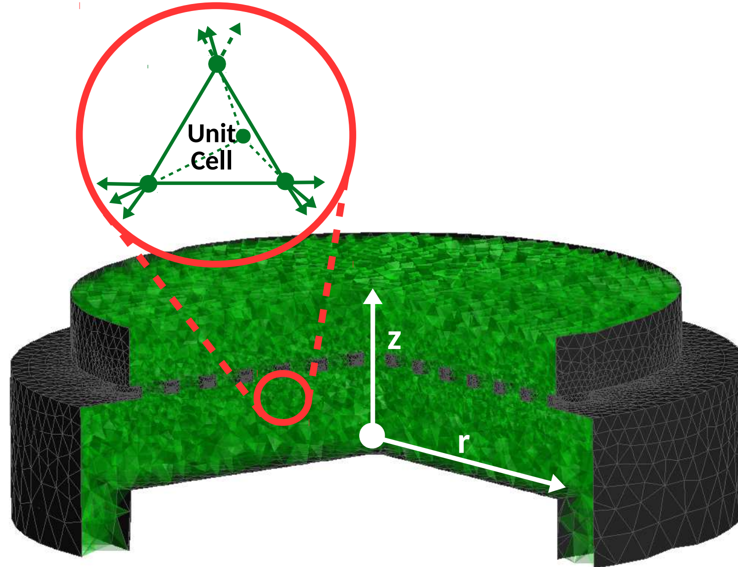

Figure 6.1: Collection of 1.5 million tetrahedral cells which define the unstructured, 3D mesh.

the study at hand. We again utilize a cylindrical PECVD reactor geometry with showerhead holes arranged in a rectangular array (see Figs. 6.2 and 6.3b). Although PECVD reactor designs vary widely between manufacturers, the spacing between the parallel plates, the diameter of the wafer substrate and the outlet port regions represent dimensions common to industry and can be thought of as a representative base case. The polar showerhead hole geometry explored in Crose et al. [16] is also applied in this study for comparison, further details of which can be found in the run-to-run control section below.

An unstructured mesh containing ∼1.5 million tetrahedral cells is used to discretize the PECVD reactor geometry to allow for numerical solutions to the partial differential equations necessary in capturing the gas phase mass, momentum and energy balances. While previous efforts in modeling PECVD systems have relied upon structured meshing (including Crose et al. [15]), the curvature of the cylindrical reactor shell and showerhead holes favor the use of unstructured mesh compositions. More specifically, the tetrahedral cells which define the mesh geometry are distributed with non-uniform cell density. As presented in Fig. 6.1, regions which are expected to experience significant gradients in temperature, flow velocity, species concentration, etc. (e.g., near walls and

highly curved surfaces) have been given higher cell density compared to the bulk fluid regions. Additionally, the boundary layers which form at the interfaces between the fluid and reactor surfaces must be considered; cell density is tuned such that the boundary layer is captured within one 'layer' of the mesh. Given the relatively low flow rate of process gas (75 SCCM) and low chamber pressure (P = 1 Torr), flow through even the narrow passages is expected to be laminar (note: preliminary results and past experiments suggest a maximum Reynold's number of Re = 2.28×10^{-1}). In order to obtain industrially relevant plasma distributions and thin film growth, accurate flow modeling of the process gas throughout the chamber is paramount.

It is important to note that while ANSYS software ([3]) is applied throughout this work, specifically to the creation of the geometric mesh and as a solver for the PDEs describing transport phenomena and chemical reactions, the software alone cannot yield the multiscale model of interest. Three predominant user defined functions (UDFs) have been developed to tailor the solver to the particular problem of non-uniform deposition of *a*-Si:H. Moreover, the connection between the UDFs, CFD domain and the parallel programming structure is of particular novelty to this work. The thirty-four dominant gas-phase reactions which define silane plasmas are accounted for via the volumetric reaction scheme discussed in the following section. A second UDF is necessary to calculate accurate electron densities throughout the cylindrical reactor space (i.e., to provide data to reactions 1-9 in Table 6.1). The third UDF facilitates the multiscale modeling on which this work is based; specifically, a microscopic simulation domain is defined which runs tandem to the transient CFD calculations. Due to the considerable complexity of this UDF, three subsections are dedicated to the discussion of the microscopic domain, 3.1 through 3.3.

6.2.1 Gas-phase model

While the ultimate goal of this work is to control the growth of amorphous silicon layers within PECVD systems, these results are tied intimately to the physio-chemical phenomena that govern the macroscopic gas phase. Traditional analytic solutions to the gas-phase model are viable only for simplified geometries (e.g., the earlier work of Crose et al. [**?**]) which often fail to provide the

resolution necessary for meaningful operation of industrially used systems. Thus, by implementing the mesh structure defined in the previous section, the governing equations may be solved with high fidelity using finite volume methods available through the ANSYS software. Again, extended functionality of the software is achieved using the aforementioned user defined functions on a cell-by-cell basis (note: Fig. 6.3a provides an example of a tetrahedral cell in which the flow field equations and UDFs reside).

Rigorous derivation of the continuity, momentum and energy equations will not be provided here due to the standard formulation used; nonetheless, a generalized vector form is given by the following system:

$$\frac{\partial}{\partial t}(\rho\vec{v}) + \nabla(\rho\vec{v}\vec{v}) = -\nabla p + \nabla\bar{\bar{\tau}} + \rho\vec{g} + \vec{F} \tag{6.1}$$

$$\bar{\bar{\tau}} = \mu[(\nabla\vec{v} + \nabla\vec{v}^T) - \frac{2}{3}\nabla\vec{v}I] \tag{6.2}$$

$$\frac{\partial}{\partial t}(\rho E) + \nabla(\vec{v}(\rho E + p)) = \nabla(k\nabla T - \Sigma h\vec{J} + (\bar{\bar{\tau}}\vec{v})) + S_h \tag{6.3}$$

$$\frac{\partial}{\partial t}(\rho Y_i) + \nabla\cdot(\rho\vec{v}Y_i) = -\nabla\cdot\vec{J}_i + R_i + S_i \tag{6.4}$$

$$\vec{J}_i = -\rho D_{i,m}\nabla Y_i - D_{T,i}\frac{\nabla T}{T} \tag{6.5}$$

where ρ is the density of the gas, $\vec{v}$ is the physical velocity vector, p is the static pressure, $\bar{\bar{\tau}}$ and I are the stress and unit tensors, J is the diffusive flux, Y_i is the mass fraction of species i, D_i is the diffusion coefficient of species i, and S_h, R_i and S_i are terms specific to the user defined functions and as such will be discussed below. Details concerning the formulation and implementation of the above PDEs may be found in the Fluent user manual [3].

The R_i term appearing in Eq. 6.4 is a product of the volumetric reaction set which defines the first UDF. As discussed previously, a set of plasma-phase reactions is used to tailor the functionality of the Fluent solver to the deposition of amorphous silicon. Although extensive reaction networks have been proposed in literature which detail all possible intermediate and aggregate species (e.g., [41]), here we limit the scope to the twelve most dominant species and their associated thirty-four

gas-phase reactions; refer to Table 6.1 for a complete listing of the reactions, mechanisms and rate constants. Thus, the R_i terms in the mass balance are updated by the first UDF during each time step of the transient solver.

Additionally, the right-hand side of Eqs. 6.3 and 6.4 contain source/sink terms for energy and mass, respectively. During the deposition of amorphous silicon, energy is exchanged through the formation and breaking of chemical bonds along the surface of the substrate (S_h has units of J s^{-1} m^{-2}). Likewise, growth of the thin film requires mass to be drawn from the gas phase in the form of SiH_3 and H radicals, while mass is similarly reintroduced to the macroscopic domain through the process of hydrogen abstraction (units of kg s^{-1} m^{-2}). Thus, S_h and S_i act as a dynamic boundary between the two simulation domains and their values are updated based on the results from each time step. This process is represented in Fig. 6.3a and discussed further in the multiscale workflow section.

6.2.2 Electron density profile

As mentioned previously, the second UDF required for this work specifies an electron density profile necessary for the generation of radical species. Reactions R^1 through R^9 in Table 6.1 involve the interaction of free elections and stable species (i.e., these nine reactions define the plasma). Park and Economou [55] have shown that for plasmas generated from radio frequency (RF) discharges within cylindrical geometries, the electron density can be accurately estimated from the product of a zero order Bessel Function and a sine function whose period is twice the distance between the showerhead and substrate:

$$n_e(r,z) = n_{eo} \cdot J_0(2.405\frac{r}{r_t}) \cdot sin(\frac{\pi z}{D}), \quad (6.6)$$

wehre n_{eo} is the maximum electron density, J_0 is the zero order Bessel function of the first kind, r_t is the radius of the reactor and D is the distance between the showerhead and the wafer (i.e., the parallel plate spacing). Implementation of the aforementioned profile to the mesh cells results

Table 6.1: Gas-phase reaction model. Note: Rate constants have units of cm^3/sec and have been adopted from the collection prepared by Kushner et al. [41].

Reaction	Mechanism	Rate constant
R^1	$e^- + H_2 \rightarrow 2H$	7.66×10^{12}
R^2	$e^- + SiH_4 \rightarrow SiH_3 + H$	9.57×10^{13}
R^3	$e^- + SiH_4 \rightarrow SiH_3^+ + H$	3.40×10^{12}
R^4	$e^- + SiH_4 \rightarrow SiH_2 + 2H$	1.13×10^{13}
R^5	$e^- + SiH_4 \rightarrow SiH + H_2 + H$	5.62×10^{12}
R^6	$e^- + SiH_4 \rightarrow Si + H_2 + 2H$	6.70×10^{12}
R^7	$e^- + Si_2H_6 \rightarrow SiH_3 + SiH_2 + H$	2.15×10^{13}
R^8	$e^- + Si_2H_6 \rightarrow H_3SiSiH + 2H$	7.41×10^{13}
R^9	$e^- + Si_3H_8 \rightarrow H_3SiSiH + SiH_4$	3.35×10^{14}
R^{10}	$H + SiH_2 \rightarrow SiH_3$	6.68×10^{11}
R^{11}	$H + SiH_2 \rightarrow SiH + H_2$	1.20×10^{13}
R^{12}	$H + SiH_3 \rightarrow SiH_2 + H_2$	1.20×10^{13}
R^{13}	$H + SiH_4 \rightarrow SiH_3 + H_2$	1.38×10^{12}
R^{14}	$H + H_2Si = SiH_2 \rightarrow Si_2H_5$	3.01×10^{12}
R^{15}	$H + Si_2H_6 \rightarrow SiH_4 + SiH_3$	4.03×10^{12}
R^{16}	$H + Si_2H_6 \rightarrow Si_2H_5 + H_2$	7.83×10^{12}
R^{17}	$H + Si_3H_8 \rightarrow Si_2H_5 + SiH_4$	1.19×10^{12}
R^{18}	$H_2 + SiH \rightarrow SiH_3$	1.20×10^{12}
R^{19}	$H_2 + SiH_2 \rightarrow SiH_4$	1.20×10^{11}
R^{20}	$SiH_2 + SiH_4 \rightarrow Si_2H_6$	6.02×10^{12}
R^{21}	$SiH_3 + SiH_3 \rightarrow SiH_4 + SiH_2$	4.22×10^{12}
R^{22}	$SiH_3 + SiH_3 \rightarrow Si_2H_6$	6.02×10^{12}
R^{23}	$SiH + SiH_4 \rightarrow Si_2H_5$	1.51×10^{12}
R^{24}	$SiH_2 + SiH_4 \rightarrow H_3SiSiH + H_2$	6.02×10^{12}
R^{25}	$SiH_2 + Si_2H_6 \rightarrow Si_3H_8$	7.23×10^{13}
R^{26}	$SiH_2 + SiH_3 \rightarrow Si_2H_5$	2.27×10^{11}
R^{27}	$SiH_3 + SiH_3 \rightarrow SiH_4 + SiH_2$	4.06×10^{13}
R^{28}	$SiH_3 + Si_2H_6 \rightarrow SiH_4 + Si_2H_5$	1.98×10^{13}
R^{29}	$Si_2H_5 + SiH_4 \rightarrow SiH_3 + Si_2H_6$	3.01×10^{11}
R^{30}	$SiH_3 + Si_2H_5 \rightarrow Si_3H_8$	9.03×10^{13}
R^{31}	$H_3SiSiH + SiH_4 \rightarrow Si_3H_8$	6.02×10^{12}
R^{32}	$Si_2H_5 + Si_2H_5 \rightarrow Si_3H_8 + SiH_2$	9.03×10^{13}
R^{33}	$H_3SiSiH \rightarrow H_2Si = SiH_2$	2.71×10^{13}
R^{34}	$H_2Si = SiH_2 \rightarrow H_3SiSiH$	2.29×10^{10}

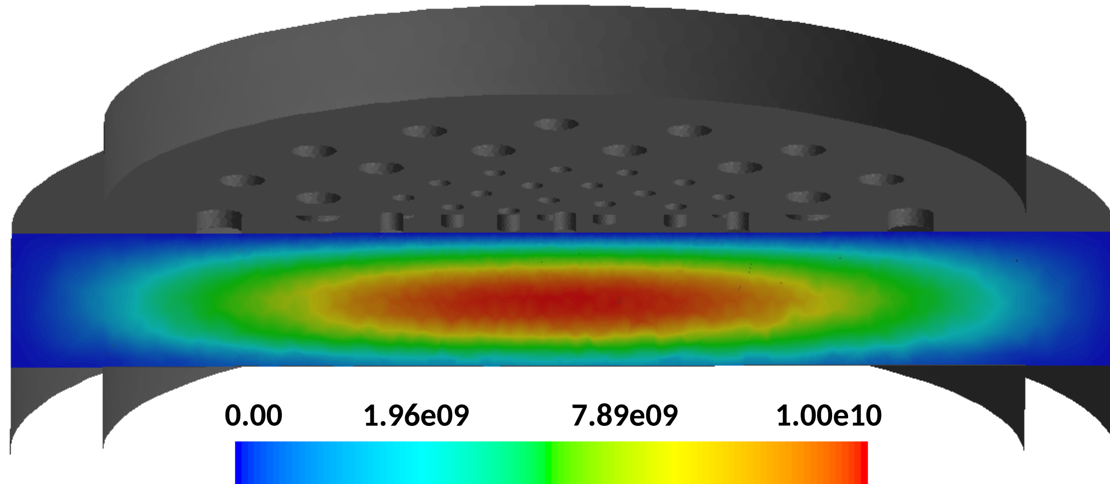

Figure 6.2: Electron density cross section within 3D axisymmetric PECVD geometry (cm^{-3}).

in the electron 'cloud' structure shown in Fig. 6.2. As expected, the Bessel function enforces a maximum density at $r = 0$ with the concentration gradually tapering off as r approaches the cylinder walls at 12 cm. The electron cloud is similarly bounded by the charged region between the parallel plates (i.e., the substrate plate at $z = 2$ cm and the showerhead at $z = 5$ cm).

6.3 Microscopic domain

Thus far the reactor domain has been well established: the CFD calculations and UDFs for the gas phase reactions and electron density define the macroscopic scale. Unclear at this point are the specific mechanisms which control the microscopic growth of amorphous silicon along the surface of the wafer substrate. The third and final UDF is of considerable complexity as it contains the whole of the microscopic domain; as such, the three subsections to follow detail the thin-film growth chemistry, triangular lattice structure and kinetic Monte Carlo algorithm which form the basis for microscopic simulation in this work.

Before moving into the model details, it is instructive to clarify the spatial connection between the two domains. Shown in Fig. 6.3a is an example of a tetrahedral cell which lies at the boundary of the wafer substrate. For cells in this region (i.e., the green region highlighted in Fig. 6.3b),

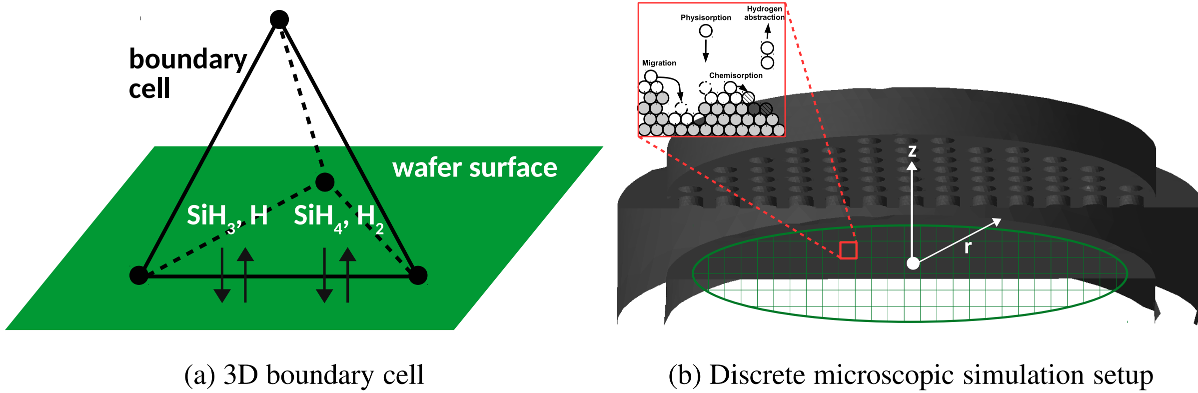

(a) 3D boundary cell

(b) Discrete microscopic simulation setup

Figure 6.3: (a) Finite element adjacent to the substrate surface with dynamic boundary condition calculated via microscopic simulation domain. (b) Kinetic Monte Carlo setup within overall multiscale simulation. Wafer substrate discretized in both the x and y directions forming a 'grid' structure.

information must be exchanged between the macroscopic, fluid calculations and the microscopic thin film growth. Specifically, each microscopic simulation relies on species concentration data which results from the volumetric reaction set. While tracking of every particle which crosses the shared boundary remains computationally infeasible, by defining discrete regions along the radial plane (e.g., Figs. 6.3b and 6.6) growth on the substrate as a whole can be accurately approximated. In other words, in each location shown in Fig. 6.6 a representative lattice is grown using a width 1200 particles and the overall wafer thickness is stitched together from this data at the end of each time step.

6.3.1 Thin-film growth chemistry

The following subsections describe at length the behavior of particles within the microscopic domain and the algorithms used to approximate those behaviors; however, it is important to first detail the chemical phenomena upon which these simulations are based. In this discussion, only SiH_3 and H appear as deposition species due to experimental results from Perrin et al. [56] and Robertson [61] which suggest that more than 98% of amorphous silicon deposition can be attributed to these species alone. A simplified chemical model is shown in Fig. 6.4 to compliment the reaction

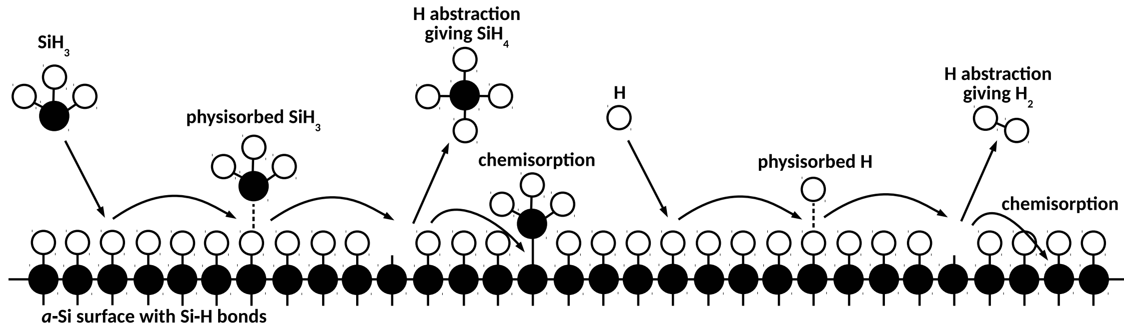

Figure 6.4: Chemical model illustration showing particle-surface interactions.

sets presented below.

Before growth of *a*-Si:H layers can occur, particles must first diffuse from the gas phase (i.e., the macroscopic domain) to the substrate surface. SiH_3 and H radicals which contact the surface may either be deflected back into the plasma or physisorption may occur at hydrogenated silicon sites ($\equiv \mathrm{Si}-\mathrm{H}$) as described by the following reaction set:

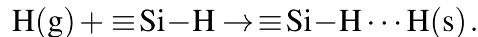

$$\begin{aligned} \mathrm{SiH_3(g)} + \equiv\mathrm{Si{-}H} &\rightarrow \equiv\mathrm{Si{-}H}\cdots\mathrm{SiH_3(s)} \\ \mathrm{H(g)} + \equiv\mathrm{Si{-}H} &\rightarrow \equiv\mathrm{Si{-}H}\cdots\mathrm{H(s)}\,. \end{aligned} \tag{6.7}$$

A sticking coefficient defines the probability that a contacting particle will remain on the surface and will be discussed further in the relative rates and kinetic Monte Carlo sections to follow. Radicals which successfully physisorb then have two mechanisms by which they may find stability; the first and mist dominant is rapid surface diffusion via migration:

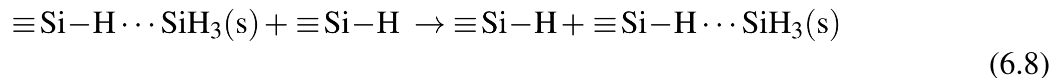
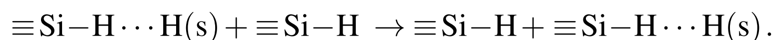

$$\begin{aligned} \equiv\mathrm{Si{-}H}\cdots\mathrm{SiH_3(s)} + \equiv\mathrm{Si{-}H} &\rightarrow \equiv\mathrm{Si{-}H} + \equiv\mathrm{Si{-}H}\cdots\mathrm{SiH_3(s)} \\ \equiv\mathrm{Si{-}H}\cdots\mathrm{H(s)} + \equiv\mathrm{Si{-}H} &\rightarrow \equiv\mathrm{Si{-}H} + \equiv\mathrm{Si{-}H}\cdots\mathrm{H(s)}\,. \end{aligned} \tag{6.8}$$

Alternatively, a surface radical may return to the macroscopic gas-phase through abstraction of a

neighboring hydrogen atom,

$$\equiv\text{Si}-\text{H}\cdots\text{SiH}_3(\text{s}) + \equiv\text{Si}-\text{H} \rightarrow \equiv\text{Si}-\text{H} + \equiv\text{Si}^0 + \text{SiH}_4(\text{g})\,. \tag{6.9}$$

In doing so, the stable species is reformed (e.g., SiH_4 or H_2 in the case of two species abstraction). The result of this process is the creation of dangling bonds ($\equiv Si^0$) which facilitate the growth of the amorphous silicon film. In turn, the mechanism by which physical growth occurs is known as chemisorption and can be defined by two distinct reactions:

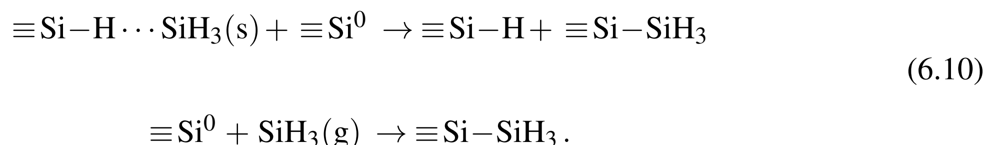

$$\begin{gathered} \equiv\text{Si}-\text{H}\cdots\text{SiH}_3(\text{s}) + \equiv\text{Si}^0 \rightarrow \equiv\text{Si}-\text{H} + \equiv\text{Si}-\text{SiH}_3 \\ \equiv\text{Si}^0 + \text{SiH}_3(\text{g}) \rightarrow \equiv\text{Si}-\text{SiH}_3\,. \end{gathered} \tag{6.10}$$

In both cases a covalent bond is formed between a preexisting dangling bond site and an SiH_3 radical. The second reaction denotes a gas-phase radical directly bonding without first sticking to the surface. While events of this type are exceedingly rare due to the relative infrequency of dangling bonds and obstructions on the substrate surface, they are not strictly forbidden and must be considered in the behavior of the microscopic model. As a final note regarding the surface chemistry, chemisorption may also occur between a dangling bond and a migrating hydrogen radical according to the following chemistry:

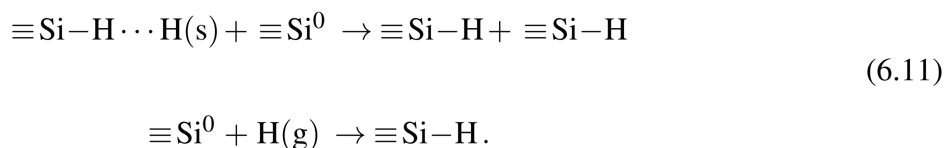

$$\begin{gathered} \equiv\text{Si}-\text{H}\cdots\text{H}(\text{s}) + \equiv\text{Si}^0 \rightarrow \equiv\text{Si}-\text{H} + \equiv\text{Si}-\text{H} \\ \equiv\text{Si}^0 + \text{H}(\text{g}) \rightarrow \equiv\text{Si}-\text{H}\,. \end{gathered} \tag{6.11}$$

However, the effect is simply to return the surface to a hydrogenated state (i.e., film growth is unaffected).

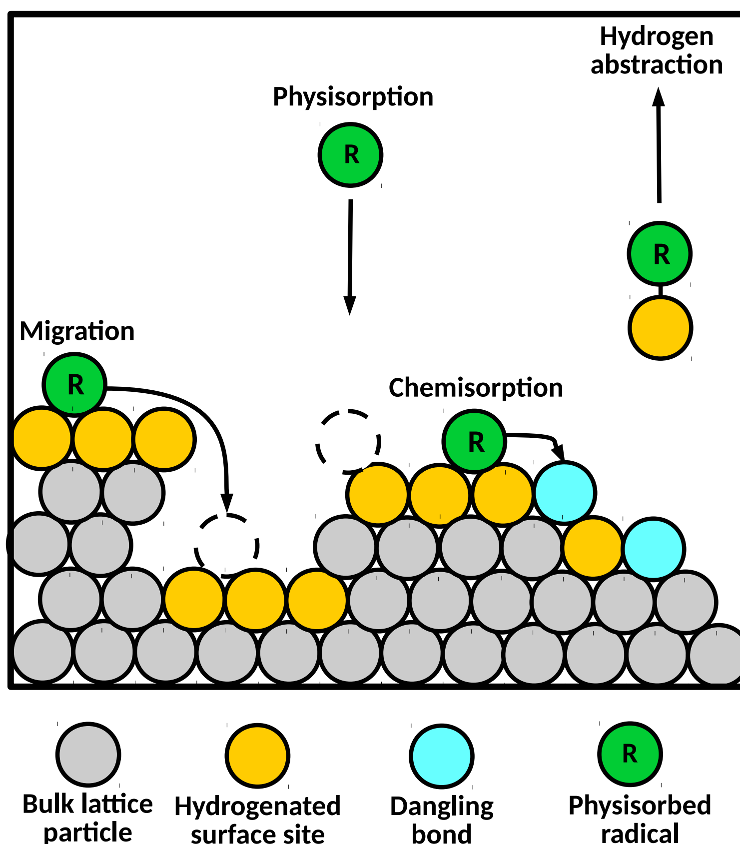

Figure 6.5: Triangular lattice representation showing four microscopic processes. Processes from left to right: migration, physisorption, chemisorption, and hydrogen abstraction.

6.3.2 Lattice characterization and relative rates

Typically, microscopic lattice models use either a solid-on-solid (SOS) or triangular arrangement of particles to define the structure of the growing thin film. The advantage of an SOS geometry (whereby each successive layer stacks directly on top of the previous layer in a rectangular grid) is computational efficiency and ease of implementation; however, no vacancies or voids are permitted within the bulk material. Given that experimentally grown *a*-Si:H layers are observed to have void fractions in the range of 10-20%, our recent works have chosen to use a triangular framework as shown in Fig. 6.5, whereby the particles of successive layers are seated between those of the previous layer. Introducing close-packed groups with a minimum of two nearest neighbors and eliminating the restrictions of SOS behavior allows for overhangs and voids to develop.

Each of the 60 grid locations defined in Fig. 6.6 represents a discrete microscopic simulation. Within individual grid cells exists a representative triangular lattice whose size can be characterized by the product of the length and thickness. L denotes the number of horizontal lattice sites and is proportional to the physical film length by $0.25 \times L$, given a hard sphere particle diameter of $\sim$0.25 nm. Thin film thickness, τ, can be calculated from the number of monolayers, H, for any location by:

$$\tau = 0.25 \cdot H \cdot \frac{\sqrt{3}}{2}, \tag{6.12}$$

where the factor 0.25 accounts for the particle diameter and $\sqrt{3}/2$ introduces a reduction in film thickness due to the offset triangular lattice layers. A length of $L = 1200$ is chosen for each microscopic simulation to allow ample room for film morphology to develop without being so large as to necessitate the inclusion of spatial variations in the species concentrations. To be clear, significant gradients exist in the concentration of SiH_3 and H across the wafer surface (see Figs. 6.12b and 6.13a); however, within each of the grid locations presented in Fig. 6.6 the finite microscopic simulations can be assumed to experience uniform deposition conditions.

It is important to note that while the overall multiscale model operates in three dimensional space, the individual microscopic simulations remain two dimensional, defined only by a horizontal and vertical dimension. Although the rules which govern the behavior of particles in two dimensional space may be applied to three dimensional movement with relatively minimal effort, the computational cost of doing so would be non-trivial. As proposed in this work, each of the 60 lattice locations requires roughly 1.3×10^6 particles per batch. Conversely, a similar triangular lattice model in three dimensions would need 1.6×10^9 particles to achieve the same growth. Given that the goal of the microscopic model is to capture the growth rate for amorphous silicon deposition, nothing stands to be gained from the inclusion of a third lattice dimension; particle interactions, void formation and steric hindrance are accurately expressed in the proposed triangular approximation.

With regard to the rates of particle movement within the microscopic domain, physisorption events originate within the gas-phase and can be described by an athermal reaction model drawn

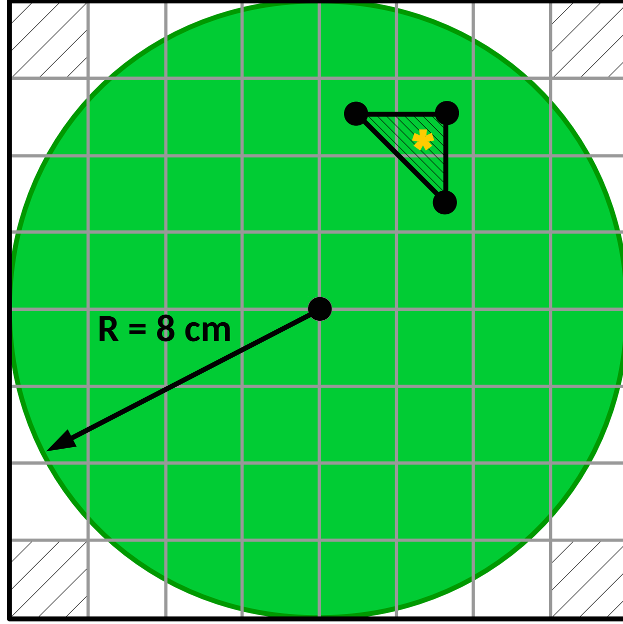

Figure 6.6: Spatial distribution of kinetic Monte Carlo simulations. One representative microscopic simulation (i.e., a 1200 particle wide lattice) is executed within each overlapping grid location. The hashed corners represent regions which do not overlap the substrate surface.

from the fundamental kinetic theory of gases:

$$r_{a,i} = J_i s_c N_a \sigma \,, \tag{6.13}$$

where J_i is the flux of gas-phase radical i, s_c is the local sticking coefficient (i.e., the probability that a particle which strikes the surface will 'stick' rather than bouncing off), N_a is the Avogadro number and σ is the average area per surface site. The flux for a given species (SiH_3 or H) at a specific wafer location can be calculated using Eqs. 6.14-6.16:

$$J_i = \eta_i \bar{u}_i \,, \tag{6.14}$$

$$\eta_i = \frac{p_i}{RT} \,, \tag{6.15}$$

$$\bar{u}_i = \sqrt{\frac{8k_B T}{\pi m_i}} \,, \tag{6.16}$$

where η_i is the number density of radical i (given a relatively low operating pressure of P = 1 Torr, the gas-phase in the microscopic domain is assumed to be ideal), $\bar{u}_i$ is the mean radical velocity, p_i is the partial pressure of i, R the gas constant, T is the temperature, k_B is the Boltzmann constant, and m_i is the molecular weight of radical i. Substitution of the expression for J_i into Eq. 6.13 yields the overall reaction rate for an athermal radical i:

$$r_{a,i} = \frac{p_i}{RT}\sqrt{\frac{8k_BT}{\pi m_i}} s_c N_a \sigma\,. \tag{6.17}$$

The second class of reactions, which dictate the behavior of particles on the surface of the growing thin film, are known as thermally activated events; migration of physisorbed SiH_3 and H species, as well as hydrogen abstraction which forms SiH_4, fall into this category. Thermally activated reactions follow a standard Arrhenius-type formulation:

$$r_{t,i} = v_i e^{-E_i/k_BT}\,, \tag{6.18}$$

where v_i is the attempt frequency prefactor (s^{-1}) and E_i is the activation energy for radial i. Values for the frequency prefactors and activation energies have been drawn from Bakos et al. [5, 6] to correspond specifically to the growth of amorphous silicon thin films via the two species deposition of SiH_3 and H. The relative magnitude of these five rates (physisorption of SiH_3 and H, abstraction, and migration of SiH_3 and H) determines their frequency within the microscopic simulation domain, as will be discussed in the following section.

6.3.3 Kinetic Monte Carlo algorithm

Monte Carlo algorithms specific to the growth of amorphous silicon thin films have been well documented in recent years through the publications of Crose et al. [**?**, 14]. This section provides an abbreviated discussion of these algorithms in order to clarify operation of the microscopic simulation domain and motivate the parallel programming architecture in the sections to follow.

While the triangular lattice defines the geometry and scope of each discrete microscopic simu-

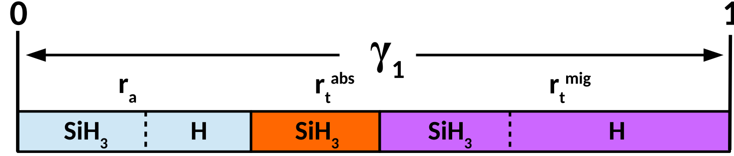

Figure 6.7: Visualization of randomized event choices.

lation, the rules governing the particle by particle growth of the film are laid out by a kinetic Monte Carlo (kMC) algorithm; the overall reaction rate for this algorithm is defined by the sum:

$$r_{\text{total}} = r_a + r_t^{abs} + r_t^{mig}, \tag{6.19}$$

where r_a is the total rate for athermal species reactions (i.e., physisorption), r_t^{abs} is the rate of abstraction and r_t^{mig} is the total rate for species migration. Each kMC cycle begins through choosing a uniform random number, $\gamma_1 \in [0,1]$. The magnitude of γ_1 compared to the normalized rate sum determines which event type to execute (refer to Fig. 6.7 for clarification). For example, if γ_1 were less than r_a, a physisorption event would be chosen; from within that subset, if γ_1 were greater than the physisorption rate for SiH_3, $r_a^{SiH_3}$, then physisorption of a hydrogen radical would occur. Likewise, for $r_a/r_{total} < \gamma_1 \leq (r_a + r_t^{abs})/r_{total}$ abstraction of hydrogen will occur. Finally, if $(r_a + r_t^{abs})/r_{total} < \gamma_1$ then migration is initiated along the surface of the film, with the species choice depending on where γ_1 fell within the r_t^{mig} range. In this manner, the five events which define the microscopic particle interactions may be rapidly sampled resulting in the growth of thin film layers. At the completion of each kMC event, a second random number, γ_2, is sampled in order to calculate the amount of time which has elapsed:

$$\delta t = \frac{-\ln(\gamma_2)}{r_{\text{total}}}, \tag{6.20}$$

where $\gamma_2 \in (0,1]$ is a uniform random number. A new value for γ_1 is then generated and kMC execution continues until the microscopic domain has caught up with the time step set by the CFD

solver. A step size of 0.25 seconds will typically require on the order of 10^{10} events for each region on the wafer substrate.

As a final note regarding the kMC algorithm, decoupling of surface migration has been explored as a means to speed up computation for single core, or small cluster size systems. Interested readers can find a detailed analysis of migration decoupling in the earlier works of Crose et al. [**?**, 14].

6.4 Multiscale workflow

The means by which the macro- and microscopic simulation domains are connected provides the foundation of this work and will be discussed in detail here. The two layers presented in Fig. 6.8 denote the successive execution of macroscopic and microscopic events which define a given time step. At the start of each batch simulation, $t = 0$, every cell of the mesh must first solve the governing equations with respect to their reduced spatial coordinates via finite volume methods, then the boundaries along adjacent cells are resolved iteratively. Forward integration in time is accomplished using an Implicit Euler scheme (note: the simulation methodology is detailed here only as it pertains to this work, detailed numerical methods may be found in the Fluent user manual, [3]). Additionally, the volumetric reaction and electron density UDFs discussed earlier are executed and the results of which are fed into Fluent's PDEs. Once a the end of a time step is reached, $t = t_1$, the upper layer of the simulation workflow completes and the temperature, pressure and species concentration along the boundary of the wafer substrate are transferred to the microscopic domain (e.g., Fig. 6.3a and the downward arrow in the right half of Fig. 6.8). This information is then used to initialize the the discrete kMC simulations discussed in the previous section allowing for the growth of *a*-Si:H thin film layers to begin. Time within the microscopic domain is advanced as described in Eq. 6.20 until all 60 wafer regions have reached t_1. The dynamic boundary condition which links the two domains is then updated for each cell bordering the wafer surface based on the exchange of mass and energy within the associated region (refer to Fig. 6.3). As before, the

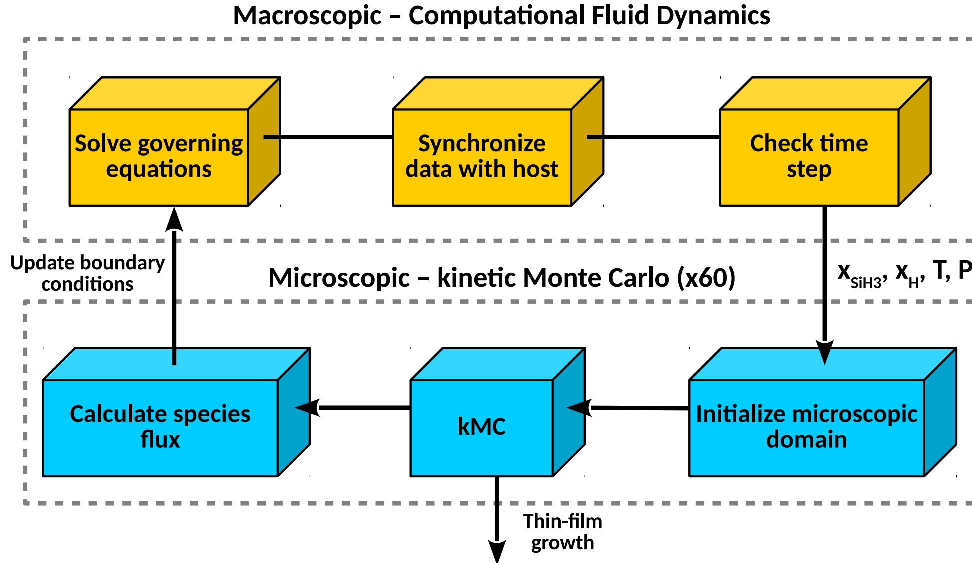

Figure 6.8: Multiscale simulation block diagram detailing the coordination between the macroscopic and microscopic events.

macroscopic PDEs are solved such that time progresses to t_2 and the cycle continues. In this way, the multiscale CFD simulation advances until the end of a batch deposition process, $t = t_{batch}$.

In the interest of transparency, two remarks concerning the interconnection of the micro- and macroscopic domains must be made: first, spatial distribution of kMC simulations has been discussed at length; however, this introduces a need to interpolate between known data points when updating the boundary conditions (i.e., the left-hand side of Fig. 6.8). Specifically, each set of three nearest data points forms a triangular surface which provides a means to interpolate boundary condition values for cells which lie between the predefined kMC locations. This methodology smooths the transition between nearby mesh cells and avoids sharp jumps between adjacent wafer regions shown in Fig. 6.6. As a secondary remark, due to the relatively brief startup time within the macroscopic domain, an obvious computational advantage could be exploited by switching off the CFD calculations after the initial transience dies out. In other words, while the batch growth of the microscopic thin films are inherently transient, it is feasible to operate the macroscopic model in a steady-state mode. This would improve the computational speed of the model in some cases at the cost of generality to other systems, not to mention a loss in accuracy at the boundary between

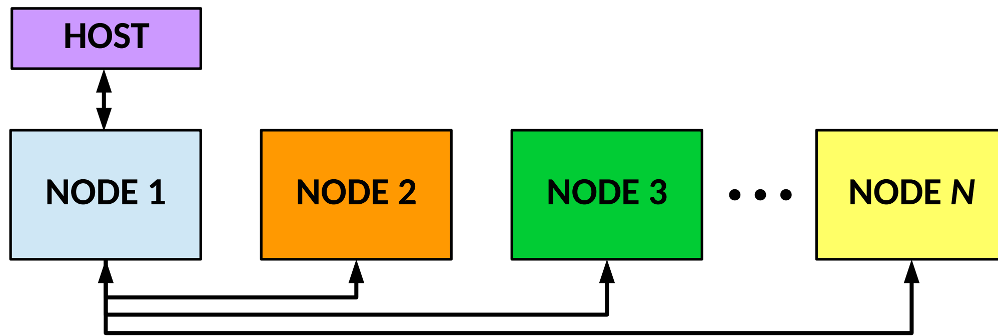

Figure 6.9: Communication between host and nodes within the MPI architecture. Node coloring corresponds to the mesh partitioning shown in Fig. 6.10.

the two domains. More importantly, applicability of the model to other reactor designs, flow rates and deposition methods would be lost (e.g., studies relating to atomic layer deposition).

6.5 Parallel computation

The use of 3D reactor models allows for detailed analysis and understanding of PECVD systems, but comes at the cost of computational efficiency. Recent publications from Crose et al. [15, 16] detail a significant jump in computational requirements in moving from 2D to 3D CFD models, with current 3D batch simulations requiring days to weeks of continuous processing. In this work, the computational demands are no less significant; not only does the macroscopic, CFD domain contain $\sim$1.5 million tetrahedral cells, but every batch requires 60 discrete kMC simulations in order to span the substrate surface. Additionally, the run-to-run operations described in the following sections require 10 consecutive batch deposition cycles per geometry, with redundant batches executed for each to improve accuracy. As a result, serial computation on a single processor or standalone workstation represents an infeasible task. To that end, a parallel computation strategy is detailed here based on the commonly used message passing interface (MPI) structure which has been well documented in literature [31, 42].

The process by which a parallel program is created can be easily understood through three elementary steps: (1) the original serial task, or tasks, are decomposed into small computational

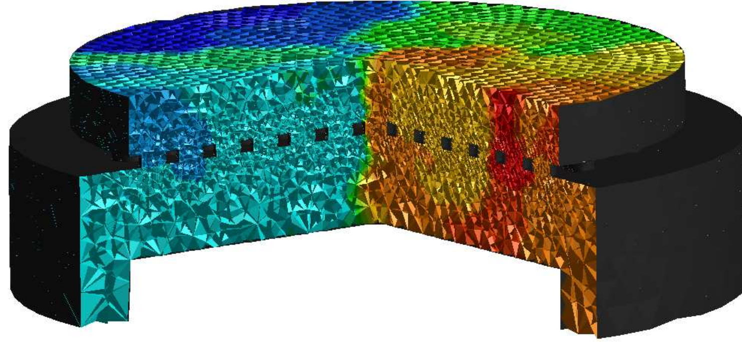

Figure 6.10: Unstructured mesh containing 1.5 million cells distributed across 128 computational cores (note: the colored regions denote different core assignments as reflected by Fig. 6.9).

elements; (2) tasks are distributed across multiple processors (nodes); and (3) a host node orchestrates communication between processors at the completion of each time step (note: for steady-state processes orchestration occurs between each iteration). A simplified illustration is shown in Fig. 6.9, where nodes 2 through N transmit information to node 1 which in turns forwards information to the host node. The number of available nodes is dependent on the architecture of the workstation or computational cluster used, and often nodes in modern systems contain multiple computing cores. In order to generalize the discussion and avoid dependence on a specific system architecture, nodes and cores will be used interchangeably throughout this section, representing a hypothetical cluster with one core per node. Fig. 6.10 provides an example of the macroscopic mesh structure distributed across 64 cores, as is the case in this work. Following the described parallel programming approach, the maximum theoretical speedup can be defined as:

$$M(N) = \frac{1}{(1+P)+\frac{P}{N}}, \tag{6.21}$$

where M is the maximum achievable speedup, P is the fraction of the simulation which is available for parallelization (i.e., the fraction of the program tasks which may be discretized), and N is the number of processors utilized [17].

In practice, the maximum expected speedup (otherwise known as the execution speed multi-

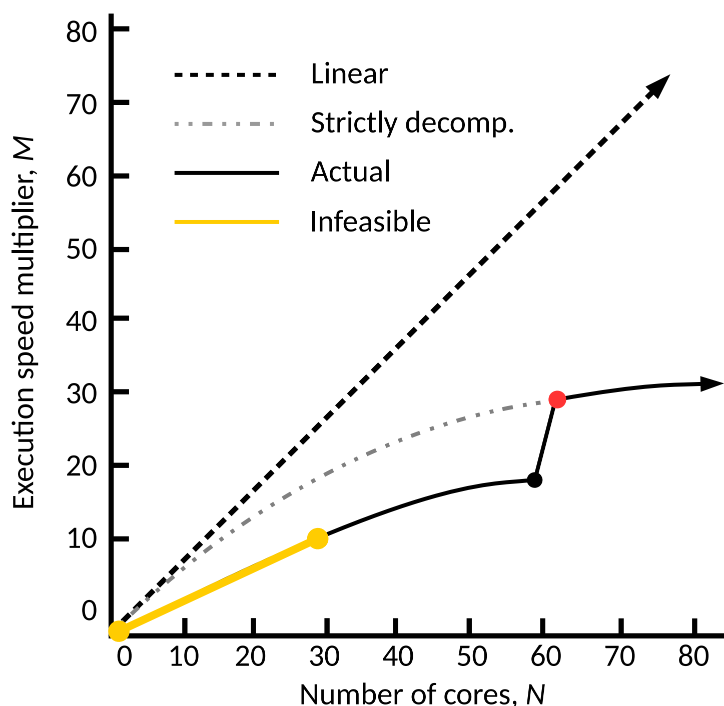

Figure 6.11: Expected speed-up due to parallelization across N nodes.

plier) deviates from this formulation for two key reasons: first, for any parallel architecture the overhead time required for communication between node and host scales with the number of nodes used. Second, only the serial computations which define the macroscopic (CFD) domain may be strictly decomposed into smaller tasks. In other words, the PECVD reactor mesh can be distributed amongst any number of computational cores within practical limits; however, the microscopic kMC simulations are unable to be further decomposed. As discussed previously, the wafer substrate requries 60 discrete kMC simulations in order to span the surface efficiently, but decomposing these 60 simulations further would require significant computational overhead in order to resolve the boundaries of the triangular lattice (refer to Fig. 6.5). The physical speedup which results from the combination of these factors can be seen in Fig. 6.11. Again, a linear 1:1 speedup is out of reach due to the communication overhead, but provides a useful benchmark for comparison. The dashed curve represents the the theoretical multiplier if the overall simulation was strictly decomposable. Lastly, the actual multiplier curve (i.e., the solid curve in Fig. 6.11)

exhibits a sharp jump between 59 and 60 cores. Synchronized parallelization is used in this work (i.e., faster nodes must wait for slower nodes to complete a task before execution continues) in order to enforce that all boundary conditions and required parameters are available to the host process. Hence, if even one node is required to run two kMC simulations, the remaining N-1 nodes must sit idle till completion. With 60 kMC locations used to span the substrate surface, the number of nodes is recommended to be greater than 60. The highlighted region between $N = 0$ and 30 is considered infeasible for this work as one or more nodes would be required to run three kMC simulations. No data was collected for this case due to excessively long computational times.

64 and 128 nodes were tested during the development and testing of the multiscale model presented here. Given negligible differences in computational time, 64 nodes were used in the collection of the following results, with each batch requiring roughly 20 hours to complete.

6.6 Open-loop results

While the simulations discussed in this work are transient in nature, the startup period of the PECVD reactor is relatively brief and therefore will not be discussed at this time. Instead, we present the long-time behavior of the reactor at standard operating conditions of $T = 475$ K, $P =$ 1 Torr and a precursor gas flow rate of 75 SCCM with a 10:1 ratio of hydrogen to silane. More specifically, the three-dimensional contour maps shown below have been drawn from $t = 320$ s, roughly half way through the batch deposition cycle. To be clear, the reactor never reaches a true steady-state due to the continually developing *a*-Si:H thin film layer; however, given a maximum film thickness of 300 nm and a chamber height of 3 cm, the change in film dimension is trivial compared to the macroscopic geometry and dynamics.

Reported thickness measurements have been drawn at the completion of batch simulations, $t_{batch} = 640$ s (i.e., the time required to deposit a 300 nm thick film at the nominal operating conditions). Additionally, each thickness data point represents an averaged value across 10 redundant batch simulations in an effort to minimize stochastic effects inherit in Monte Carlo models.

6.6.1 Non-uniform deposition

Drawn from the recent publication of Crose et al. [16], Fig. 6.12 highlights key challenges in the deposition of amorphous silicon films via PECVD. Notably, the effect of the showerhead holes in Fig. 6.12a on the flow characteristics within the reactor cannot be ignored. At the edges of the bottom plate, a relatively high flow rate is experienced compared to the significant dead zone surrounding the center of the reaction zone. For this geometry, which will be referred to as the nominal geometry in this work, the showerhead holes have uniform diameter and spacing across the showerhead region. Nonetheless, the concentration of the key deposition species, SiH_3, within the reaction zone shows significant spatial non-uniformity in both the azimuthal and radial directions (i.e., Fig. 6.12b).

Given that wafer substrates lie at the base of the reaction zone (e.g., the cross section shown in Fig. 6.13a), deposited thin films are expected to display non-uniform thickness across their radii. This phenomena was explored by Crose et al. [16] and it was concluded that the hot-spots and radial non-uniformity were due, in large part, to the design of the showerhead. Moreover, the thickness non-uniformity was quantified using transient batch simulations at the operation conditions listed above, revealing an 8% difference between the product thickness at the center of the wafer and the edge.

6.6.2 Adjusted reactor geometry

In an effort to improve product quality, an adjusted showerhead geometry was suggested by Crose et al. [16]. Specifically, the diameter of the showerhead holes near the center were halved and the spatial arrangement adjusted such that the holes were laid out in a polar array, as opposed to the rectangular array employed by the nominal geometry (compare Figs. 6.13a and 6.13b). In doing so the hot-spots were significantly reduced, as were variations along the θ direction, as evidenced by Fig. 6.14. The improvement in the spatial uniformity of x_{SiH_3} resulted in an a-Si:H product with only a 4% difference in thickness across its radius.

As mentioned in the motivations for this work, product quality in the microelectronics industry

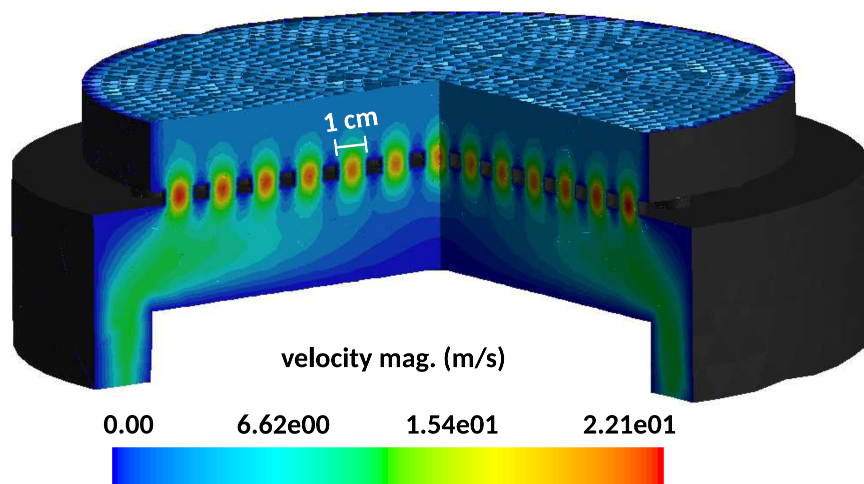

(a) Flow field

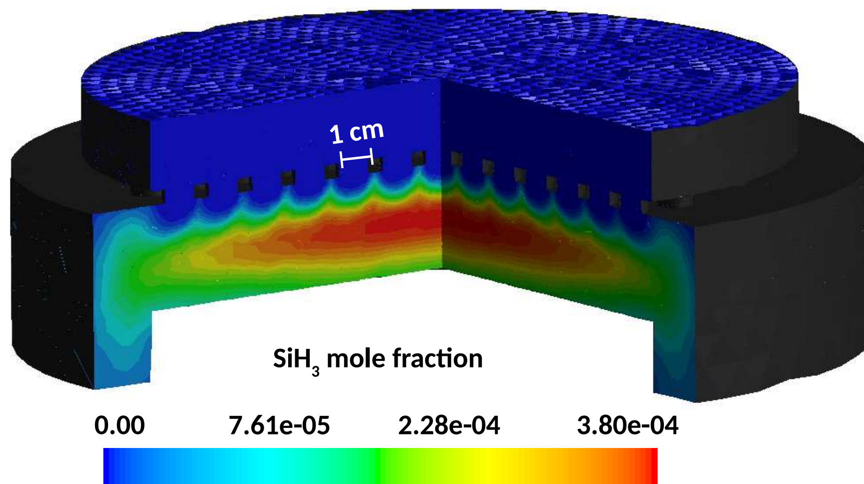

(b) SiH_3 mole fraction

Figure 6.12: (a) Velocity magnitude within 3D PECVD reactor showing dead-zone near substrate center. (b) Non-uniform, steady-state SiH_3 concentration [16].

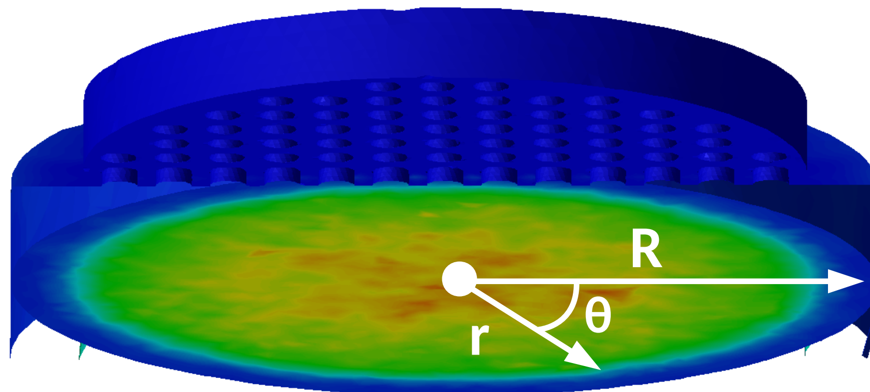

(a) Nominal PECVD geometry

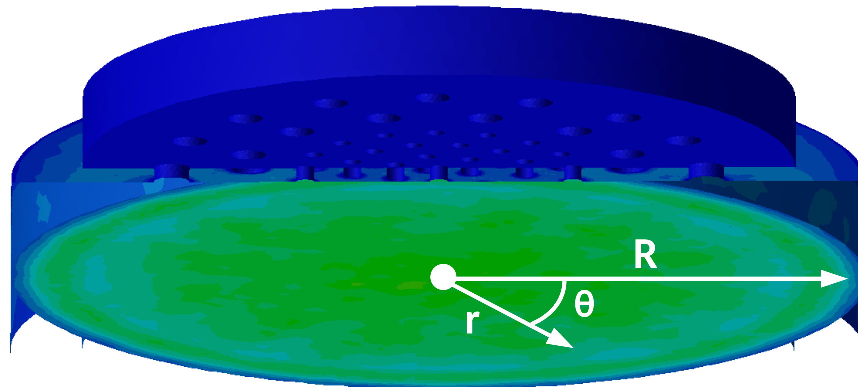

(b) Adjusted showerhead geometry

Figure 6.13: (a) Cross section of SiH_3 concentration taken just above the surface of the wafer substrate (b) SiH_3 concentration above the wafer surface for the adjusted reactor geometry [16].

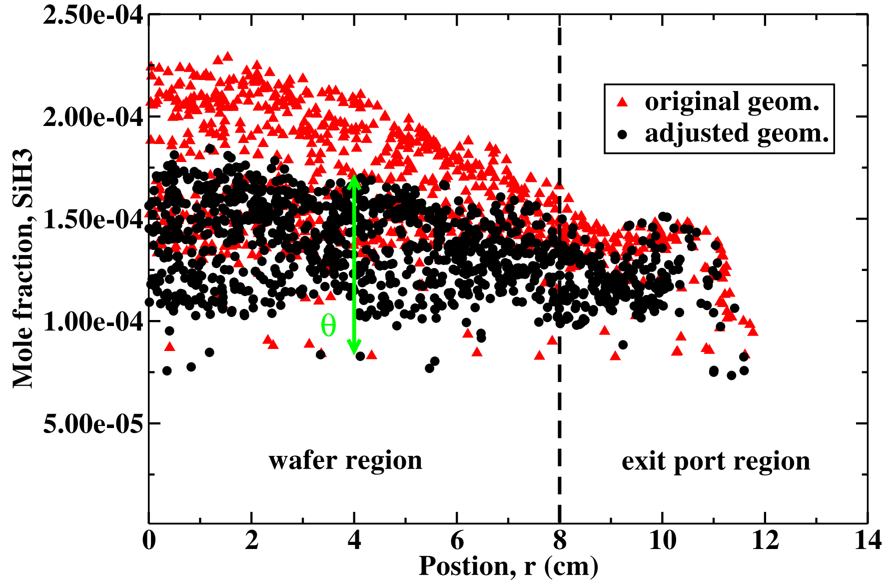

Figure 6.14: SiH_3 mole fraction as a function of radial position, r, and azimuthal position, θ.

is of the highest priority. While a reduction in thickness non-uniformity from 8% to 4% represents a non-trivial improvement to the a-Si:H product, in this work we aim to surpass that margin through the use of batch-to-batch control. The following sections provide details for the development and performance of the run-to-run control algorithm which is the key topic of this manuscript.

6.7 Run-to-run control

Given that the spatial distribution and concentration of the primary deposition species (e.g., SiH_3 and H) cannot be directly controlled, an alternative manipulated variable must be chosen in order to further improve on the remaining 4% offset from the thickness set-point of 300 nm. Fortunately, the growth rates of a-Si:H thin-film layers have recently been demonstrated to depend linearly on the temperature of the wafer substrate in the neighborhood of the nominal deposition condition of T = 475 K, for fixed species concentrations [14]. Hence, a run-to-run control strategy is applied in this work which requires only post-batch measurements of the product thickness as an input in order to update the wafer temperature for the successive batch.

Specifically, four concentric zones are defined along the surface of the wafer (see Fig. 6.15),

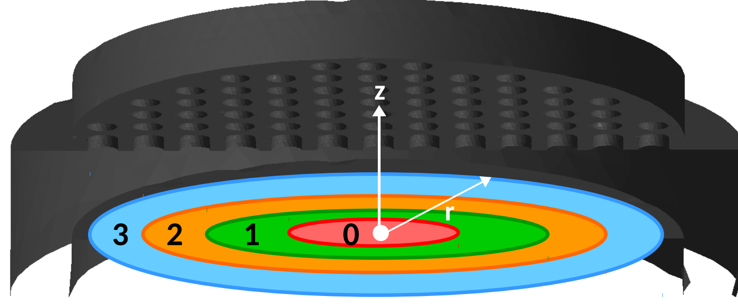

Figure 6.15: Four concentric wafer zones as defined by the EWMA algorithm.

and within each zone an exponentially-weighted moving average (EWMA) algorithm is applied in order to iteratively update the substrate temperature such that the *a*-Si:H thin film product may be driven to the desired thickness of 300 nm. It is important to note here that the choice to use four concentric zones is not arbitrary; while finer control would be made possible by the use of more zones (i.e., earlier publications have used eight wafer zones), practical restrictions on the design and manufacture of PECVD reactors limits this number.

The proposed EWMA algorithm is of the form:

$$\varepsilon_{k+1}^{i} = (1-\lambda)\varepsilon_{k}^{i} + \lambda(\tau_{s.p.} - \tau_{meas.}^{i}) \tag{6.22}$$

where ε_{k+1}^{i} is the parameter correction for the $k+1$ batch in zone i, $\tau_{s.p.}$ is the thickness set-point and $\tau_{meas.}^{i}$ is the thickness measurement for zone i. The term λ is known as a learning factor and can be thought of as the weight given to the currently measured error (i.e., $\tau_{s.p.} - \tau_{meas.}^{i}$) versus the historic, or recursively calculated, error ε_{k}^{i}.

Application of the generalized EWMA algorithm provided above requires a change of units; specifically, the error term, ε_{k+1}^{i}, has units of nanometers while the zone temperatures which must be updated have units of kelvin. Fortunately, due to the linear relationship between thin film growth rate and substrate temperature discussed previously, a growth rate function and thickness

approximation can be readily defined:

$$G(T^i) = \alpha^i T^i + \beta^i \tag{6.23}$$

$$\tau^i = G(T^i) \cdot t_{batch} \tag{6.24}$$

where $G(T^i)$ is the growth rate as a function of temperature in zone i and the parameters α^i and β^i are a product of the linearization of the growth rate around the nominal deposition temperature of T = 475 K. Given that the startup period of the reactor is relatively short lived (i.e., typically less than 5% of the deposition period, t_{batch}), the thickness for a given zone may be closely approximated by τ^i. Thus we can approximate the effect of the parameter correction, ε^i_{k+1}, as the difference between the thickness of the $k+1$ and k batches,

$$\varepsilon^i_{k+1} = \tau^i_{k+1} - \tau^i_k = \alpha^i T^i_{k+1} t_{batch} - \alpha^i T^i_k t_{batch} \tag{6.25}$$

Rearranging Eq. 6.25 yields our desired result for manipulating the substrate temperature:

$$T^i_{k+1} = T^i_k + \frac{\varepsilon^i_{k+1}}{\alpha^i \cdot t_{batch}} \tag{6.26}$$

where T^i_{k+1} is the updated substrate temperature in zone i for the $k+1$ batch and T^i_k is the substrate temperature applied to the previous batch.

As an important note, while Eqs. 6.23 and 6.25 are approximations, they do not affect the fidelity of the overall multiscale model to the physical PECVD system, only the speed of convergence to the set-point. In other words, higher order growth rate functions and more complex thickness relations may be used, but the only tangible benefit would be the speed at which the EWMA algorithm predicts correct wafer temperatures. As shown in the following section, specifically Fig. 6.16a, the simplified growth rate and thickness relations provided above quickly drive the system to the set-point and are thus sufficient for this work.

Given similarities to our previous work, the methodology for the simulation and collection of

growth rate data will not be provided here. Interested readers are encouraged to consult Crose et al. [14]. Nonetheless, the resulting linear growth relations necessary to the function of the EWMA algorithm are given below:

$$G(T^0) = 0.0350T^0 - 14.46\,(nm \cdot s^{-1}) \tag{6.27}$$

$$G(T^1) = 0.0352T^1 - 14.64\,(nm \cdot s^{-1}) \tag{6.28}$$

$$G(T^2) = 0.0322T^2 - 13.35\,(nm \cdot s^{-1}) \tag{6.29}$$

$$G(T^3) = 0.0287T^3 - 11.88\,(nm \cdot s^{-1}) \tag{6.30}$$

As a final note, the sensitivity of the system to changes in the learning factor, λ, has been shown to be low [14]; nonetheless, a higher value for λ will place more weight on the current thickness offset (i.e., $\tau_{s.p.} - \tau^i_{meas.}$) and is expected to drive the product to the set-point using fewer batches. The results presented in the following section were collected with λ = 0.75.

6.7.1 Batch-to-batch operation

Ten data sets are shown in Figs. 6.16a and 6.16b; each of which contains four data points which correspond to the concentric wafer zones. In the first data set (i.e., batch 1), all zones were maintained at the nominal deposition temperature, T = 475 K. The resulting thickness of the *a*-Si:H thin film demonstrates significant non-uniformity, most apparent in zones 2 and 3 which lie in the outer-half of the wafer substrate. This result is expected due to the loss in SiH_3 density between r = 4 and 8 cm as discussed in the open-loop results (see Figs. 6.13b and 6.14).

Readers should note that the thickness non-uniformity at the nominal operating conditions (i.e., the first batch sets shown in Figs. 6.16b and 6.18) is greater than that predicted in the recent publication of Crose et al. [16]. Despite using identical deposition conditions and multiscale models with great similarity, the thickness difference is expected for two key reasons: first, the number of zones has been reduced to four in this work due to the practical constraints discussed previously.

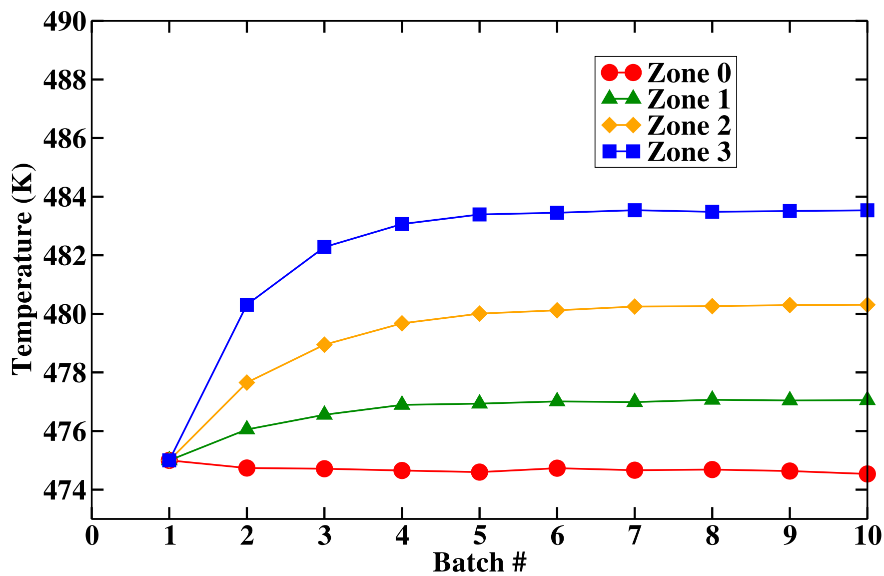

(a) EWMA influence on zone temperature

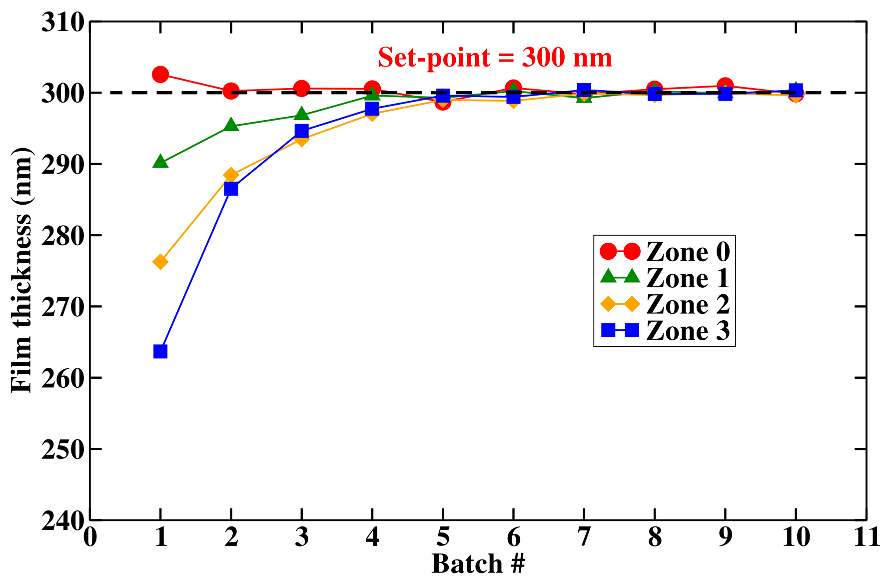

(b) R2R thickness result

Figure 6.16: (a) Control action resulting from EWMA algorithm. Temperatures shown correspond to PECVD reactor with polar showerhead geometry. (b) Batch-to-batch thin film thickness within polar PECVD geometry.

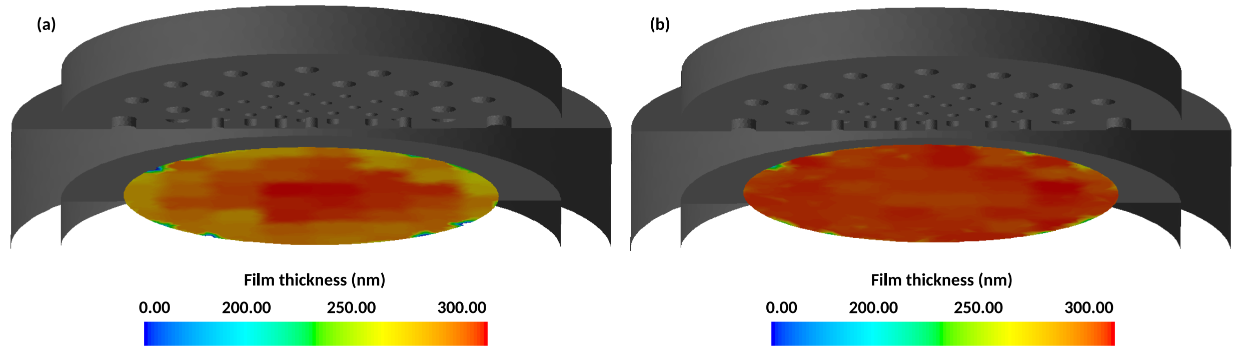

Figure 6.17: (a) Batch 1 film thickness. (b) Batch 10 film thickness.

Second, convergence of the model for each time step has been refined since last published. Specifically, the species residuals which define convergence for each cell of the mesh, in particular for the cells which lie along the wafer boundary, have been tightened from 10^{-4} to 10^{-6}. As such, the increased non-uniformity in batch 1 is more representative of physical PECVD systems and further motivates the simulation results which follow.

As the transient simulation progresses and additional batch deposition cycles complete, the EWMA algorithm begins to adjust the substrate temperature profile; see batches 2-10 in Fig. 6.16a. Zone 0 maintains a near constant 475 K as its position is in the center of the reactor and receives the highest concentration of SiH_3. Conversely, the temperature of zone 3 is set to nearly 484 K by the R2R controller (i.e., through the use of parameter correction via the EWMA algorithm) in an effort to drive the thin film product thickness to the set-point of 300 nm. The evolution of the thin film thickness in each concentric zone can be seen in Fig. 6.16. Initially zone 0 slightly overshoots the product target of 300 nm thickness, while zones 1-3 significantly undershoot. Nonetheless, by batch 5 all zones are within 1% of the product set-point and are maintained inside this margin for all batches thereafter.

While the data points discussed in Fig. 6.16b represent the average thickness within each control zone, in the interest of clarity it is worth discussing the thickness at specific spatial locations. To that end, Fig. 6.17 provides a comparison of the thin film thickness achieved in batches 1 and 10, respectively. The vast majority of the defined wafer regions (refer to Fig. 6.6) in batch 10

lie within 1% of the thickness set-point; unfortunately, along the edge of the wafer substrate there exist locations with relatively little change in thickness between batches 1 and 10. In industry these segments are typically known as edge die or edge chips and are often discarded.

It is important to note here that while the results presented thus far correspond to the PECVD reactor with improved geometry (i.e., the polar showerhead arrangement determined by Crose et al. [16]), the run-to-run control scheme described in this work may be equally applied to less-optimized reactor geometries. Specifically, the rectangular showerhead arrangement described previously is applied here and the resulting film thickness profiles are shown in Fig. 6.18. Significant thickness non-uniformity can be seen in batch 1 with offset in zone 3 greater than 16% from the 300 nm set-point. The EWMA algorithm is able to recognize the offset and drive zones 1-3 to the set-point within 6 batches of operation, only requiring one additional batch to reach the set-point compared to the optimized reactor geometry.

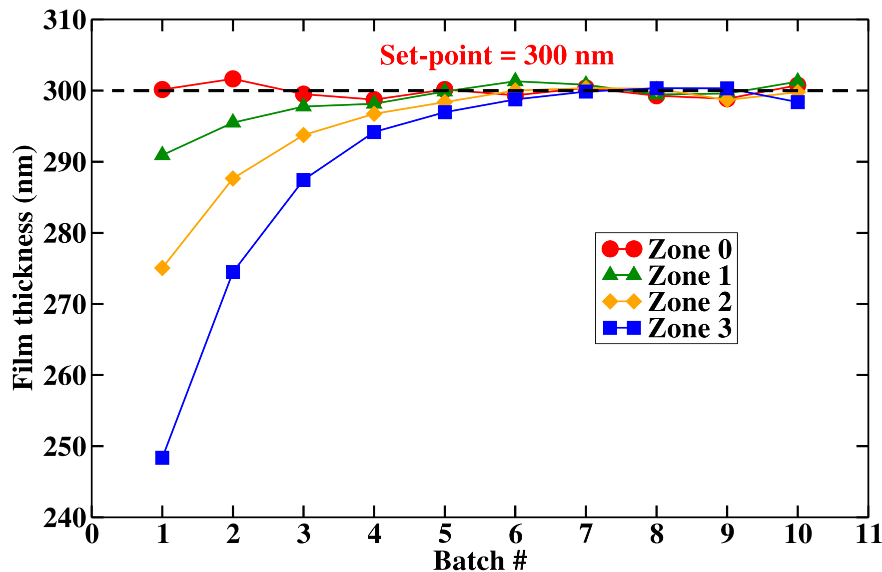

Figure 6.18: Batch-to-batch thin film thickness within nominal (i.e., rectangular) PECVD showerhead geometry.

6.8 Conclusions

Recent improvements in reactor design have shown promise for reducing thin film thickness non-uniformity. Nevertheless, demand in the microelectronics industry for products of increasing quality necessitates novel means of deposition control. A run-to-run control algorithm, which utilizes temperature correction via an exponentially-weighted moving average formulation, has been applied to 10 consecutive batch deposition cycles within a computational fluid dynamics framework. The transient, multiscale simulation which defines each batch suggests the *a*-Si:H product can be driven to the 300 nm thickness set-point within five batches of operation. Additionally, the run-to-run controller has been shown to be efficient for poorly-optimized PECVD geometries, reaching the set-point in six batches and maintaining the product within 1% of the set-point for all batches thereafter.

Chapter 7

Conclusions

This dissertation provides a number of distinct modeling techniques for accurately capturing the deposition of amorphous silicon thin films via PECVD. Moreover, operational strategies and novel reactor designs are presented which allow for significant improvement to the thickness uniformity of *a*-Si:H across large wafer surfaces. From a computational standpoint, the parallel programming structure defined in this work has been shown to be efficient for complex computational fluid dynamics geometries and distributed kinetic Monte Carlo simulations.

In Chapter 2, the gas-phase transport and reaction phenomena within an industrially-relevant PECVD reactor were captured using a first principles approach. At the microscopic scale, the rapid particle interactions that define the growth of *a*-Si:H thin film layers were tracked using a hybrid kinetic Monte Carlo algorithm. The resulting multiscale model was demonstrated to reproduce accurate *a*-Si:H growth rates and film morphologies. Thin film thickness was modulated in four concentric wafer zones through the application of an open-loop growth rate function, reducing the thickness non-uniformity from $\sim$15% to less than 1%. Additionally, the grating pattern along the surface was shown to be unaffected yielding a solar cell product with improved light capture efficiency.

In Chapter 3, the multiscale model developed in Chapter 2 was refined and a run-to-run based control strategy was introduced in order to reduce batch-to-batch variations caused by fouling on

the interior surfaces of PECVD systems. An exponentially-weighted moving average (EWMA) algorithm allowed for post batch measurements of thin film thickness to be used in updating the substrate temperature in four radial locations. In the presence of spatial variations in the concentration of SiH_3 and H, and drift caused by reactor conditioning, the run-to-run control algorithm was demonstrated to drive the thin film product to within a 1% margin of the 300 nm thickness set-point.

In Chapter 4, a computational fluid dynamics (CFD) model for PECVD systems was developed to improve upon the accuracy of the first principles model presented in Chapters 2 and 3. At the macroscopic domain, a two-dimensional axisymmetric geometry was employed to capture the key features of cylindrical, parallel-plate reactors. Within the microscopic scale, hybrid kinetic Monte Carlo simulations akin to those developed in previous chapters were distributed across the surface of the wafer substrate. Results from the multiscale model provided key insight into the operation of PECVD systems; in particular, non-uniform thin film thickness was linked to spatial variations in SiH_3 and H in the boundary layer which develops above the wafer.

In Chapter 5, the 2D CFD model was expanded to a third spatial dimension in order to explore the effect of altering the showerhead hole spacing within the reactor. A polar showerhead arrangement was shown to reduce thin film thickness non-uniformity by 4% for identical deposition conditions. This result represents a novel means for designing PECVD systems with significant cost savings compared to traditional methods of retooling production machinery. Additionally, a message passing interface (MPI) structure was adopted which allowed for distributed computation of both the macroscopic reactor mesh and microscopic kMC simulations.

In Chapter 6, a run-to-run control strategy was developed based upon the foundation provided by Chapter 3. The controller was then applied to 10 serial batch deposition cycles using the 3D multiscale CFD model defined in the previous chapter. Results from the batch-to-batch operation suggested that the *a*-Si:H thin film product may be driven to the thickness set-point of 300 nm within 6 batches of operation, even for poorly-optimized PECVD geometries. Given a reactor mesh with 1.5 million tetrahedral cell elements and 60 kMC simulations required to span the

substrate surface, the computational costs for this chapter were non-trivial compared to Chapters 2–5. Parallel programming using 64 cores of the Hoffman2 cluster was discussed at length as a means to overcome the computational challenges and to maintain practical simulation times.

In summary, thickness uniformity remains a challenge in the manufacture of amorphous silicon thin films via PECVD; however, the multiscale modeling techniques presented in this dissertation have revealed two key means to improve product quality: (1) batch-to-batch operational control through the use of EWMA algorithms which manipulate substrate temperatures, and (2) the exploration of new reactor geometries which limit spatial variations in the concentration of SiH_3 in the boundary layer above the wafer surface. These efforts have resulted in optimized PECVD showerhead designs and spatial temperature profiles which limit the thin film thickness non-uniformity to within 1% of the product specification.

Bibliography

[1] E. Amanatides, S. Stamou, and D. Mataras. Gas phase and surface kinetics in plasma enhanced chemical vapor deposition of microscrystalline silicon: The combined effect of RF power and hydrogen dilution. *Journal of Applied Physics*, 90(11):5786–5797, 2001.

[2] C. Ance and N.M. Ravindra. Departure of hydrogen from *a*-Si:H. *Physica Status Solidi*, 77:241–248, 1983.

[3] ANSYS Inc. *ANSYS Fluent Theory Guide 15.0 (November)*, November 2013.

[4] I. Aviziotis, N. Cheimarios, T. Duguet, C. Vahlas, and A. Boudouvis. Multiscale modeling and experimental analysis of chemical vapor deposited aluminum films: Linking reactor operating conditions with roughness evolution. *Chemical Engineering Science*, 155:449–458, 2016.

[5] T. Bakos, M. Valipa, and D. Maroudas. Thermally activated mechanisms of hydrogen abstraction by growth precursors during plasma deposition of silicon thin films. *Journal of Chemical Physics*, 122:1–10, 2005.

[6] T. Bakos, M. Valipa, and D. Maroudas. First-principles theoretical analysis of silyl radical diffusion on silicon surfaces. *Journal of Chemical Physics*, 125:1–9, 2006.

[7] E. Bertran, J.L. Andujar, A. Canillas, C. Roch, J. Serra, and G. Sardin. Effects of deposition temperature on properties of r.f. glow discharge amorphous silicon thin films. *Thin Solid Films*, 205:140–145, 1991.

[8] M. Brodsky, M. Frisch, J. Ziegler, and W. Lanford. Quantitative analysis of hydrogen in glow discharge amorphous silicon. *Applied Physics Letters*, 30:561–563, 1977.

[9] A. Campa, O. Isabella, R. Erven, P. Peeters, H. Borg, J. Krc, M. Topic, and M. Zeman. Optimal design of periodic surface texture for thin-film *a*-Si:h solar cells. *Progress in Photovoltaics: Research and Applications*, 18:160–167, 2010.

[10] N. Cheimarios, G. Kokkoris, and A.G. Boudouvis. A multi-parallel multiscale computational framework for chemical vapor deposition processes. *Journal of Computational Science*, 15:81–85, 2016.

[11] P. D. Christofides and A. Armaou. Control and optimization of multiscale process systems. *Computers and Chemical Engineering*, 30:1670–1686, 2006.

[12] D. Collins, A. Strojwas, and D. White. A CFD model for the PECVD of silicon nitride. *IEEE transactions on semiconductor manufacturing*, 7:176–183, 1994.

[13] M. Crose, Kwon, JSI., M. Nayhouse, D. Ni, and P. D. Christofides. Multiscale modeling and operation of PECVD of thin film solar cells. *Chemical Engineering Science*, 136:50–61, 2015.

[14] M. Crose, Kwon, JSI., A. Tran, and P. D. Christofides. Multiscale modeling and run-to-run control of PECVD of thin film solar cells. *Renewable Energy*, 100:129–140, 2017.

[15] M. Crose, A. Tran, and P. D. Christofides. Multiscale computational fluid dynamics: Methodology and application to PECVD of thin film solar cells. *Coatings*, 7:23, 2017.

[16] M. Crose, W. Zhang, A. Tran, and P. D. Christofides. Multiscale three-dimensional CFD modeling for PECVD of amorphous silicon thin films. *Computers & Chemical Engineering*, 113:184–195, 2018.

[17] D. Culler, J. Singh, and A. Gupta. *Parallel computer architecture: a hardware/software approach*. Gulf Professional Publishing, 1999.

[18] A. da Silva and N. Morimoto. Gas flow simulation in a PECVD reactor. In *2002 International Conference on Computational Nanoscience and Nanotechnology*, pages 22–25, 2002.

[19] D. Economou, S. Park, and D. Williams. Uniformity of etching in parallel plate plasma reactors. *Journal of the Electrochemical Society*, 136:188–198, 1989.

[20] C. Eisele, C. E. Nebel, and M. Stutzmann. Periodic light coupler gratings in amorphous thin film solar cells. *Journal of Applied Physics*, 89:7722–7726, 2001.

[21] H. Fritzsche, M. Tanielian, C. Tsai, and P. Gaczi. Hydrogen content and density of plasma-deposited amorphous silicon-hydrogen. *Journal of Applied Physics*, 50:3366–3369, 1979.

[22] R. Fu, T. James, D. Chung, D. Gagne, A. Lopez, and A. Dobos. Economic competitiveness of US utility-scale photovoltaics systems in 2015: Regional cost modeling of installed cost $(/W)andLCOE($/kWh). In *Photovoltaic Specialist Conference (PVSC), 2015 IEEE 42nd*, pages 1–11. IEEE, 2015.

[23] O. Gabriel, S. Kirner, M. Klick, B. Stannowski, and R. Schlatmann. Plasma monitoring and PECVD process control in thin film silicon-based solar cell manufacturing. *EPJ Photovoltaics*, 55202:1–9, 2014.

[24] A. Gallagher. Neutral radical deposition from silane discharges. *Journal of Applied Physics*, 63:2406–2413, 1988.

[25] M. Geis, D. Flanders, and H. Smith. Crystallographic orientation of silicon on an amorphous substrate using an artificial surface-relief grating and laser crystallization. *Applied Physics Letters*, 35:71–74, 1979.

[26] D. Gerogiorgis and B. Ydstie. Multiphysics CFD modelling for design and simulation of a multiphase chemical reactor. *Chemical Engineering Research & Design*, 83:603–610, 2005.

[27] M. Green, K. Emery, Y. Hishikawa, W. Warta, and E. Dunlop. Solar cell efficiency tables. *Progress in Photovoltaics: Research and Applications*, 22(7):701–710, 2014.

[28] C. Heine and H. Rudolf. Submicrometer gratings for solar enery applications. *Applied Optics*, 34(14):2476–2482, 1995.

[29] J. Huang, G. Orkoulas, and P. D. Christofides. Modeling and control of Transparent Conducting Oxide layer surface morphology for improved light trapping. *Chemical Engineering Science*, 74:135–147, 2012.

[30] J. Huang, G. Orkoulas, and P. D. Christofides. Surface morphology control of transparent conducting oxide layers for improved light trapping using wafer grating and feedback control. *Chemical Engineering Science*, 81:191–201, 2012.

[31] N. Ingle and T. Mountziaris. A multifrontal algorithm for the solution of large systems of equations using network-based parallel computing. *Computers & Chemical Engineering*, 19:671–681, 1995.

[32] O. Isabella, J. Krc, and M. Zeman. Modulated surface textures for enhanced light trapping in thin-film silicon solar cells. *Applied Physics Letters*, 97:101106, 2010.

[33] O. Isabella, F. Moll, J. Krc, and M. Zeman. Moldulated surface textures using zinc-oxide films for solar cells applications. *Physica Status Solidi*, 207:642–646, 2010.

[34] M. Kabir, S. Shahahmadi, V. Lim, S. Zaidi, K. Sopian, and N. Amin. Amorphous silicon single-junction thin-film solar cell exceeding 10% efficiency by design optimization. *International Journal of Photoenergy*, 2012:1–7, 2012.

[35] W. Kern. *Thin Film Processes II*. Academic Press, 1991.

[36] I. G. Kevrekidis, C. W. Gear, and G. Hummer. Equation-free: the computer-aided analysis of complex multiscale systems. *AIChE Journal*, 50:1346–1355, 2004.

[37] Y. Kim, J. Boo, B. Hong, and Y. Kim. Effects of showerhead shapes on the flowfields in a RF-PECVD reactor. *Surface and Coatings Technology*, 193:88–93, 2005.

[38] J. Knights and G. Lucovsky. Hydrogen in amorphous semiconductors. *Critical Reviews in Solid State and Materials Sciences*, 9:211–283, 1980.

[39] B.A. Korevaar, G.J. Adriaenssens, A.H.M. Smets, W.M.M. Kessels, H.-Z. Song, M.C.M. van de Sanden, and D.C. Schram. High hole drif mobility in a-Si:H deposited at high growth rates for solar cell application. *Journal of Non-Crystalline Solids*, 266-269:380–384, 2000.

[40] M. Kreiger, D. Shonnard, and J. Pearce. Life cycle analysis of silane recycling in amorphous silicon-based solar photovoltaic manufacturing. *Resources, Conservation and Recycling*, 70:44–49, 2013.

[41] M. Kushner. A model for the discharge kinetics and plasma chemistry during plasma enhanced chemical vapor deposition of amorphous silicon. *Journal of Applied Physics*, 63:2532–2551, 1988.

[42] Kwon, JSI., M. Nayhouse, and P. D. Christofides. Multiscale, multidomain modeling and parallel computation: Application to crystal shape evolution in crystallization. *Industrial and Engineering Chemistry Research*, 54:11903–11914, 2015.

[43] Kwon, JSI., M. Nayhouse, G. Orkoulas, D. Ni, and P. D. Christofides. A method for handling batch-to-batch parametric drift using moving horizon estimation: Application to run-to-run mpc of batch crystallization. *Chemical Engineering Science*, 127:210–219, 2015.

[44] Kwon, JSI., M. Nayhouse, G. Orkoulas, D. Ni, and P. D. Christofides. Run-to-run-based model predictive control of protein crystal shape in batch crystallization. *Industrial and Engineering Chemistry Research*, 54:4293–4302, 2015.

[45] R. Lam and D. G. Vlachos. Multiscale model for epitaxial growth of films: Growth mode transition. *Physical Review B*, 64:035401, 2001.

[46] J. Lee, Y. Choi, B. Lee, and B. Ahn. Microwave-induced low-temperature crystallization of amorphous silicon thin films. *Journal of Applied Physics*, 82:2918–2921, 1997.

[47] H. Li, Q. Wang, J. Chen, J. Krc, and W. J. Soppe. Light trapping in amorphous silicon solar cells with periodic grating structures. *Optics Communications*, 285:808–815, 2011.

[48] Y. Lou and P. D. Christofides. Estimation and control of surface roughness in thin film growth using kinetic monte-carlo models. *AIChE Journal*, 58:3115–3129, 2003.

[49] C. Manfredotti, F. Fizzotti, M. Boero, P. Pastorino, P. Polesello, and E. Vittone. Influence of hydrogen-bonding configurations on the physical properties of hydrogenated amorphous silicon. *Physical Review B*, 50:18046–18053, 1994.

[50] D. Maroudas. Multiscale modeling of hard materials: challenges and opportunities for chemical engineering. *AIChE Journal*, 46:878–882, 2000.

[51] P. Menna, G. Di Francia, and V. La Ferrara. Porous silicon in solar cells: A review and a description of its application as an AR coating. *Solar Energy Materials and Solar Cells*, 37:13–24, 1995.

[52] A. Nakano, M. Bachlechner, R. Kalia, E. Lidorikis, P. Vashishta, G. Voyiadjis, T. Campbell, S. Ogata, and F. Shimojo. Multiscale simulation of nanosystems. *Computing in Science & Engineering*, 3:56–66, 2001.

[53] P. Novikov, A. Donne, S. Cereda, L. Miglio, S. Pizzini, S. Binetti, M. Rondanini, C. Cavallotti, D. Chrastina, T. Moiseev, H. Kanel, G. Isella, and F. Montalenti. Crystallinity and microstructure in Si films grown by plasma-enhanced chemical vapor deposition: A simple atomic-scale model validated by experiments. *Applied Physics Letters*, 94:051904, 2009.

[54] S. Pandey, T. Singh, and D. Maroudas. Kinetic Monte Carlo simulations of surface growth during plasma deposition of silicon thin films. *The Journal of Chemical Physics*, 131:034503, 2009.

[55] S. Park and D. Economou. A mathematical model for etching of silicon using CF_4 in a radial flow plasma reactor. *Journal of Electrochemical Society*, 138:1499–1508, 1991.

[56] J. Perrin, M. Shiratani, P. Kae-Nune, H. Videlot, J. Jolly, and J. Guillon. Surface reaction probabilities and kinetics of H, SiH_3, Si_2H_5, CH_3, and C_2H_5 during deposition of *a*-Si:H and *a*-C:H from H_2, SiH_4, and CH_4 discharges. *Journal of Vacuum Science & Technology A*, 16:278–289, 1998.

[57] S. Rasoulian and L.A. Ricardez-Sandoval. Uncertainty analysis and robust optimization of multiscale process systems with application to epitaxial thin film growth. *Chemical Engineering Science*, 116:590–600, 2014.

[58] S. Rasoulian and L.A. Ricardez-Sandoval. A robust nonlinear model predictive controller for a multiscale thin film deposition process. *Chemical Engineering Science*, 136:38–49, 2015.

[59] B. Rech, T. Roschek, J. Muller, S. Wieder, and H. Wagner. Amorphous and microcrystalline silicon solar cells prepared at high deposition rates using RF (13.56 MHz) plasma excitation frequencies. *Solar Energy Materials & Solar Cells*, 66:267–273, 2001.

[60] B. Rech and H. Wagner. Potential of amorphous silicon for solar cells. *Applied Physics A*, 69:155–167, 1999.

[61] J. Robertson. Deposition mechanism of hydrogenated amorphous silicon. *Journal of Applied Physics*, 87(5):2608–2617, 2000.

[62] S. Rodgers and K. Jensen. Multiscale modeling of chemical vapor deposition. *Journal of Applied Physics*, 83:524–530, 1998.

[63] H. Sai, H. Fujiwara, M. Kondo, and Y. Kanamori. Enhancement of light trapping in thin-film hydrogenated microcrystalline Si solar cells using back reflectors with self-ordered dimple pattern. *Applied Physics Letters*, 93:143501, 2008.

[64] L. Sansonnens, J. Bondkowski, S. Mousel, J.P.M. Schmitt, and V. Cassagne. Development of a numerical simulation tool to study uniformity of large area PECVD film processing. *Thin Solid Films*, 427:21–26, 2003.

[65] A.H.M. Smets, W.M.M. Kessels, and M.C.M. van de Sanden. Vacancies and voids in hydrogenated amorphous silicon. *Applied Physics Letters*, 82:1547–1549, 2003.

[66] D. Staebler and C. Wronski. Optically induced conductivity changes in discharge-produced hydrogenated amorphous silicon. *Journal of Applied Physics*, 51:3262–3268, 1980.

[67] U. Stephan, J. Kuske, H. Gruger, and A. Kottwitz. Problems of power feeding in large area PECVD of amorphous silicon. *Mat. Res. Soc. Symp. Proc.*, 557:157–162, 1999.

[68] D. Tanenbaum, A. Laracuente, and A. Gallagher. Surface roughening during plasma-enhanced chemical-vapor deposition of hydrogenated amorphous silicon on crystal silicon substrates. *Physical Review B*, 56(7):4243–4250, 1997.

[69] D. Tsalikis, C. Baig, V. Mavrantzas, E. Amanatides, and D. Mataras. A hybrid kinetic Monte Carlo method for simulating silicon films grown by plasma-enhanced chemical vapor deposition. *Journal of Chemical Physics*, 139:204706, 2013.

[70] A. J. M. van Erven, R. H. Franken, J. Ruijter, P. Peeters, W. Vugts, O. Isabella, M. Zeman, and C. Haase. Controlled texturing of thin film silicon solar cell substrates. In *Proceedings of 23rd European photovoltaic Solar Energy Conference*, Valencia, Spain, 2008.

[71] D. G. Vlachos. Multiscale integration hybrid hlgorithms for homogeneous-heterogeneous reactors. *AIChE Journal*, 43:3031–3041, 1997.

[72] D. G. Vlachos. A review of multiscale analysis: examples from systems biology, materials engineering, and other fluid-surface interacting systems. *Advances in Chemical Engineering*, 30:1–61, 2005.

[73] C. Yang, L. Smith, C. Arthur, and G. Parsons. Stability of low-temperature amorphous silicon thin film transistors formed on glass and transparent plastic substrates. *Journal of Vacuum Science & Technology B*, 18:683–689, 2000.

[74] M. Zeman, J.A. Willemen, L.L.A. Vosteen, G. Tao, and J.W. Metselaar. Silicon modelling of current matching in *a*-Si:H/*a*-Si:H tandem solar cells on textured TCO substrates. *Solar Energy Materials & Solar Cells*, 46:81–99, 1997.

[75] L. Zeng, P. Bermel, Y. Yi, B. Alamariu, K. Broderick, J. Liu, C. Hong, X. Duan, J. Joannopoulos, and L. Kimberling. Demonstration of enhanced absorption in thin film Si solar cells with textured photonic crystal back reflector. *Applied Physics Letters*, 93:221105, 2008.